An optimal framework of investment strategy in brownfields redevelopment by integrating site-specific hydrogeological and financial uncertainties

by

Soonyoung Yu

A thesis

presented to the University of Waterloo

in fulfillment of the

thesis requirement for the degree of

Doctor of Philosophy

in

Earth Sciences

Waterloo, Ontario, Canada, 2009

AUTHOR'S DECLARATION

I hereby declare that I am the sole author of this thesis. This is a true copy of the thesis, including any required final revisions, as accepted by my examiners.

I understand that my thesis may be made electronically available to the public.

Abstract

Brownfields redevelopment has been encouraged by governments or the real estate market because of economic, social and environmental benefits. However, uncertainties in contaminated land redevelopment may cause massive investment risk and need to be managed so that contaminated land redevelopment is facilitated. This study was designed to address hydrogeological as well as economic uncertainty in a hypothetical contaminated land redevelopment project and manage the risk from these uncertainties through the integration of the hydrogeological and economic uncertainties. Hydrogeological uncertainty is derived from incomplete site information, including aquifer heterogeneity, and must be assessed with scientific expertise, given the short history of redevelopment projects and their unique hydrogeological characteristics. Hydrogeological uncertainty has not yet been incorporated in one framework with the economic uncertainty that has been relatively well observed in financial markets.

   Two cases of Non-Aqueous Phase Liquid (NAPL) contamination were simulated using a physically-based hydrogeological model to address hydrogeological uncertainty: one concerns the effect of an ethanol spill on a light NAPL (LNAPL) contaminated area in the vadose zone, and the other is regarding the vapour phase intrusion of volatile organic compounds, in particular, Trichloroethylene (TCE), a dense NAPL (DNAPL), into indoor air through a variably saturated heterogeneous aquifer. The first simulation replicated experimental observations in the laboratory, such as the capillary fringe depressing and the NAPL pool remobilizing and collecting in a reduced area exhibiting higher saturations than observed prior to an ethanol injection. However, the data gap, in particular, on the chemical properties between the model and the experiment caused the uncertainty in the model simulation. The second NAPL simulation has been performed based on a hypothetical scenario where new dwellings in a redeveloped area have the potential risk of vapour phase intrusion from a subsurface source into indoor air because remediation or foundation design might fail. The simulation results indicated that the aquifer heterogeneity seemed the most significant factor controlling the indoor air exposure risk from a TCE source in the saturated zone. Then, the exposure risk was quantified using Monte Carlo simulations with 50 statistically equivalent heterogeneous aquifer permeability fields. The quantified risk (probability) represents the hydrogeological

uncertainty in the scenario and gives the information on loss occurrence intensity of redevelopment failure.

Probability of failure (or loss occurrence intensity) was integrated with cost of failure (or loss magnitude) to evaluate the risk capital in the hypothetical brownfields redevelopment project. The term "risk capital" is adopted from financial literature and is the capital you can lose from high risk investment. Cost of failure involves economic uncertainty and can be defined based on a developer's financial agreement with new dwellers to prevent litigation in the case of certain events, such as an environmental event where indoor air concentrations of pollutants exceed regulatory limits during periodic inspections. The developer makes such a financial agreement with new dwellers because new dwellings have been constructed founded on flawed site information, and municipalities may require it if a land use planning approval is required. An agreement was presumed that the developer would repurchase the affected houses from new dwellers immediately, if indoor air contamination exceeded the regulatory limit. Furthermore, the developer would remediate any remaining contamination, demolish the affected houses and build new houses if they were worth investing in. With this financial plan assumed, the stochastic housing price, stochastic inflation rate and stochastic interest rate have been considered to cause the uncertainty in the cost of failure, and the information on these stochastic variables was obtained from the financial market due to its long history of observations.

This research reviewed appropriate risk capital valuation methods for hydrogeologists to apply straightforwardly to their projects, with integrating probability of failure (hydrogeological uncertainty) and cost of failure (economic uncertainty). The risk capital is essentially the probability of failure times the cost of failure with safety loading added to compensate investors against hydrogeological and financial uncertainty. Fair market prices of risk capital have been valuated using financial mathematics and actuarial premium calculations, and each method has a specific safety loading term to reflect investors' level of risk aversion. Risk capital results indicated that the price of the risk capital was much more sensitive to hydrogeological uncertainty than financial uncertainty. Developers can manage the risk capital by saving a contingency fee for future events or paying an insurance premium, given that the price of this risk capital is the price of a contingent claim, subsequent to failure in remediation or in foundation design, and equivalent to an environmental insurance premium if there is an insurance company to indemnify the liability for the developer.

The optimal framework of investment strategy in brownfields redevelopment can be built by linkage of addressing and integrating uncertainties and valuating risk capital from the uncertainties. This framework involves balancing the costs associated with each step while maximizing a net profit from land redevelopment. The optimal investment strategy, such as if or when to remediate or redevelop and to what degree, is given when the future price of the land minus time and material costs as well as the contingency fee or insurance premium maximizes a net profit.

Acknowledgements

I would like to thank my supervisor Dr. Andre J.A. Unger for his guidance, insight and patience. If it had not been for his continuous encouragement, I could not have finished my research.

I would also like to thank Dr. Edward Sudicky, Dr. James F. Barker, Dr. Beth Parker, and Dr. John A. Cherry for their technical advice as well as financial support, and give thanks to Dr. Sorab Panday for his expertise.

I also thank Dr. James E. Smith, Dr. Brent Sleep, and Dr. Margaret Insley for kindly reviewing my dissertation and giving me critical comments, and give thanks to Dr. Adam Kolkiewicz for his advice on the Chapter 4 to proceed and Dr. John Chatzis and Juliana G. Freitas for the laboratory experiments to complete the Chapter 2.

I also thank Korea Institute of Geoscience and Mineral Resources for a research grant, and thank Korea Science and Engineering Foundation for Graduate Study Abroad Scholarship.

Last, I thank my family for their love and support. Most importantly, I thank my husband, Gitak Chae for his unending love and support.

Dedication

To my husband, Gitak

Table of Contents

List of Tables

List of Figures

Chapter 1
Introduction

1.1 Background

Land contaminations have been investigated and remediated with the help of innovative techniques, and redevelopment of contaminated lands has been encouraged by governments because of the economic, social, and environmental benefits of doing so (*US EPA*, 1999; *NRTEE*, 2003; *UK Environment Agency*, 2003). In addition, the real estate market has often appraised contaminated lands to be valuable due to their optimal location for business. Brownfields are the term to name these abandoned or underused industrial and commercial facilities available for re-use. On the other hand, investors hesitate to commit to redeveloping contaminated land owing to flawed site investigation information and market uncertainties. The defective awareness causes a risk for investors, and lack of certainty makes investors risk averse. Thus, a need exists to manage this risk so that the redevelopment of contaminated lands can be facilitated. Hydrogeologists have an important role in this risk management process, given that every site has the unique hydrogeological uncertainty.

NAPLs are one of the primary land contaminants because of their application in numerous areas and notable taint of many sites. Investigation methods and remediation technologies for NAPL contaminations have been productively improved, e.g. US EPA's Technology Innovation Program since the early 1980s which marked the huge influx of groundwater contamination reports (*Rivett et al.*, 1990). However, understanding NAPL transport in subsurface environments is still challenging, in particular, LNAPL behaviour in the vadose zone. The vadose zone consists of multiple phases and is a non-linear system if numerically modeled. In addition, the estimation of DNAPL movement in a variably saturated heterogeneous aquifer is demanding as a result of its density being greater than water. These kinds of difficulties prevent investigators from obtaining clear information on subsurface environments, and subsequently, hydrogeological uncertainties hamper decision-makers. Contingent on hydrogeological strategy failures in environmental investigation and remediation, investors may face financial losses, whose magnitudes depend on uncertain economic market conditions.

Currently, numerical models are considered significant tools to assess uncertainties in many fields, including hydrogeology. In particular, hydrogeological and financial uncertainties must be assessed in contaminated land redevelopment and integrated with the expertise of hydrogeologists. On their part, hydrogeologists need to understand optimal financial strategies and how to employ optimal hydrogeological techniques on a limited budget. However, no research has tried to integrate site-specific hydrogeological uncertainty and economic uncertainty in one framework, although both significantly affect investment in contaminated land. For example, studies on hydrogeological uncertainties exist, but the results are incorporated into cost-benefit analysis without the risk capital considered (*Oamek*, 1990; *Andersson and Destouni*, 2001; *Bayer et al.*, 2005; *Zhang et al.*, 2005) or into exposure modeling (*Bennett et al.*, 1998); as well many well-developed financial models refer to insufficient historical data on hydrogeological uncertainties and simplify natural phenomena (*Paleologos and Lerche*, 2002). In addition, numerical simulations related to NAPL contamination are performed under several assumptions about contaminant properties or hydrogeological conditions, so that simulations are simplified. These assumptions leave hydrogeological uncertainties to be dealt with in model predictions (*Vrugt et al.*, 2005). In most cases, however, these uncertainties are ignored when any further action is taken; the simplified simulation leads to unsuitable actions. The absence of in-depth study may threaten remediation projects with failure, even though detailed research on NAPL contamination has been performed in the field. Moreover, partial source removal is chosen as a cost-effective remediation method due to limited budgets and incomplete hydrogeological knowledge (*ITRC*, 2002). This reality puts a big burden to decision-makers and occasionally results in very long and costly court cases due to remediation failures.

One method to alleviate the risk of investigation or remediation failures is the purchase of environmental insurance. Environmental insurance has been developed to provide a better strategy for developers and investors in highly uncertain environmental projects (*Woll et al.*, 2003; *Munich Re*, 2006). In addition, financial contracts can be used as risk transfer mechanism; a hypothesis has been tested that an option contract may be a viable instrument for achieving efficient sharing of hydrological risks by *Conrad and Lopez* (2002) and *Gomez Ramos and Garrido* (2004). However, the incomplete information on site investigation and remediation causes insurance companies (or financial sectors) to avoid indemnifying the insured against investigation and remediation failures (*Hara*, 2003). To augment this insufficient historical and site-specific information, scientific assessments are needed to better address loss occurrence intensity (probability of failure) and loss

2

magnitude (cost of failure) distribution in environmental investigation and remediation projects. Environmental insurance in brownfields redevelopment is analogous to catastrophe insurance, and many studies on catastrophe insurance pricing have highlighted the importance of well-specified risks. *Heal and Kunreuther* (2009) review federal government's liabilities arising from the environmental risk management, such as climate change, and talk about the difficulty of private insurers in insuring the low frequency risks. *Michel-Kerjan and Kousky* (2009) observe the flood insurance market and discuss how actuarial rates are determined in the yearly rate reviews, with an emphasis on the problems from National Flood Insurance Program (NFIP)'s pricing strategy of basing rates on a historical average loss year.

1.2 Objectives

This study aims to define and integrate uncertainties in a highly problematic project and price the risk capital from the uncertainties using a physically-based hydrogeological model as well as financial and actuarial valuation methods. The term "risk capital" is adopted from financial literature and is the capital you can lose from high risk investment. This study outlines a framework to incorporate hydrogeological and economic uncertainties and summarizes several methods to valuate the risk capital.

   For these objectives, this study supposes a contaminated land redevelopment project as a case study. The project has bigger investment risks due to the stigma of contamination history than uncontaminated land redevelopment. In addition, a land developer is presumed, who is an investor as well. The developer is in charge of any financial liability from failures in investment decisions. The failure risk is derived from the possibility that remediation is performed based on incomplete hydrogeological information, and the remediation and foundation design could fail and cause extra costs. The magnitude of the extra cost contingent on remediation and foundation design failures depends on uncertain economic conditions, even though the magnitude can be deterministic dependent on the agreement between the developer and new dwellers. As well, the future value of the redeveloped land, which is revenue to the investor, may not meet the total investment cost.

   Based on the scenario, three individual activities have been carried out in Chapters 2 to 4, and each activity has a detailed objective: Chapter 2, "Simulating the Evolution of an Ethanol and Gasoline

Source Zone within the Capillary Fringe", develops a sophisticated numerical model to reproduce the laboratory-scale experimental observations in a three-phase system, and deals with the uncertainty in contaminant properties; Chapter 3, "Simulating the Fate and Transport of TCE from Groundwater to Indoor Air", assesses hydrogeological uncertainties, mainly caused from the imperfect information on hydrogeological properties; Chapter 4, "Allocating Risk Capital for a Brownfields Redevelopment Project under Hydrogeological and Financial Uncertainty", integrates the hydrogeological uncertainty from Chapter 3 and the economic uncertainty of the market, and valuates the risk capital from both uncertainties. Actuarial premium calculations and financial mathematics are summarized in Chapter 4 as risk capital valuation methods. The whole concept is applicable to a real site, although the risk capital is valuated using a conceptual scenario.

1.3 Scope

Two case studies of NAPL contaminations are simulated using a scientific numerical model to address hydrogeological uncertainties: one case in Chapter 2 involves the effect of an ethanol spill on a LNAPL-contaminated site in the vadose zone, and the other in Chapter 3 is the effect of vapour phase transport of organic contaminants in the saturated zone on indoor air quality. For simulation of the two cases, a multi-phase multi-compositional numerical model, *CompFlow Bio*, is modified. The model has several advantages for simulating NAPL movement (*Forsyth*, 1993): First, it outputs a fully-coupled solution (multiple unknowns per node), using full Newton iterations to handle nonlinearities. NAPL dissolution switches, for causing NAPL appearance, and blending parameters are used to smooth out convective terms near zero. In addition, automatic primary variable (i.e., saturations, pressures, component mole fractions, and biomass) switching is applied to speed convergence of nonlinear Newton iterations and enhance robustness. Positive mole fractions and saturations are ensured, and variable spatial weighting of advective mole fraction terms can be applied, including a nonlinear flux limiter to reduce numerical dispersion. Moreover, an adaptive time stepping procedure is included, and a highly efficient conjugated gradient-like block matrix solver employing CGSTAB acceleration is used. The *CompFlow Bio* computer code is written in C++ and runs on a variety of computer platforms, including mainframes and personal computers. *CompFlow Bio* is written in a modular structure that facilitates modifications to the source code. If modifications

are made, the program must be recompiled with a C++ compiler to incorporate the changes into the executable version of the computer code. The compiling procedure varies depending on the computing system and C++ software.

Specifically, Chapter 2 provides the hydrogeological model validation. The model is developed to simulate pore-scale impacts of a cosolvent (ethanol), such as reduction in surface/interfacial tension and enhanced solubility. The simulation results, despite the uncertain chemical properties, are compared to laboratory-scale experiments. Ethanol has begun to be used as an oxygenate instead of MTBE (Ethanol Advisory Panel Report, Manitoba, Canada, 2002; MTBE Elimination Act proposed, USA, 2006), and considered an alternative fuel (Brazilian ethanol program, Brazil, 1975; Ethanol Expansion Program, Canada, 2004; Renewable Fuel Standards, USA, 2005). Therefore, the effect of ethanol spills on subsurface environments, particularly on residual gasoline in the vadose zone, needs to be addressed, given that inadvertent releases of ethanol during handling and storage into soil previously contaminated by gasoline and related hydrocarbons are possible. New observations have been reported on ethanol impacts: collapsed capillary fringe (*Capiro et al*., 2007*; Freitas* , 2009), enhanced gasoline solubility (*Heermann and Powers*, 1998; *Ji and Brusseau*, 1998), and remobilization of residual LNAPL (*McDowell and Powers,* 2003; *McDowell et al.,* 2003), which need to be simulated by numerical models to be understood clearly.

In addition, vapour phase transport in subsurface environments has been regarded as one of the long-term sources of indoor air contamination, and concerns about the relationship between indoor air quality and subsurface contamination of NAPL have arisen (*US EPA*, 2008). However, site-specific pathways of the vapour intrusion are still not understood well. In particular, the role of controlling factors of contamination pathways between the saturated zone and indoor air through the vadose zone needs to be addressed and simulated if indoor air quality is to be protected. Therefore, in Chapter 3, using the same physically-based hydrogeological model, the hydrogeological uncertainty is assessed based on a hypothetical scenario with various impact factors considered, and attenuation factors from the simulation results are compared to those from the current *de facto* industry standard approach, *Johnson and Ettinger* (1991) heuristic model. A TCE-contaminated site is assumed, which has already been cleaned up in compliance with the governing regulatory agency (Federal Contaminated Sites Action Plan, Canada; Superfund, or Comprehensive Environmental Response, Compensation, and Liability Act (CERCLA), USA) and is going to be redeveloped for a residential dwelling. Given the possibility that a residual TCE source zone remains in the saturated zone even after cleanup and

that the foundation design of new dwellings fails, some day in the future new residential houses may face indoor air contamination exceeding the regulatory limits. Various factors contributing to uncertainty in future indoor air quality include aquifer heterogeneity, source zone location, barometric pressure fluctuation, foundation slab cracks, indoor air pressure drop, capillary fringe thickness, and infiltration rates, which would affect the volatilization and transport of TCE through the vadose zone to indoor air. Last, a way to quantify hydrogeological uncertainty is shown, which takes into account the probability that indoor air contamination levels exceed recommended ones and uses the Monte Carlo method with a major controlling factor (aquifer heterogeneity) uncertain. The probability of exceeding a regulatory limit is a good representation of the environmental risk. *Andersson and Destouni* (2001) quantify the risk (probability) to exceed environmental regulation standards for ground water quality and couple this risk quantification with an analysis of abatement costs for attaining an acceptable risk level. In addition, the Monte Carlo method has been applied to uncertainty analysis for contaminant transport simulation in *Tiedeman and Gorelick* (1993); *James and Oldenburg* (1997); *Wladis et al.* (1999); *Freeze and Gorelick* (1999). *Bayer et al.* (2005) examine the performance characteristics of pump-and-treat systems under heterogeneous flow conditions based on Monte Carlo analyses comprising 500 equally probable realizations of the spatial transmissivity distribution. For a given ensemble of 500 realizations, the calculated minimum pumping rates are sorted to obtain probability density curves of the pumping rate. *James and Oldenburg* (1997) estimate the required number of Monte Carlo simulations, based on the theory of *Morgan and Henrion* (1990); while the theory is ignored in the study to save computational costs.

Risk management requires loss occurrence intensity (probability of failure or loss frequency) and loss magnitude (cost of failure or loss severity) information. The quantified hydrogeological uncertainty in the contaminated land redevelopment in Chapter 3 can be used as loss occurrence intensity of redevelopment failure, while loss magnitude distribution at environmental accidents can be defined from the economic uncertainty in the market. Many economic factors affect loss magnitude in contaminated land redevelopment, while the uncertainty in housing prices as well as uncertainty in inflation rates and interest rates is considered for this study. Then, the intensity of damage in the future for a representative building (hydrogeological uncertainty) is combined with economic loss distribution at environmental accidents (economic uncertainty) in Chapter 4, which focuses on risk capital valuation. Several methods from actuarial and financial mathematics are applied to incorporation of the economic and hydrogeological uncertainties and evaluation of the risk

capital from the uncertainties. The risk capitals from each method are then compared. *Massmann and Freeze* (1987a, b); *Freeze et al.*(1990); *Massmann et al.* (1991); *Freeze and Gorelick* (1999) consider the risk term comparable to the risk capital in Chapter 4, and their risk-cost-benefit analysis is similar to the framework this study proposes. The significant different between this study and their studies is that they assume the economic loss associated with hydrogeological failure to be a constant within a range. In contrast, this study defines the economic loss specified by an agreement between the investor and dwellers, with economic uncertainty considered.

To date, Chapter 2's numerical simulation of the ethanol impacts on a LNAPL source zone has been published as:

Yu, Soonyoung, Freitas, Juliana G., Unger, Andre J.A., Barker, James F., and Chatzis , John. 2009. Simulating the evolution of an ethanol and gasoline source zone within the capillary fringe, *Journal of Contaminant Hydrology*, 105(1-2), 1-17.

The publication was led by Yu, the author of this thesis, with the help of co-authors: Freitas, as a graduate student in the University of Waterloo, preformed the laboratory experiments to observe the evolution of an ethanol-gasoline source zone; Dr. Unger, as my supervisor, guided me to develop the numerical model and write the publication; Dr. Barker, as Freitas' supervisor, motivated this numerical model-experiment comparison and helped me to write the introduction of the publication; Dr. John provided the laboratory equipment and discussed the dispersion issue with Freitas and me. I, Soonyoung Yu, developed the numerical model to replicate the laboratory experiments with incorporating the significant impacts of chemical components on the three phase system into the model, compared the numerical model results to laboratory experiments, interpreted the comparison, and wrote the above publication as the first author.

The simulation results for vapour phase transport in Chapter 3 have been published as:

Yu, Soonyoung, Unger, Andre J.A., and Parker, Beth. 2009. Simulating the fate and transport of TCE from groundwater to indoor air. *Journal of Contaminant Hydrology*, 107(3-4), 140-161.

The objective of the publication was reached by Yu, the author of this thesis, with the encouragement of co-authors: Dr. Unger, as my supervisor, supervised me to develop the numerical model and write the publication; Dr. Parker provided the previous literature on vapor phase transport experiments and helped the writing of the above publication from the practical perspective. I, Soonyoung Yu, developed the numerical model to understand the significant factors controlling the indoor air exposure risk from a subsurface source in a variably saturated heterogeneous aquifer, compared the simulation results to those by the *Johnson and Ettinger* (1991) heuristic model, predicted the indoor air exposure risk and assessed the probability of failure, and wrote the above publication as the first author.

In addition, the research in Chapter 4, which considers the risk capital valuation, has been submitted for publication as:

Yu, Soonyoung, Unger, Andre J.A., Parker, Beth, and Kim, Taehee. 2009. Allocating risk capital for a brownfields redevelopment project under hydrogeological and financial uncertainty, submitted for publication to *Advances in Water Resources*.

The research for the publication was performed by Yu, the author of this thesis, with the support of co-authors: Dr. Unger, as my supervisor, helped me to write the publication; Dr. Parker and Dr. Kim encouraged me to finish this research with financial support. I, Soonyoung Yu, reviewed documents on brownfields redevelopment guideline to build a conceptual scenario, studied financial and actuarial literature to understand appropriate risk capital valuation methods, estimated the risk capital for the conceptual scenario, and wrote the above publication as the first author.

1.4 Contributions

This thesis provides a simplified methodology that incorporates hydrogeological and economic uncertainties in a framework so that the risk capital involved in highly problematic projects can be evaluated. The main advantages of this methodology are that hydrogeological uncertainty is site-

specifically assessed and that a fair price of the risk capital is valuated by generally accepted actuarial and financial mathematics. Little research has studied both hydrogeological uncertainty assessment and risk valuation methodology in a framework, leading to inaccurate risk management.

The proposed methodology will help hydrogeologists and investors understand the risk capital valuation in redevelopment projects. The estimation of the risk capital involved if indoor air is impacted by residual TCE in the future can be used to manage the risk in contaminated land redevelopment and facilitate the redevelopment of contaminated lands. Investors can manage their risk by saving contingency fees or buying environmental insurance; the value of risk capital from the uncertainties is equivalent to the value of contingent claim in a finance market, or insurance premium.

Mostly, the valuation of this risk capital is equivalent to an insurance premium calculation for environmental projects. Environmental insurance has been used (*Freeman and Kunreuther*, 1996; *Bell and Pearlson*, 2003; *Anonymous*, 2006), but until now, the market has been relatively small because of lack of information and experience despite the high risks (*Meyer et al.*, 2002). Therefore, environmental insurance markets need scientific support to better address loss occurrence intensity and loss distribution of environment investigation and remediation failures, which are a basis for valuing the insurance premium. This study will help environment insurance markets to define loss occurrence intensity and loss distribution. Eventually more investors will be able to purchase environmental insurances for a reasonable price to alleviate the uncertainty problems rather than to go to court after something unexpected happens (*Freeman and Kunreuther*, 1996; *Meyer et al.*, 2002).

Ultimately, understanding of risk capital valuation will help guide optimal investment strategy, given that the risk capital can be adjusted by optimization of an investment level or an investment time while maximizing a net profit. This optimization is not performed in this thesis, while a simple optimization procedure is proposed below.

1.5 A Proposed Optimization Framework

Net profit of brownfields redevelopment is defined as the subtraction of the sum of redevelopment costs and risk capitals from redevelopment benefits. At present, the site is assumed to remain

unremedied and undeveloped. Denote P the present ($t = 0$) value of the net profit at a certain time t when new dwellings are sold, as:

$$P(\boldsymbol{\psi}, t) = \max_{\boldsymbol{\psi}, t}[\exp(-\rho t)\{R(t) - C(\psi_c, t) - B(\psi_B, t) - V(\psi_B, \psi_c, t)\}] \tag{1.1}$$

where ρ is the project discount rate, R is the total revenue from the investment, including the income from selling new houses, C is time and materials costs needed to remediate the subsurface with a remediation level, ψ_C up to time t, B is time and materials costs needed to construct buildings with a building level, ψ_B up to time t, and V is the risk capital (insurance premium or contingency fee) for land redevelopment and appraised as the time t value for a guarantee period, T ($T \geq t$). Equation (1.1) indicates that the profit from the sale of a given house is the sale value minus time and materials costs needed to construct it, minus time and materials costs needed to remediate the subsurface, as well as minus the insurance premium or contingency fee.

This framework is to optimize two factors to maximize the present value of the profit. The first factor is the investment level, $\boldsymbol{\psi}$ (ψ_c, ψ_B) to what degree redevelopment (remediation, ψ_c and building new houses, ψ_B) is conducted. For instance, the remediation level (ψ_c) can be either reduced to save remediation costs (C), or increased to reduce the insurance premium or contingency fee (V). Obviously, there is a balance of ψ_c between both objectives, with the cost paid at a future date once remediation commences. The second factor is the timing (t) associated with the property redevelopment. The developer is presumed to be able to develop the site at any point in the future upon their convenience. Once the property has been redeveloped, houses can be sold at the future date at a value determined by the housing market. This market value of housing is uncertain, and can only be inferred from today's prices. The optimal investment level ($\boldsymbol{\psi}^*$) and time (t^*) are given when the present value of the profit is maximized.

Many studies have been done to find a tradeoff between economic benefits and environmental damage, but without considering the risk capital term (*Lefkoff and Gorelick*, 1986; *Forsyth*, 1997; *Reinelt*, 2005; *Booker et al.*, 2005) or with considering health risk of using a pesticide (*Tesfamichael et al.*, 2005). *Wladis et al.* (1999) as well as *Massmann and Freeze* (1987a, b); *Freeze et al.*(1990); *Massmann et al.* (1991); *Freeze and Gorelick* (1999) define an objective function which has risk

10

capital term as well as benefit and implementation cost, as shown in the Equation (1.1), and the risk capital term is defined as the product of the probability of failure and the economic consequences associated with failure, similar to the basic method in Chapter 4. However, *Wladis et al.* (1999) assume that the economic consequences associated with failure are directly proportional to the contamination area with the reasonable range of proportional constants, while this study considers the stochastic movement of their proportional constant which involves the market uncertainty.

Determining the optimal investment level (ψ^*) and the optimal time (t^*) to redevelop land subject to uncertainty in benefits (R) and costs (B, C, and V) is classically viewed as dynamic programming or American option pricing in the field of financial economics. In this context, the optionality inherent in the problem is to minimize the payoff at time zero to avoid a loss on the redevelopment cost. The present value of the option then is the opportunity value to hold the undeveloped land for future redevelopment. The application of the option pricing theory for valuing alternative management decisions which involve determining the optimal time to act given uncertainty in the risk, as well as determining the least cost decision between alternative courses of action is found in many researches (*Dixit and Pindyck*, 1994; *Lentz and TSE*, 1995; *Forsyth*, 2000; *Insley*, 2002; *Insley*, 2003; *Insley and Rollins*, 2005).

Chapter 2

Simulating the Evolution of an Ethanol and Gasoline Source Zone within the Capillary Fringe

Chapter Summary

Blending of ethanol into gasoline as a fuel oxygenate has created the scenario where inadvertent releases of E95 into soil previously contaminated by gasoline may remobilize these pre-existing NAPLs and lead to higher dissolved hydrocarbon (BTEX) concentrations in groundwater. The development of a risk-based corrective action framework addressing this issue is contributed to by conducting two laboratory experiments involving the release of ethanol into a gasoline source zone established in the capillary fringe. I then develop and apply the numerical model *CompFlow Bio* to replicate three specific experimental observations: (1) depression of the capillary fringe by the addition of the gasoline fuel mixture due to a reduction in the surface tension between the gas and liquid phases, (2) further depression of the capillary fringe by the addition of ethanol, and (3) remobilization of the gasoline fuel mixture LNAPL source zone due to the cosolvent behavior of ethanol in the presence of an aqueous phase, as well as a reduction in the interfacial tension between the aqueous/non-aqueous phases due to ethanol. While the simulated collapse of the capillary fringe was not as extensive as that which was observed, the simulated and observed remobilized non-aqueous phase distributions were in agreement following ethanol injection. Specifically, injection of ethanol caused the non-aqueous phase to advect downwards toward the water table as the capillary fringe continued to collapse, finally collecting on top of the water table in a significantly reduced area exhibiting higher saturations than observed prior to ethanol injection. Surprisingly, the simulated ethanol and gasoline aqueous phase plumes were uniform despite the redistribution of the source zone. Dissolution of gasoline into the aqueous phase was dramatically increased due to the cosolvency effect of ethanol on the non-aqueous phase source zone. I advocate further experimental studies focusing on eliminating data gaps identified here, as well as field-scale experiments to address issues associated with ethanol-BTEX biodegradation and sorption within the development of a risk-based corrective action framework.

2.1 Introduction

Despite recent suggestions that bio-fuels may not be an environmentally favored solution over gasoline (*Scharlemann and Laurance*, 2008), the practice of blending of ethanol into gasoline is dramatically increasing in North America. While Brazil has blended ethanol into gasoline for over 25 years, both the USA and Canada have only recently begun the widespread practice of blending ethanol into gasoline at a volume-based composition of up to 10% ethanol (E10). Most ethanol is shipped to petroleum refineries or bulk distribution facilities as denatured ethanol with a volume-based composition of 95% ethanol (E95), with the remaining 5% being gasoline. Inadvertent releases of E95 during handling and storage into soil previously contaminated by gasoline and related hydrocarbons are possible. The concern is that spills of E95 into these pre-existing gasoline source zones may remobilize the LNAPL and lead to higher dissolved hydrocarbon (BTEX) concentrations in groundwater. This concern is based on the premise that ethanol is known to act as a cosolvent to numerous hydrocarbons, including gasoline (*Heermann and Powers*, 2001; *Paulsen et al.*, 1992). Consequently, quantifying the extent of LNAPL remobilization and enhanced dissolution of BTEX components from the resulting ethanol-gasoline source zone is necessary to develop appropriate responses to anticipated E95 releases. While many sites are currently managed by monitored natural attenuation, it is not clear how a release of E95 into a pre-existing gasoline source zone would affect current risk-based corrective actions. This is a direct consequence of the fact that we have not yet clearly developed a definitive science-based conceptualization of the processes involved, nor the numerical models required to simulate the impact of E95 releases. Developing a conceptual and numerical modeling framework to address this concern is the subject of this Chapter.

Numerous experimental studies have been conducted to develop a conceptual model itemizing the physical process inherent in the evolution of an ethanol-gasoline source zone, with the scope of the studies ranging from the laboratory to the field scale. Within this framework, I identify *four* main thrusts related to measuring the impact of various physical processes governing the evolution of an ethanol-gasoline source zone.

First, the capillary fringe collapses following both gasoline and ethanol spills into the vadose zone due to a decrease in the surface tension between the liquid and gas phases (*Smith and Gillham*, 1999;

Henry and Smith, 2002; *Henry and Smith*, 2003). Note that the liquid phase is comprised of both the aqueous (groundwater) and non-aqueous (LNAPL) phases together, while the gas phase is present in the vadose zone above the capillary fringe. Given that both gasoline and ethanol have a mass density less than that of water, the collapse of the capillary fringe has a significant impact on the lateral distribution of the resulting source zone as it floats on top of the water table, and even the capillary fringe.

Second, the addition of ethanol causes the remobilization of a pre-exiting gasoline (LNAPL) source zone due to a decrease in the interfacial tension between the aqueous and non-aqueous phases (*McDowell et al.*, 2003; *McDowell and Powers*, 2003). This results in the remobilized source zone to collect at the bottom of the collapsed capillary fringe.

Third, ethanol acts as a cosolvent for the various components in gasoline (i.e. BTEX) which acts to increase their solubility in the aqueous phase. This results in the further remobilization of the gasoline source zone as a "mobilized NAPL bank" as described by *Falta* (1998). In addition, the BTEX groundwater plumes emanating from the gasoline source zone have been observed to be at elevated concentrations (*Heermann and Powers*, 1998; *Reckhorn et al.*, 2001). This latter observation is the main driving mechanism behind field-scale in-situ flushing experiments designed to remove NAPL source zones during site remediation (*Rao et al.*, 1997; *Sillan et al.*, 1998; *Falta et al.*, 1999; *Jawitz et al.*, 2000; *Brooks et al.*, 2004).

Fourth, simultaneous groundwater transport of ethanol with the BTEX components emanating from the gasoline source zone could diminish biodegradation of BTEX within the aquifer (*Corseuil et al.*, 1998; *Powers et al.*, 2001; *Da Silva et al.*, 2002; *Lovanh et al.*, 2002; *Molson et al.*, 2002; *McDowell et al.*, 2003; *Mackay et al.*, 2006) and hence the efficacy of monitored natural attenuation activities. In addition, the presence of ethanol can decrease sorption-related retardation of hydrocarbons (*Harley et al.*, 2000; *Powers et al.*, 2001).

Numerous numerical models have been developed to simulate issues arising from the four main thrusts described above. In the context of this work, however, it is convenient to categorize them into two main groups. The first group of numerical models focuses on issues related to ethanol in the two-phase aqueous and non-aqueous phase system. *Reitsma and Kueper* (1998a,b) develop a model that incorporates processes related to scaling interfacial tension as well as cosolvency on an ethanol impacted non-aqueous phase source zone. A limitation of this model with regards to simulating the

evolution of an ethanol-gasoline source zone, beyond the fact that it does not include a gas phase, is that the model is strictly one-dimensional and cannot simulate the observed vertical and lateral spreading of the remobilized source zone on the capillary fringe and at the water table. Numerous models (*Ji and Brusseau*, 1998; *Heermann and Powers*, 1998; *Molson et al.*, 2002; *Deeb et al.*, 2002; *Lee and Peters*, 2004) subsequently focus on the transport and biodegradation of cosolvency-enhanced concentrations of BTEX components in the groundwater while ignoring the evolution of the gasoline source zone. The second group of numerical models focuses on issues related to ethanol in the two-phase aqueous and gas phase system. *Smith and Gillham* (1994), *Smith and Gillham* (1999) and *Henry et al.* (2002) scale the surface tension between the aqueous and gas phases in the presence of a solute dissolved in the aqueous phase (i.e. ethanol or BTEX) to simulate the collapse of the capillary fringe. However, they do not address the complexity of the non-aqueous phase at the capillary fringe, or associated cosolvency issues.

The objective of this Chapter is to use a combination of experimental and numerical approaches to quantify the impact of an ethanol spill on top of a pre-existing gasoline source zone located within the capillary fringe. The methodology involves conducting two laboratory experiments involving the injection and subsequent redistribution of a gasoline fuel mixture above the water table and into the capillary fringe, followed by the injection of ethanol and the impact of this cosolvent on the further evolution of the gasoline source zone within the capillary fringe. Both experiments were conducted in a Plexiglas box filled with glass beads in order to visually record the redistribution of the gasoline (dyed with Sudan Red) and ethanol (dyed green with Fluorescein) within the box. During the first experiment the water table was held static, while in the second experiment the water-saturated zone was flowing. The purpose of these experiments was to observe the evolution of an ethanol-gasoline source zone, with a specific focus on: (1) depression of the capillary fringe by the gasoline fuel mixture due to a reduction in the surface tension between the gas and liquid phases, (2) further depression of the capillary fringe by the addition of ethanol, and (3) remobilization of the gasoline fuel mixture LNAPL source zone due to the cosolvent behaviour of ethanol in the presence of an aqueous phase, as well as a reduction in the interfacial tension between the aqueous/non-aqueous phases due to ethanol.

The new contribution that this work brings to the literature is my effort to simulate the two laboratory experiments with a numerical model. Here, I develop the three-phase compositional numerical model *CompFlow Bio* to simulate the evolution of the observed ethanol-gasoline source

zone within the capillary fringe. The purpose of this modeling effort was to adjust parameters within constitutive relationships obtained from the literature, particularly those governing the scaling of interfacial and surface tension between phases as well as cosolvency, and replicate the experimental observations using the numerical model. Given the numerous data gaps in terms of detailed measurement of the multi-phase flow properties of the porous media as well as the qualitative observations of the spatial and temporal phase distributions, I stress that this work is more of a numerical model-experiment "comparison" rather than "calibration" effort. The objective was to assess the ability of a numerical model to capture the general behavior of the ethanol-gasoline source zone rather than predicting detailed point-to-point experimental measurements.

The outcome of this work is to contribute towards the development of a supporting framework to quantify the extent of LNAPL remobilization and enhanced dissolution of BTEX components from an ethanol (E95)-impacted gasoline source zone, as well as subsequent biodegradation and sorption of the BTEX components in the aquifer, in order to develop appropriate risk-based corrective actions. Development of this supporting framework is contingent upon additional laboratory experiments to refine the numerical model-experiment "comparison" into a statistically-based calibration effort reporting the mean and uncertainty associated with all estimated parameters, as well as the design and implementation of field-scale experiments to examine issues associated with the fate and transport of ethanol and BTEX in the groundwater.

2.2 Laboratory Experiments

This work focuses on the simulation of two laboratory experiments involving the injection and subsequent redistribution of a gasoline fuel mixture above the water table and into the capillary fringe, followed by the injection of ethanol and the impact of this cosolvent on the further evolution of the gasoline source zone. Both experiments were conducted in a Plexiglas box of interior dimensions 0.48 m long × 0.025 m wide × 0.40 m high (the x-, y- and z-directions) which was packed with glass beads of diameter 390 μm to a height of 0.22 m. Effectively, the experiments were two-dimensional. The glass beads were packed in lifts of 0.02 m below the water level to prevent air entrapment. The water was then drained to establish the water table and capillary fringe.

The objectives of the two experiments were to visualize three processes impacting the evolution of the LNAPL source zone created by the ethanol-gasoline fuel mixture as identified in the introduction. The first experiment consisted of a static water-saturated zone (no flow), while the second experiment consisted of a flowing water-saturated zone. Visualization of these processes was facilitated by using the Sudan Red dye to color the gasoline, while Fluorescein was used to dye the ethanol green analogous to the experimental studies of *McDowell and Powers* (2003). The initial water in the box (i.e. aqueous phase) was left uncolored, but could easily be differentiated from the gas phase through the walls of the box as a "darkened" region. The transparent Plexiglas walls of the box, its narrow width, and the use of transparent glass beads enabled a camera to record the evolution of the LNAPL source zone, where the presence of the dyes (red and green) were used to infer the ethanol and gasoline composition of the phases. I note that no pressure, saturation or mole fraction measurements were obtained during the course of the experiments. Details involving the design of the Plexiglas box as well as other materials and methods used to conduct the experiments are provided in *Freitas* (2009). Below, I provide an outline of the two experiments that constitute the basis for this research effort.

The static water-saturated zone experiment was constructed by maintaining a water table elevation of 0.05 m above the bottom of the box throughout the duration of the experiment. This water table was maintained by using three hoses connected to the bottom of the box as depicted on Figure 2.1. Prior to the injection of gasoline, a steady-state capillary fringe was allowed to form above the water table and was observed to be approximately 0.095 m tall. The top of the capillary fringe was defined as the visual interface between high and low water saturations, and was observed to be quite sharp given the uniform diameter of the glass beads which were roughly equivalent to a medium to coarse sand. Subsequent to establishing a steady-state capillary fringe, 25 *m*l of a gasoline fuel mixture (API-91-01) provided by the American Petroleum Institute was injected 0.01 m below the glass bead surface (height of 0.21) in the centre of the domain as shown on Figure 2.1. The rate of gasoline injection was 35 *m*l/min. Pure ethanol (99.9% purity, from Commercial Alcohols Inc.) was injected one day after the gasoline was injected. Specifically, 25 *m*l of ethanol was injected at a rate of 35 *ml*/min at the identical position to where gasoline was injected. The volume of fluids drained from the system due to the collapse of the capillary fringe following the injection of gasoline and ethanol was recorded.

The flowing water-saturated zone experiment was constructed by maintaining a hydraulic gradient of 0.024 across the length of the box using two constant-head reservoirs, with a water table elevation of 0.08 m at the outflow end. A steady-state capillary fringe was established above the flowing water-saturated zone. Next, 15 ml of the same gasoline fuel mixture was injected at a rate of 30 ml/min into the box. The gasoline was also injected 0.01 m below the glass bead surface in the centre of the box as shown on Figure 2.1. Pure ethanol was then injected 20 minutes later, with 15 ml injected at a rate of 30 ml/min. The volume of fluids drained from the system due to the flowing water-saturated zone, as well as the collapse of the capillary fringe following the injection of gasoline and ethanol, was also recorded. The volume of gasoline injected was less than for the static water-saturated zone experiment because the slope of the water table and capillary fringe caused the gasoline source zone to extend towards the outflow reservoir, and it was the intent to isolate the influence of the reservoirs from the evolution of the source zone. Previous experience had indicated that these volumes would maximize the size of the gasoline-ethanol source zone within the box while minimizing the influence of the constant head reservoirs. A significant design constraint was encountered to create the flowing water-saturated zone. This involved placing a stainless steel mesh vertically at each end of the box in order to maintain two constant head reservoirs. First, this reduced the overall length of the interior of the Plexiglas box to 0.42 m. Second, unlike the saturated zone below the water table, the capillary fringe could not drain into the constant head reservoirs. I estimate that this perturbation to the flow field was limited to the ends of the domain and did not interfere with the results observed at the center of the box.

2.3 Numerical Model

Development of the numerical model consisted of two stages. First, I outline the formulation of the three-phase multi-component compositional numerical model *CompFlow Bio* to solve the relevant governing equations and constitutive relationships to quantify; the collapse of the capillary fringe due to the presence of gasoline and ethanol dissolved in the aqueous phase, the cosolvent effect of ethanol on the enhanced partitioning of gasoline from the non-aqueous to the aqueous phase, and the remobilization of the non-aqueous phase source zone due to a reduction in interfacial tension between the aqueous and non-aqueous phases. Second, I develop a conceptual model of the two experiments

described above, including the parameterization of all porous medium and chemical properties, in order to simulate the experiments using the *CompFlow Bio* model. At this point, I note a significant simplification in the conceptual model relative to the two experiments. Both experiments were conducted using a gasoline fuel mixture that was comprised of numerous organics broadly characterized as BTEX (benzene, toluene, ethylbenzene, *m*-xylene, *o*-xylene and , *p*-xylene). I simplified the composition of the gasoline to a single component only. While it is possible to simulate a *n*-component LNAPL using *CompFlow Bio*, limited availability of chemical property data for the suite of BTEX components in gasoline motivated this strategy. Relevant properties for the simulated single-component gasoline were based on the range of values measured for the individual BTEX components that were available in the literature. Therefore, the intent of the "model-experiment" comparison serves only to qualify the "general" ability of the model to represent the observed behaviour of the experimental system. I further note that the model-experiment comparison was severely restricted by the qualitative nature of the laboratory observations.

2.3.1 Formulation

Development of the numerical model *CompFlow Bio* largely follows that of *Forsyth* (1993) with enhancements to include the effects of ethanol on the evolution of a NAPL source zone, as well as dual-Monod biodegradation due to aerobic and anaerobic biomass. *CompFlow Bio* is a multi-phase multi-component compositional model that considers three mobile phases; namely the aqueous (q), non-aqueous (n) and gas (g) phases. Furthermore, the components can be summarized as; water (w), air (a), any number of organic components which in this case are the single-component gasoline (G) and ethanol (e). Assuming that components $p = \{w, a, G, e\}$ can exist in any phase $l = \{q, n, g\}$ then the conservation of moles of component p can be written as:

$$\frac{\partial}{\partial t}\left[\sum_l(\phi S_l M_l X_{pl}) + \rho_r K_{dp} M_q X_{pq}\right] = -\sum_l \nabla \cdot (M_l X_{pl} \mathbf{V}_l) + \sum_l \nabla \cdot (\phi S_l \mathbf{D}_l M_l \nabla X_{pl}) + Q_p \qquad (2.1)$$

The Darcy flux of each phase l is given by:

$$V_l = -\mathbf{K} \cdot \frac{k_{rl}}{\mu_l} \nabla(P_l + \rho_l g z) \tag{2.2}$$

and the dispersion/diffusion tensors have the form:

$$\phi S_l \mathbf{D}_l = \alpha_T^l \mathbf{V}_l \mathbf{I} + (\alpha_L^l - \alpha_T^l)\frac{\mathbf{V}_l \mathbf{V}_l}{\mathbf{V}_l} + \phi S_l \tau d_l \mathbf{I} \tag{2.3}$$

where a summary of the nomenclature is as follows:

$S_l =$ saturation of phase l $[-]$

$P_l =$ pressure of phase l [kPa]

$M_l =$ molar density of phase l [moles/m^3]

$X_{pl} =$ mole fraction of component p in phase l $[-]$

$\rho_r =$ mass density of porous media (rock) r [kg/m^3]

$\rho_l =$ mass density of phase l [kg/m^3]

$\mu_l =$ viscosity of phase l [kPa $\cdot$ day]

$\phi =$ porosity of porous media $[-]$

$\mathbf{K} =$ Intrinsic permeability of porous media [m^2]

$K_{dp} =$ sorption coefficient of component p onto porous media [m^3/kg]

$k_{rl} =$ relative permeability of phase l $[-]$

$d_l =$ molecular diffusion of all components in phase l [m^2/day]

$\tau =$ tortuosity of porous media $[-]$ from Millington (1959)

$\alpha_L^l =$ longitudinal dispersivity of phase l [m]

$\alpha_T^l =$ transverse dispersivity of phase l [m]

$Q_p =$ source (+ve) or sink (-ve) term for component p [mole/(m^3 · day)]

There exist the following constraints among the above variables:

$$S_q + S_n + S_g = 1$$

$$P_g = P_n + \hat{\alpha} P_{cgn}(S_g) + (1 - \hat{\alpha})[P_{cgq}(S_g) - P_{cnq}(S_q = 1)]$$

$$P_n = P_q + \hat{\alpha} P_{cnq}(S_q) + (1 - \hat{\alpha}) P_{cnq}(S_q = 1) \tag{2.4}$$

where

$$\hat{\alpha} = \min(1, S_n/S_n^*) \tag{2.5}$$

and P_{cgn} , P_{cgq} , and P_{cnq} are experimentally derived capillary pressure curves [kPa]. S_n^* is a blending parameter used to ensure that the capillary pressure has the correct form as the non-aqueous phase saturation goes to zero. The capillary pressure curves are scaled using a modified form of the function proposed by *Leverett* (1941):

$$P_{cl_1l_2}^D = \frac{P_{cl_1l_2}}{\sigma_{l_1l_2}} \left(\frac{\mathbf{K}}{\phi}\right)^{\tilde{\alpha}} \tag{2.6}$$

where $P^D_{cl_1l_2}$ and $P_{cl_1l_2}$ are the dimensionless and dimensional capillary pressures, respectively, between any two phases, $l_1l_2 = \{gn, gq, nq\}$, $\sigma_{l_1l_2}$ is the surface/interfacial tension between the two phases, and $\tilde{\alpha}$ is a parameter related to the pore size distribution of the porous media. Application of equations (2.4), (2.5) and (2.6) to describe the capillary pressure behavior of the three-phase system observed for the experiments described in Section 2.2 will be described in Section 2.3.2.

   Stone (1973) used the channel flow theory to construct relationships for predicting three-phase relative permeabilities obtained from experiments. The channel flow theory implies that the aqueous phase relative permeability, k_{rq}, and P_{cnq} are functions of only the aqueous phase saturation. Further, they are the same function in the three-phase system as in the two-phase aqueous/non-aqueous system in which the experimental data was collected. Similarly, the gas phase relative permeability, k_{rg}, and P_{cgn} are functions of the gas phase saturation (*Leverett*, 1941; *Leverett and Lewis*, 1941; *Corey et al.*, 1956). The non-aqueous phase relative permeability, k_{rn}, was observed to be a function of both the gas and aqueous phase saturations. Stone's second model is used in *CompFlow Bio* to estimate k_{rn} and is normalized using the method introduced by *Aziz and Settari* (1979). Therefore, the relative permeability of the aqueous, gas and non-aqueous phases for the three-phase system is given by:

$$k_{rq} = F(S_q)$$

$$k_{rg} = F(S_g)$$

$$k_{rn} = k_{r(nq_c)}\left[\left(\frac{k_{r(nq)}}{k_{r(nq_c)}} + k_{rq}\right)\left(\frac{k_{r(ng)}}{k_{r(nq_c)}} + k_{rg}\right) - \left(k_{rq} + k_{rg}\right)\right] \tag{2.7}$$

where $k_{r(nq)}$ and $k_{r(ng)}$ are the non-aqueous phase relative permeabilities measured in the two-phase non-aqueous/aqueous and non-aqueous/gas systems at the aqueous and gas phase saturations in the full three-phase system, respectively. The normalization forces Stone's model to be consistent with the two-phase aqueous/non-aqueous system when $k_{r(nq)}$ is not unity at connate water saturation $(k_{r(nq_c)} \neq 1)$. *Fayers and Matthews* (1984) compared Stone's second model against multiple three-phase relative permeability data sets. They found that it gave reasonable predictions for the gas and

22

aqueous phase relative permeabilities over the full range of their respective saturations. The accuracy of the predicted non-aqueous phase relative permeability was reasonable at high non-aqueous phase saturations but diminished as the non-aqueous phase saturations decreased to residual in the presence of both the gas and aqueous phases. Application of Equation (2.7) to describe the relative permeability behavior of the three-phase system observed for the experiments described in Section 2.2 will be described in Section 2.3.2.

Partitioning of components between phases is assumed to be at equilibrium. In this context, the following constraint applies to any phase l which is present:

$$\sum_p X_{pl} = 1 \qquad (2.8)$$

p partitions between the aqueous and non-aqueous phases according to:

$$X_{pq} = Z_{pqn} X_{pn} \qquad (2.9)$$

while between the gas and aqueous phases, the relationship is:

$$X_{pg} = Z_{pgq} X_{pq} \qquad (2.10)$$

where both Z_{pqn} and Z_{pgq} are dependent on the systems pressure P_g and temperature T as presented by *Forsyth* (1993). In the context of this work, both P_g and T vary within a narrow range (with temperature variations only occurring due to volatilization of components) and hence both Z_{pqn} and Z_{pgq} are assumed constant for the purposes of this work.

Although Equation (2.1) is given in the most general sense, some simplifying assumptions are made that restrict the composition of various phases. Specifically, the non-aqueous phase consists of

23

only components $p = \{G, e\}$ which implies $X_{wn} = 0$ and $X_{an} = 0$, the aqueous phase consists of components $p = \{w, G, e\}$ which implies $X_{aq} = 0$, and the gas phase consists of all available components $p = \{w, a, G, e\}$. The rationale for this restricted system is provided in *Forsyth* (1993).

Phase appearance and disappearance rules are used to develop meaningful tests to detect which subset of phases exists at a node given the moles of component p present. These rules follow from the set of primary variables, which in general consist of P_l, X_{pl}, S_l and T, and are aligned with Equations (2.1) to (2.3) . Following the formulation introduced by *Forsyth* (1993), I also assume the gas phase is always present to at least some minimal saturation $S_g^{\min} = 10^{-3}$ to alleviate numerical issues associated with the non-condensible air component.

2.3.1.1 Cosolvency

Ethanol acts as a cosolvent for the water and gasoline components between the aqueous and non-aqueous phases. The impact of this cosolvent effect is dependent on the amount of ethanol present in the aqueous and non-aqueous phases that are in contact. As ethanol is first introduced into the system and exists at low mole fractions in both the aqueous and non-aqueous phases, equilibrium partitioning of gasoline from the non-aqueous into the aqueous phase is enhanced. Similarly, equilibrium partitioning of water from the aqueous into the non-aqueous phase is enhanced. Note that both the aqueous and non-aqueous phases are still present. As more ethanol is introduced into the system and exists at high mole fractions in both the aqueous and non-aqueous phases, the aqueous and non-aqueous phase disappear and are replaced by a single "miscible" phase $l = \{m\}$ in which the ethanol, water and gasoline are completely dissolved. This cosolvent behavior has been studied by *Oliveira* (1997), *Reitsma and Kueper* (1998a) as well as *Lee and Peters* (2004) and is represented by a ternary phase diagram based on experimental measurements as well as semi-empirical models. Alternatively, *Arey and Gschwend* (2005) have represented this partitioning behavior using a linear salvation energy relationship.

In the context of this work, I consider the appearance of the "miscible" phase to occur the instant the non-aqueous phase disappears at a node, with the "miscible" phase denoting the continued presence of the aqueous phase at the given node. Specifically, the "miscible" phase is simply the pre-

existing aqueous phase with an enhanced composition of ethanol and gasoline due to cosolvency. The non-aqueous phase disappears because the pre-existing aqueous phase is able to solubilize all of the moles of ethanol and gasoline present at the given node. I simplify the complex behavior of the enhanced equilibrium partitioning of gasoline from the non-aqueous into the aqueous phase by choosing a constant equilibrium partitioning coefficient to distribute ethanol between the aqueous and non-aqueous phases, and then to enhance the solubility of gasoline from the non-aqueous into the aqueous phase based on the presence of ethanol. As mentioned above, water is not allowed to partition into the non-aqueous phase.

A representative value of Z_{eqn} describing the equilibrium partitioning of ethanol between the aqueous and non-aqueous phases was obtained using the UNIFAC-derived ternary phase diagram shown on Figure 1a of *Lee and Peters* (2004) for the three-component water-ethanol-benzene system. To calculate Z_{eqn}, I assumed that the interfacial tension between the aqueous and non-aqueous phase was fixed at $\sigma_{nq} = 5.0$ dyne/cm invariant of the ethanol content of the system. The resulting composition of the aqueous and non-aqueous phase for $p = \{w, G, e\}$ was then obtained where the tie line intersected the binodal line on either side of the Plait point. The resulting equilibrium partitioning of ethanol between the aqueous and non-aqueous phase, given by the slope of the tie line (*Falta*, 1998), was then estimated to be $Z_{eqn} = 2.4$. Although the choice of $\sigma_{nq} = 5.0$ *m*N/m was arbitrary, I note that the experimental data on the same ternary phase diagram shows tie lines that have a rather uniform slope over the entire range of measured tie lines for a given σ_{nq}. Hence, as long as the aqueous and non-aqueous phases are present based on the composition of the system as specified by the ternary phase diagram, I expect that this approach should yield reasonable results. However, note that the value of Z_{eqn} obtained here was in the presence of benzene and not the gasoline fuel mixture used in Figure 1a of *Lee and Peters* (2004).

The equilibrium partitioning coefficient for the single-component gasoline, $p = \{G\}$, between the aqueous and non-aqueous phases in the presence of ethanol was simulated using a log-linear relationship as described by *Ji and Brusseau* (1998) as well as *Molson et al.*, (2002). This relationship effectively results in an enhancement factor for Z_{Gqn} that can be represented as:

$$X_{Gq} = 10^{\alpha_G X_{eq}^{\text{vol}}} Z_{Gqn} X_{Gn} \tag{2.11}$$

where α_G is the cosolvency power of ethanol on gasoline $[-]$, and X_{eq}^{vol} is the volume fraction of ethanol in the aqueous phase $[-]$.

2.3.1.2 Surface Tension

Smith and Gillham (1994) measured the change in surface tension between the gas and liquid (aqueous or non-aqueous) phase containing a single dissolved non-ionized organic at equilibrium, and is adapted here to be:

$$\frac{\sigma_{gl}^*}{\sigma_{gl}} = \left[1 - \vartheta_{eq} \ln\left(\frac{X_{eq}^{\mathrm{mass}}}{\zeta_{eq}} + 1\right)\right]^{-1} \times \left[1 - \vartheta_{Gq} \ln\left(\frac{X_{Gq}^{\mathrm{mass}}}{\zeta_{Gq}} + 1\right)\right]^{-1} \tag{2.12}$$

where σ_{gl}^* is the unscaled surface tension between gas and liquid $l = \{q, n\}$ phases, σ_{gl} is the scaled surface tension, X_{pq}^{mass} is the mass fraction of component p in the aqueous phase, and ϑ_{pq} and ζ_{pq} are fitting parameters for component $p = \{e, G\}$ in the aqueous phase . The magnitude of this combined scaling effect when both gasoline and ethanol components are dissolved in the aqueous phase is assumed to be the product of their independent effects. *Jajuee et al.* (2006) provides experimental evidence that the reduction in the surface tension of the aqueous phase in the presence of two dissolved components (specifically, *p*-xylene and naphthalene) is complex, beyond the simple product of their independent effects. However, I am unaware of any constitutive relationship that predicts this behavior. Note that $\frac{\sigma_{gl}^*}{\sigma_{gl}} = \frac{\sigma_{gq}^*}{\sigma_{gq}} = \frac{\sigma_{gn}^*}{\sigma_{gn}}$ where σ_{gq} and σ_{gn} are used within Equation (2.6) to scale the capillary pressures P_{cgq} and P_{cgn} listed in Equation (2.4).

26

2.3.1.3 Interfacial Tension

Oliveira (1997) measured the change in interfacial tension between the aqueous and non-aqueous phase in the presence of ethanol, and is adapted here to be:

$$\frac{\sigma_{nq}^*}{\sigma_{nq}} = \left[exp\{-5.9461\ X_{eq}\}\right]^{-1} \qquad (2.13)$$

where σ_{nq}^* is the interfacial tension with no ethanol present, and σ_{nq} is the interfacial tension in the presence of ethanol. Note that σ_{nq} is used within Equation (2.6) to scale the capillary pressure P_{cnq} listed in Equation (2.4).

2.3.2 Conceptual Model

The computational domain was discretized using 48 × 1 × 44 nodes of dimension 0.01 m × 0.025 m × 0.005 m in the x-, y- and z-directions, respectively. The top and bottom boundaries were impermeable, while the sides of the computation domain were assigned a hydrostatic boundary condition to maintain the water table at an elevation of 0.05 m with no flow, and alternatively maintain a hydraulic gradient of 0.024 across the domain in order to replicate the two experiments. Porous medium properties of the glass beads including permeability, porosity, and dispersivity are shown on Table 2.1, with the longitudinal dispersivity $\alpha_L^q = 0.001$ m estimated from *Kim et al.* (2004), which is about two-and-a-half times greater than the diameter of the glass beads. Given the clean surfaces of the glass beads, sorption and biodegradation were assumed negligible.

All parameter values listed in this section constitute the base scenario model. Deviations from these parameters are used during a sensitivity analysis and listed separately where appropriate.

Capillary pressure as well as relative permeability versus saturation curves were not measured for the glass beads. However, given the observed height of the capillary fringe of 0.095 m, the air-entry

capillary pressure was estimated to be $P_{cqg} = 0.930$ kPa. The remainder of the curves needed to specify Equations (2.4) and (2.7) were based on an attempt to reproduce the observed with the simulated non-aqueous phase distribution in the static and flowing water-saturated zone experiments, prior to ethanol injection. Specifically, the relative permeability was initially estimated using the "fourth-order" relationship of *Corey* (1954) with $k_{rq} = S_e^4$ and $k_{r(nq)} = (1 - S_e^4)$ where $S_e = (S_q - S_{q_c})/(1 - S_{q_c})$. The resulting non-aqueous phase appeared too immobile, so I increased the non-aqueous phase relative permeability to the "third-order" *Wyllie* (1962) relationship and finally a "second-order" relationship. The resulting capillary pressure as well as relative permeability versus saturation curves are shown on Table 2.2 and 2.3, where $S_{q_c} = 0.1$. Apart from permeability and porosity, capillary pressure and relative permeability curves are of fundamental importance to simulating the advection of phases through porous media. Lack of this information is a significant data gap in this analysis.

Equilibrium partitioning parameters described in Equations (2.9), (2.10) and (2.11) are summarized on Table 2.4. These parameters are strongly temperature dependant, and are evaluated here to be at 20°C which was the ambient temperature under which the experiments were conducted. The equilibrium partitioning parameters for the single-component gasoline used in the simulations were assumed to be that of benzene. The rationale for this choice was that benzene is the most soluble of the prominent BTEX components in the gasoline fuel-mixture used in the experiments, and I had ethanol-water-benzene partitioning data from the UNIFAC-derived ternary phase diagram shown on Figure 1a of *Lee and Peters* (2004). Implications of this assumption will be discussed in the text where relevant.

The cosolvency power of ethanol on gasoline for the base-scenario model was set to $\alpha_G = 1.7$ assuming the simulated gasoline component was comprised of pure benzene (*Heermann and Powers*, 1998; *Reckhorn et al.*, 2001). However, the complex gasoline fuel mixture that was used in the experiments contained components with both lower and higher solubilities than benzene, with a lower solubility generally indicating a higher cosolvency power and vice-versa. Therefore, I adjusted the cosolvency over the range $\alpha_G = 1.3$ to $\alpha_G = 2.0$ as part of sensitivity analysis to understand the implications of representing the gasoline fuel mixture with a single-component gasoline exhibiting benzene properties for α_G only during the model-experiment comparison. The results of this sensitivity analysis will be shown later.

Surface tension parameters itemized in Equation (2.12) are listed on Table 2.5. Parameters needed to quantify the impact of ethanol in the aqueous phase (ϑ_{eq} and ζ_{eq}) were obtained by fitting data available in *Lide* (2008). Identical parameters for gasoline in the aqueous phase (ϑ_{Gq} and ζ_{Gq}) were obtained by fitting *p*-xylene data presented by *Jajuee et al.* (2006) due to a lack of published data on other BTEX components present in the complex gasoline fuel mixture used in the experiment. Note that this is a critical data gap in the ability to correctly simulate the collapse of the capillary fringe when gasoline is first injected. Figure 2.2 shows the change in surface tension as a function of the mole fraction of ethanol and gasoline in the aqueous phase. Given that gasoline has a maximum mole fraction in the aqueous phase of $X_{Gq} = 0.000411$ when in contact with a pure gasoline non-aqueous phase $X_{Gn} = 1.0$, Figure 2.2b shows that this relatively small mole fraction will significantly reduce the surface tension from 72 *m*N/m to 46.2 *m*N/m (based on the *p*-xylene data which were assumed to apply to gasoline $p = \{G\}$). Furthermore, the gasoline fuel mixture used in the experiments consisted of approximately 25% per volume of light organics such as butane and pentane that are extremely volatile and have very low surface tensions ranging from 14 *m*N/m to 17 *m*N/m. The impact of the data gap on the simulated versus observed collapse of the capillary fringe will be discussed shortly.

The impact of scaling the interfacial tension based on the mole fraction of ethanol in the aqueous phase, as described by Equation (2.13), is depicted on Figure 2.2a. I note that this scaling relationship was derived for a two-phase aqueous/non-aqueous system with no gas phase present. In addition, ethanol was the only organic component present. Therefore, the presence of gasoline BTEX components dissolved in the aqueous phase may complicate this scaling relationship.

Additional parameters and constitutive relationships needed to represent the physical system are provided in Table 2.6 for completeness.

2.4 Results

The objective of the numerical model-experiment comparison is to parameterize the numerical model and assess the relative importance of physical process controlling the evolution of a gasoline and ethanol source zone in the capillary fringe. In particular, I focus on three processes: (1) depression of the capillary fringe by the gasoline fuel mixture due to a reduction in the surface tension between the

gas and liquid phases, (2) further depression of the capillary fringe by the addition of ethanol, and (3) remobilization of the gasoline fuel mixture LNAPL source zone due to the cosolvent behavior of ethanol in the presence of an aqueous phase, as well as a reduction in the interfacial tension between the aqueous/non-aqueous phases due to ethanol. The procedure for conducting the numerical model-experiment comparison is to first obtain an understanding of the three above processes where the water table is static. Then, the same parameters are applied when the water-saturated zone is flowing to ensure that the general behavior of system can still be replicated given this perturbation to the dynamics of the system. Results of the numerical model-experiment comparison are provided below.

2.4.1 Static Water-saturated Zone Experiment

2.4.1.1 LNAPL Injection Stage

Following the experimental methodology outlined in Section 2.2, the static water-saturated zone experiment was simulated using *CompFlow Bio*. The first stage of this effort involved injecting 25 *m*l of the single-component gasoline described in Section 2.3.2 at a rate of 35 *m*l/min into the computation domain with a steady-state capillary fringe established above a static water table. I reiterate that no saturation, pressure, or mole fraction data were obtained during the course of the experiments. The only point of comparison between the experimental and simulated results within the porous medium is the inferred position of the aqueous, gas and non-aqueous phases as well as their relative composition of gasoline and ethanol based on the intensity of the Sudan Red and Fluorescein dyes used to colour the gasoline red and ethanol green, respectively. Additionally, the volume of liquids drained as the gasoline was injected and allowed to redistribute during the experiment was measured as a reflection of the magnitude of the collapse in the capillary fringe. The outcome of the numerical model-experiment comparison at this point is to address the first of the three processes itemized in Section 2.4, namely: (1) depression of the capillary fringe by the gasoline fuel mixture due to a reduction in the surface tension between the gas and liquid phases.

Figure 2.3 depicts the results of the numerical model-experiment comparison one day after gasoline was injected and after the resulting non-aqueous phase had redistributed itself in the porous media, and immediately prior to ethanol being injected. In interpreting the experimental results, I assume the Sudan Red dye cannot dissolve into the aqueous phase even as components of the gasoline fuel-mixture partition from the non-aqueous into the aqueous phase. Therefore, the intensity of the red color is indicative of non-aqueous phase saturation. Inspection of the simulation results shows that the gasoline non-aqueous phase source zone resides entirely within the capillary fringe (above the water table) in keeping with the experimental observations. Both the observed and simulated non-aqueous phase source zones, as depicted on Figures 2.3a and 2.3b, show extensive lateral spreading on top of the capillary fringe subsequent to its collapse, with the highest non-aqueous phase saturations appearing at the very top center of the capillary fringe. In contrast, the simulated lateral spreading of the non-aqueous phase is not as extensive as the observed spreading. I attribute this mismatch to two processes; uncertainty in parameters that control the scaling of the gas-aqueous phase surface tension, and uncertainty in the relative permeability and capillary pressure curves.

Uncertainty in parameters that control the scaling of the gas-aqueous phase surface tension was previously discussed in Section 2.3.2 where it was mentioned that the complex gasoline fuel mixture used in the experiments was represented by a single-component gasoline only in the numerical simulations. Specifically, surface tension scaling parameters for the simulated single-component gasoline in the aqueous phase (ϑ_{Gq} and ζ_{Gq}) were adopted from p-xylene values, with the solubility mole fraction of benzene being characteristic of gasoline (i.e. $X_{Gq} = 0.000411$ when $X_{Gn} = 1.0$), causing the surface tension of the aqueous phase to be reduced from 72 mN/m to 46.2 mN/m. However, during the simulations I ignored the 25% per volume of light organics such as butane and pentane in the gasoline fuel mixture. These organics are extremely volatile and have very low surface tensions ranging from 14 mN/m to 17 mN/m. As a consequence of these above approximations, the simulated collapse of the capillary fringe was not as extensive as that observed in the static water-saturated zone experiment. This can be seen by comparing Figure 2.3a to 2.3d. The magnitude of this discrepancy is given by the simulated base scenario volume of fluid drained as shown on Figure 2.4. Figure 2.3c shows that volatilization and molecular diffusion of gasoline in the gas phase has created widespread transport of gasoline within and above the capillary fringe. The gasoline in the gas phase then partitions into the aqueous phase, held under capillary tension above the water table, under equilibrium conditions. However, the resulting gasoline in the aqueous phase does not appear to

31

collapse the capillary fringe beyond the region in immediate contact with the non-aqueous phase. I speculate that the extremely volatile organics with low surface tensions in the gasoline fuel mixture were responsible for the observed collapse of the capillary fringe in regions distant from the non-aqueous phase. One might expect that the extensive collapse of the capillary fringe in the experiment enabled greater lateral advection of the non-aqueous phase relative to the model simulation. To test this hypothesis, I modified the surface tension scaling parameters to be $\vartheta_{Gq} = 0.12$ and $\zeta_{Gq} = 1.0 \times 10^{-5}$ in order to match the cumulative volume of fluid drained (see Figure 2.4) and consequently the extensive lateral collapse of the capillary fringe. This further reduced the surface tension of the aqueous phase when $X_{Gq} = 0.000411$ from 46.2 mN/m to 27.2 mN/m. Although I do not show the results for brevity[1], the resulting non-aqueous phase distribution during the LNAPL injection stage was not significantly different relative to the base scenario parameter set from Section 2.3.2.

   Uncertainty in the relative permeability and capillary pressure curves has a significant impact on the advection of the phases due to a given gradient in potential. Specifically, there is uncertainty in the actual magnitude or "shape" of the relative permeabilities, as well as the residual saturation where the relative permeability becomes zero. This residual saturation generates the non-aqueous phase residuals trapped in the vadose zone behind the mobile non-aqueous front. The shape of the relative permeability curve controls the saturation at which the front of the non-aqueous phase source zone is mobile. As described in Section 2.3.2, my choice of relative permeability curves was based on an attempt to replicate the observed non-aqueous phase distribution with that simulated by the numerical model. Ultimately, the calibration effort focused on increasing the mobility of the non-aqueous phase at low to intermediate saturations by reducing the power of the curves from "three" to "two", and also by making $k_{r(nq)} = 0$ when $S_n = 0, S_q = 1$ (see Table 2.2). I also assessed the impact of uncertainty in the capillary pressure of the porous media between the liquid and gas phases by reducing all capillary pressures by a factor of two. Note that given the well-sorted nature of the glass beads, there is a sharp transition between $S_q \sim 1$ at the top of the capillary fringe decreasing to residual water saturation immediately above the capillary fringe. Although I do not show the results for brevity[2], by reducing the height of the capillary fringe, I significantly increased lateral spreading of the gasoline source zone in agreement with the laboratory results. However, the simulated gasoline source zone

---

[1] See Figure A.1 in Appendix A for details.
[2] See Figure A.2 in Appendix A for details.

came to rest at a lower elevation above the water table relative to the experimental results indicating a measure of disagreement.

2.4.1.2 Ethanol Injection Stage

Following the experimental methodology outlined in Section 2.2, the second stage of modeling the static water-saturated zone experiment using *CompFlo Bio* involved injecting 25 *m*l of pure ethanol at a rate of 35 *m*l/min into the computation domain one day after the gasoline fuel mixture was injected. I start this section by discussing what I observed during this stage of the experiment. I then follow by interpreting the experimental observations by attempting to replicate the experimental results using the numerical model. A point of reference during this discussion is the work of *Falta* (1998), in which the use of phase diagrams to predict the performance of cosolvent floods for NAPL remediation is discussed. While the philosophical intent of this experiment is somewhat different than the motivation behind the discussion found in *Falta* (1998), the experimental methodology used here is directly amenable to the analysis that the author presented. Specifically, *Falta* (1998) uses ternary phase diagrams of the cosolvent/NAPL/water component system in conjunction with one-dimensional fractional flow theory to quantify non-dispersive two-phase flow of the aqueous and non-aqueous phases (both in terms of saturations and mole fractions) during a cosolvent flood, assuming no capillarity. The complexity of the experiment presented here is significantly greater for several reasons; three phases are present (aqueous, non-aqueous, and gas), the system is two-dimensional, and both dispersion and capillary forces are present and significant transport mechanisms. The outcome of the numerical model-experiment comparison at this point is to address the second and third processes itemized in Section 2.4, namely: (2) further depression of the capillary fringe by the addition of ethanol due to a reduction in the surface tension between the gas and liquid phases, and (3) remobilization of the gasoline fuel mixture LNAPL source zone due to the cosolvent behavior of ethanol in the presence of an aqueous phase, as well as a reduction in the interfacial tension between the aqueous/non-aqueous phases due to ethanol.

Figure 2.5a presents experimental results at times 210, 360, 1080 and 4200 seconds after the start of ethanol injection on rows one to four, respectively. In keeping with the discussion in the previous section, I assume the Sudan Red dye cannot dissolve into the aqueous phase even as gasoline

partitions from the non-aqueous into the aqueous phase. Therefore, the intensity of the red color is indicative of non-aqueous phase saturation only. Furthermore, I assumed that because Fluorescein is a hydrophilic dye, the intensity of the green color is indicative of the amount of Fluorescein present in the aqueous phase. Note that ethanol and Fluorescein were injected simultaneously into the domain and are assumed here to be transported together in the aqueous phase. Consequently, intensely green regions immediately adjacent to red regions are indicative of areas where the cosolvency behavior of ethanol is causing the disappearance of the non-aqueous phase.

Experimental results indicate that once the ethanol component was injected into the box, it immediately caused the downward advection of the aqueous phase above the capillary fringe in the vadose zone. This ethanol-water aqueous phase then contacted the top of the capillary fringe where the gasoline fuel mixture was residing as a non-aqueous phase, and causing two significant events. First, the ethanol in the aqueous phase appeared to cause the further collapse of the capillary fringe. The collapse was uniform across the entire width of the box due to the lateral spread of ethanol across the box as evidenced by the green hue. Second, the saturation of the non-aqueous phase appeared to increase as a circular ring at the bottom of the collapsed capillary fringe, as evidenced by the intensification of the red color. The remobilized non-aqueous phase sank through the capillary fringe and almost reached the water table. *McDowell et al.* (2003) also observed a similar remobilization and increase in non-aqueous phase saturations and attributed this phenomenon to a reduction in interfacial tension between the aqueous/non-aqueous phases due to the presence of ethanol, allowing the non-aqueous phase to fill smaller pores. In contrast, *Falta* (1998) indicate that the mobilized non-aqueous phase bank ahead of the cosolvent front location will exhibit significantly higher saturations than those initially present due to precipitation of organic chemical component (here, the gasoline fuel mixture) ahead of the cosolvent front. The key assumption in the *Falta* (1998) interpretation is that the cosolvent does not partition into the non-aqueous phase by diffusion or capillary forces ahead of advective transport in the cosolvent front. When the injected cosolvent mole fraction is above the critical tie line extension, the result is that there is sharp interface representing the transition from the cosolvent front (where $S_q = 1$ and $S_n = 0$) to the mobilized non-aqueous phase bank (where $0 < S_q, S_n < 1$). Following the observed collapse of the capillary fringe and remobilization of the non-aqueous phase due to the downward movement of the injected ethanol, the ethanol-water aqueous phase spread laterally on top of the capillary fringe causing it to be further depressed across the entire width of the box.

Figures 2.5b and 2.5c present simulation results at times 210, 360, 1080 and 4200 seconds after the start of ethanol injection on rows one to four, respectively. Simulation results indicate that as the ethanol component was injected, it immediately partitioned into the aqueous phase within the vadose zone. The resulting water-ethanol aqueous phase mixture then advected downwards through the vadose zone until it reached the top of the capillary fringe established one day after gasoline injection. During the downward advection of the water-ethanol aqueous phase mixture, the ethanol did not undergo significant lateral spreading due to dispersive fluxes in the aqueous phase. This is a consequence of the small aqueous-phase dispersivity listed in Table 2.1 ($\alpha_L^q = 0.001$ m) as well as the refined mesh used to minimize numerical dispersion. Dispersion due to aqueous phase molecular diffusion is also an insignificant transport mechanism at the early simulation times provided on Figures 2.5b, 2.5c, 2.6b and 2.6c. However, dispersion due to gas phase molecular diffusion is significant and has resulted in the lateral spreading of the ethanol above the capillary fringe, especially given the affinity for ethanol to volatilize. Once the water-ethanol aqueous phase mixture reached the capillary fringe established one day after gasoline injection, the surface tension between the gas and liquid phases was further reduced. This caused the capillary fringe to collapse even further as seen during the experiment. Beneath the ethanol injection point at the center of the domain, the collapsed capillary fringe almost reached the water table in agreement with the experiment. However, the lateral extent of the simulated capillary fringe collapse was not as significant as that which was observed during the experiment. I anticipate that this is a consequence of the fact that the simulated capillary fringe collapse after gasoline injection was not as extensive as that observed in the experiment. This prevented the ethanol from spreading laterally on top of the capillary fringe, which had collapse uniformly (and was essentially horizontal) in the experiments but had collapsed only in the centre of the domain during the simulation. The magnitude of the discrepancy between the simulated and observed collapse in the capillary fringe is given by volume of fluids drained during the ethanol injection stage as shown on Figure 2.4. Once again, by adjusting the surface tension scaling parameters for gasoline and ethanol to be; $\vartheta_{eq} = 0.1616$, $\zeta_{eq} = 1.212 \times 10^{-2}$, $\vartheta_{Gq} = 0.12$ and $\zeta_{Gq} = 1.0 \times 10^{-5}$, I was able to simulate the cumulative volume of fluids drained as observed during the experiment. Although not shown for brevity[3], the extensive lateral collapse of the capillary fringe was better represented by the modified parameters, while the non-aqueous phase distribution

---

[3] See Figure A.3 in Appendix A for details

exhibited less agreement with the laboratory results after ethanol injection relative to the base scenario parameters provided in Section 2.3.2.

Figures 2.5b and 2.5c show that once the simulated ethanol-water aqueous phase mixture reached the non-aqueous phase, the source zone was remobilized at the leading edge of the injected ethanol-water aqueous phase mixture. Of course, at this point the ethanol-water aqueous phase mixture behind the remobilized non-aqueous phase also contained an elevated gasoline mole fraction, reaching a maximum value of $X_{Gq} = 0.004$ due to the cosolvent behavior of ethanol. Note that the solubility of gasoline in the aqueous phase without ethanol present is $X_{Gq} = 0.000411$ as discussed in Section 2.3.2. The mole fraction of ethanol in the aqueous phase immediately behind the remobilized non-aqueous phase ranged from a high of $X_{eq} = 0.83$ at early time (210 seconds) down to $X_{eq} = 0.73$ at the end of the ethanol injection stage (4200 seconds), indicating that the ethanol composition of the aqueous phase was maintained above the critical tie line extension extrapolated from Figure 1a of *Lee and Peters* (2004) during the experiment. The saturation of the non-aqueous within the remobilized non-aqueous phase increased over time in agreement with the experimental observations, with a maximum value of $S_n = 0.42$ before ethanol injection to $S_n = 0.83$ at the end of the simulated ethanol injection stage. Conceptually, the simulated remobilization of the non-aqueous phase proceeded in a manner as shown on Figure 3b of *Falta* (1998) when the injected cosolvent (ethanol) mole fraction is above the critical tie line extension. Note that on Figure 2.6b I contour $X_{eq} = 0.55$ which is approximately the Plait Point shown on Figure 1a of *Lee and Peters* (2004). The Plait Point represents the transition between a single "miscible" phase and the two-phase aqueous-non-aqueous system. This contour is at the contact between the injected ethanol-water aqueous phase mixture and the remobilized non-aqueous phase.

Two physical processes contribute to the evolution of the simulated gasoline/ethanol source zone beyond the discussion presented by *Falta* (1998). First, dispersion has caused the cosolvent (ethanol) to be transported ahead of the advective front of the injected ethanol-water aqueous phase mixture causing ethanol to partition into the remobilized non-aqueous phase. The analysis presented by *Falta* (1998) assumes that the mobilized NAPL bank does not contain cosolvent. Second, scaling the interfacial tension between the aqueous and non-aqueous phases reduced the capillary pressure in the presence of ethanol. This enabled the non-aqueous phase to fill smaller pores with a resulting increase

in saturation. In addition, it also created a gradient in the potential of the non-aqueous phase from regions of low to high saturation. In effect, a contraction of the non-aqueous phase source zone.

As discussed in Section 2.3.2, I adjusted the cosolvency over the range $\alpha_G = 1.3$ to $\alpha_G = 2.0$ to understand the implications of representing the gasoline fuel mixture with a single-component gasoline only. Although I do not show the results for brevity[4], as the cosolvency power is reduced to $\alpha_G = 1.3$, the saturation of the non-aqueous phase at the very bottom of the remobilized non-aqueous phase front increases while along the sides it is decreased. Conversely, the opposite effect occurs as the cosolvency power is increased to $\alpha_G = 2.0$. Given that the numerical model-experiment comparison does not constitute a parameter calibration effort given the use of a single-component gasoline within the model as a substitute for the complex gasoline fuel mixture used in the experiment, I cannot ascribe a particular cosolvency to best represent this numerical model-experiment comparison. However, it does appear that the base scenario cosolvency power of $\alpha_G = 1.7$ does yield the most representative results.

2.4.2 Flowing Water-saturated Zone Experiment

Following the parameterization of the *CompFlow Bio* model during the static water-saturated zone numerical model/experiment comparison, the numerical model using the identical parameters was used to simulate the flowing water-saturated zone experiment discussed in Section 2.2. In essence, the flowing water-saturated zone experiment served to test the predictive capability of the model under a perturbation in the dynamics of the system. Note that the flowing water-saturated zone experiment is one step closer (relative to the static water-saturated zone experiment) to the conceptual model for the evolution of an ethanol-gasoline source zone at the field scale. I hypothesize that the anatomy of the source zone could significantly influence the structure of the gasoline (i.e. BTEX) and ethanol plume emanating from the source zone, and potential for the biodegradation of the BTEX components in the aquifer. Therefore, the transition from the static to the flowing water-saturated zone experiment represents the first step in building a methodology to test this hypothesis.

---

[4] See Figure A.4 in Appendix A for details.

Figure 2.7 presents experimental results and simulated aqueous and non-aqueous phase saturations at a time of 20 minutes after gasoline injection (and before ethanol injection), as well as 2 minutes, 20 minutes, and 1 hour and 40 minutes after the start of ethanol injection on rows one to four, respectively. Figure 2.8 only shows simulated mole fractions of ethanol and the single-component gasoline in the aqueous phase 2 minutes, 20 minutes, and 1 hour and 40 minutes after the start of ethanol injection on rows one to three, respectively. In general, the results of this numerical model/experiment comparison exhibit points of agreement and disagreement in a manner identical to the static water-saturated zone experiment. For instance, following the gasoline injection stage, the collapse of the simulated capillary fringe was not as extensive as that observed causing the simulated non-aqueous phase to collect more in the center of the domain rather than spread out on top of the capillary fringe. Once ethanol was injected, remobilization of the simulated non-aqueous phase proceeded in manner similar to that observed, in keeping with the static water-saturated zone numerical model/experiment comparison. Furthermore, the ethanol-water aqueous phase mixture behind the mobilized non-aqueous phase contained an elevated gasoline mole fraction, reaching a maximum value of $X_{Gq} = 0.004$ due to the cosolvent behavior of ethanol. Once again, note that the solubility of gasoline in the aqueous phase without ethanol present is $X_{Gq} = 0.000411$. I conclude that the parameterized numerical model developed from the static water-saturated zone simulation effort was able to satisfactorily predict the behavior of the flowing water-saturated zone experiment, and suffered no undue bias due to the perturbation in the dynamics of the system.

A significant outcome from the simulated results is that the simulated gasoline and ethanol aqueous phase plumes are identical (and uniformly smooth) in shape despite the complex evolution of the non-aqueous phase source zone. Gasoline concentrations decrease monotonically from a high of $X_{Gq} = 0.004$, due to the cosolvent behavior of ethanol, down to background levels in the direction of aqueous phase flow. Hence, the co-transport of ethanol and gasoline is advecting an elevated gasoline composition in the aqueous phase down-gradient of the source zone. Unfortunately this observation could not be confirmed by the experimental results because the Sudan Red dye does not partition into the aqueous phase along with the gasoline and hence is not an indicator of aqueous phase transport.

2.5 Conclusions

The objective of this Chapter was to examine the impact of an ethanol spill on a pre-existing gasoline source zone located within the capillary fringe. This was achieved by conducting two laboratory-scale experiments involving a Plexiglas box and glass beads to visually record the evolution of the ethanol-gasoline source zone using both a static and flowing water-saturated zone. The purpose of these experiments was to observe the: (1) depression of the capillary fringe by the gasoline fuel mixture due to a reduction in the surface tension between the gas and liquid phases, (2) further depression of the capillary fringe by the addition of ethanol, and (3) remobilization of the gasoline fuel mixture LNAPL source zone due to the cosolvent behaviour of ethanol in the presence of an aqueous phase, as well as a reduction in the interfacial tension between the aqueous/non-aqueous phases due to ethanol. Next I developed and applied the three-phase compositional numerical model *CompFlow Bio* to simulate the evolution of the observed ethanol-gasoline source zone within the capillary fringe. The purpose of the resulting numerical model-experiment comparison was to adjust parameters within constitutive relationships obtained from the literature, particularly those governing the scaling of interfacial and surface tension between phases as well as cosolvency, and replicate the experimental observations.

The procedure for conducting the numerical model-experiment comparison was to first obtain an understanding of the three above processes when the water table was static. Then, the same parameters were applied when the water-saturated zone was flowing to ensure that the general behavior of system could still be replicated given this perturbation to the dynamics of the system. A significant simplification during the development of the conceptual model needed to conduct the numerical simulations was the assumption that the complex gasoline fuel mixture used in the experiments could be represented by a single-component gasoline. This simplification was motivated by data availability constraints rather than numerical model limitations.

Results of the static water-saturated zone numerical model-experiment comparison indicate that the simulated non-aqueous phase distribution prior to ethanol injection appeared similar to the observed distribution, with a slight mismatch in the degree of lateral spreading on top of the capillary fringe. However, the simulated collapse of the capillary fringe was not as extensive as that observed. Presumably this was due to the significant fraction of light and highly volatile organics, such as butane and pentane, in the gasoline fuel mixture used in the experiments. These light organics

39

generate a greater reduction in the surface tension between the gas and liquid (aqueous and non-aqueous) phases than generated by the single-component gasoline simulated in the model. Volatilization and lateral transport of these light organics in the gas phase in the vadose zone probably caused significant collapse of the capillary fringe in regions distant from the non-aqueous phase source zone. I expect that the more extensive collapse of the capillary fringe in the experiment enabled greater lateral advection of the non-aqueous phase on top of the capillary fringe relative to the model simulation.

Results of the static water-saturated zone numerical model-experiment comparison subsequent to ethanol injection indicate that simulated non-aqueous phase distribution evolved in a manner identical to that observed in the experiment. Specifically, the capillary fringe collapsed further and the non-aqueous phase was remobilized, advected downwards, and contracted inwards resulting in elevated saturations at the water table. Key processes governing the success of the numerical model-experiment comparison involved adjusting parameters controlling two distinct processes. The first involves an additional reduction in the surface tension between the gas and liquid phases due to the presence of ethanol, leading to a further collapse of the capillary fringe. The second involves remobilization of the non-aqueous phase due to the cosolvent behavior of ethanol in the presence of an aqueous phase, as well as a reduction in the interfacial tension between the aqueous and non-aqueous phases due to ethanol. Numerous data gaps were identified during the numerical model-experiment comparison process; however, parameters controlling cosolvency enhanced portioning of gasoline from the non-aqueous in the aqueous phase appeared to be the most significant factor controlling the simulated evolution of the ethanol-impacted source zone. Finally, I concluded that the parameterized numerical model developed from the static water-saturated zone simulation effort was able to satisfactorily predict the behavior of the flowing water-saturated zone experiment, and suffered no undue bias due to the perturbation in the dynamics of the system.

A key insight from this numerical model-experiment comparison effort is that while the evolution of a pre-existing gasoline source zone impacted by an ethanol spill is highly complex, the ethanol and BTEX groundwater plumes that will emanate from the resulting source zone should be "smooth and regular", and hence diminish in a monotone manner centered around the ethanol-impacted source zone to the extremities of the groundwater plume. The magnitude of the BTEX concentration in the groundwater will be greatly elevated due to the cosolvency effect of ethanol on the gasoline fuel mixture. Therefore, at this point in time I suggest that future development of risk-based corrective

40

actions focus on issues associated with cosolvency-enhanced solubility rather than remobilization of an LNAPL source zone provided that the cosolvent-impact source zone continues to float on the water table. I do not, however, suggest that this will apply to a DNAPL source zone that could be remobilized and sink further below the water table. In addition, I wish to note that remobilization and subsequent contraction of the non-aqueous phase at higher saturations may affect longevity of the source zone as the surface area of the source zone in contact with the surrounding groundwater is reduced. This may counter-balance any reduction in the longevity of the source zone due to cosolvency-enhanced dissolution. Finally, I wish to stress that these conclusions be verified by conducting additional laboratory experiments involving detailed point-to-point measurements of saturation, pressure, mole fractions, and temperature, as well as resolving the data gaps identified in this study. Furthermore, field-scale experiments need to be conducted to address issues associated with biodegradation and sorption inherent in the risk-based corrective action framework but were not addressed in this study.
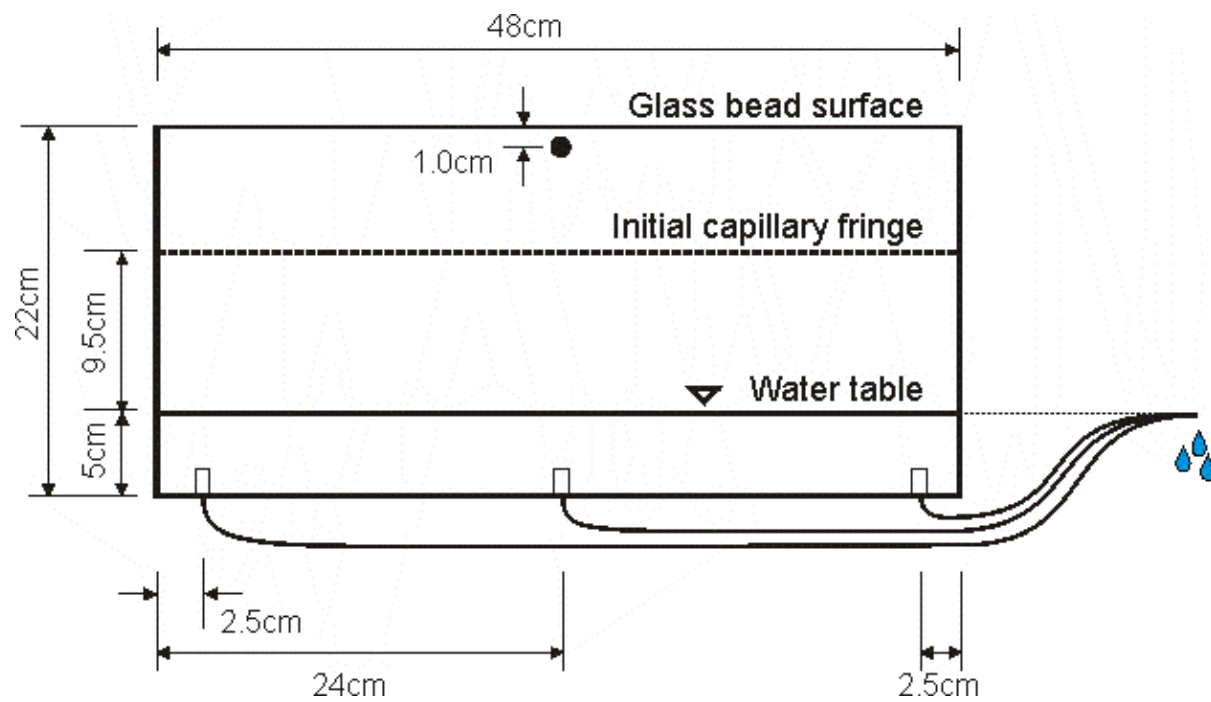
Figure 2.1. Laboratory experiment setup.
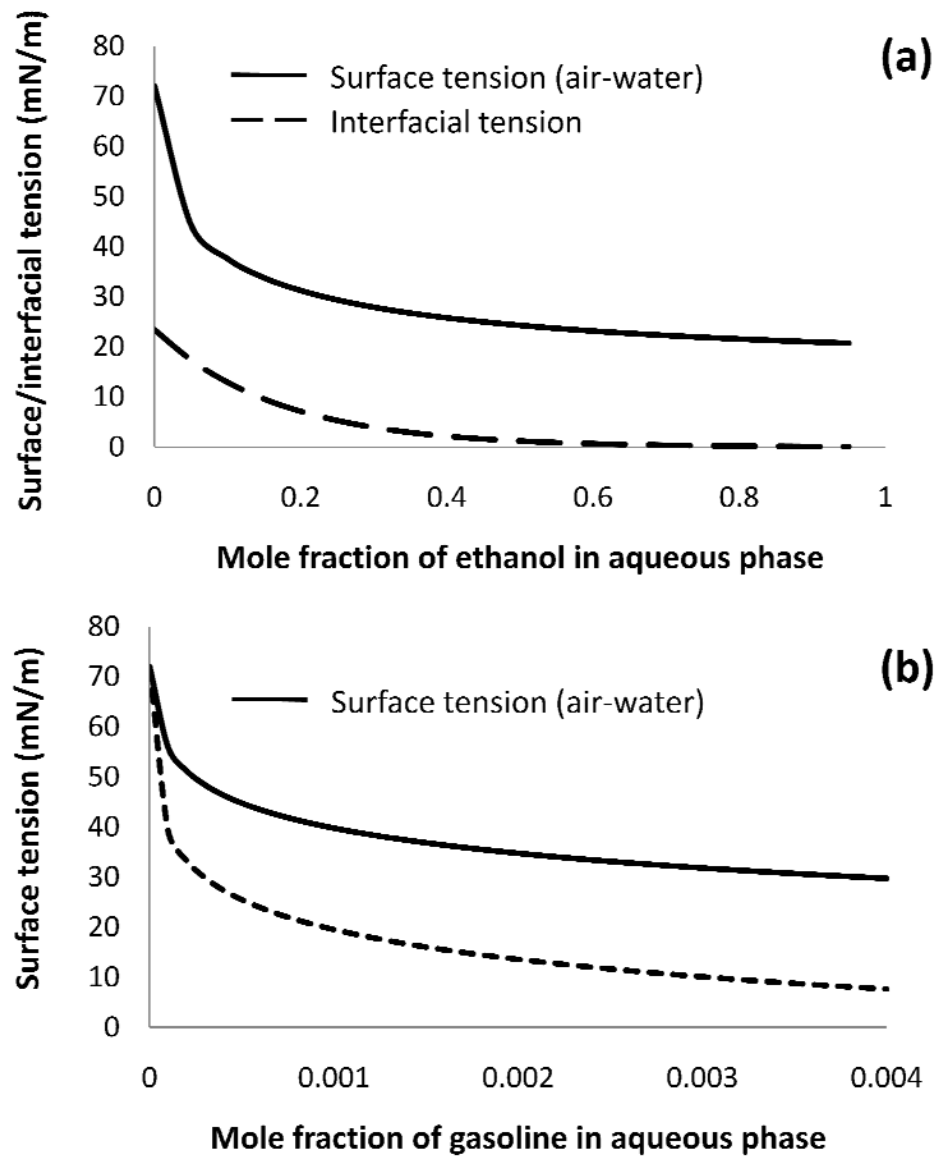
Figure 2.2. (a) Scaling of the surface and interfacial tension as a function of the mole fraction of ethanol in the aqueous phase, and (b) scaling of the surface tension with the mole fraction of gasoline in the aqueous phase, with the solid line representing the base scenario parameters described in Section 2.3.2, and the dashed line with $\vartheta_{Gq} = 0.12$ and $\zeta_{Gq} = 1.0 \times 10^{-5}$.
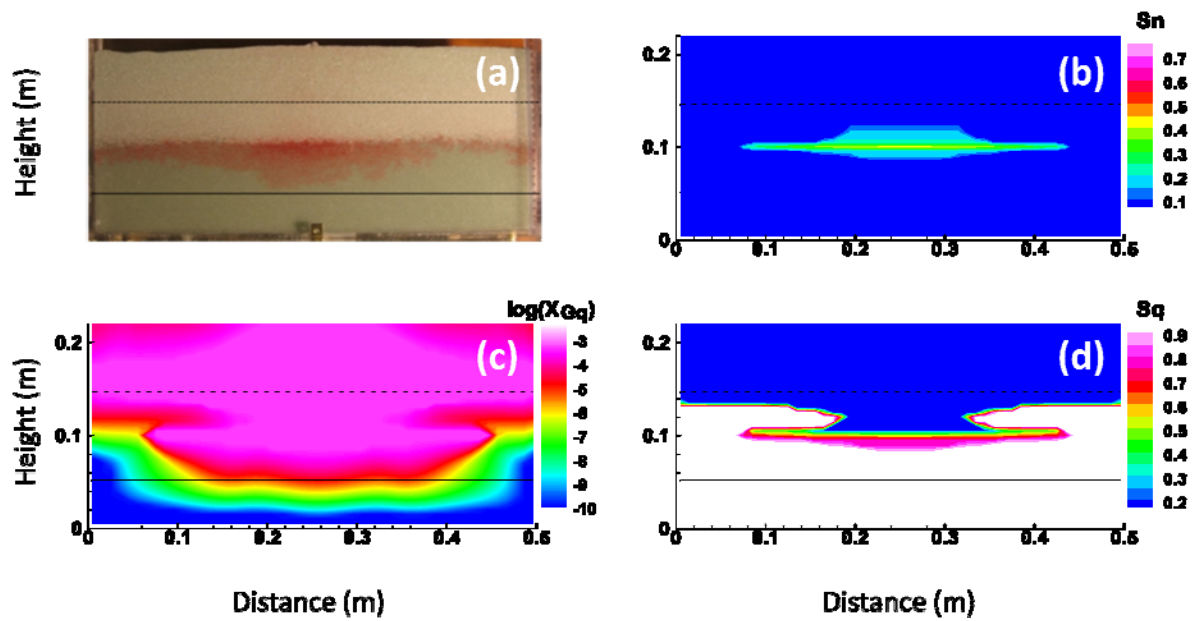
Figure 2.3. Results of the static water-saturated zone numerical model-experiment comparison one day after gasoline injection, and immediately prior to ethanol injection, for the (a) experiment, as well as the simulated (b) non-aqueous phase saturations, (c) mole fraction of gasoline in the aqueous phase, and (d) aqueous phase saturations.
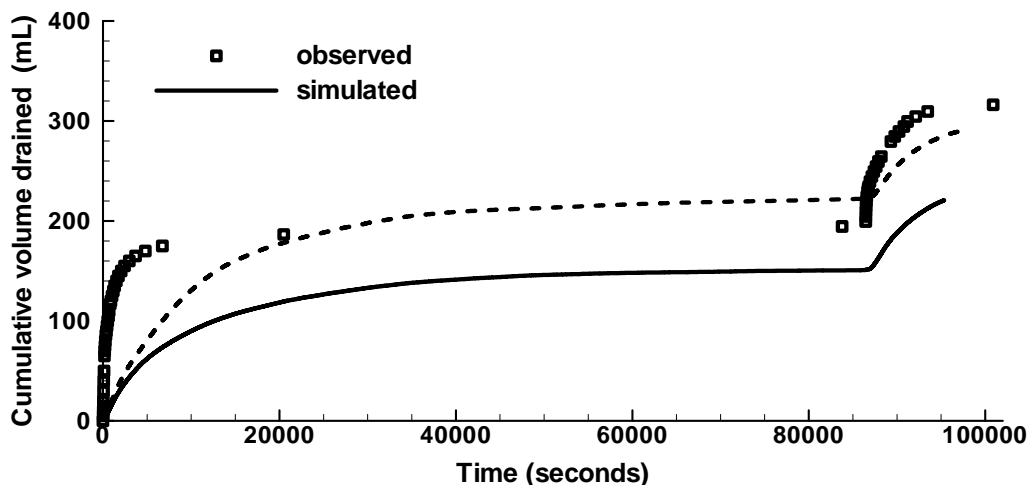
Figure 2.4. Cumulative volume of fluids drained during the static water-saturated zone experiment. The solid line represent simulated results obtained using the base scenario parameters described in Section 2.3.2, and the dashed line with $\vartheta_{Gq} = 0.12$ and $\zeta_{Gq} = 1.0 \times 10^{-5}$.
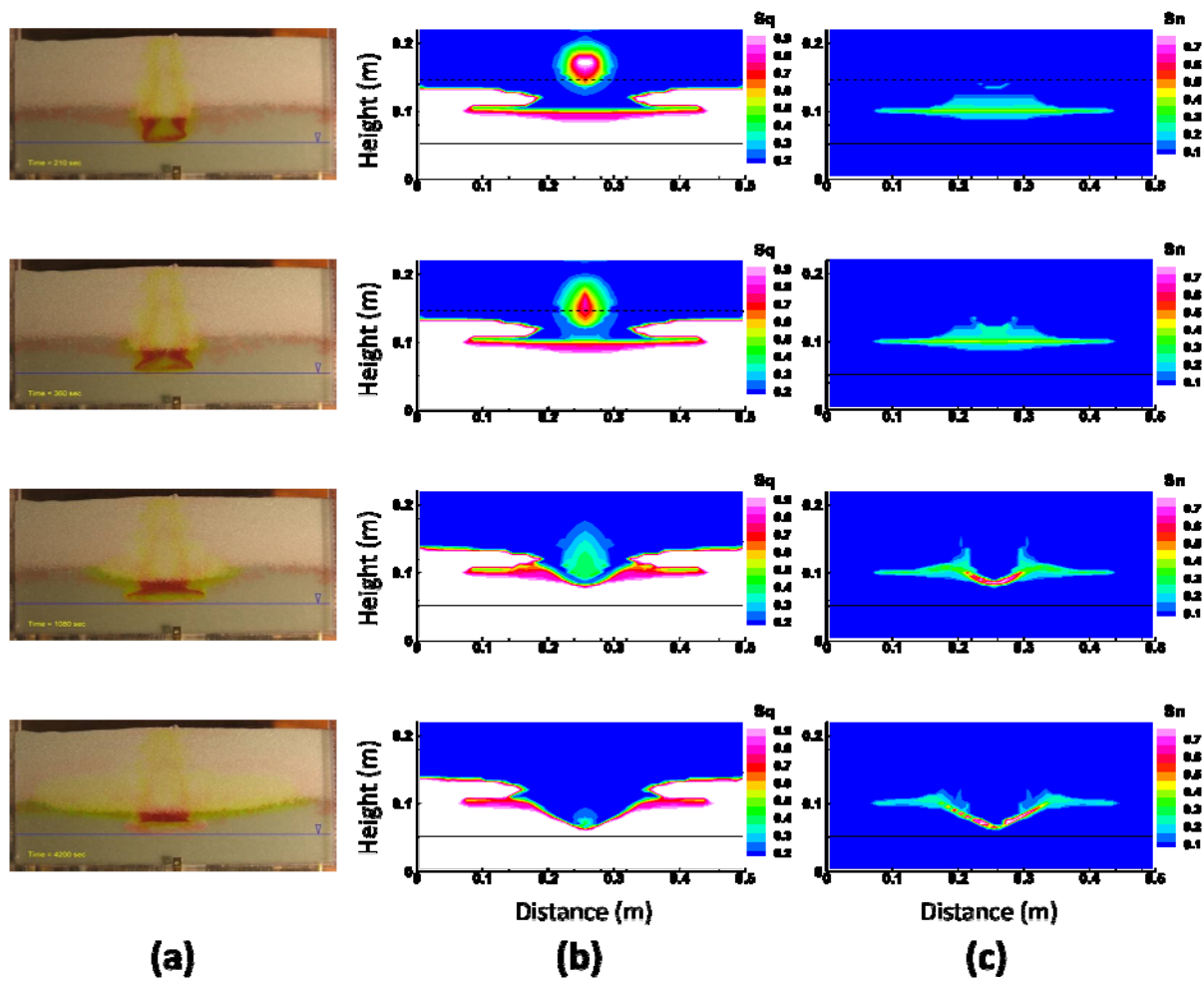
Figure 2.5. (a) Experimental results at times 210, 360, 1080 and 4200 seconds after the start of ethanol injection on rows one to four. Corresponding numerical results of (b) aqueous phase saturation and (c) non-aqueous phase saturation are presented for comparison.
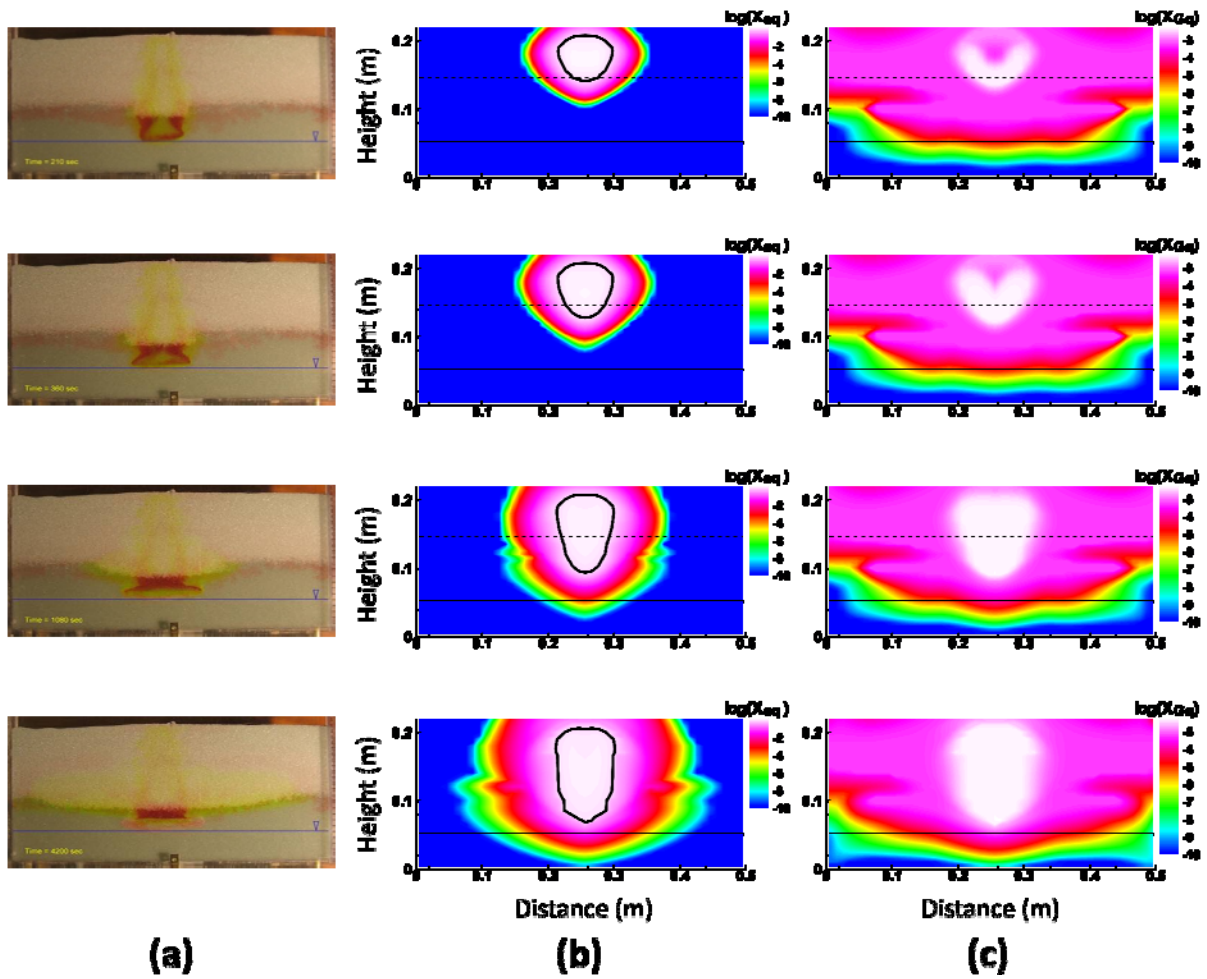
Figure 2.6. (a) Experimental results at times 210, 360, 1080 and 4200 seconds after the start of ethanol injection on rows one to four. Corresponding numerical results of (b) mole fraction of ethanol in the aqueous phase and (c) mole fraction of gasoline in the aqueous phase are presented for comparison. The black contour line on (b) represents $X_{eq} = 0.55$ which is the Plait Point from Figure 1a of *Lee and Peters* (2004).
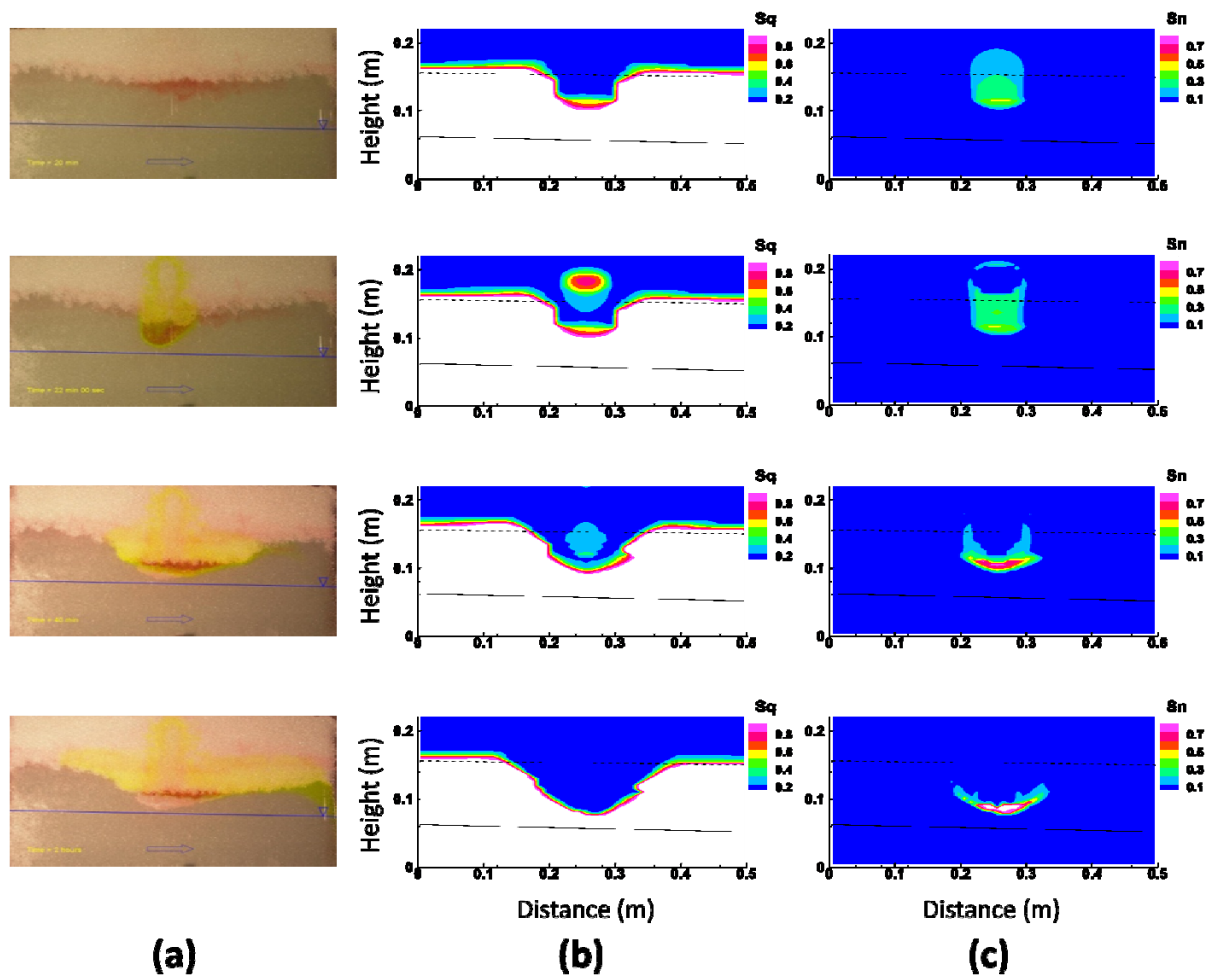
Figure 2.7. (a) Experimental results at times of 20 minutes after gasoline injection (and before ethanol injection), as well as 2 minutes, 20 minutes, and 1 hour and 40 minutes after the start of ethanol injection on rows one to four, respectively. Corresponding numerical results of (b) aqueous phase saturation and (c) non-aqueous phase saturation are presented for comparison.

48
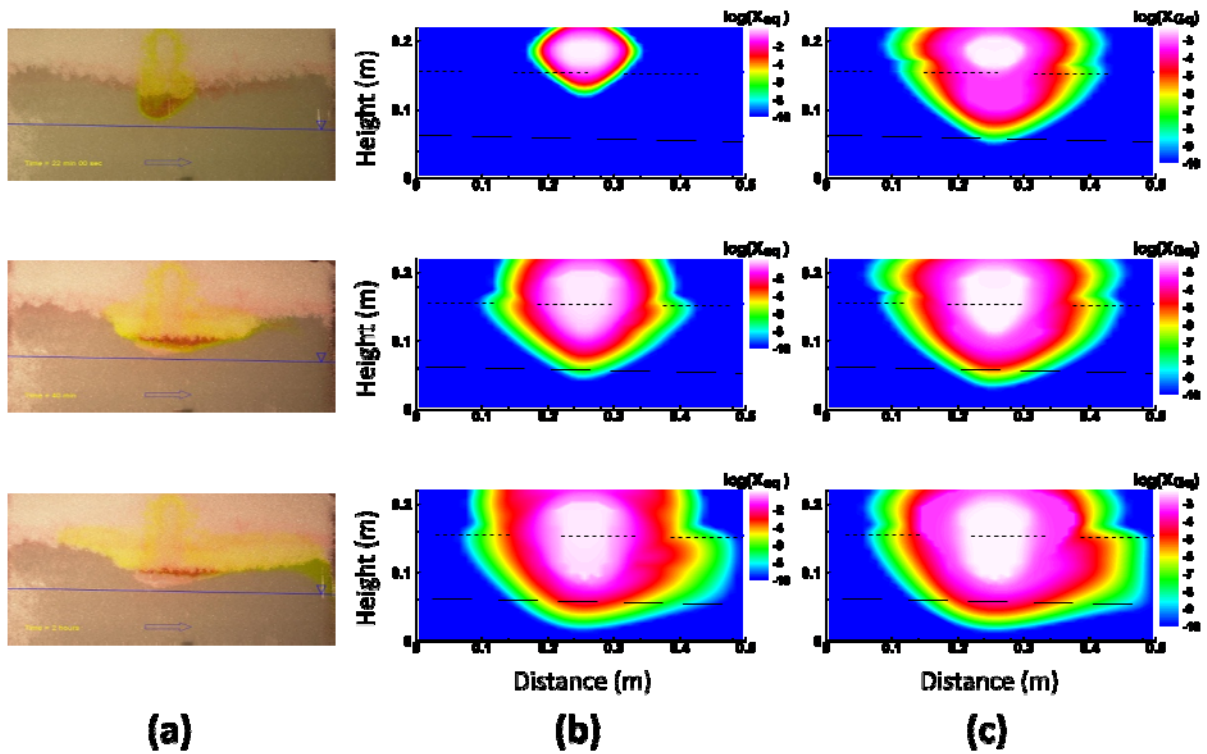
Figure 2.8. (a) Experimental results at times 2 minutes, 20 minutes, and 1 hour and 40 minutes after the start of ethanol injection on rows one to three, respectively. Corresponding numerical results of (b) mole fraction of ethanol in the aqueous phase and (c) mole fraction of gasoline in the aqueous phase are presented for comparison.

49

Table 2.1. Porous medium properties.

Property	Value
Porosity: ϕ [$-$]	0.4
Permeability: $\mathbf{K}$ [m^2]	1×10^{-11}
Dispersivity: α_L^l and α_T^l [m], $l = \{q, n, g\}$	
$\quad\quad \alpha_L^q$	0.001
$\quad\quad \alpha_L^n, \alpha_L^g$	0.0
$\quad\quad \alpha_T^q, \alpha_T^n, \alpha_T^g$	0.0
Surface and interfacial tension: $\sigma_{l_1 l_2}$ [mN/m], $l_1 l_2 = \{gn, gq, nq\}$	
$\quad\quad \sigma_{gq}$	72
$\quad\quad \sigma_{gn}$	21
$\quad\quad \sigma_{nq}$	23.4

Table 2.2. Capillary pressure and relative permeability aqueous/non-aqueous phase table.

S_q [−]	k_{rq} [−]	$k_{r(nq)}$ [−]	P_{cnq} [kPa]
0.1[a]	0.0	1.0	0.52
0.2	0.01	0.79	0.33
0.3	0.05	0.60	0.33
0.4	0.11	0.44	0.33
0.5	0.20	0.31	0.32
0.6	0.31	0.20	0.31
0.7	0.44	0.11	0.31
0.8	0.60	0.05	0.31
0.9	0.79	0.01	0.31
1.0	1.0	0.0	0.30

[a] S_{qc} − connate water saturation, $k_{rq}(S_{qc}) = 0$

Table 2.3. Capillary pressure and relative permeability liquid/gas phase table.

$S_q + S_n$ [−]	k_{rg} [−]	$k_{r(ng)}$ [−]	P_{cng} [kPa]	P_{cgq} [kPa]
0.1	1.0	0.0	0.47	1.60
0.2	0.79	0.01	0.30	1.02
0.32	0.57	0.06	0.295	1.01
0.4	0.44	0.11	0.292	1.00
0.5	0.31	0.20	0.283	0.970
0.6	0.20	0.31	0.280	0.960
0.7	0.11	0.44	0.279	0.955
0.8	0.05	0.60	0.277	0.950
0.9	0.01	0.79	0.274	0.940
0.95	0.0	0.89	0.272	0.932
1.0	0.0	1.0	0.271	0.930

Table 2.4. Equilibrium partitioning coefficients Z_{pqn} and Z_{pgq} (at 20°C).

Property	Value
water: $p = \{w\}$	
$\quad Z_{wqn}$ [−]	—[a]
$\quad Z_{wgq}$ [−]	0.01[c]
air: $p = \{a\}$	
$\quad Z_{aqn}$ [−]	—[b]
$\quad Z_{agq}$ [−]	—[b]
gasoline: $p = \{G\}$	
$\quad Z_{Gqn}$ [−]	0.000411
$\quad Z_{Ggq}$ [−]	241.62[c]
ethanol: $p = \{e\}$	
$\quad Z_{eqn}$ [−]	2.4
$\quad Z_{egq}$ [−]	0.024[c]

[a] water is not allowed to partition from the aqueous into the non-aqueous phases

[b] air is a non-condensible component and is not allowed to partition from the gas phase into either the aqueous or non-aqueous phases

[c] at $P_g = 100$ kPa and $T = 293$°K (reference temperature and pressure – see Table 2.6)

Table 2.5. Surface tension scaling parameters ϑ_{pq} and ζ_{pq}.

Property	Value
gasoline: $\quad p = \{G\}$	
$\quad \vartheta_{Gq}$ [−]	0.102 [a]
$\quad \zeta_{Gq}$ [−]	5.45×10⁻⁵ [a]
ethanol: $\quad p = \{e\}$	
$\quad \vartheta_{eq}$ [−]	0.1616
$\quad \zeta_{eq}$ [−]	1.212×10⁻²

[a] p-xylene parameters applied to gasoline

Table 2.6. Component and phase property data

Property	Value
Compressibilities	
$\hat{C}_q$ [kPa^{-1}]	4.4×10^{-7}
$\hat{C}_n$ [kPa^{-1}]	3.0×10^{-6}
$\hat{C}_r$ [kPa^{-1}]	1.0×10^{-7}
Standard component densities	
M_w^* [mole/m^3]	5.6×10^{4}
M_a^* [mole/m^3]	41.1
M_b^* [mole/m^3]	1.1×10^{4}
M_e^* [mole/m^3]	1.7×10^{4}
Molecular weights	
ω_w [kg/mole]	18.02×10^{-3}
ω_a [kg/mole]	28.97×10^{-3}
ω_b [kg/mole]	78.1×10^{-3}
ω_e [kg/mole]	46.1×10^{-3}
Reference pressure and temperature	
P^{ref} [kPa]	100.0
T^{ref} [°K]	293.0
Capillary pressure blending parameter	
S_n^* [−]	0.1
Viscosities (at 20ºC)	
μ_q [kPa · day]	1.43×10^{-11}
μ_g [kPa · day]	1.66×10^{-13}
μ_e [kPa · day]	1.24×10^{-11}
μ_G [kPa · day]	7.51×10^{-12}
Molecular diffusion coefficient	
d_q [m^2/day]	1.7×10^{-5}
d_n [m^2/day]	1.7×10^{-5}
d_g [m^2/day]	1.7×10^{-5}

Molar density

$$M_l = \frac{1 + \hat{C}_l\left(P_l - P^{\text{ref}}\right)}{\sum_p \max\left(0, X_{pl}\right)/M_p^*} \quad l = \{q, n\}, \qquad M_g = \frac{P_g}{RT}$$

Mass density

$$\rho_l = \sum_p X_{pl}\omega_p$$

Non-aqueous phase viscosity

$$\mu_n = \mu_e^{X_{en}} \cdot \mu_G^{X_{Gn}}$$

Chapter 3

Simulating the Fate and Transport of TCE from Groundwater to indoor Air

Chapter Summary

This Chapter provides an exploratory analysis on the relative importance of various factors controlling the fate and transport of volatile organic contaminants (in this case, TCE) from a DNAPL source zone located below the water table and into the indoor air. The analysis is conducted using the multi-phase compositional model *CompFlow Bio*, with the base scenario problem geometry reminiscent of a field experiment conducted by *Rivett* (1995) at the Borden aquifer where groundwater was observed to transport a contaminant plume a substantial distance without vertical mass transport of the contaminant across the capillary fringe and into the vadose zone. Results for the base scenario model indicate that the structure of the permeability field was largely responsible for deflecting the groundwater plume upward towards the capillary fringe, permitting aqueous phase diffusion to transport the TCE into the vadose zone. Alternative permeability realizations, generated as part of a Monte Carlo simulation process, at times deflected the groundwater plume downwards causing the extended thickness of the saturated zone to insulate the vadose zone from exposure to the TCE by upward diffusive transport. Comparison of attenuation coefficients calculated using the *CompFlow Bio* and *Johnson and Ettinger* (1991) heuristic model exhibited fortuitous agreement for the base scenario problem geometry, with this agreement diverging for the alternative permeability realizations as well as when parameters such as the foundation slab fracture aperture, the indoor air pressure drop, the capillary fringe thickness, and the infiltration rate were varied over typical ranges.

3.1 Introduction

The development of science-based regulatory criteria to evaluate the fate and transport of volatile organic contaminants from the subsurface into the indoor air of residential dwellings began with the

Johnson and Ettinger (1991) heuristic model (the J&E model). A key assumption in the application of the J&E model is that the non-aqueous phase (NAPL) source zone for the volatile organic contaminant is located above the water table and directly beneath the foundation slab. Despite numerous additional simplifying assumptions use to develop the closed-form analytical solution constituting the J&E model, limited site characterization budgets have motivated the wide-spread practical application of the J&E model as a preliminary screening tool to virtually all sites in the US and Canada. It is currently the *de facto* approach for assessing potential indoor air concentrations resulting from vapor intrusion into buildings. The state of the industry is such that professional judgment and regulatory guidance (*USEPA*, 2002; *USAF*, 2006; *ITRC*, 2007a,b) combine to interpret the application of the J&E model under a multitude of scenarios of practical concern even if the known hydrogeological conditions violate any of the assumptions inherent in the J&E model. To address some of the limitations of the J&E model, *Abreu and Johnson* (2005, 2006) developed a three-dimensional numerical model to assess the fate and transport of contaminants from NAPL source zones located in the vadose zone to the indoor air. Notable extensions to the J&E model inherent in the numerical modeling approach include; variable lateral offset between the source zone and foundation slab, variable footprint dimensions of the source zone and foundation slab, and dual-Monod aerobic biodegradation.

Numerous real-world sites that have groundwater plumes of volatile organic contaminants emanating from NAPL source zones located below the water table also exhibit indoor air concentrations of the same compounds within residential dwellings located above the plume. Consequently, the assumption is that the pathway for the contaminant from the source zone and into the indoor air is; advective and diffusive transport in the groundwater from the source zone to beneath the foundation slab of the residential dwelling, upward diffusive transport across the capillary fringe into the vadose zone, and advective and diffusive transport in the gas phase within the vadose zone through a crack in the foundation slab and into the residential dwelling (see Figure 3.1a). A field experiment conducted by *Rivett* (1995) involving a DNAPL source zone located a short distance below the water table indicated that the groundwater could transport contaminants a significant distance without vertical mass transport of these contaminants across the capillary fringe and into the vadose zone due to weak vertical transverse transport resulting from hydrodynamic dispersion below the water table. *McCarthy and Johnson* (1993) conducted a laboratory experiment and confirmed the above assumption that vertical mass transport of contaminants across the capillary fringe is controlled

by aqueous phase diffusion. In practice, the J&E model is also used when the NAPL source zone is located within the capillary fringe or below the water table, in part because typically insufficient site data are available to constrain the vertical and lateral location of the source zone relative to the residential dwelling with any degree of confidence. *USAF* (2006) indicates that the J&E model tends to significantly over-predict indoor air concentrations when the source zone is located in the capillary fringe or when the site-specific building and hydrogeological conditions are poorly characterized, and therefore will lead to overly conservative regulatory guidance.

The objective of this Chapter is to use the multi-phase compositional numerical model *CompFlow Bio* to examine the fate and transport of volatile organic contaminants originating from a NAPL source zone located below the water table, and their potential exposure in the indoor air of a residential dwelling located down-gradient of the source zone. The conceptual model forming this analysis follows directly from the *Rivett* (1995) field experiment and hence is reminiscent of the Borden aquifer as depicted on Figure 3.1, and involves mobile aqueous, gas and non-aqueous phases as well as equilibrium mass transfer between phases (specifically, volatilization and dissolution of an organic contaminant from the NAPL source zone). I have three fundamental questions that I wish to explore through the use of the conceptual and numerical model. First, what is the role of heterogeneity in the subsurface permeability structure of a stratigraphically continuous aquifer and diffusion across the capillary fringe in controlling the flux of contaminant from the groundwater plume across the capillary fringe and into the vadose zone at the field scale? Second, how does the soil gas beneath the foundation slab interact with pressure fluctuations in the indoor air to advect contaminant, as it emerges into the vadose zone across the capillary fringe, into the residential dwelling? Third, what is the relative importance of variability in factors such as; source zone location, aperture of the crack in the foundation slab, pressure drop within the house, capillary fringe thickness and infiltration rate (relative to heterogeneity in the subsurface permeability structure of the stratigraphically continuous aquifer itself) on simulated indoor air concentrations? These three questions are addressed by using the *CompFlow Bio* model to perform a suite of simulations designed to explore the relative balance between these factors on uncertainty in indoor air concentrations.

The scope of the proposed suite of simulations follows from the work of *Nazaroff et al.* (1985) and *Abreu and Johnson* (2005) who indicate that transient fluctuations in: indoor/outdoor temperature; wind speed against the walls of the house; operation of heating, ventilation and HVAC systems; atmospheric pressure fluctuations; operation of the sump; precipitation events and consequently soil

58

moisture; could impact the flow of soil gas into the house as well as the indoor air exchange rate. In addition, I identify the issue of ground cover (i.e., impervious pavement, cement, or frozen soil) as a possible factor which could impact the three fundamental questions that I wish to examine. For instance, *Sorek et al.* (2005) observed that buildings could be a conduit for the escape of vapor from the vadose zone to the atmosphere where the surrounding ground is impervious under isothermal conditions. In contrast, *Conant et al.* (1996) observed that seasonal temperature changes had a greater impact than the condition of the ground surface. *James and Oldenburg* (1997) conducted a numerical analysis similar in spirit to ours, but with a TCE source zone in the unsaturated zone. The significant difference between this work and theirs is that my discretization is substantially more refined in order to minimize numerical dispersion and compute the weak vertical transverse transport observed by *Rivett* (1995) across the capillary fringe. *Bozkurt et al.* (2009) use a numerical model to examine the impact that discontinuous but homogenous stratigraphic units have in controlling the fate and transport of contaminants within the soil gas into the indoor air. To keep this work focused on the three fundamental questions that I pose above, the proposed suite of numerical simulations focuses on uncertainty in hydrogeological conditions rather than the geometry of the house (i.e. size and depth of the foundation slab). This was motivated by in-depth knowledge of the Borden aquifer obtained from previous studies (such as *Rivett and Cherry*, 1991; *Rivett*, 1995) whereas I have yet to instrument an actual building at the Borden site in a manner analogous to *Nazaroff et al.* (1985). These Borden studies clearly demonstrate that the evolution of the groundwater plume from the DNAPL source zone is a transient process. Furthermore, transient hydrological and building occupation conditions can impact the fate and transport of contaminants from the soil gas into the indoor air. Consequently, the conceptual model that I use to examine the three fundamental questions above is inherently based on transient fate and transport simulations.

I endeavor to compare indoor air attenuation factors computed for the suite of *CompFlow Bio* simulations with values from the J&E model. The emphasis of the comparison is to illustrate the sensitivity of the calculated attenuation factor to the structure of the conceptual model being used to interpret or predict indoor air concentration exposure. I anticipate that the outcome of providing this comparison of attenuation factors will be further motivation for regulatory agencies to develop an enhanced closed-form (or semi-) analytical model to serve as a more appropriate screening level tool (relative to the J&E model) for conditions where the NAPL source zone is at or below the water table, and consequently produce cost-effective science-based regulatory guidance. High-risk sites identified

with this next generation model would then warrant further investigation using a combination of detailed site investigation (*Parker et al.*, 2003; *Guilbeault et al.*, 2005), site-specific numerical modeling (such as with *CompFlow Bio*), and professional judgment.

3.2 Conceptual and Numerical Model

Development of the numerical model consisted of two stages. First, I outline the formulation of the three-phase multi-component compositional numerical model *CompFlow Bio* to solve the relevant governing equations and constitutive relationships to simulate the fate and transport of TCE emanating from a non-aqueous phase source zone located in a variably saturated aquifer. The pathway includes either dissolution of TCE into the ambient groundwater (when the source zone is located below the water table) or volatilization into the ambient soil gas (when the source zone is located in the vadose zone) with mass transfer across the capillary fringe and subsequent advective-dispersive transport in the mobile soil gas and groundwater towards the foundation slab of a structure located below grade. Second, I develop a conceptual model of the variably saturated aquifer, including; (1) the approximation of the system as two-dimensional, (2) boundary conditions governing ambient groundwater and soil gas flow, (3) a methodology for incorporating the foundation of the building that is below grade into the model and simulating the interaction between the aquifer and the building, (4) the parameterization of all porous media and chemical properties governing flow and transport, (5) location of the TCE source zone below the water table, at the water table (in the capillary fringe), and above the water table (within the vadose zone), and (6) a methodology for calculating the indoor air TCE concentration based on the interaction between the aquifer and building. The intent of this conceptual model is to serve as a process-based model to assess the indoor air concentration of prototypical residential dwelling located in a heterogeneous sandy variably-saturated aquifer with a shallow water table. A such, this model (i.e., the *CompFlow Bio* model) will act as a benchmark to compute the impact of factors controlling the attenuation of indoor air concentrations for direct comparison to the *de facto* industry standard approach developed by *Johnson and Ettinger* (1991) (i.e., the J&E model).

3.2.1 Formulation

Development of the numerical model *CompFlow Bio* largely follows that of *Forsyth* (1993).
CompFlow Bio is a multi-phase multi-component compositional model that considers three mobile
phases; namely the aqueous (q), non-aqueous (n) and gas (g) phases. Furthermore, the components
can be summarized as; water (w), air (a), any number of organic contaminants which in this study
are only TCE (c_{TCE}). Assuming that components $p = \{w, a, c_{TCE}\}$ can exist in any phase $l = \{q, n, g\}$ then the conservation of moles of component p can be written as:

$$\frac{\partial}{\partial t}\left[\sum_l \left(\phi S_l M_l X_{pl}\right) + \rho_r K_{dp} M_q X_{pq}\right] = -\sum_l \nabla \cdot \left(M_l X_{pl} \mathbf{V}_l\right) + \sum_l \nabla \cdot \left(\phi S_l \mathbf{D}_l M_l \nabla X_{pl}\right) + Q_p \qquad (3.1)$$

The Darcy flux of each phase $\mathbf{V}_l$ is given by:

$$\mathbf{V}_l = -\mathbf{K} \cdot \frac{k_{rl}}{\mu_l} \nabla(P_l + \rho_l gz) \qquad (3.2)$$

and the dispersion/diffusion tensors $\mathbf{D}_l$ have the form:

$$\phi S_l \mathbf{D}_l = \alpha_T^l V_l \mathbf{I} + \left(\alpha_L^l - \alpha_T^l\right)\frac{\mathbf{V}_l \mathbf{V}_l}{V_l} + \phi S_l \tau d_l \mathbf{I} \qquad (3.3)$$

where the nomenclature is as in Chapter 2. There exist the following constraints among the above
variables:

$$S_q + S_n + S_g = 1$$

$$P_g = P_n + \hat{\alpha}P_{cgn}(S_g) + (1 - \hat{\alpha})[P_{cgq}(S_g) - P_{cnq}(S_q = 1)]$$

$$P_n = P_q + \hat{\alpha}P_{cnq}(S_q) + (1 - \hat{\alpha})P_{cnq}(S_q = 1) \tag{3.4}$$

where

$$\hat{\alpha} = \min(1, S_n/S_n^*) \tag{3.5}$$

and P_{cgn}, P_{cgq}, and P_{cnq} are experimentally derived capillary pressure curves [kPa]. S_n^* is a blending parameter used to ensure that the capillary pressure has the correct form as the non-aqueous phase saturation goes to zero. The capillary pressure curves are scaled using a modified form of the function proposed by *Leverett* (1941):

$$P_{cl_1l_2}^D = \frac{P_{cl_1l_2}}{\sigma_{l_1l_2}}\left(\frac{\mathbf{K}}{\phi}\right)^{\tilde{\alpha}} \tag{3.6}$$

where $P_{cl_1l_2}^D$ and $P_{cl_1l_2}$ are the dimensionless and dimensional capillary pressures, respectively, between any two phases, $l_1l_2 = \{gn, gq, nq\}$, $\sigma_{l_1l_2}$ is the surface/interfacial tension between the two phases, and $\tilde{\alpha}$ is a parameter related to the pore size distribution of the porous media.

Stone's second model (*Stone*, 1973) is used in *CompFlow Bio* to estimate k_{rn} and is normalized using the method introduced by *Aziz and Settari* (1979). Therefore, the relative permeability of the aqueous, gas and non-aqueous phases for the three-phase system is given by:

$$k_{rq} = F\left(S_q\right)$$

$$k_{rg} = F\left(S_g\right)$$

$$k_{rn} = k_{r(nq_c)}\left[\left(\frac{k_{r(nq)}}{k_{r(nq_c)}} + k_{rq}\right)\left(\frac{k_{r(ng)}}{k_{r(nq_c)}} + k_{rg}\right) - \left(k_{rq} + k_{rg}\right)\right] \tag{3.7}$$

where $k_{r(nq)}$ and $k_{r(ng)}$ are the non-aqueous phase relative permeabilities measured in the two-phase non-aqueous/aqueous and non-aqueous/gas systems at the aqueous and gas phase saturations in the full three-phase system, respectively.

Partitioning of components between phases is assumed to be at equilibrium. In this context, the following constraint applies to any phase l which is present:

$$\sum_p X_{pl} = 1 \tag{3.8}$$

Component p partitions between the gas and non-aqueous phases according to:

$$X_{pg} = Z_{pgn}X_{pn} \text{ where } Z_{pgn} = exp\{a_{pgn}\}/P_g \tag{3.9}$$

while between the gas and aqueous phases, the relationship is:

$$X_{pg} = Z_{pgq}X_{pq} \text{ where } Z_{pgq} = exp\{a_{pgq}\}/P_g$$

$$X_{wg} = Z_{wgq}X_{wq} \text{ where } Z_{wgq} = a_{wgq}/P_g \tag{3.10}$$

where both Z_{pgn} and Z_{pgq} are dependent on the systems pressure P_g.

Although Equation (3.1) is given in the most general sense, some simplifying assumptions are made that restrict the composition of various phases. Specifically, the non-aqueous phase consists of only component $p = \{c_{TCE}\}$ which implies $X_{wn} = 0$ and $X_{an} = 0$, the aqueous phase consists of components $p = \{w, c_{TCE}\}$ which implies $X_{aq} = 0$, and the gas phase consists of all available components $p = \{w, a, c_{TCE}\}$. The rationale for this restricted system is provided in *Forsyth* (1993).

Phase appearance and disappearance rules are used to develop meaningful tests to detect which subset of phases exists at a node given the moles of component p present. These rules follow from the set of primary variables, which in general consist of P_l, X_{pl}, and S_l and are aligned with Equations (3.1) to (3.3). Following the formulation introduced by *Forsyth* (1993), I also assume the gas phase is always present to at least some minimal saturation $S_g^{min} = 10^{-3}$ to alleviate numerical issues associated with the non-condensable air component.

Numerical discretization of Equation (3.1) follows directly from *Unger et al.* (1996). Specifically, a fully-implicit temporal discretization is used to ensure an adaptive and aggressive time-stepping scheme can be used that maintains monotonicity of the solution (in X_{pl}, S_l, P_l etc.) irrespective of the time step size. A Van Leer flux limiter is used for $X_{c_{TCE}g}$ and $X_{c_{TCE}q}$ in the advective flux term to facilitate an unconditionally monotone TCE transport solution irrespective of the local Peclet number, as well as a solution that approaches second-order accuracy in space. Upstream spatial weighting is used for all other advective mole fraction terms.

3.2.2 Base Scenario Model

I wish to use the conceptual model to test two processes controlling the fate and transport of TCE from the source zone into the indoor air. First, heterogeneity in the permeability of the aquifer may cause the plume to be deflected upwards and approach the water table while the flow of water that has infiltrated from precipitation will act to push the plume downward. Once the plume is sufficiently near the water table, hydrodynamic dispersion (mechanical dispersion plus molecular diffusion) will then cause the upward transport of TCE across the capillary fringe and into the vadose zone. Second, once TCE has reached the vadose zone, transport of TCE towards the foundation slab of the

64

residential dwelling will be driven by advection and diffusion. I assume that the operation of a high-efficiency furnace (or alternatively heating/ventilation/HVAC system) will induce a "stack effect" causing the basement to be slightly under-pressurized with respect to the main floor and the ambient atmospheric pressure. For simplicity, I assume this slight under-pressurization is constant in time even though *Nazaroff et al.* (1985) observe that it is highly transient as household utilization of heating/ventilation/HVAC systems changes. Assuming there is a crack in the foundation slab in the basement, slight depressurization of the basement may induce advective flow of the soil gas beneath the foundation slab into the indoor air. Therefore, the balance between advection and diffusion is controlled by the proximity of the TCE in the vadose zone to the foundation slab. Far away from the foundation slab, transport is diffusion dominated. Near the foundation slab, it is advection dominated.

Figure 3.2 depicts the structure of the base scenario numerical model. Of particular note is that the model is only two-dimensional. Therefore, the groundwater plume emanating from the TCE source zone is constrained to advect beneath the foundation. In addition, horizontal diffusion transverse to the direction of groundwater advection cannot diminish TCE concentrations before they reach the vadose zone. Consequently, simulated indoor air concentrations of TCE will be elevated relative to results simulated using a three-dimensional numerical model. Hence, this conceptual model will yield conservative results. The motivating factor for using a two-dimensional numerical model was the intensive mesh refinement needed to minimize numerical dispersion and ensure that the groundwater plume could travel the entire length of the domain, for some heterogeneous permeability realizations, without TCE ever reaching the vadose zone. This resulted in a mesh containing $42 \times 1 \times 35$ nodes with a minimum discretization of 2.5 m $\times$ 1.0 m $\times$ 0.2 m in the x–, y– and z–directions. Figure 3.3 depicts a single realization of a heterogeneous and statistically anisotropic permeability field with properties listed on Table 3.1. Values on Table 3.1 are characteristic of the Borden aquifer as measured by *Woodbury and Sudicky* (1991) and *Conant et al.* (1996), with the variance increased substantially to be similar to that of the more heterogeneous Cape Cod aquifer (*Hess et al.*, 1992). The permeability realization was generated using the algorithm described by *Robin et al.* (1993).

Boundary conditions controlling the ambient aqueous and gas phase flow are illustrated on Figure 3.2. In summary, for the base scenario conceptual model which is reminiscent of the Borden aquifer, the ambient atmospheric pressure is held constant at $P_g = 100$ kPa (P^{ref}) using a penalty-source-sink term that either allows the air $p = \{a\}$ component to flow in or all gaseous components $p = \{w, a, c_{TCE}\}$ to flow out, the ambient aquifer temperature is 10°C, infiltration from recharge occurs at

an annual average rate of 0.2 m/yr (*Solomon et al.*, 1992), the ambient groundwater pore velocity is 0.09 m/day (*Woodbury and Sudicky*, 1991), and the TCE source zone is located $L = 55$ m up-gradient of the foundation slab at a depth of 1.5 m below the water table. Tables 3.1 to 3.5 itemize all relevant physical and chemical properties of the system.

The foundation slab and basement interior of the residential dwelling are directly incorporated into the numerical model by altering properties of mesh nodes to represent the interaction between soil gas and indoor air between the basement and the surrounding aquifer. The objective of discretizing the basement directly into the numerical model is to be able to directly compute two metrics needed to calculate the resulting indoor air concentration of TCE within the residential dwelling. The two metrics are: (1) the volumetric flow rate of the soil gas $Q_a[\text{m}^3/\text{day}]$, represented by component $p = \{a\}$, into the basement across a crack in the foundation slab, and (2) the concentration of TCE $\mathbb{C}_{c_{TCE}g}$ [ppmV] within the soil gas entering the basement. These two metrics are then used in a post-processing step to compute the indoor concentration within the entire residential dwelling, which includes the ground floor that is not directly represented in the numerical model.

Interaction between the soil gas and the indoor air is limited to occur across the foundation slab only. To facilitate this in the numerical model, I assumed there was a single crack of length 11 m encircling the 5.0 m × 1.0 m cross-sectional area of the basement in the x– and y– directions, consistent with a shrinkage crack forming along the periphery of the poured concrete floor where it intersects the footings of the basement walls. Given that I am only representing a unit-width of the house in the y –direction, an alternative view would be 2.2 m length of crack per unit surface area of foundation slab, where the genesis of the cracks is due to foundation settlement. The aperture of the crack for the base scenario is $2b = 100\ \mu\text{m}$ resulting in a permeability of $\mathbf{K}_{slab_C} = 8.33 \times 10^{-10}\ \text{m}^2$, while the foundation slab matrix is comprised of concrete and is essentially impermeable which is approximated by assigning it a permeability of $\mathbf{K}_{slab_M} = 1 \times 10^{-20}\ \text{m}^2$, with the resulting bulk permeability of the foundation slab being $\mathbf{K}_{slab_B} = 1.83 \times 10^{-13}\ \text{m}^2$. These properties were calculated using the following series of relationships:

$$\phi_{slab_C} = \frac{V_C}{V_{slab}}$$

$$\phi_{slab_M} = 1 - \phi_{slab_C}$$

$$\mathbf{K}_{slab_C} = \frac{(2b)^2}{12}$$

$$\mathbf{K}_{slab_B} = \mathbf{K}_{slab_C}\,\phi_{slab_C} + \mathbf{K}_{slab_M}\,\phi_{slab_M} \tag{3.11}$$

where V_C and V_{slab} are the volume $[\text{m}^3]$ of the crack and entire foundation slab, respectively. Advective flux of the gas phase is forced to occur across the foundation slab only by reducing the gas phase pressure along the top row of the basement interior nodes so that for the base scenario they are $\Delta P_g^{basement} = 10\ \text{Pa}$ below that of the ambient atmospheric pressure P^{ref}. This applied vacuum is at the lower range of values reported by *Johnson and Ettinger* (1991) and *Nazaroff et al.* (1985) of $\Delta P_g^{basement} = 1 - 50\ \text{Pa}$, although I adjust the applied vacuum over a range of values as part of a sensitivity analysis later in this work. Diffusive flux of components within the gas phase occurs naturally across the foundation slab and is driven by gradients in the mole fraction composition of the soil gas beneath the foundation slab and that within the indoor air. The walls of the basement are made impermeable by cutting the edges (i.e. the influence coefficients for advective and dispersive mass flux between the basement and aquifer nodes), and the interior nodes of the basement are assigned a permeability of $\mathbf{K}_{basement} = 1 \times 10^{-9}\ \text{m}^2$ to ensure that the foundation slab is the limiting factor allowing gas phase flow to enter the basement. The porosity of the nodes representing the interior volume of the basement was reduced to $\phi_{basement} = 0.001$ to minimize the mixing volume within the basement. These properties are summarized on Table 3.6.

Once the two metrics described above are computed using *CompFlow Bio*, the indoor air concentration of TCE is computed as a post-processing step. This methodology proceeds by first computing the concentration of TCE in the soil gas $\mathbb{C}_{c_{TCE}g}$ that is entering the basement at current *CompFlow Bio* simulation time $n + 1$ as:

$$\mathbb{C}_{c_{TCE}g}^{n+1} = \frac{Q_{c_{TCE}}^{n+1}}{Q_a^{n+1}\,M_a^*} \times 10^6\ [\text{ppmV}] \tag{3.12}$$

where $Q_{c_{TCE}}^{n+1}$ [moles/day] and Q_a^{n+1} [m^3/day] are the flow rate of TCE and air into the basement at timestep $n+1$. Next, I assume two possibilities concerning the ventilated condition of the house, namely; without air exchange, and alternatively with air exchange. Without air exchange, the heating/ventilation/HVAC activity does not introduce any outside air into the house, the air within the house is perfectly circulated via the ventilation system, and any soil gas entering $Q_a^{n+1}|_1$ (or exiting $Q_a^{n+1}|_2$) the indoor air of the house across the foundation slab is compensated by an equal flow of indoor air out of $Q_a^{n+1}|_3$ (or atmospheric air into $Q_a^{n+1}|_4$) the house through leaks around the windows and doors. The indoor air concentration of TCE, $\mathbb{C}_{c_{TCE}IA}^{n+1}$, at current *CompFlow Bio* time step $n+1$ is computed as:

$$
\frac{\mathbb{C}_{c_{TCE}IA}^{n+1} - \mathbb{C}_{c_{TCE}IA}^{n}}{\Delta t} V_H = \underbrace{Q_a^{n+1}|_1 \, \mathbb{C}_{c_{TCE}g}^{n+1}}_{F_1\left\{\begin{array}{l}\text{into house}\\\text{across slab}\end{array}\right.} - \underbrace{Q_a^{n+1}|_2 \, \mathbb{C}_{c_{TCE}IA}^{n+1}}_{F_2\left\{\begin{array}{l}\text{out of house}\\\text{across slab}\end{array}\right.}
$$

$$
- \underbrace{Q_a^{n+1}|_3 \, \mathbb{C}_{c_{TCE}IA}^{n+1}}_{F_3\left\{\begin{array}{l}\text{out of house}\\\text{around doors}\\\text{and windows}\end{array}\right.} + \underbrace{Q_a^{n+1}|_4 \, \mathbb{C}_{c_{TCE}ATM}^{n+1}}_{F_4\left\{\begin{array}{l}\text{into house}\\\text{from atmosphere}\end{array}\right.}
$$

(3.13)

where $Q_a^{n+1}|_1 + Q_a^{n+1}|_4 = Q_a^{n+1}|_2 + Q_a^{n+1}|_3$ and the concentration of TCE in the atmospheric air $\mathbb{C}_{c_{TCE}ATM}^{n+1} = 0$ ppmV for the base scenario. The fluxes of TCE, F_1, F_2, F_3 and F_4 [ppmV TCE $\times$ m^{3}air/day], are depicted on Figure 3.4. The volume of the house V_H is calculated under the assumption that it consists of a basement and main floor, and each floor including supporting beams is 3 m tall, resulting in a total indoor air volume of $V_H = 30$ m^{3}per unit width in the y–direction. Note that timestep $\Delta t = t^{n+1} - t^n$, where n denotes the prior *CompFlow Bio* simulation time. With air exchange, $Q_a^{n+1}|_4 = V_H \times A_{ex}$ where $A_{ex} = 0.5/hr$ is the number of air volumes flowing into the house per unit time for the base scenario model. The value of A_{ex} was adopted to be consistent with *Johnson and Ettinger* (1991). Note that $Q_a^{n+1}|_1$ is enforced using a penalty sink term for Q_a in Equation (3.1) and is implemented as:

$$Q_a^{n+1}|_{1,i} \frac{M_a^*}{V_i} = B \, X_{ag|i} \, M_{g|i} \frac{k_{rg|i}}{\mu_{g|i}} \left(P_g^{basement} - P_{g|i}^{n+1} \right) \tag{3.14}$$

where $P_g^{basement} = P^{ref} - \Delta P_g^{basement}$, node i is basement node in which the sink term is placed, V_i is the volume of node i, and $B = 10^5$ in order to ensure a grid-converged air flow rate $Q_a^{n+1}|_{1,i}$ for the simulated pressure difference.

3.3 Results

Simulations using the *CompFlow Bio* model consist of three main stages. First, I develop an appropriate initial condition for the base scenario model establishing both steady-state aqueous and gas phase flow in the subsurface for three development stages, namely; before construction, after construction and before occupation, as well as after construction and occupation of a residential dwelling. Second, I introduce a TCE source zone within the base scenario model, with the variations on the DNAPL source zone location including; below the water table, at the water table (within the capillary fringe), and above the water table (within the vadose zone above the capillary fringe). TCE was injected at a rate of 0.18 m^3/day over a period of one day forming a source with a volume of 0.18 m^3. The start of TCE injection is denoted as time $t = 0$ days . The TCE source zone was then allowed to redistribute itself as necessary, and TCE contamination then emanates from the DNAPL source zone and is transported within the steady-state aqueous and gas phase flow fields towards the basement of the residential dwelling, which is located down-gradient of the source zone. Third, I conduct a sensitivity analysis to determine the impact of various factors on the attenuation of concentrations within the indoor air. These factors are described below.

3.3.1 Initial Condition

An initial condition was established for each of the three stages in the construction and occupation of the residential unit. All stages occur prior to TCE being introduced into the aquifer. These stages can be interpreted as variations on the base scenario model, and are meant to determine the impact that construction and occupation of the house have on the ambient aqueous and gas phase flow fields in the subsurface. Prior to construction, nodes within the basement (as shown on Figure 3.3) simply contain the original heterogeneous permeability field. In addition, the entire surface of the domain is assigned a constant atmospheric pressure of $P_g = 100$ kPa with an infiltration rate of 0.2 m/yr. After construction and before occupation, the entire base scenario modifications shown on Figure 3.2 are adopted except there is no vacuum applied in the basement. In other words, I assume the residential dwelling has been built but the heating/ventilation/HVAC system has not been used yet. Once the residential dwelling is occupied, the system is turned on and a vacuum is applied in the basement.

Figure 3.5 depicts the steady-state aqueous and gas phase flow fields for the post-construction with occupation base scenario. The other two development stages are omitted for brevity[5]. The steady-state aqueous phase flow field, as shown on Figure 3.5a for the heterogeneous permeability realization shown on Figure 3.3, exhibits two regions in which the ambient groundwater flow field is deflected upwards towards the capillary fringe up-gradient of the foundation slab. This occurs despite the downward flow of infiltrating water from precipitation as shown by the aqueous phase pathlines originating at the ground surface. The steady-state gas phase flow field, as depicted on Figure 3.5b for the same heterogeneous permeability realization, shows that the vacuum in the basement of $\Delta P_g^{basement} = 10$ Pa induces atmospheric flow across the foundation slab from as far as 20 m on either side of the basement, with the gas phase pathlines reaching down to the top of the capillary fringe.

3.3.2 Indoor Air Concentrations for the Base Scenario Model

3.3.2.1 Source Zone Below the Watertable

---

[5] See Figures B.1 and B.2 in Appendix B for details.

As described in Section 3.2.2, the base scenario model consists of a TCE source zone located below the water table, $L = 55$ m up-gradient of a residential dwelling with the foundation slab located 2 m below grade. Following from the initial condition as described in Section 3.3.1, indoor air concentrations for the base scenario model were simulated for each of the three development stages, namely; before construction, after construction and before occupation, as well as after construction and occupation of a residential unit.

Figure 3.6 shows the mole fraction of TCE in the gas phase within the aquifer 1000 days after TCE was introduced (below the water table) for each of the three development scenarios. Figure 3.7 shows the two metrics computed by *CompFlow Bio* as: (a) the volumetric flow rate of the soil gas into the basement through a crack in the foundation slab, and (b) the concentration of TCE within the soil gas entering the basement. Figure 3.7 part (c) and (d) show the resulting indoor air concentrations of TCE computed using Equation (3.13) without and with air exchange, respectively.

Prior to construction, Figure 3.6a shows that the TCE groundwater plume is transported upwards by advection towards the capillary fringe due to the structure of the heterogeneous permeability field (as described in Section 3.3.1). After 1000 days of transport, the near proximity of the TCE groundwater plume to the water table permits vertical diffusion of TCE into the capillary fringe and the vadose zone. Note that extensive vertical grid refinement was performed to minimize numerical dispersion in this region and establish a grid-converged solution, and that vertical physical dispersion is only caused by molecular diffusion as all dispersivities α_L^q and α_T^q (resulting in mechanical dispersion) were set to zero. Once TCE reaches the vadose zone, molecular diffusion in the gas phase causes the lateral and vertical spreading of the TCE soil gas plume. Advection of TCE in the soil gas is negligible as the gas pressure is uniformly atmospheric along the surface and the TCE composition of the soil gas is too low to induce density driven advection.

After construction and before occupancy, Figure 3.6b shows that the mole fraction of TCE in the gas phase after 1000 days of transport is nearly identical to before construction (Figure 3.6a). This is expected as $\Delta P_g^{basement} = 0$ Pa and hence there is no additional advective flux of TCE in the soil gas in the static soil gas column below the foundation slab ($Q_a = 0$ m^3/day in Figure 3.7a) beyond the diffusive flux already present before construction. The only perturbation to the system is the "rain shadow" created by the house below the foundation slab. However, this rain shadow which does

reduce water saturations in the vadose zone below the foundation slab, does not appear to significantly impact the mole fraction distribution of TCE in the gas phase.

With occupancy, Figure 3.6c shows that the mole fraction of TCE in the gas phase below the foundation slab after 1000 days of transport is higher than without occupancy. This is due to the vacuum induced by the heating/ventilation/HVAC system which creates an advective flux of the gas phase from the vadose zone, across the foundation slab, and into the indoor air of the basement at a rate of $Q_a = 0.1$ m^3/day (see Figure 3.7a). As described in Section 3.3.1, the pathlines of advective gas phase flow originate at the ground surface approximately 20 m on either side of house, and reach down to the capillary fringe before crossing the foundation slab. Gas phase originating at the ground surface (from the atmosphere) does not contain any TCE. However, these pathlines pick up TCE from the top of the capillary fringe and advect it upwards towards the foundation slab. Of particular note is that there does not appear to be a significant amount of dilution of the TCE soil gas concentrations arising from the introduction of clean atmospheric air into the subsurface relative to that prior to construction. These results imply that diffusion is the dominant transport mechanism of TCE in the soil gas in regions distant from the basement, while advection is the dominant transport mechanism immediately beneath the foundation slab. This assumption is fundamental to the heuristic model formulated by *Johnson and Ettinger* (1991). Consequently, despite the differences in the geometry between my conceptual model and that of *Johnson and Ettinger* (1991), I observe that the flux of contaminants beneath the foundation slab is dominated by advection in a vertically upward direction (i.e. one dimensional) in support of one of the fundamental assumption in the J&E model.

In this study, I adopt an arbitrary indoor air regulatory limit for TCE of 0.25 ppmV as a compromise between the dramatically different values of; 25 ppmV as established by *OEHHA-CEPA* (2007), and 0.000927 ppmV given by *NYSDOH* (2005). Introducing an indoor air regulatory limit into this study serves three purposes. First, regulatory guidance documents such as *OEHHA-CEPA* (2007) and *NYSDOH* (2005) present indoor air regulatory limits to safeguard the public based on established scientific and engineering principles. Therefore, as a point of comparison, it is useful to determine whether a given simulated scenario exceeds a regulatory limit and therefore demands some sort of remedial action. Second, I wish to demonstrate that within the confines of my conceptual model, the process of determining whether a simulated indoor air concentration exceeds a regulatory limit involves a transient simulation and cannot be represented using a steady-state fate and transport simulation akin to the J&E model. Third, in a companion work to this study, I calculate the

probability of indoor air concentrations exceeding an indoor air regulatory limit (defined as "the probability of failure") within 100 day intervals over a period of 1300 days following construction and occupancy of the house in Chapter 4. I then prescribe a "cost of failure" to a given failure event, which when adjusted for the time value of money, leads to a definition of "risk" arising from potential indoor air exposure and the societal costs and benefits of indoor air regulation.

Following this discussion, indoor air concentrations for the base scenario after construction and with occupancy indicate that TCE reaches a maximum indoor air concentration of 0.068 ppmV (see Figure 3.7d – with air exchange) approximately 1500 days after TCE was introduced into the aquifer, with approximately two-thirds of the non-aqueous phase source zone remaining[6]. Consequently, for the base scenario model after construction and with occupancy, the indoor air concentration does not exceed the regulatory limit with an air exchange rate of $A_{ex} = 0.5/hr$. Conversely, without air exchange (see Figure 3.7c), the indoor air concentration is dramatically above the regulatory limit. Clearly it is imperative to obtain field measurements of air exchange rates along with science-based regulatory exposure limits to make defensible statements whether indoor air TCE concentrations have exceeded a threshold limit or not.

Of particular interest is that the TCE concentration within the indoor air declines rapidly after 1500 days (with or without air exchange) even though the NAPL source zone remains below the water table until 5000 days. This is in direct contrast to the J&E model where a key assumption involved in its derivation is that the indoor air concentration reaches a steady state value in response to the non-diminishing source zone. The simulated decline after 1500 days was a consequence of the upper portion of the TCE source zone dissolving only with the bottom portion remaining. Once the upper portion of the source zone was removed, the groundwater plume was no longer in near proximity to the water table diminishing the diffusive flux of TCE across the capillary fringe into the vadose zone. I conclude that spatial distribution of the subsurface properties can exert a significant temporal response on the observed indoor air concentrations as the source zone diminishes over time.

I endeavor to compare the J&E model to the base scenario *CompFlow Bio* model with the TCE source zone located below the water table. The basis of comparison is an "attenuation coefficient" representing the ratio of the indoor air concentration to that of the source, as described by Equation (20) of *Johnson and Ettinger* (1991). For the *CompFlow Bio* model, α_{CFB} is computed when the TCE

---

[6] See Figure B.3 in Appendix B for details.

indoor air concentration reaches its peak value at 1500 days (see Figure 3.7d). For the J&E model, parameters involved in calculating $\alpha_{J\&E}$ are itemized in Equation (21) of *Johnson and Ettinger* (1991). Values used for these parameters to compare the base scenario *CompFlow Bio* to the J&E model are listed on Table 3.7. Of particular note is that $Q_{soil} = 0.0691 \text{ m}^3/\text{day}$ as calculated using Equation (24) of *Johnson and Ettinger* (1991) while $Q_a^{n+1}|_1 = 0.1 \text{ m}^3/\text{day}$ for the *CompFlow Bio* base scenario as used in Equation (3.13). To resolve this discrepancy, I computed values of $\alpha_{J\&E}$ using two methods: first, values of $\alpha_{J\&E}^{(1)}$ were calculated using J&E model parameters entirely from Table 3.7; and second, values of $\alpha_{J\&E}^{(2)}$ were calculated using with $Q_{soil} = Q_a^{n+1}|_1$. The latter method provides a more direct comparison between the *CompFlow Bio* to the J&E model independent of the assumptions inherent in the calculation of Q_{soil} by *Johnson and Ettinger* (1991). Specifically, I wish to note that Q_{soil} in the J&E model is computed assuming flow is proportional to the gradient in gas phase pressure instead of the gradient in gas phase potential – in effect, the gravitational potential term is neglected. Note that on Figure 3.5b, I present contours of the gas phase potential given by Equation (3.2) as: $\Gamma_g = P_g + \rho_g g z$. Clearly, it is gradients in contours of the gas phase potential that drive advection in the gas phase from the ground surface to beneath the foundation slab and into the indoor air.

   Results of the comparison of $\alpha_{J\&E}$ and α_{CFB} are summarized on Table 3.8, where the base scenario with construction and without occupancy ($\Delta P_g^{basement} = 0$ Pa) is identified as "Scenario 1a", and the base scenario with construction and occupancy ($\Delta P_g^{basement} = 10$ Pa) is identified as "Scenario 1b". With construction and occupancy (Scenario 1b) with a vacuum imposed in the basement, both $\alpha_{J\&E}^{(1)}$ and $\alpha_{J\&E}^{(2)}$ are only a factor of at most 3.6 greater than α_{CFB}. The excellent agreement is entirely fortuitous and perhaps only holds for the base scenario parameters presented in this study. In fact, shortly I will present results of a sensitivity analysis in which I perturb parameters in my base scenario model over reasonable ranges and observe the agreement between the *CompFlow Bio* and J&E model diverges. A case in point is the base scenario with construction and without occupancy (Scenario 1a). Both $\alpha_{J\&E}^{(1)}$ and $\alpha_{J\&E}^{(2)}$ are a factor of 2.2×10^5 greater than α_{CFB} indicating that the J&E model significantly over-predicts the indoor air concentration when the source zone is located below the water table and transport of TCE into the indoor air is diffusion controlled due to no advection of the gas phase.

74

In summary, I identify three major differences between the conceptual model inherent in the *CompFlow Bio* base scenario and the J&E model that could generate discrepancies between values of $\alpha_{J\&E}$ and α_{CFB} . First, for the *CompFlow Bio* model, the TCE source is located below the water table and TCE must diffuse across the capillary fringe before it can be advected upwards in the gas phase as it flows towards the foundation slab. For the J&E model, the TCE source zone is located within the vadose zone. Fortuitously, this was not a significant issue for the base scenario as long as advective transport was dominant over diffusive transport of TCE into the indoor air. Second, the heterogeneous permeability field in the *CompFlow Bio* model is largely responsible for deflecting the TCE groundwater plume upward towards the capillary fringe, permitting aqueous phase diffusion to transport the TCE into the vadose zone. Alternative permeability realization may just as well deflect the groundwater plume downwards causing the extended thickness of the saturated zone to insulate the vadose zone from exposure to the TCE by upward diffusive transport. In the case of the J&E model, the subsurface is assumed to be homogeneous. I explore the impact of heterogeneity in the subsurface on the indoor exposure later in this work. Third, the TCE source zone in the CompFlow *Bio* model diminishes over time as TCE partitions from the non-aqueous into the aqueous phase. This causes the peak indoor air concentration to decline as the source zone dissolves into the groundwater. In contrast, the J&E model assumes steady-state transport and indoor air concentrations with a non-diminishing source zone. I note that the field experiment conducted in the Borden aquifer by *Rivett et al.* (1994), *Rivett* (1995), and *Frind et al.* (1999) supports the concept of a diminishing source zone, as simulated here by the *CompFlow Bio* model.

3.3.2.2 Source Zone At and Above the Water Table

As a variation of the base scenario model described in Section 3.3.2.1, I placed the TCE source zone at and above the water table as shown on Figure 3.1b. For the case with the source zone at the water table (Scenario 2 – see Table 3.8), the source zone was relocated to be 1.5 m above that shown on Figure 3.2. For the case with the source zone above the water table (Scenario 3 – see Table 3.8), it was relocated 3.0 m above that shown on Figure 3.2. Both of these scenarios are a closer approximation of the J&E conceptual model. Hence, aqueous phase diffusive transport of TCE across the capillary fringe is not a limiting process for attenuating indoor air concentrations. Note that the

source zone is still located $L = 55$ m up-gradient (in the direction of ground water flow) of the basement whereas in the J&E model, the source zone is located directly below the basement. Both Scenario 2 and 3 involve occupation of the house with $\Delta P_g = 10$ Pa, analogous to Scenario 1b.

Figures 3.8a and 3.8b show the mole fraction of TCE in the gas phase within the aquifer 1000 days after TCE was introduced into the aquifer with the source zone at and above the water table, respectively. Analogous to Scenario 1b, diffusive flux of TCE in the gas phase within the vadose zone is a significant transport mechanism in regions distant from the basement, with the advective flux becoming dominant in the vicinity of the foundation slab. In contrast to Scenario 1b, the mole fraction of TCE in the gas phase is significantly greater when the TCE source zone is located at or above the water table, than when it is below the water table. This is shown on Figure 3.7b which depicts the concentration of TCE in the soil gas beneath the foundation slab, and Figures 3.7c and 3.7d which exhibit the resulting indoor air concentration of TCE without and with air exchange as a function of time. Once again, the regulatory limit of TCE in the indoor air of 0.25 ppmV is arbitrary and is chosen here as a compromise between two significantly different standards. However, the regulatory limit chosen here does serve as a standard by which to compare indoor air concentrations simulated using the different scenarios. Consequently, I observe that while the indoor air concentration is below the regulatory limit of 0.25 ppmV (with air exchange) when the TCE source is located below the water table, it is much greater than the regulatory limit when the source zone is locate at or above the water table.

Once again, I compare the attenuation coefficients $\alpha_{\text{J\&E}}$ and α_{CFB} with the source zone located at and above the water table using identical parameters for Scenario 1b (see Table 3.7), when the source zone was located below the water table. Attenuation coefficient values are provided on Table 3.8. In summary, both $\alpha_{\text{J\&E}}^{(1)}$ and $\alpha_{\text{J\&E}}^{(2)}$ are at most a factor of 0.77 and 2.07 times α_{CFB} for Scenario 2 and 3, respectively. Therefore, I conclude that for this particular base scenario, the *CompFlow Bio* and J&E models show excellent agreement independent of whether the source zone is located below, at, or above the water table. Note that values of α_{CFB} were obtained when indoor air concentrations reach a peak value, which for Scenario 2 occurs at about 3000 days, and for Scenario 3 occurs after 3000 days and remains constant for the remainder of the simulation. In effect, Scenario 3 with the source zone located above the water table appears to exhibit steady state indoor air concentrations consistent with the J&E model. The apparent steady state indoor air concentrations are due to the longevity of

the TCE source zone for Scenario 3, with 57% remaining after 5000 days[7]. In contrast, Scenario 2 and 1b have 27% and 5% remaining after 5000 days, respectively. The simulated longevity of the source zones for Scenarios 1b, 2 and 3 is site and contaminant specific, and cannot be generalized from this particular conceptual model.

3.3.3 Sensitivity Analysis

3.3.3.1 Aquifer Heterogeneity

Imperfect knowledge of the point-to-point structure of subsurface properties is a fundamental issue when assessing the fate and transport of contaminants into the indoor air. I address this issue by generating 50 alternative, but statistically equivalent, heterogeneous permeability realizations to that shown on Figure 3.3. Next, I used *CompFlow Bio* to compute the resulting indoor air concentration for the base scenario with air exchange and with the TCE source zone located below the water table (Scenario 1b). These results are shown on Figure 3.9a. Although not shown for brevity[8], the volumetric flow of air into the basement is insensitive to heterogeneity while the concentration of TCE in the soil gas beneath the foundation slab is very sensitive to heterogeneity. This latter observation is demonstrated by the significant variability in indoor air TCE concentrations, of which 8/50 of the simulations appear to exceed the exposure limit of 0.25 ppmV. Note that this variability in indoor air TCE concentrations also indicates that the attenuation coefficient computed using the base scenario *CompFlow Bio* model is sensitive to aquifer heterogeneity, implying that agreement with the J&E model is restricted to the permeability realization shown on Figure 3.3. Given that many of the permeability realizations yield indoor air concentrations that are either greater or less than Scenario 1b, I further note that the J&E model does not necessarily yield overly-conservative regulatory guidance as mentioned by *USAF* (2006).

---

[7] See Figure B.4 in Appendix B for details.
[8] See Figure B.5 in Appendix B for details.

A key observation from this Monte Carlo analysis is that numerous realizations yield indoor air concentrations that are significantly lower than when using the heterogeneous permeability realization shown on Figure 3.3. These situations arose when the groundwater plume was deflected downwards by the permeability structure of the saturated zone effectively diminishing the ability for aqueous phase diffusion to transport TCE across the capillary fringe. These particular Monte Carlo realizations yield results consistent with the field observations of *Rivett* (1995) where monitoring of both the groundwater plume and the soil gas above the plume indicated that the groundwater could transport contaminants a significant distance without vertical mass transport of these contaminants across the capillary fringe and into the vadose zone. In contrast, the heterogeneous permeability realization shown on Figure 3.3 yielded opposite results. I remind the reader that I increased the variance of permeability field relative to the known statistics of the Borden aquifer. This will impact the results by artificially inflating the effect whereby the plume is either deflected upwards or downwards by the structure of the permeability field. I observe that $\sigma_Y = 1.0$ is at the upper range whereby the simulated results are still consistent with the field observations of *Rivett* (1995).

3.3.3.2 Lateral Offset of the Source Zone

Aside from imperfect knowledge of the point-to-point structure of subsurface properties, the actual location of the source zone is typically unknown due to either sparse sampling data or unknown details concerning the location and timing of surface releases of the contamination. To examine this issue, I adjusted the lateral offset of the source zone from the base scenario value of $L = 55$ m to be $L = 35$ m and $L = 15$ m up-gradient of the basement. In both cases, the source zone was placed below the water table for comparison to Scenario 1b. Given the heterogeneous permeability structure of the aquifer, it was necessary to conduct each of the 50 Monte Carlo realizations from Section 3.3.3.1 with each source zone offset to determine the impact of uncertainty in the source zone location.

Indoor air concentration of TCE with air exchange and the progression in the lateral offset of the source zone at $L = 55$ m, 35 m and 15 m up-gradient of the basement are shown on Figures 3.9a, 3.9b and 3.9c, respectively. Results indicate that probability of indoor air TCE concentrations exceeding the regulatory limit of 0.25 ppmV as the lateral offset diminishes from $L = 55$ m, 35 m and 15 m is

8/50, 12/50 and 11/50, respectively. Consequently, with the source zone located below the water table, the maximum expected probability of exposure exceeding the regulatory limit occurs when the source zone is around 35 m up-gradient of the basement. Note that when the source zone is located at (Scenario 2) and above (Scenario 3) the water table, the indoor air concentration of TCE with air exchange (see Figure 3.7d) is approximately the same as that simulated for the one Monte Carlo realization exhibiting the highest concentrations with the source zone located below the water table (see Figure 3.9a). I did not conduct Monte Carlo simulations with the source zone located at and above the water table because results from Figure 3.8 lead me to believe that TCE transport in the vadose zone at distances greater than 20 m on either side of the basement is diffusion controlled. Therefore, I conclude that the resulting indoor air concentration should be insensitive to heterogeneity in the permeability structure of the aquifer. This hypothesis follows from *James and Oldenburg* (1997) who compared simulated TCE soil gas concentrations (emanating from a source zone located above the water table) beneath a residence using both a single realization of a heterogeneous permeability field and an equivalent homogeneous aquifer, and did not observe a significant impact .

3.3.3.3 Barometric Pressure Fluctuations

I extended the analysis of the base scenario model with the source zone located below the water table (Scenario 1b) by enforcing barometric pressure fluctuations along the surface boundary of the model. This sensitivity analysis is called Scenario 4 on Table 3.8. The motivation for this scenario follows directly from *Nazaroff et al.* (1985) who observed that transient indoor air concentrations of radon originating from the soil gas are correlated to the transient barometric pressure signal. The barometric pressure data was obtained from Year 2005 measured at the University of Waterloo Weather Station (see Figure 3.10) with the mean adjusted to be $P_g = 100$ kPa. This one year cycle was then repeated over the duration of the simulation. The identical barometric pressure fluctuations were repeated in the basement under a constant vacuum of $\Delta P_g^{basement} = 10$ Pa. The objective of this sensitivity analysis was to investigate the impact of dampening of soil gas pressures induced by the permeability and porosity of the porous media on inward as well as outward flow across the foundation slab assuming that the operation of the heating/ventilation/HVAC system remains constant over the

simulation. I leave the issue of including transient fluctuations in $\Delta P_g^{basement}$ along with the barometric pressure for future work.

Figures 3.11a and 3.11b show the two *CompFlow Bio* metrics of soil gas flow across the foundation slab and TCE concentration immediately beneath the foundation slab, while Figure 3.11c and 3.11d show the resulting indoor air concentrations without and with air exchange, respectively. Results indicate that where the barometric pressure is constant (Scenario 1b), there is a steady flow of soil gas into the basement. In contrast, when the barometric pressure is allowed to fluctuate, there are very large fluctuations in the flow of soil gas into the basement as well as indoor air into the subsurface. The concentration of TCE in the soil gas beneath the foundation slab diminishes dramatically by a factor of about 100 to indoor air levels when indoor air flows into the subsurface, and increases to values approaching twice that of Scenario 1b when soil gas flows into the basement. The indoor air concentration without air exchange (Figure 3.11c) shows dramatically less sensitivity to the wild variations in the two *CompFlow Bio* metrics due to the "storage" and hence dilution created by the interior volume of the house V_H (see Equation 3.13), although the resulting indoor air concentrations are approximately twice that of Scenario 1b. With air exchange (Figure 3.11d), the fluctuations in the two metrics are preserved in the resulting indoor air concentration, with values always exceeding that of Scenario 1b and momentarily exceeding the regulatory limit of 0.25 ppmV on multiple occasions. Ultimately, the net result is that indoor air concentrations remain marginally higher when barometric pressure are allowed to fluctuate than when they are held constant.

I conclude this section by noting that increase in indoor air TCE concentrations due to barometric pressure fluctuations is insignificant in magnitude relative to the variability induced by subsurface heterogeneity. Consequently, I recommend that a detailed site investigation to characterize subsurface material properties and source zone location be primary considerations in interpreting or predicting indoor air impacts, while uncertainty induced by barometric pressure fluctuations being considered inconsequential.

3.3.3.4 Residential Dwelling Factors

Numerous factors related to the physical structure of the residential dwelling can influence the interaction between the soil gas beneath the foundation slab and the indoor air. However, I focus on two items; the aperture of the foundation crack, and the vacuum induced by the heating/ventilation/HVAC system. A sensitivity analysis exploring the relative importance of these factors is described below. All of the simulations in this sensitivity analysis involve the TCE source zone located beneath water table for direct comparison to Scenario 1b.

The average aperture of the foundation crack over its entire length is impossible to measure in a typical residential dwelling given that settlement cracks in a concrete foundation slab will be irregular in shape along the basement floor, and variable in aperture across the thickness of the slab. The objective of this sensitivity analysis was to vary the aperture thickness over orders of magnitude to determine the range of impact on simulated indoor air concentrations. I denote this sensitivity analysis as Scenario 5 on Table 3.8. Indoor air concentrations with air exchange are shown on Figure 3.12a. Results indicate that as the aperture decreases from 1000 μm, 100 μm, 10 μm to 1 μm, for a fixed vacuum of $\Delta P_g^{basement} = 10$ Pa, the flow of soil gas into the basement diminishes precipitously from 0.46 m³/d, 0.1 m³/d, 0.0001 m³/d, to 3×10^{-7} m³/d, respectively. In contrast, the peak soil gas concentration beneath the foundation slab increased from 64 ppmV, 251 ppmV, 710 ppmV to 702 ppmV, respectively[9]. The net result is that the indoor air concentration diminishes to essential "non-detect" levels with the decline in fracture aperture. Of particular interest is that the indoor air concentration does not change significantly as the aperture increases beyond 100 μm. Therefore, I conclude that the limiting process controlling the increase in indoor air concentration when the source zone is located below the water table remains the diffusive flux of TCE in the aqueous phase across the capillary fringe. The aperture of the foundation crack only serves to further limit the TCE flux across the foundation slab once the vadose zone is impacted, further diminishing indoor air concentrations. I note that this only follows basic engineering judgment, with the obvious remediation effort being to seal foundation cracks to mitigate indoor air exposure. As a result, little effort need be expended attempting to characterize the aperture of the foundation crack (assuming appropriate site investigation activities have been completed) given that a conservative estimate of TCE exposure in the indoor air can be obtained with a fictitiously large aperture.

---

[9] See Figure B.6 in Appendix B for details.

As part of establishing the base scenario model with the source zone located below the water table (Section 3.3.2.1), I used two alternative vacuum pressures within the basement. Specifically, they involved a vacuum of $\Delta P_g^{basement} = 0$ Pa (Scenario 1a) and $\Delta P_g^{basement} = 10$ Pa (Scenario 1b). The objective of this analysis was to examine the sensitivity of indoor air concentrations to a change in applied vacuum pressure with additional simulations involving $\Delta P_g^{basement} = -10, 1, 5, 50$ Pa which are listed as Scenario 6 on Table 3.8. The resulting indoor air concentrations with air exchange are shown on Figure 3.12b. Results indicate that as the applied vacuum decreases from 50 Pa, 10 Pa, 5 Pa , 1 Pa, to 0 Pa for a fixed fracture aperture of $2b = 100\ \mu m$, the flow of soil gas into the basement diminishes precipitously from 0.56 m³/d, 0.1 m³/d, 0.042 m³/d, 0.0017 m³/d, to 4×10^{-7} m³/d, respectively. In contrast, the peak soil gas concentration beneath the foundation slab generally increased from 52 ppmV, 251 ppmV, 441 ppmV, 710 ppmV and 603 ppmV, respectively[10]. The net result is that indoor air concentrations (with air exchange) increase as the vacuum in the basement increases. Note that *Johnson and Ettinger* (1991) indicate the practical range of observed vacuum pressures in basements is $\Delta P_g^{basement} = 1 - 50$ Pa . Therefore there is a practical upper limit on the indoor air concentration imposed by a vacuum in the basement. Increasing the vacuum from 10 Pa to 50 Pa has significantly less impact on increasing the indoor air concentration relative to uncertainty in the structure of the heterogeneous permeability field. Of particular interest is that the concentration of TCE in the soil gas beneath the foundation slab is significant even when there is no advective flow towards the basement ($\Delta P_g^{basement} = 0$ Pa) due to the large diffusive flux of TCE in the gas phase (Figure 3.6b). In fact, there is even some TCE in the soil gas beneath the foundation slab when $\Delta P_g^{basement} = -10$ Pa (Figure 3.6d). This is a consequence of the large diffusive flux of TCE in the gas phase within the vadose zone. Once again, I conclude that the process controlling the upper-limit on indoor air concentration when the source zone is located below the water table remains the diffusive flux of TCE in the aqueous phase across the capillary fringe, yielding the mass flux of TCE into the vadose zone.

Finally, I compare the attenuation coefficients $\alpha_{J\&E}$ and α_{CFB} for Scenarios 5 and 6 as described above. Although $\alpha_{J\&E}$ and α_{CFB} exhibit close agreement for the base scenario model parameters, this agreement significantly diverges as the aperture of the foundation crack decreases from $2b = 100\ \mu m$ to $2b = 1\ \mu m$. At this point, $\alpha_{J\&E}$ over-predicts α_{CFB} by a factor of 5700. Similarly, as the applied

---

[10] See Figure B.7 in Appendix B for details.

vacuum decreases from $\Delta P_g^{basement} = 10$ Pa to 1 Pa, $\alpha_{J\&E}$ over-predicts α_{CFB} by a factor of 68. Clearly, the agreement between the *CompFlow Bio* and the J&E models is completely fortuitous for the specific base scenario model parameters, and diminishes as these values are adjusted over reasonable ranges. In fact, there may be no reasonable point of comparison for a different *CompFlow Bio* problem geometry than specified in Figure 3.2.

3.3.3.5 Controls on Aqueous Phase Transport

Imperfect knowledge of subsurface conditions can have a significant impact on uncertainty in predicting, or interpreting, indoor air concentrations arising from subsurface contamination. This was discussed in Section 3.3.3.1 where I evaluated the impact of heterogeneity in the permeability of the aquifer material and observed that indoor air concentration were dramatically influenced by whether the groundwater plume emanating from the TCE source zone was either deflected upward toward the capillary fringe or not. When the groundwater plume advects within close proximity of the capillary fringe, aqueous phase diffusion is able to transport TCE across the capillary fringe and into the vadose zone. Consequently, aqueous phase diffusive flux of TCE across the capillary fringe appears to be the limiting hydrologic process controlling indoor air exposure. Building upon this observation, I conducted a sensitivity analysis on two controls that could impact the aqueous phase fate and transport of TCE between the source zone (located below the water table) and eventual diffusive transport across the capillary fringe. These factors are; the thickness of the capillary fringe, and the rate of infiltration from precipitation. All of the simulations in this sensitivity analysis involve the TCE source zone located beneath water table for direct comparison to Scenario 1b. The motivation for these simulations follows that of *Nazaroff et al.* (1985) and *Rivett and Cherry* (1991) who observe that the soil moisture content as a consequence of transient precipitation events has an impact on the fate and transport of contaminants in the soil gas. In addition, *McCarthy and Johnson* (1993) observe that the fate and transport of contaminants from below the water table to above the capillary fringe is limited by molecular diffusion in the aqueous phase. Finally, I note that increasing the thickness of the capillary fringe is not identical to increasing the depth of the source zone below the water table

because water in the capillary fringe is held under tension, and does not undergo lateral advection along with the ambient groundwater flow field.

I hypothesize that increasing the thickness of the capillary fringe will diminish the diffusive flux of TCE in the aqueous phase. This is because the upward diffusive flux across the capillary fringe is essentially proportional to the gradient in TCE concentrations across this region. Note that the concentration of TCE in the groundwater at the point just below the water table where it begins to diffuse upward towards the vadose zone remains unchanged despite the thickness of the capillary fringe, and the concentration of TCE in the aqueous phase at the top of the capillary fringe is negligible in comparison to that at the bottom of the capillary fringe. Then, the gradient in TCE concentrations across this region is only sensitive to the distance across which this difference in TCE concentrations is applied. In other words, as the thickness of the capillary fringe increases, the gradient of TCE concentrations in the aqueous phase decreases, and the diffusive flux of TCE in the aqueous phase decreases. I test this hypothesis using the sensitivity analysis denoted as Scenario 7 on Table 3.8. In this case, the thickness of the capillary fringe was increased by adjusting all values of P_{cgq} in the base scenario model (see Table 3.3) upward by 5.0 kPa. This resulted in a capillary fringe that was approximately 0.5 m thick. In contrast, the base scenario model (Scenario 1b) does not have a capillary fringe, with S_q decreasing below unity immediately above the water table.

Figure 3.13 shows indoor air concentrations with air exchange and for the thicker capillary fringe. Because the foundation slab of the basement is approximately 1.2 m above the water table, the increased water saturation with the thicker capillary fringe does not significantly affect the flow of soil gas into the indoor air (with $Q_a^{n+1}|_1 = 0.056$ m^3/day) relative to Scenario 1b[11]. However, the indoor air concentration with air exchange does decrease appreciably to a peak value of 0.023 ppmV. This result follows from my hypothesis above, because decreasing the flux of TCE into the soil gas at the top of the capillary fringe will ultimately reduce TCE concentrations within the soil gas beneath the foundation slab and finally within the indoor air. Finally, I note that $\alpha_{J\&E}$ over-predicts α_{CFB} by a factor of 25, once again indicating a departure from the fortuitous agreement exhibited by the base Scenario 1b.

I expect that adjusting the rate of infiltration from precipitation will have three impacts on the transport of TCE from the source zone below the water table and into the indoor air. First, by

---

[11] See Figure B.8 in Appendix B for details.

increasing the infiltration rate, the water saturation in the vadose zone will increase, thereby decreasing the relative permeability of the gas phase and consequently the flow of air into the basement. Second, increasing the infiltration rate will also push the TCE groundwater plume downward as the additional water recharges the water table. This will increase the distance across which the diffusive flux of TCE in the aqueous phase must transport TCE into the vadose zone diminishing indoor air concentrations as described above. Third, increasing the infiltration rate will increase the downward advective flux of TCE in the aqueous phase. Because the total flux of TCE in the aqueous phase is the sum of the advective and diffusive flux, the result of increased infiltration will be to reduce the total upward flux of TCE across the capillary fringe and into the vadose zone. Ultimately this will reduce indoor air concentrations. I explore the impact of doubling and alternatively eliminating the infiltration rate of water using the sensitivity analysis denoted as Scenario 8 on Table 3.8.

Figure 3.13 also shows indoor air concentrations (with air exchange) with no infiltration and double the infiltration rate relative to the base scenario. Note that *Solomon et al.* (1992) estimated that the annual average infiltration at the Borden aquifer ranged between 0.14 m/yr to 0.62 m/yr, with the base scenario model assigned a value of 0.2 m/yr. Although not shown for brevity[12], the flow of soil gas into the indoor air, $Q_a^{n+1}|_1$, was insensitive to the infiltration rate and was 0.1 m³/day with no infiltration and with double infiltration. In contrast, the indoor air concentration is very sensitive to the infiltration rate and diminishes to a peak value of 0.01 ppmV as the rate is doubled, and increases to a peak value of 0.55 ppmV as infiltration is eliminated. The ratio of $\alpha_{J\&E}$ to α_{CFB} also diverges with a value of 0.44 and 24 for no infiltration and double infiltration, respectively. I note that this is essentially over a two-order-of-magnitude deviation simply due to what could easily be seasonal variations in infiltration rates due to precipitation and evapotranspiration factors. Furthermore, I speculate that since precipitation events are highly transient in nature, I anticipate that indoor air concentrations will exhibit a signal that is correlated to the rate at which corresponding infiltration fronts advect downwards through the vadose zone and recharge the saturated zone consistent with the observations of *Nazaroff et al.* (1985).

I conclude this section by observing that the variability in indoor air concentrations due to my sensitivity analysis involving the capillary fringe thickness and infiltration rate was of the same order-

---

[12] See Figure B.8 in Appendix B for details.

of-magnitude as the sensitivity observed due to aquifer heterogeneity as discussed in Section 3.3.3.1. Therefore, I further suggest that measuring parameters controlling the aqueous phase transport of TCE in the vadose zone be included as part of a detailed site investigation to characterize subsurface material properties and source location in order to interpret or predict indoor air impacts.

3.4 Conclusions

The objective of this Chapter was to use the multi-phase compositional numerical model *CompFlow Bio* to examine the fate and transport of volatile organic contaminants (in this case, TCE) originating from a NAPL source zone located below the water table, and their potential exposure on the indoor air of a residential dwelling located down-gradient of the source zone. The base scenario conceptual model used in this study is reminiscent of a field experiment conducted at Borden by *Rivett* (1995) involving a DNAPL source zone located a short distance below the water table. Monitoring of both the groundwater plume and the soil gas above the plume indicated that the groundwater could transport contaminants a significant distance without vertical mass transport of these contaminants across the capillary fringe and into the vadose zone.

The conceptual model was designed to examine two process controlling the fate and transport of TCE from the source zone into the indoor air. First, heterogeneity in the permeability of the aquifer may cause the plume to be deflected upwards and approach the water table while the flow of water that has infiltrated from precipitation will act to push the plume downward. Once the plume is sufficiently near the water table, hydrodynamic dispersion will then cause the upward transport of TCE across the capillary fringe and into the vadose zone. Second, once TCE has reached the vadose zone, transport of TCE towards the foundation slab of the residential dwelling will be driven by gas phase advection and diffusion. I assume that the operation of a heating/ventilation/HVAC system will induce a "stack effect" causing the basement to be slightly under-pressurized with respect to the main floor and the ambient atmospheric pressure. Assuming there is a crack in the foundation slab in the basement, slight depressurization of the basement may induce advective flow of the soil gas beneath the foundation slab into the indoor air. Therefore, the balance between advection and diffusion is

controlled by the proximity of the TCE in the vadose zone to the foundation slab. Far away from the foundation slab, transport is diffusion dominated. Near the foundation slab, it is advection dominated.

The base scenario model consisted of one specific realization of a heterogeneous permeability field, and with the TCE source zone located 1.5 m below the water table $L = 55$ m up-gradient of basement with the foundation slab 2 m below grade and approximately 1.2 m above the water table. The heating/ventilation/HVAC system was assumed to impose a vacuum of $\Delta P_g^{basement} = 10$ Pa within the basement.

Results for the base scenario model indicate that the structure of the permeability field is largely responsible for deflecting the groundwater plume upward towards the capillary fringe, permitting aqueous phase diffusion to transport the TCE into the vadose zone. Alternative permeability realizations, generated as part of a Monte Carlo simulation process, at times deflected the groundwater plume downwards causing the extended thickness of the saturated zone to insulate the vadose zone from exposure to the TCE by upward diffusive transport. Comparison of the *CompFlow Bio* to the J&E model on the basis of the computed attenuation coefficient indicates that, for the base scenario model, $\alpha_{J\&E}$ and α_{CFB} exhibit close agreement. However, this agreement is entirely fortuitous given the sensitivity of the simulated indoor air concentrations to aquifer heterogeneity. Surprisingly, $\alpha_{J\&E}$ and α_{CFB} for the base scenario model remained in close agreement even when the TCE source zone was located at and above the water table presumably, in part, because TCE transport at distances greater than 20 m on either side of basement was diffusion dominated. Within the 20 m zone, air flow occurred from the ground surface on either side of the basement down to the capillary fringe and then upward beneath the foundation slab and into the indoor air, in agreement with the fundamental one-dimensional vertical transport assumption inherent in the J&E model. As expected, indoor air concentrations simulated using *CompFlow Bio* remain sensitive to aquifer heterogeneity as the source zone is moved 35 m and then 15 m up-gradient of the basement, beneath the water table. At 35 m up-gradient of the basement, indoor air concentrations exhibit a slight peak in the probability of exceeding a regulatory concentration of 0.25 ppmV for the various Monte Carlo permeability realizations.

Pressure fluctuations in the soil gas beneath the foundation slab induced by an observed barometric pressure signal have a distinct impact on the simulated indoor air concentrations. For instance, a sharp increase in the barometric pressure within the basement may induce indoor air to flow across

the foundation into the subsurface. Both the rate of air flow across the foundation slab and the indoor air concentrations exhibited large fluctuations in magnitude due to the transient barometric pressure signal. While this variability in indoor air concentrations was significantly greater than that observed when adjusting the pressure drop within the basement over the range observed in practice of $\Delta P_g^{basement} = 1 - 50$ Pa, the variability was minor in comparison to that resulting from the various Monte Carlo permeability realizations. Consequently, I recommend that a detailed site investigation to characterize subsurface material properties and source zone location be primary considerations in interpreting or predicting indoor air impacts, with uncertainty induced by barometric pressure fluctuations being considered inconsequential.

The relative importance of variability in additional factors on indoor air concentrations was explored, specifically; the aperture of the foundation crack, the thickness of the capillary fringe, and the rate of infiltration. The aperture of the foundation crack serves to further limit the TCE flux across the foundation slab once the vadose zone is impacted, further diminishing indoor air concentrations. I note that this only follows basic engineering judgment, with the obvious remediation effort being to seal foundation cracks to mitigate indoor air exposure. As a result, little effort need be expended attempting to characterize the aperture of the foundation crack (assuming appropriate site investigation activities have been completed) given that a conservative estimate of TCE exposure in the indoor air can be obtained with a fictitiously large aperture. I also note that the agreement between $\alpha_{J\&E}$ and α_{CFB} significantly diverged as the aperture was decreased further implying that their agreement for the base scenario model was fortuitous. Finally, while alternatively increasing or decreasing the thickness of the capillary fringe and recharge rate served to either decrease or increase the aqueous phase diffusive flux of TCE across the capillary fringe and consequently indoor air concentrations, their impact was less significant than that resulting from the various Monte Carlo permeability realizations.

I anticipate that the next step in this preliminary attempt to provide science-based regulatory guidance on indoor air concentrations for conditions where the NAPL source zone is at or below the water table is to extent the *CompFlow Bio* base scenario model by using a three-dimensional heterogeneous permeability field. This will alleviate the overly-conservative estimates of indoor air concentrations predicted in this analysis generated using a two-dimensional model where the groundwater plume is forced to advect beneath the foundation slab. Finally, I anticipate using the *CompFlow Bio* model to assess the performance of alternative foundation designs capable of

attenuating the impact of contaminated soil gas on indoor air given imperfect knowledge of the condition of the foundation slab or hydrogeological properties of the subsurface.
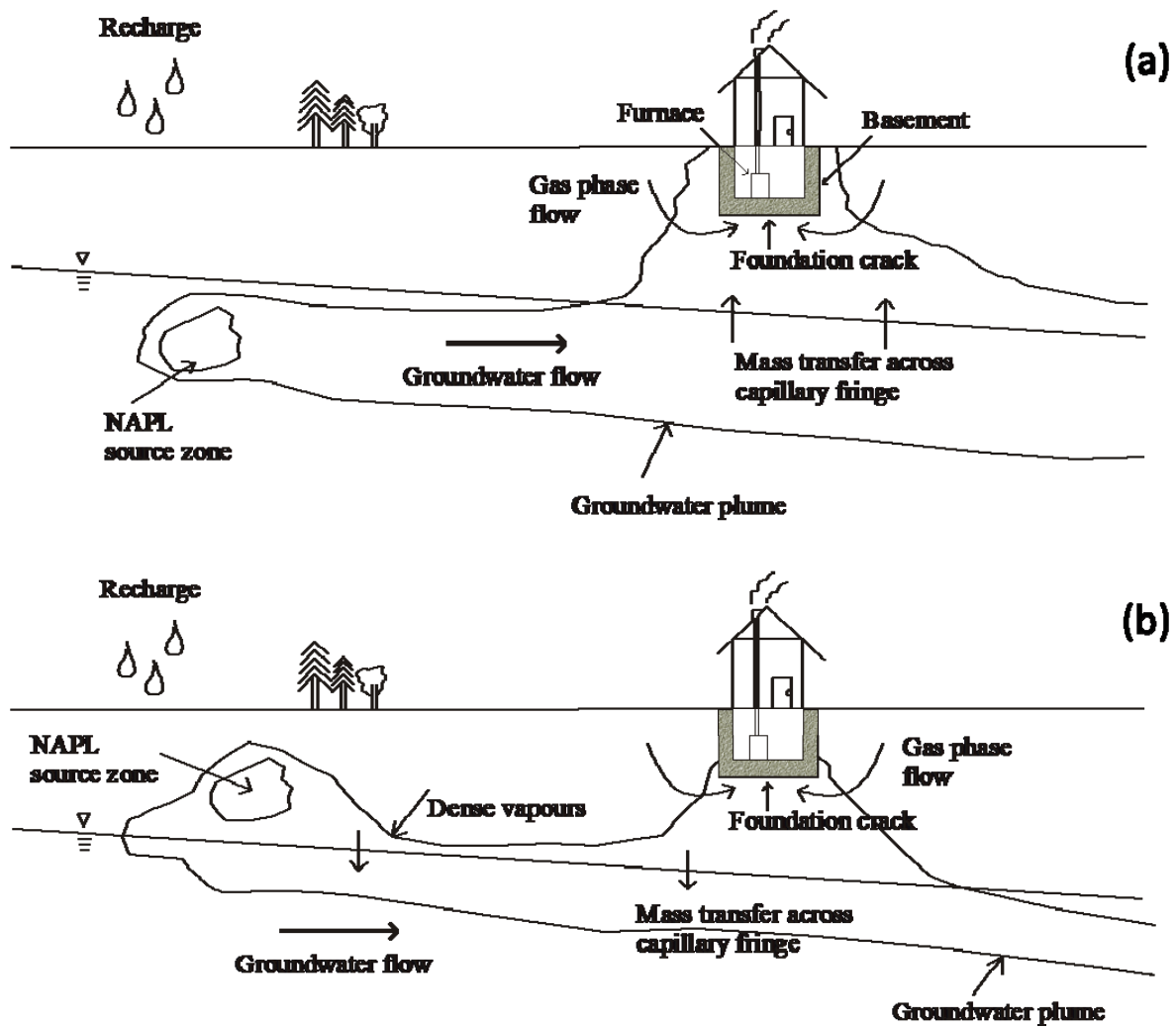
Figure 3.1. Conceptual model depicting the fate and transport of volatile organic contaminates from a NAPL source zone located (a) below and (b) above the water table.
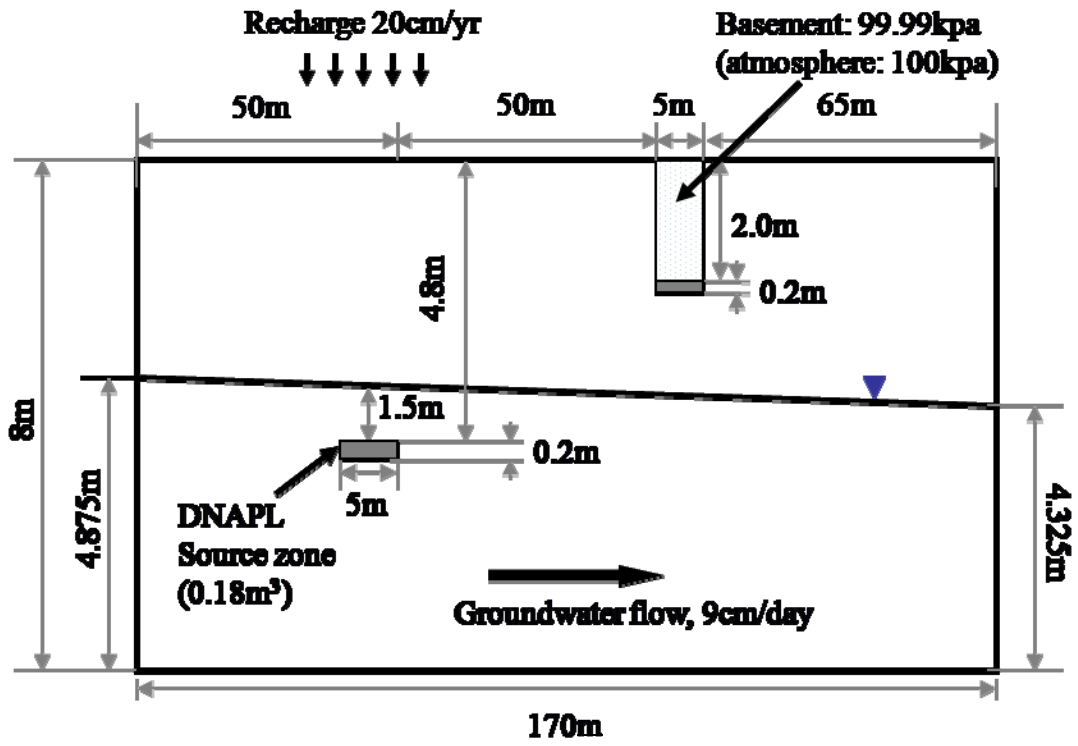
Figure 3.2. Numerical model for the base scenario.
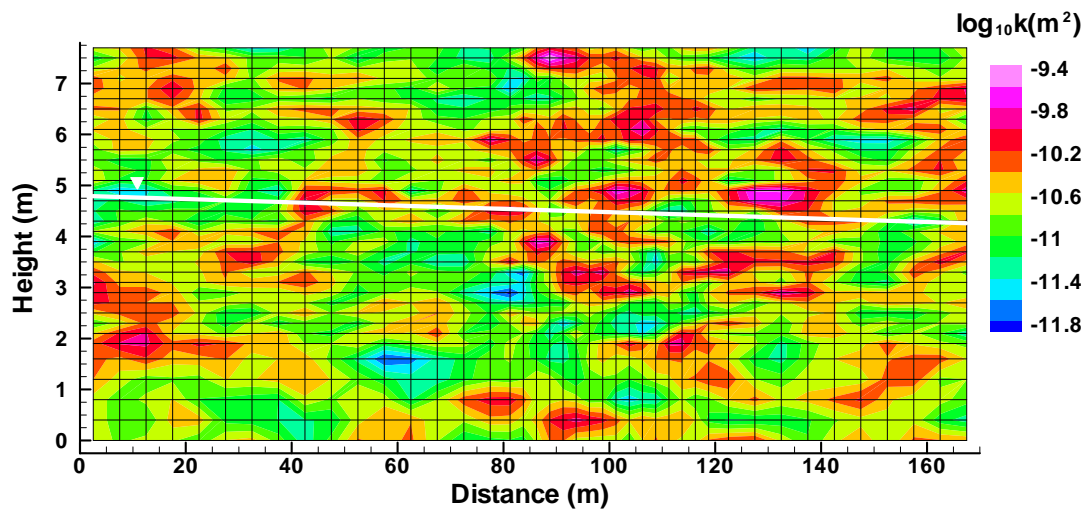
Figure 3.3. Heterogeneous permeability field realization with mesh used in discretization.
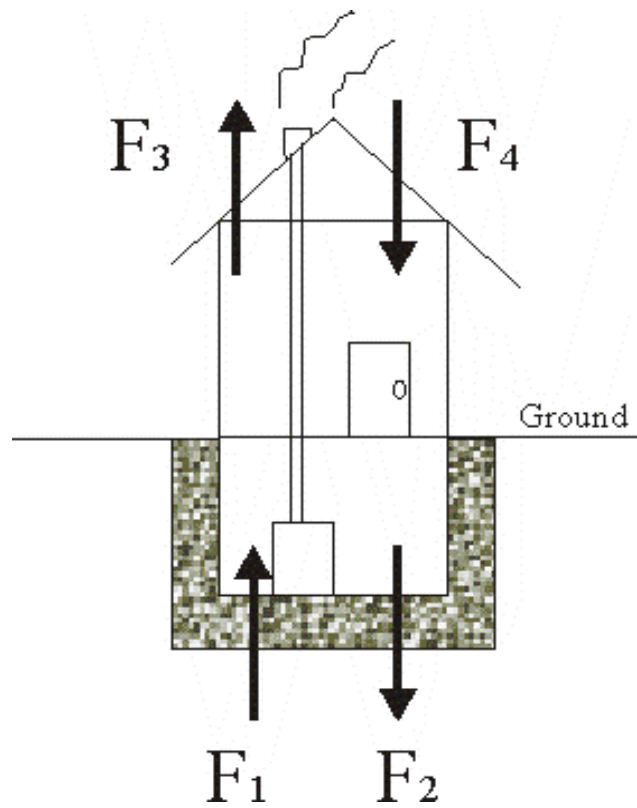
Figure 3.4. Contaminant flux into and out of house, denoted by F_1, F_2, F_3 and F_4 $\left[\text{ppmV TCE} \times \text{m}^3\text{air/day}\right]$, as calculated using Equation (3.13).
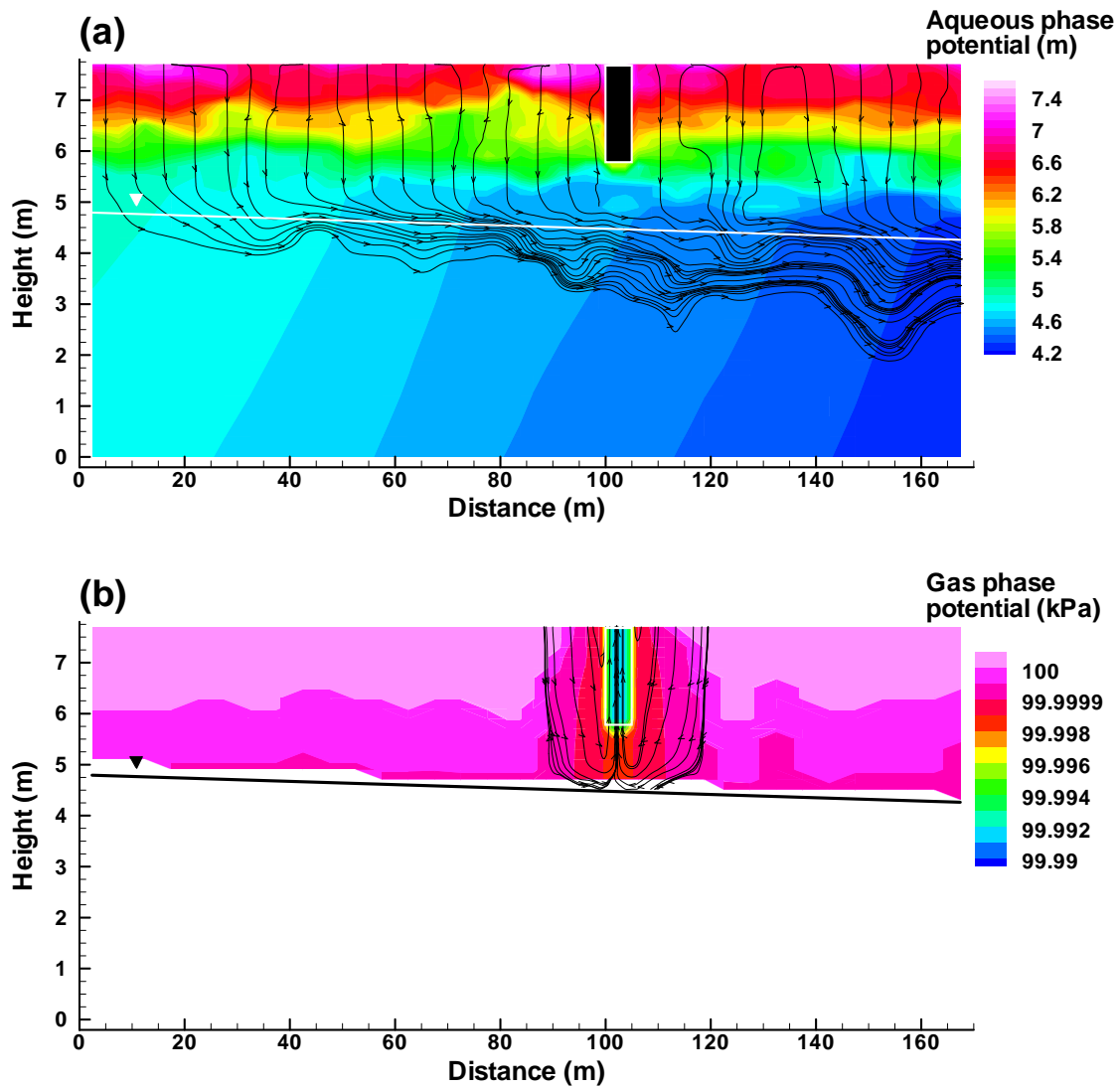
Figure 3.5. (a) Contours of aqueous phase potential with pathlines originating from ground surface due to infiltration from precipitation. (b) Contours of gas phase potential with pathlines originating from the ground surface and terminating in the basement.
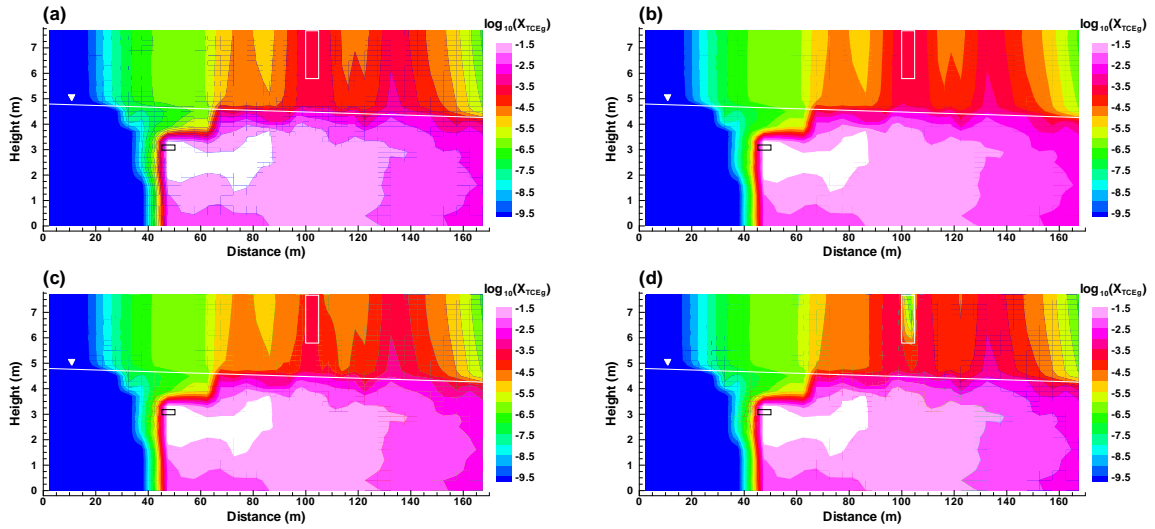
Figure 3.6. Mole fraction of TCE in the gas phase within the aquifer 1000 days after TCE was introduced into the aquifer (below the water table) for the following development scenarios: (a) before construction, (b) after construction and before occupation ($\Delta P_g^{basement} = 0$ Pa), (c) after construction and with occupation $\Delta P_g^{basement} = 10$ Pa , and (d) over-pressurization in the residential dwelling ($\Delta P_g^{basement} = -10$ Pa). Results are for the base scenario with the TCE source zone located below the water table (Scenario 1 – see Table 3.8).
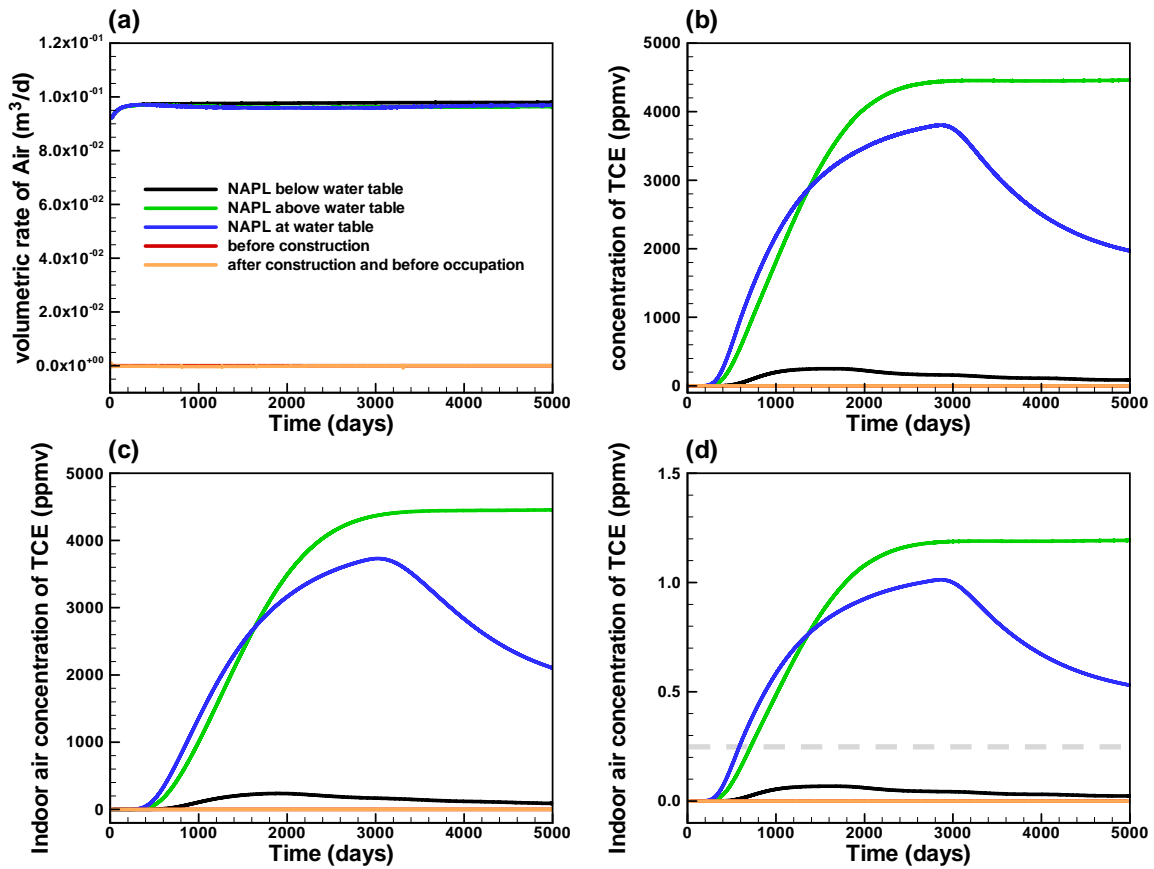
Figure 3.7. *CompFlow Bio* metrics for the base scenario with the TCE source zone located below the water table (Scenario 1b – see Table 3.8), at the water table (Scenario 2) and above the water table (Scenario 3), and include the scenario before construction as well as after construction and before occupation (Scenario 1a): (a) the volumetric flow rate of the soil gas $[\text{m}^3/\text{day}]$, represented by component $p = \{a\}$, into the basement across a crack in the foundation slab Q_a, (b) the concentration of TCE within the soil gas entering the basement $\mathbb{C}_{c_{TCE}g}$, (c) the resulting indoor air concentration of TCE $\mathbb{C}_{c_{TCE}IA}$ computed using Equation (3.13) without air exchange, and (d) with air exchange of 0.5/hr.

96
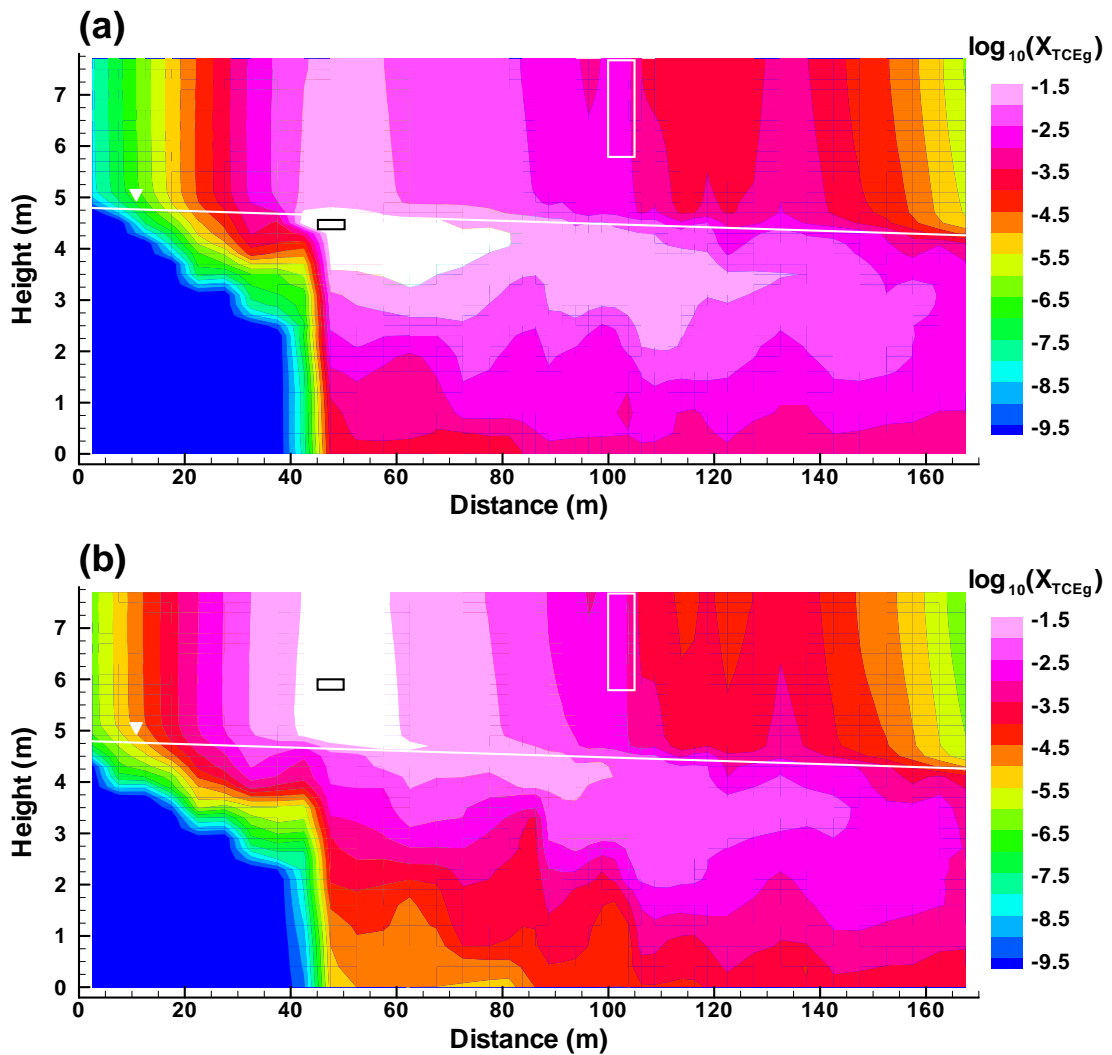
Figure 3.8. Mole fraction of TCE in the gas phase within the aquifer 1000 days after TCE was introduced into the aquifer (a) at the water table (Scenario 2 – see Table 3.8), and (b) above the water table (Scenario 3 – see Table 3.8).
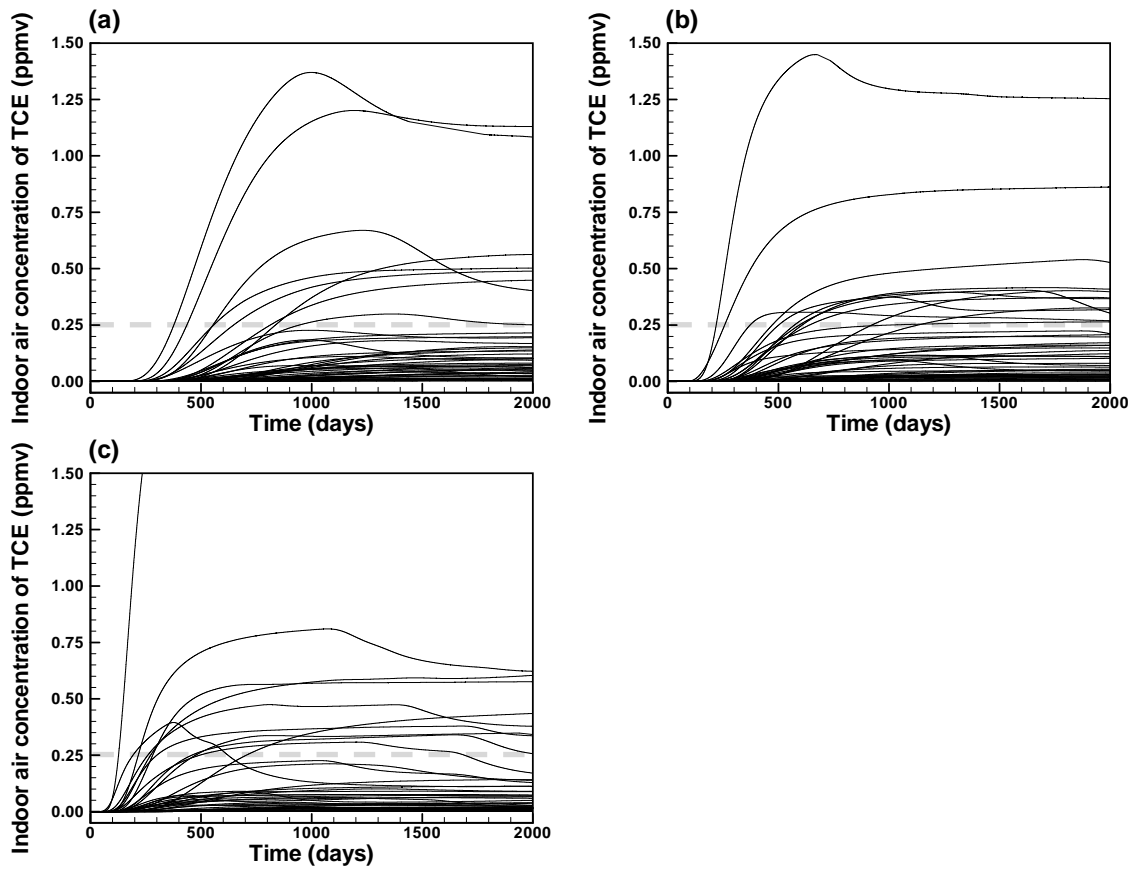
Figure 3.9. Indoor air concentration of TCE $\mathbb{C}_{c_{TCE}IA}$ computed using Equation (3.13) with air exchange of 0.5/hr for the base scenario with the TCE source zone located below the water table (Scenario 1b – see Table 3.8) for 50 permeability realizations : (a) source zone at a lateral distance of $L = 55$m from the basement; (b) $L = 35$m, and (c) $L = 15$m, respectively. If I assume the TCE indoor air regulation of 0.25ppmV, the probability that the indoor air exceeds the regulation in 2000 days after the redevelopment is 8/50, 12/50, and 11/50 respectively.
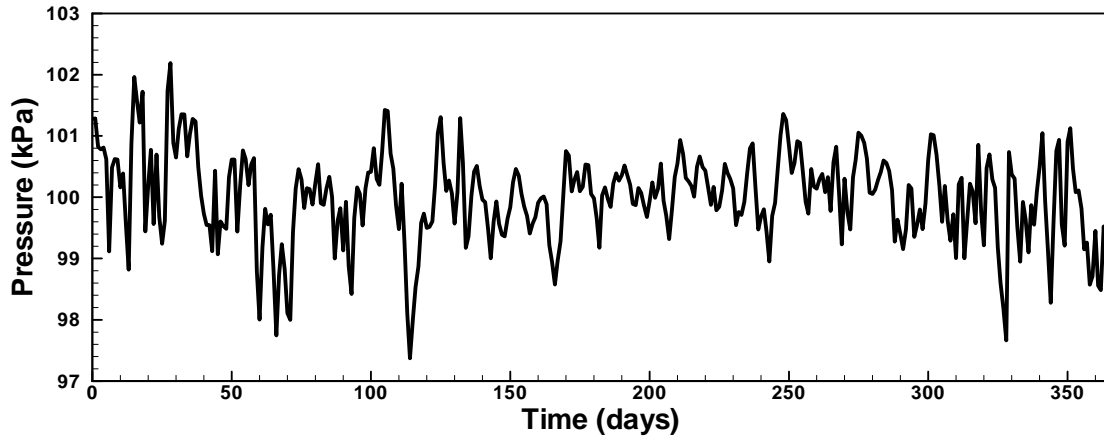
Figure 3.10. Barometric pressure fluctuation data representing Year 2005 from the University of Waterloo Weather Station. The mean has been adjusted to be 100 kPa.
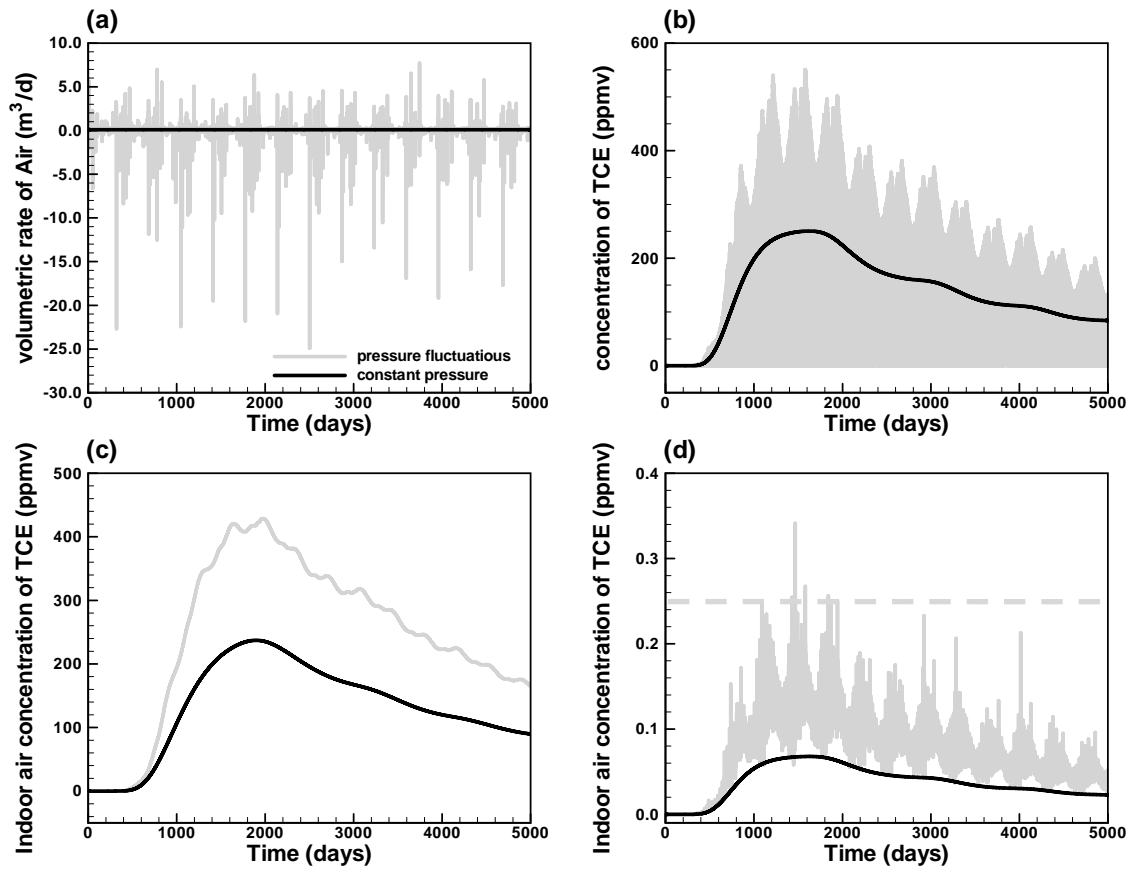
Figure 3.11. Scenario 4 *CompFlow Bio* metrics representing: (a) the volumetric flow rate of the soil gas [m^3/day], represented by component $p = \{a\}$, into the basement across a crack in the foundation slab Q_a, (b) the concentration of TCE within the soil gas entering the basement $\mathbb{C}_{c_{TCE}g}$, (c) the resulting indoor air concentration of TCE $\mathbb{C}_{c_{TCE}IA}$ computed using Equation (3.13) without air exchange, and (d) with air exchange of 0.5/hr.
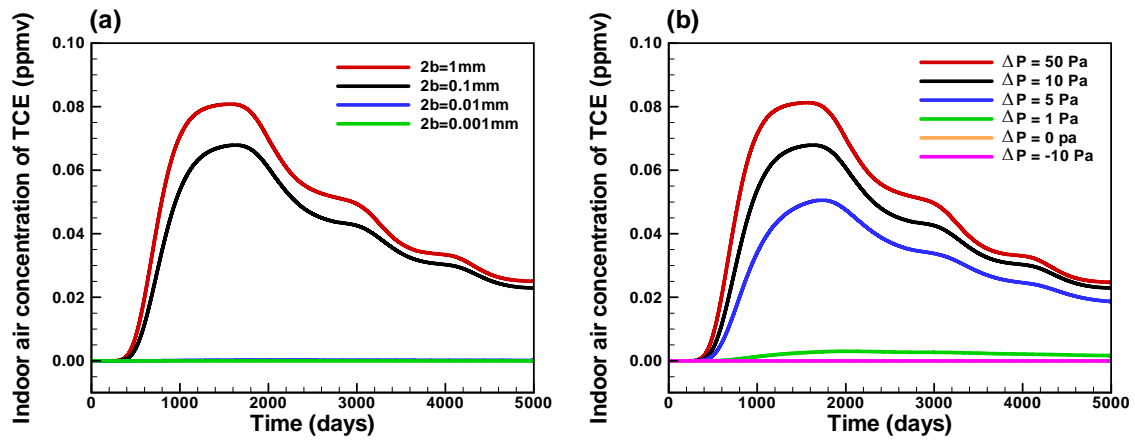
Figure 3.12. Indoor air concentration of TCE $\mathbb{C}_{c_{TCE}IA}$ computed using Equation (3.13) with air exchange of 0.5/hr for the base scenario with the TCE source zone located below the water table : (a) a sensitivity analysis on the aperture of the foundation crack (Scenario 5 – see Table 3.8), (b) a sensitivity analysis on the vacuum induced by the heating/ventilation/HVAC System (Scenario 6 – see Table 3.8).
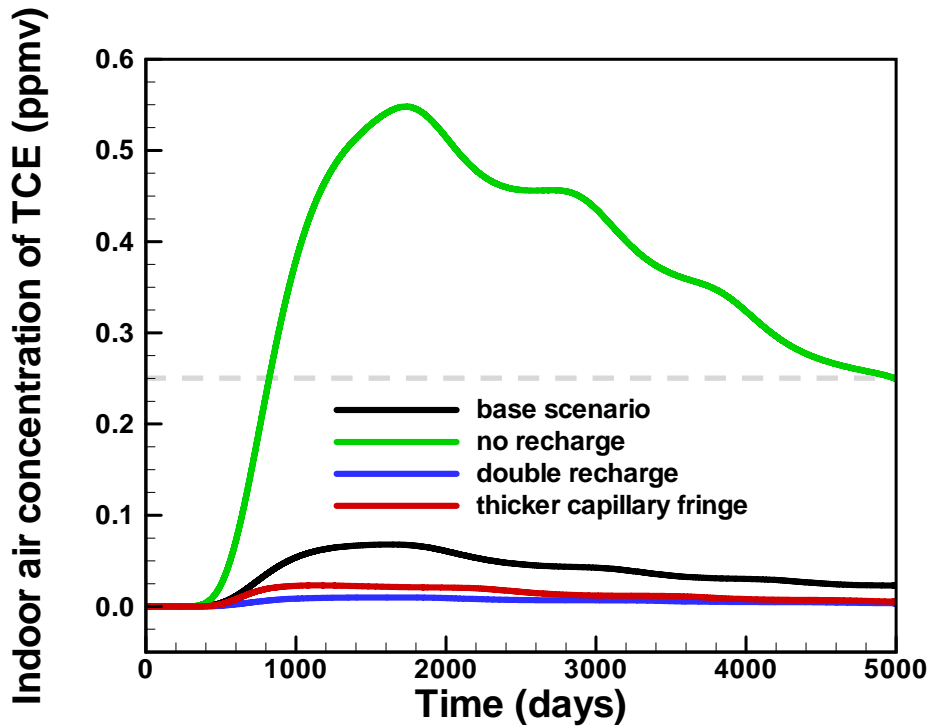
Figure 3.13. Indoor air concentration of TCE $\mathbb{C}_{c_{TCE}IA}$ computed using Equation (3.13) with air exchange of 0.5/hr for the base scenario with the TCE source zone located below the water table : a sensitivity analysis on increased thickness of capillary fringe (Scenario 7 – see Table 3.8) and infiltration rate (Scenario 8 – see Table 3.8).

Table 3.1. Porous medium properties.

Property	Value
Porosity: ϕ $[-]$	0.33
Geometric mean permeability: $\mathbf{K}$ $[m^2]$	2×10^{-11}
Variance of $Y = \ln \mathbf{K}$: σ_Y $[-]$	1.0
Correlation length of $\mathbf{K}$ in principal bedding direction: λ_1 $[m]$	5.0
Correlation length of $\mathbf{K}$ perpendicular to bedding direction: λ_2 $[m]$	0.15
pore size distribution of the porous media: $\tilde{\alpha}$	0.5
Dispersivity: α_L^l and α_T^l $[m]$, $l = \{q, n, g\}$	0.0
Mass density of porous media: ρ_r $[kg/m^3]$	1810
Organic carbon content of porous media: f_{oc} $[-]$	0.0002
Sorption of TCE onto porous media: $K_{dc_{TCE}}$	1.1×10^{-5}

Table 3.2. Capillary pressure and relative permeability aqueous/non-aqueous phase table.

S_q [−]	k_{rq} [−]	$k_{r(nq)}$ [−]	P_{cnq} [kPa]
0.2	0.0	0.68	9.0
0.3	0.04	0.55	5.4
0.4	0.10	0.43	3.9
0.5	0.18	0.31	3.3
0.6	0.30	0.20	3.0
0.7	0.44	0.12	2.7
0.8	0.60	0.05	2.4
0.9	0.80	0.0	1.53
1.0	1.0	0.0	0.0

Table 3.3. Capillary pressure and relative permeability liquid/gas phase table.

$S_q + S_n$ [−]	k_{rg} [−]	$k_{r(ng)}$ [−]	P_{cng} [kPa]	P_{cgq} [kPa] [a]	P_{cgq} [kPa] [b]
0.2	0.64	0.0	9.0	6.6	11.6
0.32	0.46	0.0	3.0	4.5	9.5
0.4	0.36	0.0009	2.4	3.9	8.9
0.5	0.25	0.045	2.1	3.6	8.6
0.6	0.16	0.116	1.8	3.3	8.3
0.7	0.09	0.21	1.5	3.0	8.0
0.8	0.04	0.34	1.2	2.0	7.0
0.9	0.01	0.49	0.9	1.0	6.0
0.95	0.0	0.58	0.5	0.5	5.5
1.0	0.0	0.68	0.0	0.0	5.0

[a] base scenario capillary fringe

[b] scenario with thicker capillary fringe

Table 3.4. Equilibrium partitioning coefficients (at 10°C)

Property	Value
water: $p = \{w\}$	
Z_{wgn} $[-]$	—[a]
a_{wgq} $[-]$	1.07
air: $p = \{a\}$	
Z_{agn} $[-]$	—[b]
Z_{agq} $[-]$	—[b]
TCE: $p = \{c_{TCE}\}$	
$a_{c_{TCE}gn}$ $[-]$	1.96
$a_{c_{TCE}gq}$ $[-]$	10.52

[a] water is not allowed to partition from the gas into the non-aqueous phases

[b] air is a non-condensible component and is not allowed to partition from the gas phase into either the aqueous or non-aqueous phases

Table 3.5. Component and phase property data (at 10°C).

Property	Value
Compressibilities	
$\hat{C}_q$ [kPa^{-1}]	3.0×10^{-6}
$\hat{C}_n$ [kPa^{-1}]	4.3×10^{-7}
$\hat{C}_r$ [kPa^{-1}]	1.0×10^{-7}
Standard component densities	
M_w^* [mole/m^3]	5.5×10^4
M_a^* [mole/m^3]	41.1
$M_{c_{TCE}}^*$ [mole/m^3]	1.1×10^4
Molecular weights	
ω_w [kg/mole]	18.02×10^{-3}
ω_a [kg/mole]	28.97×10^{-3}
$\omega_{c_{TCE}}$ [kg/mole]	131.4×10^{-3}
Reference pressure and temperature	
P^{ref} [kPa]	100.0
T^{ref} [$^{\circ}$K]	283.0
Capillary pressure blending parameter	
S_n^* [−]	0.1
Viscosities	
μ_q [kPa · day]	2.44×10^{-11}
μ_g [kPa · day]	1.62×10^{-13}
$\mu_{c_{TCE}}$ [kPa · day]	9.75×10^{-12}
Molecular diffusion coefficient	
d_q [m^2/day]	3.8×10^{-5}
d_n [m^2/day]	3.8×10^{-5}
d_g [m^2/day]	0.394 [a]
Molar density	

$$M_l = \frac{1 + \hat{C}_l\left(P_l - P^{\text{ref}}\right)}{\sum_p \max\left(0, X_{pl}\right)/M_p^*} \quad l = \{q, n\}, \qquad M_g = \frac{P_g}{RT}$$

Mass density

$$\rho_l = \sum_p X_{pl}\omega_p$$

[a] *Rivett* (1995)

Table 3.6. Foundation slab and basement properties

Property	Value
Foundation slab	
aperture of crack in slab: $2b$ [μm]	100
permeability of slab matrix (concrete): $\mathbf{K}_{slab_M}$ [m^2]	1×10^{-20}
permeability of crack in slab: $\mathbf{K}_{slab_C}$ [m^2]	8.33×10^{-10}
bulk permeability: $\mathbf{K}_{slab_B}$ [m^2]	1.83×10^{-13}
bulk porosity: ϕ_{slab_B} [$-$]	0.00022
Basement (walls and interior)	
vertical permeability (i.e. interior): $\mathbf{K}_{basement}$ [m^2]	1×10^{-9}
porosity: $\phi_{basement}$ [$-$]	0.001 [a]

[a] value is chosen to minimize mixing volume of basement interior

Table 3.7. Parameters used to compute $\alpha_{\text{J\&E}}$ and α_{CFB} for the base scenario *CompFlow Bio* model with the source zone located below the water table.

Parameter		Value
J&E model		
D_T^{eff} [m^2/day]	assuming $S_g\phi = S_q\phi = \frac{1}{2}\phi$	0.009 [a]
D^{crack} [m^2/day]	assumed equal to d_g from Table 3.5	0.394
A_B [m^2]	5×1 (foundation slab) + 2×1×2 (two basement walls)	9
A_{crack} [m^2]	11 m (long) × 2b (wide), with 2b from Table 3.5	1.1×10^{-3}
Q_{soil} [m^3/day]	calculated using Equation (24) in *Johnson and Ettinger* (1991)	0.0691
$Q_{building}$ [m^3/day]	$V_H \times A_{ex}$ where $V_H = 30$m^3 and $A_{ex} = 0.5/hr$	360
L_T [m]	horizontal and vertical offset between source zone and the center of the foundation slab	55.1
L_{crack} [m]	thickness of the foundation slab	0.2
K_g [m^2]	permeability to gas phase	1.83×10^{-13} [b]
CompFlow Bio model		
$\mathbb{C}_{building}$ [ppmV]	Scenario 1b – from Figure 3.7d (around 1500 days[c])	0.068
$\mathbb{C}_{source}$ [ppmV]	from Table 3.4 (for TCE)	6.05×10^{4} [d]

[a] $D_T^{eff} = D_g^{eff} + D_q^{eff}/H = d_g(S_g\phi)^{3.33}/\phi^2 + d_q(S_q\phi)^{3.33}/\phi^2 H$ where ϕ is from the Table 3.1; d_g and d_q are from Table 3.5; Henry constant $H = 6.44$ [m^3 aq/m^3 g] based on Table 3.4.

[b] J&E model assumes a homogeneous and isotropic permeability field, and the given value is for the foundation slab in the heterogeneous field of Figure 3.3.

[c] α_{CFB} was computed when indoor air concentrations reached their peak in the *CompFlow Bio* simulation

[d] maximum TCE concentration in the gas phase in the presence of non-aqueous phase, assuming $P_g = 117$ kPa (hydrostatic pressure at the depth of the source zone)

Table 3.8. Scenario description and resulting values of $\alpha_{J\&E}$ and α_{CFB}. The values of α_{CFB} were computed when indoor air concentrations reached their peak in the *CompFlow Bio* simulation scenario with an air exchange rate of $A_{ex} = 0.5/hr$. Values of $\alpha_{J\&E}^{(1)}$ were calculated using J&E model parameters from Table 3.7 while values of $\alpha_{J\&E}^{(2)}$ were calculated using with Q_{soil} from *CompFlow Bio* at the time when α_{CFB} was obtained.

	Scenario	$\alpha_{J\&E}^{(1)}$	$\alpha_{J\&E}^{(2)}$	α_{CFB}
1a	Base scenario model with TCE source zone below the water table and $\Delta P_g^{basement} = 0$ Pa (see Section 3.3.2.1)	2.4278×10^{-6}	2.4280×10^{-6}	1.1174×10^{-11}
1b	Base scenario model with TCE source zone below the water table and $\Delta P_g^{basement} = 10$ Pa (see Section 3.3.2.1), $2b = 100\ \mu m$, P_{cgq} [kPa] [a] on Table 3.3, Infiltration = 20 cm/yr	3.9845×10^{-6}	4.0088×10^{-6}	1.1224×10^{-6}
2	Base scenario model with TCE source zone at the water table (see Section 3.3.2.2)[a]	1.1577×10^{-5}	1.1775×10^{-5}	1.5019×10^{-5}
3	Base scenario model with TCE source zone above the water table (see Section 3.3.2.2)[b]	3.3780×10^{-5}	3.5546×10^{-5}	1.7169×10^{-5}
4	Barometric pressure fluctuations (see Section 3.3.3.3)[c]	3.9845×10^{-6}	4.0650×10^{-6}	5.6405×10^{-6}
5	Variable aperture thickness in foundation slab (see Section 3.3.3.4)[d]			
	$\quad 2b = 1\ \mu m$[e]	5.9383×10^{-8}	5.9762×10^{-8}	1.0335×10^{-11}
	$\quad 2b = 10\ \mu m$[f]	5.8644×10^{-7}	6.8230×10^{-7}	4.6115×10^{-9}
	$\quad 2b = 1000\ \mu m$[g]	4.0689×10^{-6}	4.0559×10^{-6}	1.3359×10^{-6}
6	Variable vacuum pressure in basement (see Section 3.3.2.4)			
	$\quad \Delta P_g^{basement} = 1$ Pa	3.3818×10^{-6}	2.7397×10^{-6}	4.9751×10^{-8}
	$\quad \Delta P_g^{basement} = 5$ Pa	3.9035×10^{-6}	3.9295×10^{-6}	8.3591×10^{-7}
	$\quad \Delta P_g^{basement} = 50$ Pa	4.0518×10^{-6}	4.0584×10^{-6}	1.3429×10^{-6}
	$\quad \Delta P_g^{basement} = -10$ Pa	2.696×10^{-18}	5.699×10^{-24}	0
7	Capillary fringe thickness (see Section 3.3.3.5)			
	$\quad$ thicker capillary fringe: P_{cgq} [kPa] [b] on Table 3.3	3.9845×10^{-6}	3.9636×10^{-6}	3.8132×10^{-7}
8	Infiltration rate (see Section 3.3.3.5)			
	$\quad$ Infiltration = 0 cm/yr	3.9845×10^{-6}	4.0082×10^{-6}	9.0602×10^{-6}
	$\quad$ Infiltration = 40 cm/yr	3.9845×10^{-6}	4.0086×10^{-6}	1.6371×10^{-7}

[a] $D_T^{eff} = 0.027$ with $S_g\phi = 0.23$ and $S_q\phi = 0.1$; $L_T = 55$m; $\mathbb{C}_{source} = 6.7\times10^4$ [ppmV]

[b] $D_T^{eff} = 0.090$ with $S_g\phi = \phi = 0.33$, and this value is within the range of values reported by *Abreu and Johnson* (2005); $L_T = 55$ m; $\mathbb{C}_{source} = 7.1\times10^4$ [ppmV]

[c] Q_{soil} from *CompFlow Bio* is highly variable with many values occurring during the time interval when indoor air concentrations reach their peak

[d] $2b$ is used to adjust A_{crack} and r_{crack} in parameter η of Equation (25) in *Johnson and Ettinger* (1991)

[e] $K_g = 1.83\times10^{-19}$ m^2, [f] $K_g = 1.83\times10^{-16}$ m^2, and [g] $K_g = 1.83\times10^{-10}$ m^2 for the J&E model

Chapter 4

Allocating Risk Capital for a Brownfields Redevelopment Project under Hydrogeological and Financial Uncertainty

Chapter Summary

In this Chapter, I defined risk capital as the contingency fee or insurance premium that a brownfields redeveloper needs to set aside from the sale of each house in case they need to repurchase it at a later date because the indoor air has been detrimentally affected by subsurface contamination. The likelihood that indoor air concentrations will exceed a regulatory level subject to subsurface heterogeneity and source zone location uncertainty is simulated by physics-based hydrogeological model using Monte Carlo realizations, yielding the probability of failure. The cost of failure is the future value of the house indexed to the stochastic US National Housing index. The risk capital is essentially the probability of failure times the cost of failure with a surcharge to compensate the developer against hydrogeological and financial uncertainty, with the surcharge acting as safety loading reflecting the developers' level of risk aversion. I review five methodologies taken from the actuarial and financial literature to price the risk capital. The objective of this Chapter is to use these methods to develop an actuarially consistent approach for combining the hydrogeological and financial uncertainty into insurance products that a developer may wish to purchase in order to transfer or hedge their risk exposure during brownfields redevelopment projects. Results from my highly stylized brownfields redevelopment project indicate that the price of the risk capital is much more sensitive to hydrogeological rather than financial uncertainty.

4.1 Introduction

Redevelopment of brownfields land with depressed real-estate values into high-value end uses such as residential and commercial development presents a significant challenge given that these end uses

may expose people to legacy contamination at the site. This contamination may continue to exist even after extensive remediation efforts prior to redevelopment given the difficult nature of characterizing the subsurface hydrogeological properties (*Turckea and Kueper*, 1996; *Hyndman et al.*, 2007), locating the sources of contamination (*Lesage and Jackson*, 1992; *Laird et al.*, 2005), and subsequently removing them from the soil in compliance with regulatory criteria (*Russell*, 1992; *Ward et al.*, 1997; *ITRC*, 2002; *Longino*, 2005). Two hurdles face the developer contemplating the purchase, remediation, and redevelopment of the brownfields land. First, the cost of redevelopment plus the initial purchase price of the site may be greater than the value of its end use. Second, the possibility that people occupying the redeveloped site may suffer adverse health impacts from lingering subsurface contamination could expose the developer to future punitive damages of unlimited value. To overcome these hurdles, governmental agencies help promote redevelopment of brownfields land by providing tax advantages and subsidies as well as liability protection (*US EPA*, 1999; *NRTEE*, 2003; *Hara*, 2003; *UK Environmental Agency*, 2003; *Hollis et al.*, 2005). Despite these incentives, the market for the redevelopment of brownfields land is growing more slowly than expected (*Meyer et al.*, 2002; *Meyer*, 2003) due largely to the combination of hydrogeological and economic uncertainties affecting the total cost of redevelopment and the subsequent value of the redeveloped land. However, for brownfields sites that are in optimal business locations in terms of transportation, social infrastructure, and population density and affluence, *Schoenbaum* (2002) found that pre-existing contamination did not systematically affect land use and development.

I speculate that one of the greatest difficulties in promoting brownfields redevelopment is the lack of a systematic methodology to value the contaminated property. *Kilpatrick* (2007) reviews numerous strategies including: a standard real estate appraisal which typically fails due to a lack of comparable properties given the uniqueness of the subsurface contamination; contingent valuation which relies on the subjective values that individuals attach to their willingness to pay or alternatively accept costs which cannot be observed in the market such as the stigma of living on a site with subsurface contamination, and possible consequences of adverse health impacts; and case studies which also suffer from a lack of comparable properties. *Massmann and Freeze* (1987a,b) provide a cost-benefit-risk framework that is directly amenable to this contaminated land redevelopment valuation problem in that it combines hydrogeological and economic information into an estimate of the projects value. Briefly, hydrogeological data collected at a site is obtained at a cost, and is used to constrain the probability that contamination evolving from the site will exceed a regulatory limit at a sensitive

ecological receptor, given imperfect knowledge of subsurface conditions. The consequence of exceeding the regulatory limit is a penalty applied at a fixed cost. A fixed interest rate based either on market information or the inferred social/economic discount rate (*Gruber*, 2007) is used to discount all costs including penalties (resulting from the "risk of failure" in their analysis) and benefits to a net present value for the project valuation. I comment that while the framework presented by *Massmann and Freeze* (1987a,b) appears sophisticated in its inclusion of the hydrogeological model culminating in assessing the probability of exceeding a regulatory limit, the financial aspects of the framework needed to estimate future costs, benefits and risks, and discount them to present value are rudimentary in light of the current actuarial and financial literature.

The objective of this Chapter is to build upon the framework presented by *Massmann and Freeze* (1987a,b), with a focus on its application to the valuation of brownfields redevelopment. To further introduce my objectives, it is best to begin by stating how I perceive a developer is viewing the balance of hydrogeological and financial uncertainties and their combined impact on the value of the project. This scenario is consistent with Ontario's current regulation regarding brownfields development (*OME*, 1997; *OMMAH*, 2007). My highly stylized brownfields project commences with the proposition that a company owns a property that contains legacy NAPL contamination. At this point, they have already remediated the subsurface to their satisfaction and in compliance with the governing regulatory agency (Federal Contaminated Sites Action Plan, Canada; Superfund, or Comprehensive Environmental Response, Compensation, and Liability Act (CERCLA), USA). However, they are aware that there is a possibility that some source zones of NAPL contamination may remain below the water table. They now wish to construct multiple residential dwellings on the site. The possibility therefore exists that contaminant may dissolve from the remaining NAPL source zone and advect within the groundwater to within the vicinity of the capillary fringe, at which point it may advect within the soil gas of the vadose zone towards the foundation slab due to a slight suction arising from the occupation of the house. I assume the concrete foundation slab contains multiple settlement fractures which allow contaminated soil gas to enter the indoor air. I am not concerned with the occurrence of these fractures, but assume they occur instantaneously and ubiquitously. Uncertainties in various hydrogeological factors that lead to the probability that indoor air concentrations will exceed a regulatory limit are discussed in Chapter 3. To entice buyers, the developer guarantees that they will repurchase any affected house at the original sale price appreciated by the US national home price index posted by Standard and Poor's. Indoor air

concentrations are monitored every $\Delta t_{monitor}$ days, and their guarantee lasts for the first T days. Thereafter, the government indemnifies the developer (*OME*, 1997; *OMMAH*, 2007). In return for the repurchase agreement and continuous monitoring, the residents agree not blame any reasonably foreseeable health issues arising from potential long-term exposure of indoor air contamination on the developer given their due diligence. To maintain the development, the developer remediates the subsurface to resolve the source of contamination, and demolishes/rebuilds the house to prevent further intrusion of soil gas. The house is then resold. I assume that once a house is resold there is no chance that the air quality will again exceed the regulatory threshold. The central question facing the developer is to be able to correctly value the contingency fee that they must set aside from the sale of each house to cover the possibility or "risk" that they may need to repurchase it and maintain the development at a later date. Alternatively, this contingency fee could be viewed as the value of an insurance policy with the "risk" transfer to an insurance company following from the upfront payment of the premium. At this point, the term "risk" is used broadly and will be narrowly defined shortly.

I acknowledge that the above contingency fee may be different than a market insurance premium asked by insurers to cover the same risk. This is due to the fact that the developer's willingness to pay for insurance is generally lower than what an insurance company would like to charge. In this Chapter, I aim to estimate the willingness to pay for insurance by a developer as a contingency fee (or risk capital) rather than what an insurance company should charge for such a policy. Both will meet at an equilibrium price if the market is complete.

Within the scope of this highly stylized brownfields redevelopment project, the objective of this Chapter is to present five extensions to the *Massmann and Freeze* (1987a,b) framework. These extensions all focus on evaluating the "risk" $R(t)$ term in Equation (1) of *Massmann and Freeze* (1987a), while I ignore the "benefit" $B(t)$ and "cost" $C(t)$ terms due to the limited scope of this study. First, the future repurchase cost of the house arising from the probability of failure is no longer fixed, but is now a stochastic process given by the US national home price index posted by Standard & Poor's. Second, an appropriate discount rate for the project is estimated consistent with the Capital Asset Pricing Model (CAPM) based on market information from the S&P 500 index, and with the risk free interest rate inferred from US Treasury bonds. Third, actuarial methods are applied to resolve ambiguities arising in the use of the utility function as presented in Equations (2) and (3) of *Massmann and Freeze* (1987a). Fourth, time and materials costs needed to remediate remaining

114

contamination and demolish/rebuild an affected house are appreciated by a stochastic process given by the Consumer Price Index as a proxy to inflation. Fifth, applicable financial and actuarial methods are reviewed that are amenable to incorporating the probability of failure as estimated by the hydrogeological model from Chapter 3 and the above financial market information, with the methods then adapted to price the contingency fee.

Addition of the above five extensions to the *Massmann and Freeze* (1987a,b) framework results in a very narrow definition of risk which I adopt from the financial literature called "risk capital". By definition, risk capital is the money that a person allocates to invest in a high-risk security for which default resulting in partial or complete loss of the investment principal is a possible outcome. In the context of the stylized brownfields project described above, the value of the risk capital includes a surcharge in excess of the expected present value of the probability of failure times the cost of failure. This surcharge represents the value that a rational and risk adverse person places on investing in the brownfields project due to their anticipated loss of investment principal, given that they could just as easily purchase a different investment within the market. Consequently, I anticipate that my valuation of the contingency fee or insurance premium by way of risk capital is necessary to ensure that the developer or insurer remains solvent during the guarantee period.

The motivation behind this work is the premise that a liquid environmental insurance market is a necessary condition to a sustainable brownfields redevelopment market. Therefore, there is a need for both the insurer and developer to understand the terms of the policy and then rationally price the insurance premium. *Munich Re* (2006) provides a brief overview of available environmental insurance policies to the brownfields redevelopment market, including: accidental clean-up policies, waste disposal policies, historical pollution policies, and clean-up cost cap policies. While numerous specialty insurers offer these policies to brownfields developers, I found no empirical or theoretical assessments of how to price these products in the peer-reviewed literature probably due to the infancy of the market. However, it is clear that their valuation must follow from the extensive body of literature focusing on property and casualty (P&C) insurance, as well as automobile liability insurance (*Merrifield*, 2002). The novel contribution that this work makes is to use a hydrogeological model to simulate the probability of failure, where the model is based on constitutive relationships inherent to the physical process, using available data to constrain its prediction uncertainty. This follows from *Kozlowski and Mathewson* (1997), and is part of the *Massmann and Freeze* (1987a,b) framework. However, I use relevant market information to compare and contrast the value of the

contingency fee and/or insurance premium calculated by applicable financial and actuarial (P&C) methods for the proposed brownfields redevelopment project. The outcome of this work is to outline a strategy in which the insurer and developer can calculate an appropriate estimate of the risk capital based on accepted scientific/engineering and financial/actuarial principles.

4.2 Conceptual model

The conceptual model presented here, that is used to estimate the risk capital for the highly stylized brownfields development described above, consists of two separate components. The first involves estimating the "probability of failure" whereby I used the numerical hydrogeological model developed in Chapter 3 to quantify the probability that indoor air concentrations will exceed a regulatory limit within a house built on the site. The second involves estimating the "cost of failure" whereby I use market information to estimate appreciation in housing values and demolition/rebuilding/ renovation costs, as well as the depreciation rate for the brownfields project as a whole. These two components are described in detail below.

4.2.1   Probability of failure

The probability of failure is prescribed by the hydrogeological model presented in Chapter 3, following from the hydrogeological aspects of the stylistic brownfields redevelopment project presented above in Section 4.1. For brevity, I only present those aspects from Chapter 3 that pertain directly to this work.

   Briefly, the conceptual hydrogeological model is presented in Figure 3.1a which depicts the pathway that TCE takes from the DNAPL source zone to the indoor air of house. Specifically, the pathway involves dissolution of TCE into the ambient groundwater with the source zone located below the water table, advective-dispersive transport of the TCE in the groundwater downstream of the source zone and towards the house, upward diffusive mass transfer of TCE in the aqueous phase across the capillary fringe, and subsequent advective-dispersive transport in the mobile soil gas

116

towards the foundation slab of a structure located below grade. In Chapter 3, it is assumed that the operation of a heating/ventilation/HVAC system in the basement will induce a "stack effect" causing the basement to be slightly under-pressurized with respect to the main floor and the ambient atmospheric pressure. Assuming there is a crack in the foundation slab in the basement, slight depressurization of the basement will induce advective flow of the soil gas beneath the foundation slab into the indoor air.

Following from the conceptual hydrogeological model, the multi-phase compositional model *CompFlow Bio* is used to construct a base scenario numerical model as depicted on Figure 3.2. Development of this base scenario model was driven by a field experiment at Borden conducted by *Rivett* (1995) involving a DNAPL source zone located a short distance below the water table. Monitoring of both the groundwater plume and the soil gas above the plume indicated that the groundwater could transport contaminants a significant distance without vertical mass transport of these contaminants across the capillary fringe and into the vadose zone. I endeavored to mimic this observation by constraining the geometry and hydrologic properties of the aquifer to be reminiscent of the *Rivett* (1995) experiment conducted in the Borden aquifer. Details concerning the parameterization of this base scenario numerical model, as utilized in this work, can be found in Chapter 3 denoted as Scenario 1b.

Imperfect knowledge of the point-to-point structure of the subsurface heterogeneous permeability structure has the most significant impact on prediction uncertainty in indoor air TCE concentrations in Chapter 3. It was observed that heterogeneity in the permeability of the aquifer may cause the plume to be either deflected upwards and consequently approach the water table, while the flow of water that has infiltrated from precipitation will act to push the plume downward. Alternatively, heterogeneity may also deflect the groundwater plume downwards causing the groundwater above the plume to insulate the soil gas and indoor air from any potential TCE exposure. Provided that the plume is sufficiently near the water table, hydrodynamic dispersion will then cause the upward transport of TCE across the capillary fringe and into the vadose zone. Figure 3.3 depicts a single realization of a heterogeneous and statistically anisotropic permeability field that has properties characteristic of the Borden aquifer as measured by *Woodbury and Sudicky* (1991) and *Conant et al.* (1996), with the variance increased substantially to be similar to that of the more heterogeneous Cape Cod aquifer (*Hess et al.*, 1992). The permeability realization was generated using the algorithm described by *Robin et al.* (1993).

Failure is denoted when the indoor air concentration exceeds a regulatory criterion of 0.25 ppmV. Figure 3.9 shows the indoor air concentration simulated using the *CompFlow Bio* model using 50 statistically-identical heterogeneous permeability realizations. No prior information from point measurements of permeability were used to constrain these realizations. This Monte Carlo simulation utilized a TCE source zone located at three distinct distances up-gradient of the basement, namely; $L = 55$ m, 35m and 15m. The probability of failure is calculated in the following two steps. First, I assume that the developer monitors the indoor air quality periodically every $\Delta t_{monitor} = 100$ days for the duration of the guarantee period which lasts for the first $T = 2000$ days (5.5 years). For a given monitoring interval $(t_{i-1}, t_i]$ where $t_i = i \times \Delta t_{monitor}$ with $i = \{1, 2, \dots, m\}$ and $m = T/\Delta t_{monitor}$, the probability of exceedence P_i is calculated as the sum of the number of Monte Carlo realizations for which the indoor air concentration of TCE first exceeds the regulatory criterion of 0.25 ppmV, defined as $n_{conc_i > regu}^{(t_{i-1}, t_i]}$, divided by the total number of Monte Carlo realizations $n_{realizations}$:

$$P_i = \frac{n_{conc_i > regu}^{(t_{i-1}, t_i]}}{n_{realizations}} \ . \qquad (4.1)$$

The resulting probability of exceedence/failure as a function of monitoring interval and source zone location is provided on Table 4.1. The probability after $t_i = 1300$ days is zero and is omitted from Table 4.1.

At this point, it is prudent to make three qualifying comments regarding the simulated probability of failure results. First, by using a TCE source zone located at the three up-gradient distances, I am attempting within the confines of the two-dimensional hydrogeological model to accommodate source zone location uncertainty. Second, I acknowledge that 50 Monte Carlo realizations is probably not a sufficient sample to make statistically significant statements regarding the probability of failure. However, I was limited by available computation resources given the numerical difficulty of the simulated problem. Consequently, these probability of failure results are intended to illustrate my methodology rather than provide statistically significant estimates. In comparison, *James and Oldenburg* (1997) indicate that thousands of Monte Carlo simulations may be required on the basis of theory presented by *Morgan and Henrion* (1990) and *Peck et al.* (1988). Third, a combination of

detailed site investigation (*Parker et al.*, 2003; *Guilbeault et al.*, 2005), site-specific numerical modeling (such as with *CompFlow Bio*), and professional judgment will substantially change the simulated probability of failure distribution. By not conditioning the permeability realizations with prior permeability measurements, I am in effect introducing a maximum degree of uncertainty into the probability of failure distribution. However, I did endeavor to constrain the hydrogeological model by available data pertaining to the geostatistical nature of the Borden aquifer.

4.2.2 Cost of failure

The cost of failure follows from the stylistic brownfields redevelopment project presented above in Section 4.1, and follows from the developers' guarantee that they will immediately repurchase any affected house at the original sale price appreciated by the US national home price index posted by Standard and Poor's. To maintain the development, the developer then remediates the subsurface to resolve the source of contamination, and demolishes/rebuilds the house to prevent further intrusion of soil gas. The house is then resold. I assume the developer is not liable for any reasonably foreseeable detrimental health impacts arising from long-term exposure of contaminants in the indoor air given their due diligence. Consequently, the cost of failure $c_i(t_i)$ valued at time t_i (at the ith monitoring time) assuming that a house has been affected by indoor air contamination exceeding the regulatory criterion in the interval $(t_{i-1}, t_i]$ is:

$$c_i(t_i) = S_i + \left(C^{remediate} + C^{demolition} + C^{rebuild}\right) \exp\{\int_{t_0}^{t_i} r_J \, dt\} \tag{4.2}$$

where $S_i(t_0)$ (hereafter referred to as S_0) is the present value of the house at time t_0 and is assumed to be \$1, S_i is then the value of the house at time t_i as appreciated by the US national home price index posted by Standard and Poor's, $C^{remediate} + C^{demolition} + C^{rebuild} = C^{total}$ are the sum of the fixed costs to enable an affected house to be resold using cost estimates from time t_0, with these costs appreciated to time t_i at the inflation rate r_J using the Consumer Price Index as a proxy. The present value of the cost of failure in the interval $(t_{i-1}, t_i]$ from Equation (4.2) is defined as $c_i(t_0)$ and is given by:

$$c_i(t_0) = c_i(t_i) \exp\{\int_{t_0}^{t_i} -\rho \, dt\} \tag{4.3}$$

where ρ is the discount rate for the brownfields redevelopment project.

Parameterization of Equations (4.2) and (4.3) is the first step towards a defensible estimate of the cost of failure, which is needed to price the risk capital required for the brownfields development project. I begin the parameterization by stating that time t_0 is March 2008. The rationale for this choice is that I observed actual market information up to this date in order to constrain the value of $c_i(t_0)$. Four pieces of market information are used for parameter estimation, and are: (1) the US national home price index, S_i, (2) the annual rate of inflation using the Consumer Price Index as a proxy, r_J, (3) the nominal annual interest rate inferred from risk-free US Treasury securities, r_N, (4) and the general performance of the US market using the S&P 500 as a proxy. Figure 4.1 shows these data in the time interval between March 1987 and March 2008. Interpretation of these data is described below.

The US national home price index S posted by Standard and Poor's is assumed to follow a stochastic process defined by a Geometric Brownian Motion (GBM) process with drift given by:

$$dS = \alpha S dt + \sigma_S S dZ_S \tag{4.4}$$

where α is the annual rate of appreciation in the US housing market, σ_S is the volatility in the market, and dZ_S is a Wiener process. Building upon Equations (4.2) and (4.3), I derive some relationships which I will make extensive use of later when pricing the risk capital. I begin by assuming that $C^{total} = \$0$ at time t_0 resulting in:

$$c_i(t_i) = S_i = S_0 \exp\{\left(\alpha - \frac{\sigma_S^2}{2}\right) t_i + \sigma_S Z_S(t_i)\} \tag{4.5}$$

where S_0 is the value of the US national home price index at time t_0. Equation (4.5) provides an estimate of $c_i(t_i)$ with the expectation:

$$E[c_i(t_i)] = E[S_i] = S_0 \exp\{\alpha t_i\} \tag{4.6}$$

and variance :

$$\text{Var}[c_i(t_i)] = \text{Var}[S_i] = S_0^2 \exp\{2\alpha t_i\}(\exp\{\sigma_S^2 t_i\} - 1) . \tag{4.7}$$

Estimates of α and σ_S obtained by calibrating Equation (4.4) to Figure 4.1a are provided in Table 4.2. Details of the parameter estimation are provided in Appendix C. Since $c_i(t_i)$ appears frequently in this work and is always evaluated at time t_i, I will simplify its notation to c_i .

The annual rate of inflation $r_{\mathcal{J}}$ using the Consumer Price Index as a proxy is assumed to follow a stochastic process defined by the mean-reverting arithmetic Ornstein-Uhlenbeck model given by:

$$dr_{\mathcal{J}} = \kappa_{\mathcal{J}}(\theta_{\mathcal{J}} - r_{\mathcal{J}})dt + \sigma_{\mathcal{J}} \, dZ_{\mathcal{J}} \tag{4.8}$$

where $\kappa_{\mathcal{J}}$ denotes the speed of adjustment, $\theta_{\mathcal{J}}$ is the reversion level, $\sigma_{\mathcal{J}}$ is the volatility, and $dZ_{\mathcal{J}}$ is a Weiner process. Equation (4.8) was chosen to emulate Figure 4.1b given that it admits negative values of the inflation rate. Following the methodology outlined in *Dixit and Pindyck* (1994) (page 76), estimates of $\kappa_{\mathcal{J}}$, $\theta_{\mathcal{J}}$ and $\sigma_{\mathcal{J}}$ were obtained by calibrating Equation (4.8) to Figure 4.1b, and are provided in Table 4.2. Details of the parameter estimation are provided in Appendix C.

The nominal annual interest rate $r_{\mathcal{N}}$ is assumed to follow a stochastic process defined by the mean-reverting Cox-Ingersoll-Ross (CIR) model (*Cox et al.*, 1985) given by:

$$dr_{\mathcal{N}} = \kappa_{\mathcal{N}}(\theta_{\mathcal{N}} - r_{\mathcal{N}})dt + \sigma_{\mathcal{N}}\sqrt{r_{\mathcal{N}}} \, dZ_{\mathcal{N}} \tag{4.9}$$

where $\kappa_{\mathcal{N}}$ denotes the speed of adjustment, $\theta_{\mathcal{N}}$ is the reversion level, $\sigma_{\mathcal{N}}$ is the volatility, and $dZ_{\mathcal{N}}$ is a Weiner process. *Duan and Simonato* (1999) obtain estimates of $\kappa_{\mathcal{N}}$, $\theta_{\mathcal{N}}$ and $\sigma_{\mathcal{N}}$ by using Equation (4.9) to develop a zero-coupon bond model, and then use the model to price US Treasury securities which, by their nature, are risk free and represent the nominal rate. As part of the calibration

procedure, they also obtain the market price of risk $\hat{q}_{\mathcal{N}}$ for any financial instrument trading on $r_{\mathcal{N}}$. These parameters are provided on Table 4.2. I note that *Duan and Simonato* (1999) do not present $r_{\mathcal{N}}$ as a time-series in their work. Consequently, I present multiple hypothetical realizations of $r_{\mathcal{N}}$ using Equation (4.9) on Figure 4.1c using parameters from Table 4.2.

The S&P 500 is used as a proxy of the overall market performance, and is used in Section 4.3.6 to estimate ρ in Equation (4.3) which is the discount rate for the brownfields redevelopment project. Therefore, I present this data on Figure 4.1d for completeness.

4.3 Risk capital valuation

Following from my estimation of the probability and cost of failure, I am now in a position to estimate the risk capital needed to develop the brownfields project. I remind the reader that the value of the risk capital includes a surcharge in excess of the expected present value of the probability of failure times the cost of failure. This surcharge represents the value that a rational and risk adverse person places on investing in the brownfields project due to their anticipated loss of investment principal, given that they could just as easily purchase a different investment within the market. In effect, the risk capital is the amount of money that the developer should set aside (and invest in a risk-free account) from the sale of a given house within the brownfields development given that they have a regulatory obligation to remain solvent during the guarantee period and be able to repurchase the house should the indoor air become affected. I call this amount of money a contingency fee. Alternatively, this contingency fee could be viewed as the value of an insurance policy with the risk transfer to an insurance company following from the upfront payment of the premium.

Following a review of the available literature, I identify five distinct methodologies which can be used to value the risk capital. Here, I review each of these methodologies below as I adapt them to my brownfields redevelopment project. To simplify the presentation of these five methods in Section 4.3.1 to 4.3.5, I assume that $C^{total} = \$0$ and the discount factor, taken as either ρ or $r_{\mathcal{N}}$, is constant. This assumption is then relaxed in Section 4.3.7 when I use a stochastic discount and inflation rate.

4.3.1 Method 1

I begin the valuation of risk capital with the most basic approach which essentially only considers the probability of failure times the cost of failure as described in Section 4.2. Elements of this approach are present in the other four methods that I introduce. In the context of my brownfields problem, probability and cost of failure are combined within a given time interval $(t_{i-1}, t_i]$ as:

$$H_i(t_0) = c_i \exp\{-\rho t_i\} \mathbf{1}_{conc_i > regu} \tag{4.10}$$

where $\mathbf{1}_{conc_i > regu}$ is a Bernoulli random variable of the value 1 with the probability P_i that the indoor air concentration $conc_i$ in the interval $(t_{i-1}, t_i]$ will exceed the regulatory limit $regu$, and has a value of 0 with probability $1 - P_i$. At this point I am careful to note that $H_i(t_0)$ is not a complete estimate of the risk capital valued at time t_0 needed to cover the time interval $(t_{i-1}, t_i]$ in that it does not account for their preference of risk aversion when managing their portfolio of contracts and policies. Instead, I will simply denote it as "risk", which is distinct from all other measures of risk described in this work by virtue of the fact that it has no qualifiers. Therefore, the total risk inherent in the project H is given by:

$$H(t_0) = \sum_{i=1}^m H_i(t_0) \tag{4.11}$$

and is valued at time t_0. Since $H_i(t_0)$ and $H(t_0)$ appear frequently throughout Section 4.3 and are always evaluated at time t_0, I will simplify their notation to simply H_i and H.

Standardized risk measures as well as recent theoretical developments of risk measures are summarized in *Brachinger* (2002). One of the approaches is Fishburn's measure of risk with lower partial moments given that economic agents are often more concerned with the risk of under-performance than the risk of over-performance (*Fishburn*, 1977; *Gatzert and Kling*, 2007). The measure is adapted here as:

$$LPM_n = \sum_{i=1}^m E^{\mathbb{P}}[(c_i \exp\{-\rho t_i\})^n \mathbf{1}_{conc_i > regu}] \tag{4.12}$$

where varying n controls the degree of risk aversion, specifically: for $n = 0$, only the number of failure occurrences is counted; for $n = 1$, all deviations are weighted equally; and for $n = 2$, large deviations are weighted more heavily than small deviations. Note that I do not have a guarantee (zero deductible in insurance or zero strike price in options) and deviations are the losses themselves. I can exclude $\mathbf{1}_{conc_i > regu}$ from $\mathrm{E}^{\mathbb{P}}$ assuming that the probability of failure is independent of the cost of failure, and that n loads the cost of failure to effectively account for the developer's risk preferences. Also, $\mathrm{E}^{\mathbb{P}}$ denotes the expectation under the physical measure $\mathbb{P}$ assuming that developers do not follow perfect hedging strategies (*Andrew et al.*, 2006; *Gatzert and Kling*, 2007).

The risk capital is denoted in this work as $V(H)$, and can be estimated from Equation (4.12) by setting $n = 1$ resulting in:

$$
\begin{aligned}
V(H) &= \sum_{i=1}^{m} \mathrm{E}^{\mathbb{P}}[\, c_i \, \exp\{-\rho t_i\}\,] \, \mathrm{E}^{\mathbb{P}}\!\left[\mathbf{1}_{conc_i > regu}\right] \\
&= \sum_{i=1}^{m} S_0 \, \exp\{\alpha t_i\} \exp\{-\rho t_i\} \, P_i \\
&= \sum_{i=1}^{m} S_0 \, \exp\{(\alpha - \rho)t_i\} \, P_i \\
&= \sum_{i=1}^{m} \mathrm{E}^{\mathbb{P}}[\, H_i \,] \\
&= \mathrm{E}^{\mathbb{P}}[\, H \,]
\end{aligned}
\tag{4.13}
$$

where $\mathrm{E}^{\mathbb{P}}[\, H \,]$ is simply the present t_0 value of the probability of failure times the cost of failure. This estimate of the risk capital $V(H)$ represents its least cost given that there is no safety loading applied to $\mathrm{E}^{\mathbb{P}}[\, H \,]$ to account for the developers' preference of risk aversion. *Faure and Fiore* (2008) show that the Equation (4.13), or the expected value of loss, is the most basic element of the insurance premium.

4.3.2 Method 2

Insurance valuation with safety loading provides an estimate for the risk capital as:

$$V(H) = \sum_{i=1}^{m}\{E^{\mathbb{P}}[\,H_i\,] + A(H_i)\} \tag{4.14}$$

where $A(H_i)$ is the safety loading term used to account for the developers' preference of risk aversion in the time interval $(t_{i-1}, t_i]$, following classical P&C insurance policies (*Sondermann*, 1991; *Moller*, 2002). Two of the most widely used safety loading strategies involve the variance and standard deviation principles, given as:

$$A(H_i) = a_{(2)i}\text{Var}[\,H_i\,]$$
$$A(H_i) = a_{(2)i}\sqrt{\text{Var}[\,H_i\,]} \tag{4.15}$$

respectively, where $a_{(2)i}$ is the safety loading parameter in the time interval $(t_{i-1}, t_i]$. Given that $A(H_i) \geq \$0$ within all the time intervals $(t_{i-1}, t_i]$ $i = \{1,2,\ldots,m\}$, then $V(H) \geq E^{\mathbb{P}}[\,H\,]$.

In this work, I restrict my attention to the variance principle. Following *Goodman* (1962), I calculate the variance of the product of random variables where the variables are mutually independent as:

$$\begin{aligned}
\text{Var}[\,H_i\,] &= \{\text{Var}[c_i\,\exp\{-\rho t_i\}] + (E[c_i\,\exp\{-\rho t_i\}])^2\} \\
&\quad \times \{\text{Var}[\mathbf{1}_{conc_i>regu}] + (E[\mathbf{1}_{conc_i>regu}])^2\} \\
&\quad - (E[c_i\,\exp\{-\rho t_i\}])^2 \times (E[\mathbf{1}_{conc_i>regu}])^2 \\
&= \exp\{-2\rho t_i\} \times \left(\text{Var}[c_i]\,P_i + E[c_i]^2 P_i\,(1 - P_i)\right)
\end{aligned} \tag{4.16}$$

Therefore, I can write an estimate for the risk capital as:

$$V(H) = \sum_{i=1}^{m}\{E^{\mathbb{P}}[\,H_i\,] + a_{(2)i}\text{Var}[\,H_i\,]\} \tag{4.17}$$

I conclude the presentation of this method with two comments. First, this method has versatility by virtue of its simplicity and the fact that it requires no assumptions regarding market conditions. In other words, the market can be incomplete with an individual developer simply adjusting $a_{(2)i}$ to

reflect their preference of risk aversion. Second, this safety loading strategy estimates the risk capital by surcharging Method 1 with a factor that combines uncertainty in the cost of failure in combination with the probability of failure.

4.3.3 Method 3

Utility functions, $\boldsymbol{u}$, are commonly used in actuarial mathematics to quantify a developer's preference of risk aversion under the physical measure $\mathbb{P}$. Utility is a measure of the relative satisfaction from a desire to consume various goods and services. Rational individuals maximize the expected value of the utility of wealth rather than the expected value of wealth, given that what is important is the utility derived from the money received rather than the money itself. The utility function approach is the *de-facto* standard method used in incomplete markets. The difficulty in its application rests in defining an adequate and tractable utility function that captures the preferences of decision makers for the problem at hand. I note that *Massmann and Freeze* (1987a) introduce the idea of a utility function in their framework. Here, I expand upon the idea in the context of the proposed brownfields redevelopment project.

   I begin by assuming the developer is a risk averse representative agent who, everything else being equal, would prefer to avoid risk. Utility functions that address risk averse behaviour have the property where the value of the utility function is increasing in wealth, but each extra dollar of wealth increases utility at a decreasing rate, called the decreasing marginal utility of wealth:

$$\frac{d\boldsymbol{u}}{dW} > 0; \ \frac{d^2\boldsymbol{u}}{dW^2} < 0 \tag{4.18}$$

where W is wealth. The principle of equivalent utility is defined in the classical expected utility theory as:

$$\boldsymbol{u}\big(W(t_0) + CE(X)\big) = \mathrm{E}^{\mathbb{P}}[\boldsymbol{u}(W(t_0) + X)] \tag{4.19}$$

126

where $CE(X)$ is the certainty equivalent, X is a random payoff, and $W(t_0)$ is the initial wealth. The certainty equivalent is used to price random payoffs given:

$$CE(X) = \boldsymbol{u}^{-1}\big(\mathrm{E}^{\mathbb{P}}[\boldsymbol{u}(W(t_0) + X)]\big) - W(t_0) \ . \tag{4.20}$$

If the utility function represents risk averse behavior, then:

$$CE(X) \leq \mathrm{E}^{\mathbb{P}}[X] \ . \tag{4.21}$$

for all X (*Cvitanic and Zapatero*, 2004). This relationship implies that most people are not willing to pay up to $\mathrm{E}^{\mathbb{P}}[X]$ to participate in an investment with random payoff X. Given that most people are risk averse when facing gains, Equation (4.21) holds true when X is a random gain. However, most people are risk takers when facing losses and willing to pay more than $\mathrm{E}^{\mathbb{P}}[X]$ for protection against a loss of random size X. This clearly fits the notion of the brownfields developer purchasing insurance, where the insurance premium $\mathcal{P}$ is the risk capital needed to cover the potential expense that they may have to repurchase homes at some future date. This implies that:

$$\mathcal{P}(X) > \mathrm{E}^{\mathbb{P}}[X] \ . \tag{4.22}$$

Gerber and Pafumi (1998) show that the insurance premium $\mathcal{P}$, payable at time t_0, can be calculated by:

$$\boldsymbol{u}\big(W(t_0)\big) = \mathrm{E}^{\mathbb{P}}[\boldsymbol{u}(W(t_0) + \mathcal{P}(X) - X)] \ . \tag{4.23}$$

In the context of this work, I use an exponential utility function because *Gerber and Pafumi* (1998) provide closed-form expressions of $CE(X)$ and $\mathcal{P}(X)$, and furthermore these expressions do not depend on the initial wealth $W(t_0)$, which is beyond the scope of this work to evaluate, in order to provide estimates of the risk capital. At this point, I note that $H_i = X_i$ and is a random loss (but not negative) in the interval $(t_{i-1}, t_i]$ and $V(H_i) = \mathcal{P}(X_i)$. Now, using the exponential utility function defined as:

$$\boldsymbol{u}(H_i) = \frac{1}{a_{(3)i}}\left(1 - e^{-a_{(3)i}\,H_i}\right) \text{ with } a_{(3)i} > 0 \tag{4.24}$$

I can estimate the certainty equivalent and risk capital as:

$$CE(H) = -\sum_{i=1}^{m}\frac{1}{a_{(3)i}}\,\ln \mathrm{E}^{\mathbb{P}}\!\left[e^{-a_{(3)i}\,H_i}\right]$$

$$V(H) = \sum_{i=1}^{m}\frac{1}{a_{(3)i}}\,\ln \mathrm{E}^{\mathbb{P}}\!\left[e^{a_{(3)i}\,H_i}\right] \tag{4.25}$$

$$\quad = \sum_{i=1}^{m}\frac{1}{a_{(3)i}}\,\ln \mathrm{E}^{\mathbb{P}}\!\left[\exp\{a_{(3)i}\,\exp\{-\rho\,t_i\}\,S_i\,\mathbf{1}_{conc_i>regu}\}\right]$$

I could not proceed further in obtaining a closed-form solution for Equation (4.25) because a moment-generating function for the log-normal distribution does not exist. Instead, I resorted to Monet-Carlo simulation to find $\ln \mathrm{E}^{\mathbb{P}}$. Finally, while alternative utility functions will provide a different functional form for pricing $CE(H)$ and $V(H)$, I note that the developer is able to adjust $a_{(3)i}$ within Equation (4.25) to account for their preference of risk aversion. As with Method 2, this approach also formally incorporates the combined probability and cost of failure into the safety loading of the risk capital.

4.3.4 Method 4

The no-arbitrage principle in option pricing theory is used here to determine the fair price of the risk capital. This approach follows from the real option methodology (*Trigeorgis*, 1996), with numerous applications in the realm of project finance (*Schwartz and Trigeorgis*, 2001). The market assumption behind this method is that the risk capital has a replicating portfolio of traded assets whose stochastic fluctuations are perfectly correlated with that of the stochastic process for S, enabling the risky component of the risk capital to be exactly hedged. This market is called arbitrage free. The corner stone to this approach is to evaluate expectations involving future uncertainty in cash flows under the risk-neutral $\mathbb{Q}$ probability measure. To this end, I modify Equation (4.4) as:

$$dS = (\alpha - \hat{q}_S \sigma_S)Sdt + \sigma_S S dZ_S^{\mathbb{Q}} \tag{4.26}$$

where $\hat{q}_S$ is the market price of risk for any traded instrument depending on S, and $Z_S^{\mathbb{Q}}$ is Weiner process under the risk-neutral measure. In the context of the brownfields redevelopment project, I note that because S is an index, S itself cannot be bought or sold. However, the risk capital when transferred to an insurer is obviously being bought and sold in the market and is subject to $\hat{q}_S$. In fact, shares in a company specializing in these brownfields redevelopment projects will also be subject to $\hat{q}_S$. The concept that a unique estimate of $\hat{q}_S$ can be observed in the market is a fundamental assumption inherent in this no-arbitrage approach. *Oikarinen* (2008) found empirical evidence for the no-arbitrage condition in the housing market.

Denote a replicating portfolio $\phi(c_i)$ of the loss c_i at time t_i. Then, the price of the risk capital is equivalent to a call option with the payoff $\phi(c_i)$ at maturity t_i and zero strike price:

$$V(H) = \sum_{i=1}^{m} \mathrm{E}^{\mathbb{Q}}\big[\exp\{-r_{\mathcal{N}} t_i\}\, \phi(c_i)\, \mathbf{1}_{conc_i > regu}\big] \tag{4.27}$$

where $\phi(c_i) = [c_i - \text{zero}]^+ = c_i$. Next, $\phi(c_i)$ and $\mathbf{1}_{conc_i > regu}$ are assumed to be independent, with the hydrogeological risk being diversifiable (*Jaimungal and Wang*, 2006) and risk neutral (*Bacinello and Persson*, 2000) with $\mathrm{E}^{\mathbb{Q}}\big[\mathbf{1}_{conc_i > regu}\big] = P_i$. Note that Equation (4.27) is depreciated by $r_{\mathcal{N}}$ instead of ρ because Equation (4.26) is a risk-neutral process with respect to S. Consequently, I can discount all cash flows arising from S at the nominal risk-free rate $r_{\mathcal{N}}$. Thus,

$$
\begin{aligned}
V(H) &= \sum_{i=1}^{m} \exp\{-r_{\mathcal{N}} t_i\}\, \mathrm{E}^{\mathbb{Q}}\big[\phi(c_i)\, \mathbf{1}_{conc_i > regu}\big] \\
&= \sum_{i=1}^{m} \exp\{-r_{\mathcal{N}} t_i\}\, S_0 \exp\{(\alpha - \hat{q}_S \sigma_S)t_i\}\, P_i \\
&= \sum_{i=1}^{m} S_0 \exp\{(\alpha - \hat{q}_S \sigma_S - r_{\mathcal{N}})t_i\}\, P_i
\end{aligned}
\tag{4.28}
$$

At this point I note that Equation (4.28) is identical to Equation (4.13) provided $\rho \equiv r_{\mathcal{N}} + \lambda_S \sigma_S$, an issue I will revisit in Section 4.3.6.

The option pricing approach seems advantageous over the utility function approach given the difficulty in choosing an appropriate utility function. However, the option pricing approach requires that the market has a replicating portfolio of the asset to be valued. In this case, it is that portion of the risk capital arising from the cost of failure and subsequently made risk neutral by the market price of risk $\hat{q}_S$. The resulting price of the risk capital is then unique in the complete market, while not in the incomplete market. In fact, the market price of risk $\hat{q}_S$ is uniquely defined only in the complete (equilibrium) market. A disadvantage of the option pricing approach is that it does not provide a methodology to achieve safety loading of the risk capital due to the probability of failure arising from hydrogeological uncertainty. In this regard, despite the wide-spread application of this methodology to investment strategies in projects involving natural resources subject to geological uncertainty (*Brennan and Schwartz*, 1985; *Schwartz and Trigeorgis*, 2001), Method 4 is no more sophisticated than Method 1.

4.3.5 Method 5

This methodology is unique relative to the previous four in that the risk capital is valued by loading both the probability of failure and the cost of failure simultaneously. Motivation for this approach follows that of empirical studies that seek implied loss distributions from market prices (*Christensen*, 2001; *Hayek and Ghanem*, 2002; *Torresetti et al*, 2007; *Hardle and Lopez Cabrera*, 2007). Application of this approach here does require a slight re-interpretation of the probability of failure as outlined in Section 4.2.1. The previous four methods have essentially focused on the probability of failure at a single house. Now, I must abstract this idea to that of any single house within a residential development. Assuming that all affected houses within the development are repaired to a normal condition immediately after indoor air concentrations are observed to exceed a regulatory level, then the redeveloper has the following compound Poisson loss distribution at time t_i with h_i houses affected in the time interval $(t_{i-1}, t_i]$:

$$H_i(t_0) = \exp\{-\rho t_i\} \sum_{z=1}^{h_i}(c_i)_z \tag{4.29}$$

130

where $(c_i)_z$ is a sequence of independent and identically distributed strictly positive random values, assuming that all houses in the redevelopment have approximately the same value. The probability that there are exactly h_i occurrences in the time interval $(t_{i-1}, t_i]$ is:

$$f(h_i, \lambda_i) = \frac{(\lambda_i \Delta t_i)^{h_i} e^{-\lambda_i \Delta t_i}}{h_i!} \tag{4.30}$$

assuming these events occur with a known rate λ_i in the time interval $\Delta t_i = (t_{i-1}, t_i]$ independent of the time since the last event. Furthermore, I assume h_i is a homogenous Poisson process in the time interval Δt_i, while it is non-homogeneous with a set of $\{\lambda_i\}$ during T. Then the Poisson distribution has the following mean and variance:

$$\mathrm{E}[h_i] = \mathrm{Var}[h_i] = \lambda_i \, \Delta t_i \, . \tag{4.31}$$

Table 4.1 includes estimates of both P_i and λ_i within each time interval $\Delta t_i = (t_{i-1}, t_i]$, with values of λ_i computed as:

$$\lambda_i = \frac{n_{conc_i > regu}^{(t_{i-1}, t_i]}}{\Delta t_i} \quad . \tag{4.32}$$

I concede that this choice of λ_i was made to ensure $\lambda_i \, \Delta t_i / n_{realizations} = P_i$ for reasons to be made clear below.

I define an insurance premium density $\mathcal{P}_i^{\mathbb{P}}$ in the time interval $(t_{i-1}, t_i]$ and under the $\mathbb{P}$ measure as:

$$\begin{aligned} \mathcal{P}_i^{\mathbb{P}} = \mathrm{E}^{\mathbb{P}}[H_i] &= \exp\{-\rho t_i\} \, \mathrm{E}^{\mathbb{P}}\left[\sum_{z=1}^{h_i} (c_i)_z\right] \\ &= \exp\{-\rho t_i\} \, \mathrm{E}^{\mathbb{P}}[h_i] \, \mathrm{E}^{\mathbb{P}}[(c_i)_1] \end{aligned} \tag{4.33}$$

where I take only the loss distribution from the first house $(c_i)_1$ given that all houses have nearly the same value. Next, I replace the $\mathbb{P}$ by the $\mathbb{Q}$ measure, where H_i remains a compound Poisson process

under $\mathbb{Q}$, and so that I give more weight to less favorable events. Now, I define the insurance premium as:

$$\mathcal{P}_i^{\mathbb{Q}} = \mathrm{E}^{\mathbb{Q}}[H_i] = \exp\{-r_{\mathcal{N}} t_i\} \, \mathrm{E}^{\mathbb{Q}}[h_i] \, \mathrm{E}^{\mathbb{Q}}[(c_i)_1] \tag{4.34}$$

which is finite and includes safety loading, i.e.:

$$\mathcal{P}_i^{\mathbb{P}} < \mathcal{P}_i^{\mathbb{Q}} < \infty . \tag{4.35}$$

Notice that I have replaced ρ in Equation (4.33) by $r_{\mathcal{N}}$ in Equation (4.34) since I have adopted the risk neutral $\mathbb{Q}$ measure.

Delbaen and Haezendonck (1989) introduce a random process on $(\Omega, \mathcal{F}_{\infty}, \mathbb{P})$ to change the premium density $\mathcal{P}_i^{\mathbb{P}}$ to $\mathcal{P}_i^{\mathbb{Q}}$ as:

$$M_t^{(\beta)} = \exp\left\{ \sum_{l=1}^{N_t} \beta(X_l) - \lambda \, t \mathrm{E}^{\mathbb{P}}\left[e^{\beta(X_1)} - 1\right] \right\} \tag{4.36}$$

which is a strictly positive martingale with $\mathrm{E}^{\mathbb{P}}\left[M_t^{(\beta)}\right] = 1$ in Proposition 2.1 of *Delbaen and Haezendonck* (1989), and is equivalent to $\frac{d\mathbb{Q}}{d\mathbb{P}}$ which is the Radon-Nikodym derivative. Equation (4.36) changes the intensity and claim distributions as:

$$\mathrm{E}^{\mathbb{Q}}[N_1] = \mathrm{E}^{\mathbb{P}}[N_1] \, \mathrm{E}^{\mathbb{P}}[\exp\{\beta(X_1)\}]$$
$$\mathrm{E}^{\mathbb{Q}}[X_1] = \frac{\mathrm{E}^{\mathbb{P}}[X_1 \exp\{\beta(X_1)\}]}{\mathrm{E}^{\mathbb{P}}[\exp\{\beta(X_1)\}]} \quad . \tag{4.37}$$

where N_1 is the number of events at unit time **1** and X_1 is the magnitude of the first loss. I adapt Equations (4.36) and (4.37) to my brownfields redevelopment project as follows: let $t = \tau$ ($0 \leq \tau \leq \Delta t$, $\Delta t = t_i - t_{i-1}$); $N_t = (h_i)_{\tau}$; $X_l = (c_i)_z$; $\lambda = \lambda_i$. Then,

$$\mathrm{E}^{\mathbb{Q}}[(h_i)_1] = \mathrm{E}^{\mathbb{P}}[(h_i)_1]\,\mathrm{E}^{\mathbb{P}}[\,\exp\{\beta((c_i)_1)\}\,]$$

$$\mathrm{E}^{\mathbb{Q}}[(c_i)_1] = \frac{\mathrm{E}^{\mathbb{P}}[\,(c_i)_1\,\exp\{\beta((c_i)_1)\}\,]}{\mathrm{E}^{\mathbb{P}}[\,\exp\{\beta((c_i)_1)\}\,]}\quad.$$

(4.38)

Now, I restate Equation (4.34) as:

$$\mathcal{P}_i^{\mathbb{Q}} = \exp\{-r_{\mathcal{N}}t_i\}\,\mathrm{E}^{\mathbb{P}}[(h_i)_1]\,\mathrm{E}^{\mathbb{P}}[\,\exp\{\beta((c_i)_1)\}\,]\,\frac{\mathrm{E}^{\mathbb{P}}[\,(c_i)_1\,\exp\{\beta((c_i)_1)\}\,]}{\mathrm{E}^{\mathbb{P}}[\,\exp\{\beta((c_i)_1)\}\,]}$$

$$= \exp\{-r_{\mathcal{N}}t_i\}\,\mathrm{E}^{\mathbb{P}}[(h_i)_1]\,\mathrm{E}^{\mathbb{P}}[\,(c_i)_1\,\exp\{\beta((c_i)_1)\}\,]\quad.$$

(4.39)

At this point, I only restrict the definition of β with assumptions allowing a Borel measureable mapping from $\mathbb{R}_+$ into $\mathbb{R}$ with $\mathrm{E}^{\mathbb{P}}[\exp(\beta((c_i)_1))] < \infty$ and $\mathrm{E}^{\mathbb{P}}[(c_i)_1\exp(\beta((c_i)_1))] < \infty$. Consequently, when comparing Equations (4.33) and (4.34), I can verify that:

$$\mathrm{E}^{\mathbb{Q}}[(h_i)_1] \geq \mathrm{E}^{\mathbb{P}}[(h_i)_1]$$

$$\mathrm{E}^{\mathbb{Q}}[(h_i)_1]\,\mathrm{E}^{\mathbb{Q}}[(c_i)_1] > \mathrm{E}^{\mathbb{P}}[(h_i)_1]\,\mathrm{E}^{\mathbb{P}}[(c_i)_1]\quad.$$

(4.40)

However, the same definition of β does not allow me to compare the magnitude of $\mathrm{E}^{\mathbb{Q}}[(c_i)_1]$ to that of $\mathrm{E}^{\mathbb{P}}[(c_i)_1]$. Instead, Proposition 3.1 of *Delbaen and Haezendonck* (1989) states that the mapping β is increasing if and only if $\mathrm{E}^{\mathbb{Q}}[(c_i)_1] \geq \mathrm{E}^{\mathbb{P}}[(c_i)_1]$. Finally, I note that Equation (4.35) is dependent on the relationship between ρ and $r_{\mathcal{N}}$, once again an issue I will revisit in Section 4.3.6.

Following example 3.1 of *Delbaen and Haezendonck* (1989), I now complete the presentation of the method with the following definition of β:

$$\beta((c_i)_1) = a_{(5)i}\,t_i$$

(4.41)

where $\mathrm{E}^{\mathbb{P}}[\exp(\beta((c_i)_1)]$ exists , $M_t^{(\beta)}$ in Equation (4.36) exists, and $a_{(5)i}$ is a constant in the time interval $(t_{i-1}, t_i]$. Next, I again define a payoff derived from a replicating portfolio as $\phi(c_i) = [c_i - \mathrm{zero}]^+ = c_i$, then the value of the risk capital as:

133

$$V(H) = \sum_{i=1}^{m} \mathcal{P}_i^{\mathbb{Q}}$$

$$= \sum_{i=1}^{m} \exp\{-r_{\mathcal{N}} t_i\} \, \mathrm{E}^{\mathbb{Q}}[\, \phi(c_i) h_i | \mathcal{F}_t]$$

$$= \sum_{i=1}^{m} \exp\{-r_{\mathcal{N}} t_i\} \, \lambda_i \, \Delta t_i \, \exp\{a_{(5)i} \, t_i\} \, \mathrm{E}^{\mathbb{P}}[c_i] \qquad (4.42)$$

$$= \sum_{i=1}^{m} S_0 \, \exp\{(\alpha + a_{(5)i} - r_{\mathcal{N}}) t_i\} \, \lambda_i \, \Delta t_i \quad .$$

Finally, $V(H)$ must be divided by $n_{realizations}$ to price the risk capital per house within the development.

I comment that *Delbaen and Haezendonck* (1989) derive this method under the assumption of a no-arbitrage market, although the market may be incomplete. My choice of β as defined by Equation (4.41) in combination with my interpretation of the probability of failure in Equation (4.32) was made specifically to compare Equation (4.42) to that of the option pricing approach given by Equation (4.28). I conclude that $a_{(5)i}$ is a no-arbitrage incomplete market interpretation of $-\hat{q}_S \sigma_S$. Given that the market price of risk $\hat{q}_S$ can only uniquely be defined in a complete market, the arbitrary choice of $a_{(5)i}$ implies that Method 5 for this choice of β and $M_t^{(\beta)}$ effectively achieves safety loading of the risk capital arising from the cost of failure by manipulating the implied market price of risk $\hat{q}_S$. An alternative explanation of $a_{(5)i}$ is that it achieves safety loading of the risk capital arising from the combined probability and cost of failure by transforming the inequalities expressed by Equation (4.40) into an interest rate-like term. This rate then changes between time intervals along with λ_i.

4.3.6   Estimating the discount rate

At this point, a reasonable comparison of Methods 1 to 5 is contingent upon obtaining a defensible estimate of the discount rate ρ. I note that *Massmann and Freeze* (1987a) on their Table 3a follow the conventional approach of using a range of values to reflect the decision-makers' subjective evaluation of risk, in their case $\rho = 0.05 - 0.20$ per annum with a base case value of $\rho = 0.10$ per annum. *Schwartz* (1994) disagrees with this common practice, and states "…there is only one way to deal with the problem, which is firmly based on arbitrage or equilibrium in financial markets. If what the

decision-maker is trying to get is the market value of the project, then, obviously, a subjective discount rate will not do the job." To address this issue, I follow the work of *Insley and Wirjanto* (2008). Their methodology is based on the idea of being able to construct a portfolio and hedge three contracts in the market, namely; the project which in this case is the risk capital, a traded asset that also depends on the stochastic underlying variable S such as shares in a competitors firm specializing in brownfields redevelopment, and a contract that depends linearly on S which in this case is simply the individual houses that the developer has guaranteed to repurchase at a price appreciated by the US national housing index. I acknowledge that this is a simplistic approach used for illustrative purposes, and an alternate approach is to use futures prices (*Hull*, 2006; *Kolos and Ronn*, 2008).

Hull (2006, pages 716-777) as well as *Insley and Wirjanto* (2008) show that the market price of risk $\hat{q}_S$ for a contract that depends linearly on the stochastic underlying variable S can be estimated using the CAPM as:

$$\mu_S = r_N + (\mathrm{E}[\mu_M] - r_N)\,\beta_{SM} \tag{4.43}$$

where μ_S is the total return on the contract above from all sources, $\mathrm{E}[\mu_M]$ is the expected return on the market portfolio M, and β_{SM} is the correlation between μ_S and μ_M. I use the S&P 500 as a proxy for M, with historical data shown on Figure 4.1d. *Insley and Wirjanto* (2008) also show that:

$$\mu_S = r_N + \hat{q}_S \sigma_S \tag{4.44}$$

resulting in:

$$\hat{q}_S = \frac{(\mathrm{E}[\mu_M] - r_N)\,\beta_{SM}}{\sigma_S}\ . \tag{4.45}$$

Finally, I choose a discount rate that uses a risk premium consistent with the CAPM as:

$$\rho \equiv \mu_S\ . \tag{4.46}$$

Consequently, for lack of better information, I have chosen in Equation (4.46) an equilibrium (and complete) market interpretation of the discount rate ρ for use in Methods 1, 2 and 3 despite that the versatility of these approaches is based on their applicability in an incomplete market scenario. Not surprisingly, substitution of Equation (4.46) following from (4.44) into Equation (4.13) of Method 1 produces an identical result to Equation (4.28) of Method 4.

The estimated value of $\beta_{SM} = 0.0197\pm0.0666$ 95% C.I. is determined by ordinary least-squares regression of Equation (4.43) on Figure 4.2 with details provided in Appendix C. *Siegel and Schwartz* (2004) estimate the expected return on the market portfolio $\mathrm{E}[\mu_M] = 0.12$. Because $r_{\mathcal{N}}$ is a mean-reverting stochastic process given by Equation (4.9), I estimate the long-run nominal interest rate in Equation (4.43) and (4.44) as $r_{\mathcal{N}} = \theta_{\mathcal{N}} = 0.06$. Finally, I estimate $\hat{q}_S = 0.0316\pm0.1066$ 95% C.I. and $\rho = 0.0612\pm0.0040$. I conclude this section with the observation that the relatively weak positive correlation between returns on S and M (as shown on Figure 4.2) implies that the market introduces a small risk premium on the cost of failure.

4.3.7 Stochastic discount and inflation rates

For the purposes of this work, I make the simplifying assumption that the stochastic process governing the discount rate (see Equation (4.9)) and the inflation rate (see Equation (4.8)) are uncorrelated. However, I acknowledge that the nominal interest rate $r_{\mathcal{N}}$ is approximately the sum of the real risk free market return rate and the inflation rate $r_{\mathcal{I}}$. *Mehta et al.* (1984) discuss the inflation-adjusted CAPM for an uncertain inflationary environment and when the nominal risk free interest rate is generated by a diffusion process. I proceed with the following definition:

$$D(r_{\mathcal{N}}, t_0, t_i) = \mathrm{E}^{\mathbb{Q}}\left[\exp\left\{\int_{t_0}^{t_i} -r_{\mathcal{N}}(t)\,dt\right\}\right] \tag{4.47}$$

which is used in place of a constant discount rate $r_{\mathcal{N}}$ in Methods 4 and 5. In addition, the following integral:

$$\int_{t_0}^{t_i} r_{\mathcal{I}}(t)\,dt \tag{4.48}$$

is used in place of a constant inflation rate $r_\jmath$ in Equation (4.2). Details concerning the evaluation of these integrals are presented in Appendix D. Note that I do not consider ρ to be stochastic for Methods 1, 2 and 3 because, unless I adopt the complete market definition of ρ from Section 4.3.6 where $\rho = r_\mathcal{N} + \hat{q}_S \sigma_S$, ρ is arbitrary and cannot be observed.

The basic principle governing my strategy for including stochastic discount and inflation rates into the estimate of the risk capital is to redefine the cost of failure given by Equations (4.2) and (4.3) as:

$$c_i = S_i + C^{total}\exp\left\{\int_{t_0}^{t_i} r_\jmath(t)\, dt\right\} \tag{4.49}$$

where $r_\jmath(t)$ is now stochastic. The resulting equation for the risk capital from Method 4 is:

$$V(H) = \sum_{i=1}^{m} D(r_\mathcal{N}, t_0, t_i)\, P_i\, \mathrm{E}^{\mathbb{Q}}[c_i] \tag{4.50}$$

where:

$$\mathrm{E}^{\mathbb{Q}}[c_i] = S_0 \exp\{(\alpha - \hat{q}_S \sigma_S)t_i\} + C^{total}\mathrm{E}^{\mathbb{Q}}\left[\exp\left\{\int_{t_0}^{t_i} r_\jmath(t)\, dt\right\}\right]. \tag{4.51}$$

Similarly, the resulting equation for the risk capital from Method 5 with the same β given by Equation (4.41) is:

$$V(H) = \sum_{i=1}^{m} D(r_\mathcal{N}, t_0, t_i)\, \lambda_i \Delta t_i\, \exp\{a_{(5)i}\, t_i\}\, \mathrm{E}^{\mathbb{P}}[c_i] \tag{4.52}$$

where:

$$\mathrm{E}^{\mathbb{P}}[c_i] = S_0 \exp\{\alpha t_i\} + C^{total}\mathrm{E}^{\mathbb{P}}\left[\exp\left\{\int_{t_0}^{t_i} r_\jmath(t)\, dt\right\}\right]. \tag{4.53}$$

137

and $V(H)$ in Equation (4.52) must be divided by $n_{realizations}$ to price the risk capital per house within the development.

4.4 Results

Following the presentation of the five methodologies to price the risk capital, the question remaining is the relative balance that the probability and the cost of failure contribute to the price of the risk capital. In other words, what is the relative merit in considering financial versus hydrogeological uncertainty when attempting to quantify the risk capital.

I begin this analysis by assuming $C^{total} = \$0$ at time t_0, and that the discount rate is constant. Method 1 provides a convenient place to proceed given that it neglects the contribution of the probability of failure, and only focuses on the cost of failure, when safety loading the risk capital. In addition, when $\rho = r_\mathcal{N} + \hat{q}_S \sigma_S$, Method 1 and 4 are identical (as well as when $a_{(5)i} = -\hat{q}_S \sigma_S \ \forall \ i$ in Method 5). Given that $\rho = r_\mathcal{N} + \hat{q}_S \sigma_S$ is only strictly correct in an equilibrium (complete) market whereas Method 1 was derived with ρ being arbitrary in the sense that it reflects a specific developer's preference for risk aversion, I priced the risk capital with ρ varying over a variety of reasonable values. These values are shown on Table 4.3 where; $\rho = r_\mathcal{N} + \hat{q}_S \sigma_S = 0.0612$, $\rho = r_\mathcal{N} + \hat{q}_S^{+95\% \ C.I.} \sigma_S = 0.0652$ and $\rho = r_\mathcal{N} + \hat{q}_S^{-95\% \ C.I.} \sigma_S = 0.0572$ with $r_\mathcal{N} = \theta_\mathcal{N}$. For all three values of ρ, the probability of failure is computed with a source zone lateral offset of $L = 55$ m, 35 m and 15 m. As discussed previously, I did not condition the structure of the heterogeneous subsurface permeability with prior data, beyond the geostatistical nature of the Borden aquifer. Consequently, varying the source zone lateral offset is my attempt to mimic uncertainty in the source zone location. The range in the price of the risk capital over the three values of ρ with a source zone lateral offset of $L = 55$ m, 35 m and 15 m was $\$0.1542 - \$0.1565$ ($\$0.0023$), $\$0.2319 - \$0.2352$ ($\$0.0033$) and $\$0.2155 - \$0.2174$ ($\$0.0018$), respectively. However, for $\rho = r_\mathcal{N} + \hat{q}_S \sigma_S$, the price of the risk capital as the source zone lateral offset decreases from $L = 55$ m, 35 m, to 15 m is $\$0.1554$, $\$0.2335$, and $\$0.2164$, respectively. Clearly, in the context of this brownfields development project, hydrogeological uncertainty has a greater impact on the risk capital than uncertainty in the discount rate when inferred from market data.

Methods 2, 3 and 5 provide a formal methodology to evaluate safety loading of the risk capital due to the combined influence of the probability and cost of failure. On Figure 4.3, I explore the range in values of $a_{(2)i}$, $a_{(3)i}$, and $a_{(5)i}$ needed to bridge the price gap in the risk capital calculated by Method 1 with $\rho = r_N + \hat{q}_S\sigma_S$ between a source zone lateral offset $L = 55$ m, 35 m, and 15m. I presume that since the developer has no way of knowing where the source zone is located at time t_0 when the premium (risk capital) is paid by the developer and the policy is written, then this range in values of $a_{(2)i}$, $a_{(3)i}$, and $a_{(5)i}$ would reflect their level of risk aversion given the hydrogeological uncertainty. Note that at a source zone lateral offset $L = 55$ m and 35 m, Method 1 computes a minimum and maximum value of the risk capital. As described earlier, $a_{(5)i}$ provides the most convenient interpretation of the safety loading needed to compensate the developer for uncertainty in both the probability and cost of failure by expressing the safety loading in a convenient interest rate-like term. Results indicate that $a_{(5)i}$ should be as large as 0.2123 to generate sufficient safety loading to bridge the price gap between minimum and maximum value of the risk capital, and make the developer indifferent about uncertainty in the source zone lateral offset. In comparison, $a_{(2)i}$ should be as large as 0.5280. However, I was unable to adjust $a_{(3)i}$ sufficiently to bridge the price difference and suggest that an alternative utility function be used in future work. 0.2123 for $a_{(5)i}$ and 0.5280 for $a_{(2)i}$ yield the similar range of the risk capital around \$0.25 to \$0.35.

I interpret the above results on the basis that in order for the developer to remain indifferent about uncertainty in the source zone location, $a_{(5)i} \leq 0.2123$ $\forall$ i. However, I know from Method 4 and the CAPM that market forces set a lower limit of $a_{(5)i} = -\hat{q}_S\sigma_S = -0.0012$. This component of $a_{(5)i}$ acts on the project discount rate to ensure $\rho = r_N + \hat{q}_S\sigma_S$. I surmise that another component of $a_{(5)i}$ acts on the project appreciation rate α to inflate the expected returns to compensate for the hydrogeological uncertainty. Effectively, I rewrite Equation (4.42) as:

$$V(H) = \sum_{i=1}^{m} S_0 \exp\{([\alpha + a_{(5)i}^{\alpha}] - [r_N + \hat{q}_S\sigma_S])t_i\} \lambda_i \, \Delta t_i \quad . \tag{4.54}$$

This implies that $a_{(5)i}^{\alpha} = a_{(5)i} + \hat{q}_S\sigma_S = 0.2135$. In other words, the value of the project would have to appreciate at a rate of $\alpha + a_{(5)i}^{\alpha} = 25.91\%$ per annum when all cash flows are discounted to present

value at a rate of $\rho = r_{\mathcal{N}} + \hat{q}_S \sigma_S = 6.12\%$ per annum for the developer to be willing to purchase a policy premium from an insurer and provide no information about the source zone location. Obviously, it seems prudent for the developer to constrain this hydrogeological uncertainty. Method 2 provides a dramatically different way of interpreting these results, given that it achieves safety loading of the basic idea of risk being the "probability of failures times the cost of failure" (i.e. Method 1) by adding the factor $a_{(2)i}$ times the risk arising from uncertainty expressed as the variance in the combined probability and cost of failure. The stochastic hydrology literature is rife with estimates of the expected mean and variance of measures like contaminant plume concentrations as a function of heterogeneity. Consequently, I see Method 2 as being particularly amenable to the development of risk-based hydrologic scoping models designed to develop and enforce regulatory criteria. The arbitrary parameter $a_{(2)i}$ can then be constrained by $a_{(5)i}$ which has obvious interpretations in light of market information.

Methods 2, 3, and 5 are all being applied in insurance markets, while a preference to a specific method depends on a given insurance company. In addition, insurance companies exhibit "economics of scale with respect to risk taking" (*Albrecht*, 1992). In other words, companies with more security capital or larger collectives may insure identical risks at lower prices (i.e. with a lower $a_{(2)i}$, $a_{(3)i}$ and $a_{(5)i}$ applied in Methods 2, 3, and 5, respectively). However, in general an insurer would prefer the larger $a_{(2)i}$ and $a_{(5)i}$ than 0.5280 and 0.2123, respectively, whereas a developer prefers the lower $a_{(2)i}$ and $a_{(5)i}$ than 0.5280 and 0.2123, respectively, for the same insurance policy in my highly stylized brownfields project. Further, I note that an insurance company cannot apply $a_{(2)i}$ and $a_{(5)i}$ much larger than those values given that insurance buyers, or developers have alternative insurance policy for the same risk provided by a different insurance company in the market and would not be interested in this policy asking much higher premium than the range of $0.25 to $0.35. In fact, the range of the risk capital around $0.25 to $0.35 is the maximum willingness to pay by developers for the insurance and it would be an equilibrium price if the environmental insurance market is complete.

I wish to examine the impact of stochastic nominal risk-free $r_{\mathcal{N}}$ and inflation $r_{\mathcal{I}}$ rates on the price of the risk capital. At this point, I set $C^{total} = \$1$, $r_{\mathcal{N}}(t_0) = 0.06$, and $r_{\mathcal{I}}(t_0) = 0.04$ at time t_0. Methods 4 and 5 provides a convenient place to proceed, as shown by Equations (4.50) and (4.52), given that they are formulated with a discount rate $r_{\mathcal{N}}$. When introducing a stochastic inflation rate into the risk-neutral Method 4 using the Consumer Price Index as a proxy, I must consider the market price of risk

on inflation $\hat{q}_{\mathcal{J}}$. While this could be inferred from US Treasury Inflation-Protected Securities (TIPS) in much the same manner as *Duan and Simonato* (1999) estimate $\hat{q}_{\mathcal{N}}$, I am unaware of such a study. Instead, I simply assume it is in the range of -0.1, 0, to 0.1. As a point of comparison, I first compute the risk capital with constant $r_{\mathcal{N}} = \theta_{\mathcal{N}}$ and $r_{\mathcal{J}} = \theta_{\mathcal{J}}$, with values for source zone lateral offset of $L = 55$ m, 35 m and 15 m shown on Table 4.4. I note that when $r_{\mathcal{N}}$ is stochastic, the discount rate in Equation (4.47) is slightly greater than when $r_{\mathcal{N}}$ is constant at the reversion level $\theta_{\mathcal{N}}$. Conversely, when $r_{\mathcal{J}}$ is stochastic, the appreciation rate of C^{total} in Equation (4.2) is slightly greater than when $r_{\mathcal{J}}$ is constant at the reversion level $\theta_{\mathcal{J}}$. However, $r_{\mathcal{N}}$ as produced by the CIR model is always greater than zero, whereas $r_{\mathcal{J}}$ as produced by the mean-reverting arithmetic Ornstein-Uhlenbeck model may be negative. The net result is that uncertainty in the discount rate over-compensates for uncertainty in inflation. Finally, I conclude that neither variability in the market price of risk on inflation $\hat{q}_{\mathcal{J}}$ nor uncertainty in $r_{\mathcal{N}}$ and $r_{\mathcal{J}}$ contributed significantly to the value of the risk capital in comparison to uncertainty in the TCE source zone location.

When I have a stochastic inflation rate $r_{\mathcal{J}}$ with non-zero C^{total} costs, interpretation of $a_{(5)i}$ into an interest rate-like safety loading factor that acts on the project discount rate ρ as well as the project appreciation rate α is problematic. However, when I look at Table 4.4 with $\hat{q}_{\mathcal{J}} = 0$, for the purposes of this work, I can safely assume $\mathrm{E}^{\mathbb{P}}\left[\exp\left\{\int_{t_0}^{t_i} r_{\mathcal{J}}(t)\, dt\right\}\right] \cong e^{r_{\mathcal{J}} t_i}$ when $r_{\mathcal{J}} = \theta_{\mathcal{J}}$. I can then simplify Equation (4.52) and (4.53) to:

$$V(H) \cong \sum_{i=1}^{m} D(r_{\mathcal{N}}, t_0, t_i)\, \lambda_i \Delta t_i \left(S_0 \exp\{(\alpha + a_{(5)i})\, t_i\} + C^{total}\exp\{(r_{\mathcal{J}} + a_{(5)i})\, t_i\}\right) \qquad (4.55)$$

It is now clear that $a_{(5)i}$ in essence also acts as an interest rate-like safety loading factor for the risk capital against C^{total} costs that appreciate with inflation. Figure 4.4 indicates that $a_{(5)i}$ should be as large as; (a) 0.2136 with constant $r_{\mathcal{N}}$ and $r_{\mathcal{J}}$, and (b) 0.2141 with stochastic $r_{\mathcal{N}}$ and $r_{\mathcal{J}}$, to generate sufficient safety loading to bridge the price gap between minimum and maximum value of the risk capital, and make the developer indifferent about uncertainty in the source zone lateral offset. Both values are only slight larger than the $a_{(5)i}$ computed above without including inflation and C^{total} costs.

4.5 Conclusions

In this work, I reviewed the actuarial and financial literature to obtain five methodologies which were applicable for pricing the risk capital needed to develop a highly stylized brownfields redevelopment project under hydrogeological and financial uncertainty. In the context of the proposed brownfields redevelopment project, the risk of failure was given by the probability of indoor air concentrations exceeding a regulatory level for houses built at the redevelopment site. The source of the contaminant concentrations was a TCE source zone located below the water table in a heterogeneous aquifer, with uncertainty in concentrations generated by simulating fate and transport in multiple statistically equivalent realizations of the aquifer using a Monte Carlo approach in Chapter 3. The cost of failure was then value of the house appreciated by the stochastic US National Housing Index, given that the developer had guaranteed that they would repurchase any affected dwellings within a predefined period. The risk capital was then essentially the probability of failure times the cost of failure plus a surcharge to provide safety loading, to ensure that the developer would remain solvent over the guarantee period. The objective of this work was then to incorporate uncertainty in the probability and cost of failure into the safety loading term for each of the five methodologies.

Three of the methodologies provided unique insights on how to value the risk capital. Method 4, which is the real options approach, provided a strategy to determine the market price of risk arising from stochastic US National Housing Index, and its impact on safety loading the cost of failure and consequently the value of the risk capital. However, I was unable to incorporate safety loading the probability of failure using Method 4. Method 5, which follows from *Delbaen and Haezendonck* (1989), provided a strategy to transform safety loading of both the probability and cost of failure into a simple interest-rate like term. This term could be used to include the market price of risk arising from stochastic US National Housing Index as derived in Method 4, as well as project returns in excess of the US National Housing Index that the developer would need to accrue in order to remain indifferent about hydrogeological uncertainty regarding imperfect knowledge of the TCE source zone location. Method 2 calculates safety loading by using a constant times the variance in the combined probability and cost of failure. This safety loading is then added to Method 1 to compute the total risk capital. This method appears attractive to the stochastic hydrology community given that they routinely compute the expected mean and variance of physical measures such as concentration within

the aquifer. While it is difficult to interpret the constant in a financial context, comparison of the safety loading produced using this method to that of Method 5 does provide reasonable constraints. Finally, I was unsuccessful in using an exponential utility function to generate sufficient safety loading to make the developer indifferent about uncertainty in the TCE source location. Given that the utility function approach is the *de-facto* standard approach for pricing risk by actuaries, I recommend that alternative utility functions be explored in future work.

I conclude this Chapter with the observation that my approach for using a hydrogeological model to compute the probability of failure and market data to compute the cost of failure is sufficiently general that it could be applied to a variety of engineering problems that require risk assessment. The probability of failure could be computed by any physics-based process model relating to the occurrence of; hurricanes, earthquakes, global warming, and even biological events. As long as the cost of failure at some future date can be indexed to some asset traded on the market (i.e. timber, oil, metals, agriculture futures), then this approach should in principle be applicable.
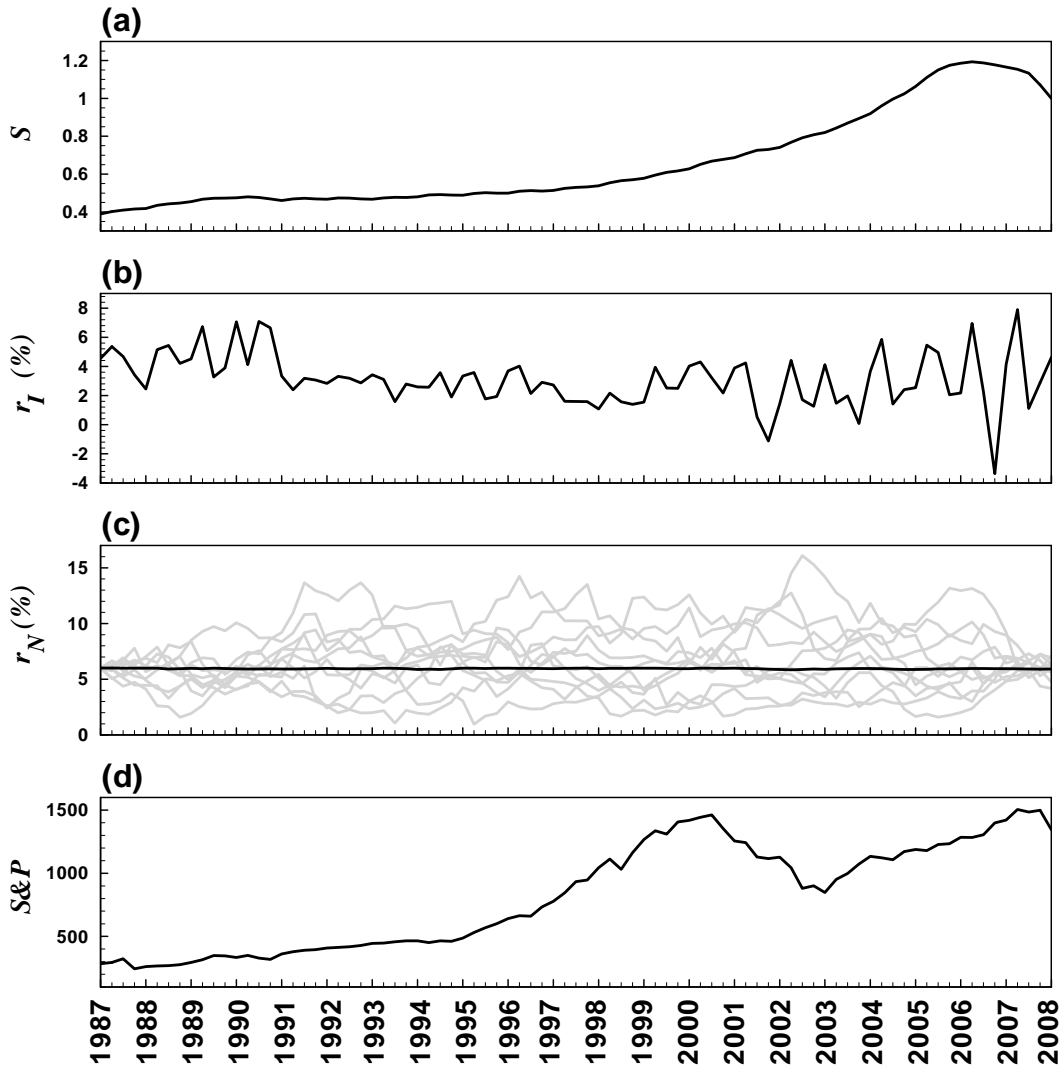
Figure 4.1. (a) US national home price index, S_i normalized by the index of March 2008 (source : http://www2.standardandpoors.com), (b) the annual rate of inflation (%) using the Consumer Price Index as a proxy, r_I (source : http://www.bls.gov/CPI/#data), (c) the nominal annual interest rate (%) inferred from risk-free US Treasury securities, r_N; 10 Monte Carlo realizations of short term interest rate using parameters for the CIR model in Table 4.2. Interest rate at the first quarter in 1987 was assumed to be 6 % and Δt of ¼ year was used for the Monte Carlo simulation. The black solid line represents the mean of 1000 realizations at each time, and (d) the general performance of the US market using the S&P 500 as a proxy. The closing price on the last trading day of the month was used (source: http://finance.yahoo.com/q?s=%5EGSPC).
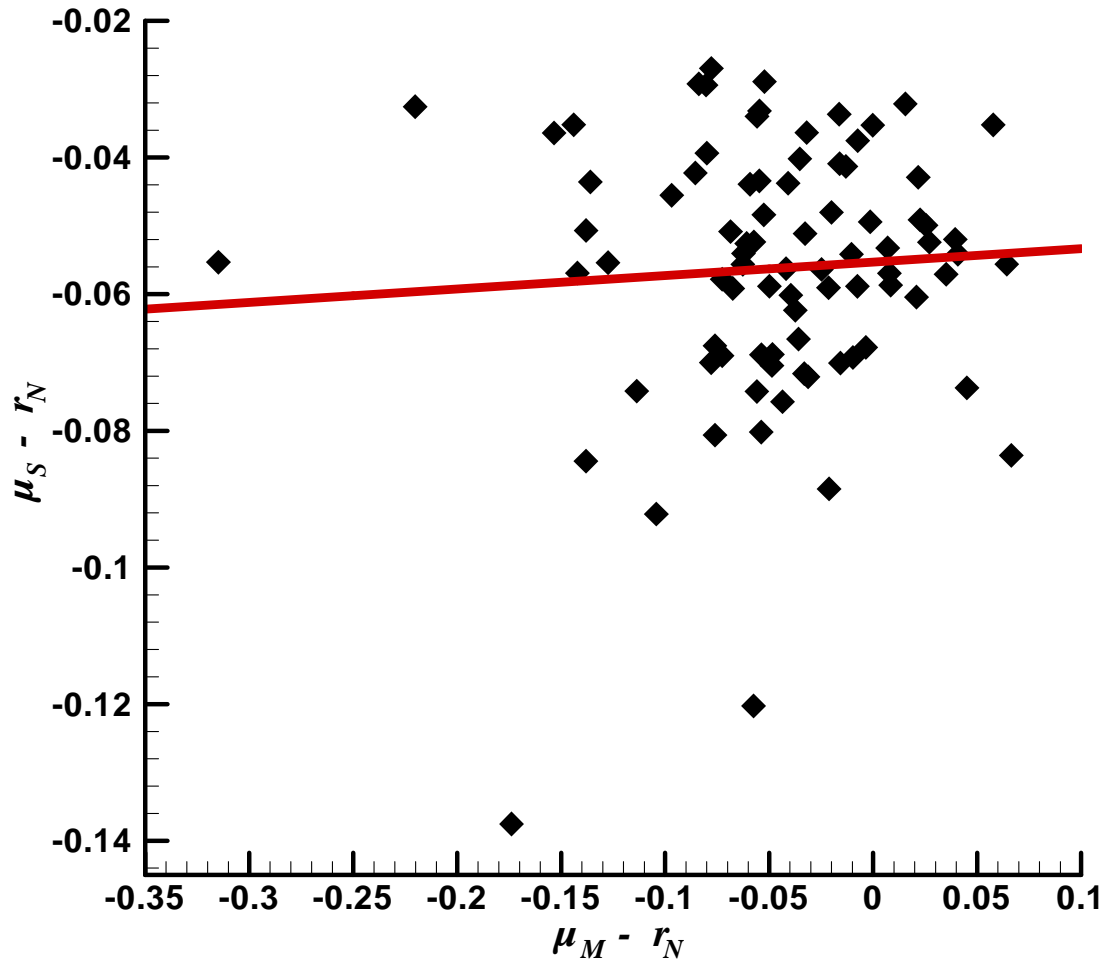
Figure 4.2. Change in housing price versus the S&P 500 Index return (source : http://finance.yahoo.com/q?s=%5EGSPC). Slope of the line yields β_{SM} used in CAPM to estimate $\hat{q}_S$. The solid line has the average $\beta_{SM} = 0.0197$ with $R^2 = 0.0042$. Details of this parameter estimation procedure are provided in Appendix C.
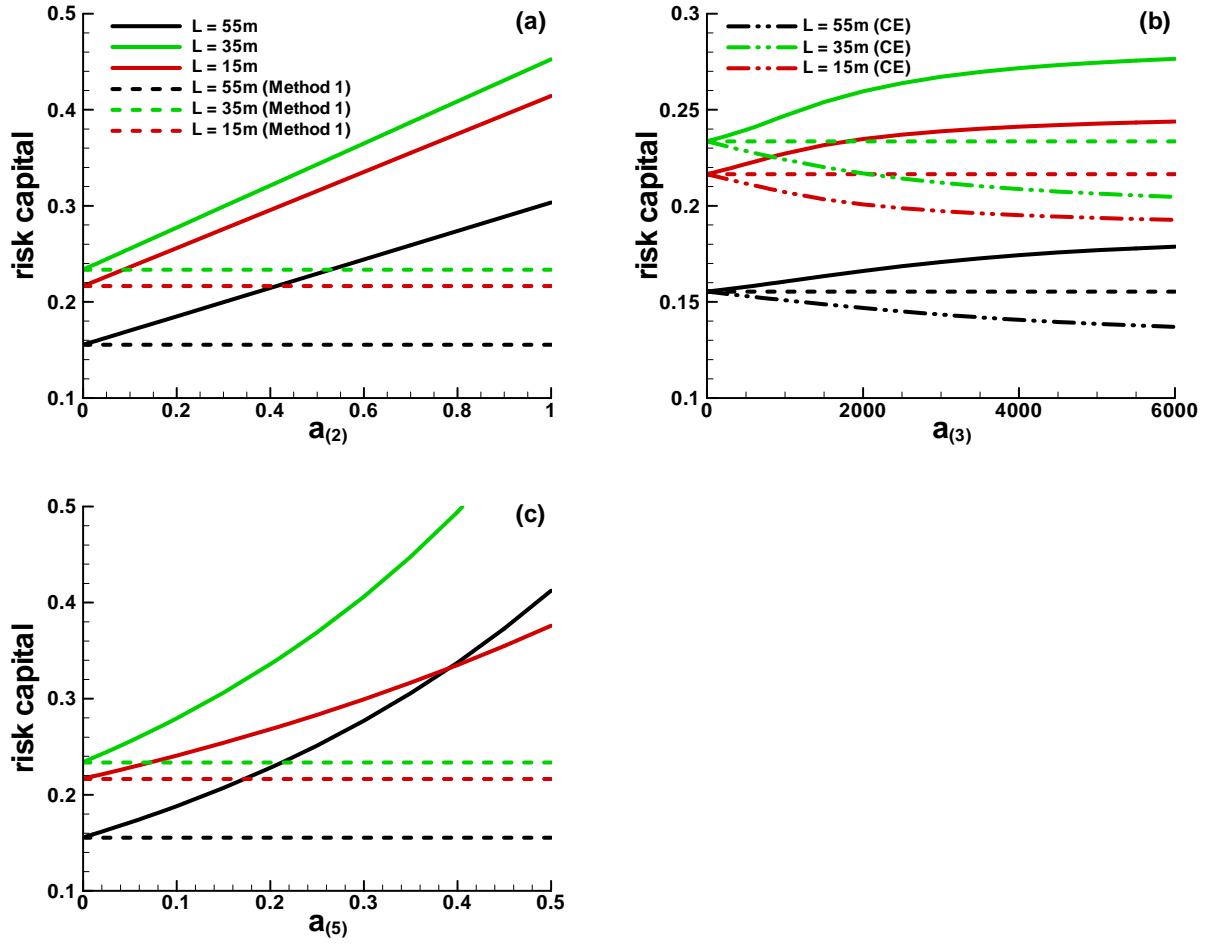
Figure 4.3. Price of risk capital $V(H)$ with $S_0 = \$1$ and with $C^{total} = \$0$ at time t_0 as a function of; (a) $a_{(2)i}$ for Method 2, (b) $a_{(3)i}$ for Method 3, and (c) $a_{(5)i}$ for Method 5. Each of $a_{(2)i}$, $a_{(3)i}$ and $a_{(5)i}$ are constant $\forall\ i$. Values of $V(H)$ for Methods 2, 3 and 5 are calculated with the probability of failure arising from a source zone lateral offset of $L = 55$ m, $\rho = r_\mathcal{N} + \hat{q}_S \sigma_S$ and constant $r_\mathcal{N} = \theta_\mathcal{N}$. For comparison, Method 1 (or Method 4) with constant $r_\mathcal{N} = \theta_\mathcal{N}$ and Methods 1, 2, 3 and 5 with source zone lateral offsets of $L = 35$m and 15 m are also provided. Note that (b) has $CE(X)$ from Equation (4.25). I see that $CE(X) < \mathrm{E}^\mathbb{P}[X] < \mathcal{P}(X)$. Method 5 produces the same result as Method 4 (or Method 1) when $a_{(5)i} = -\hat{q}_S \sigma_S = -0.0012$.
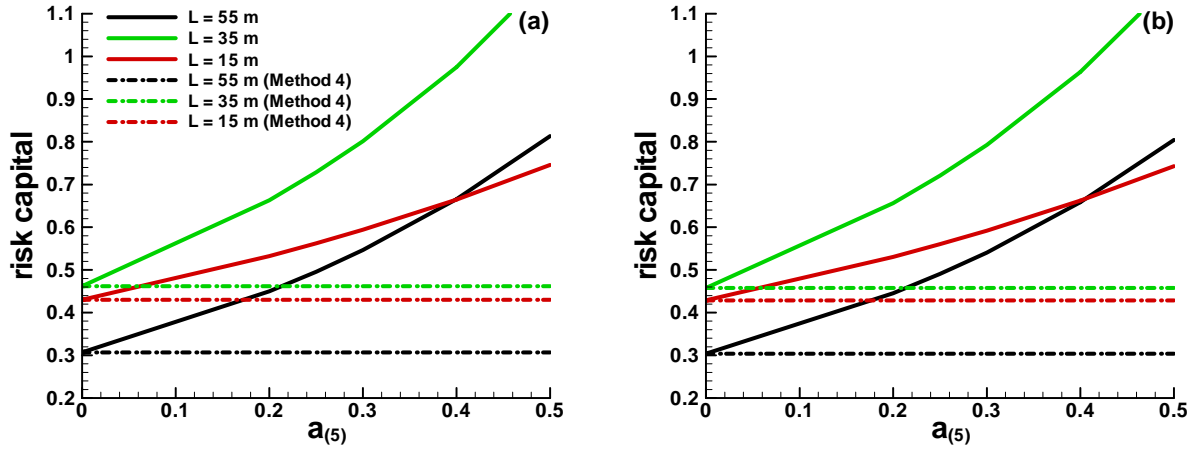
Figure 4.4. Price of risk capital $V(H)$ with $S_0 = \$1$ and with $C^{total} = \$1$ at time t_0 as a function of $a_{(5)i}$ for Method 5. (a) Constant $r_{\mathcal{N}} = \theta_{\mathcal{N}}$ and $r_{\mathcal{J}} = \theta_{\mathcal{J}}$ (b) Stochastic $r_{\mathcal{N}}$ and $r_{\mathcal{J}}$. For ease of comparison between Methods 4 and 5, the dash-dot line in (b) is calculated with $\hat{q}_{\mathcal{J}} = 0$. In both (a) and (b), Method 5 produces the same result as Method 4 when $a_{(5)i} = -0.0006$ which is greater than $-\hat{q}_S \sigma_S$ due to safety loading of C^{total} costs.

147

Table 4.1. Probability of failure distribution as a function of TCE source zone location.

Time (days)	Source zone lateral offset (L)					
$(t_{i-1}, t_i]$	55 m		35 m		15 m	
	P_i	$\lambda_i [day^{-1}]$	P_i	$\lambda_i [day^{-1}]$	P_i	$\lambda_i [day^{-1}]$
(0, 100]	0.0	0.0	0.0	0.0	0.0	0.0
(100, 200]	0.0	0.0	0.0	0.0	0.04	0.02
(200, 300]	0.0	0.0	0.04	0.02	0.1	0.05
(300, 400]	0.02	0.01	0.02	0.01	0.0	0.0
(400, 500]	0.02	0.01	0.04	0.02	0.06	0.03
(500, 600]	0.04	0.02	0.06	0.03	0.0	0.0
(600, 700]	0.02	0.01	0.02	0.01	0.0	0.0
(700, 800]	0.02	0.01	0.0	0.0	0.02	0.01
(800, 900]	0.02	0.01	0.0	0.0	0.0	0.0
(900, 1000]	0.02	0.01	0.04	0.02	0.0	0.0
(1000, 1100]	0.0	0.0	0.0	0.0	0.0	0.0
(1100, 1200]	0.0	0.0	0.02	0.01	0.0	0.0
(1200, 1300]	0.0	0.0	0.0	0.0	0.0	0.0

Table 4.2. Parameters for estimating the probability and cost of failure.

Parameter		Value
General		
t_0	start date for brownfields project	March 2008
$\Delta t_{monitor}$	indoor air monitoring interval	100 days
T	guarantee period for brownfields project	2000 days
US national housing index parameters for S		
S_0	unit price of house at time t_0	$1
α	annual rate of appreciation	0.0456 per annum
σ_S	volatility	0.0375
$\hat{q}_S$	market price of risk	0.0316±0.1066 95% C.I.
Annual rate of inflation $r_{\mathcal{J}}$		
$\kappa_{\mathcal{J}}$	speed of adjustment	5.83
$\theta_{\mathcal{J}}$	reversion level	0.0312 per annum
$\sigma_{\mathcal{J}}$	Volatility	0.0619
$\hat{q}_{\mathcal{J}}$	market price of risk	−0.1 to 0.1 (see Table 4.4)
Nominal annual interest rate $r_{\mathcal{N}}$		
$\kappa_{\mathcal{N}}$	speed of adjustment	0.2
$\theta_{\mathcal{N}}$	reversion level	0.06 per annum
$\sigma_{\mathcal{N}}$	Volatility	0.07
$\hat{q}_{\mathcal{N}}$	market price of risk	−0.1
S&P 500 parameters for M		
$E[\mu_M]$	expected return on the market portfolio M	0.12
β_{SM}	correlation between μ_S and μ_M	0.0197±0.0666 95% C.I.

Table 4.3. Values of risk capital $V(H)$ calculated using Method 1 with $C^{total} = \$0$ at time t_0.

Method 1:	Source zone lateral offset (L)		
risk capital $V(H)$	55 m	35 m	15 m
$\rho = r_\mathcal{N} + \hat{q}_S \sigma_S$	\$0.1554	\$0.2335	\$0.2164
$\rho = r_\mathcal{N} + \hat{q}_S^{+95\% \text{ C.I.}} \sigma_S$	\$0.1542	\$0.2319	\$0.2155
$\rho = r_\mathcal{N} + \hat{q}_S^{-95\% \text{ C.I.}} \sigma_S$	\$0.1565	\$0.2352	\$0.2174

note: for constant discount rate, I set $r_\mathcal{N} = \theta_\mathcal{N}$

Table 4.4. Values of risk capital $V(H)$ calculated using Method 4 with $C^{total} = \$1$ at time t_0.

Method 4: risk capital $V(H)$	Source zone lateral offset (L)		
	55 m	35 m	15 m
Constant $r_{\mathcal{N}} = \theta_{\mathcal{N}}$ and $r_{\mathcal{J}} = \theta_{\mathcal{J}}$	$0.3069	$0.4617	$0.4299
Stochastic $r_{\mathcal{N}}$ and $r_{\mathcal{J}}$			
$\hat{q}_{\mathcal{J}} = -0.1$	$0.3043	$0.4580	$0.4289
$\hat{q}_{\mathcal{J}} = 0$	$0.3040	$0.4576	$0.4287
$\hat{q}_{\mathcal{J}} = 0.1$	$0.3038	$0.4573	$0.4285

note: when $\hat{q}_{\mathcal{J}} = 0$, $\mathrm{E}^{\mathbb{Q}}\left[\exp\left\{\int_{t_0}^{t_i} r_{\mathcal{J}}(t)\, dt\right\}\right] = \mathrm{E}^{\mathbb{P}}\left[\exp\left\{\int_{t_0}^{t_i} r_{\mathcal{J}}(t)\, dt\right\}\right]$

Chapter 5
Summary and Conclusions

This study was designed to develop an optimal investment strategy framework for brownfields redevelopment as shown in Equation (1.1). The framework manages potential risks of future residents being exposed to contaminants located in the subsurface. In particular, this thesis focused on the risk capital, V valuation given that many researches ignore or simplify the risk term. As an example, TCE-contaminated industrial land was discussed; the industrial land redevelopment has a potential risk of vapor phase intrusion into indoor air from a residual NAPL source in the saturated zone. Three major elements below comprise the core of this optimal investment strategy framework.

The first element consists of numerical assessment to determine the extent and nature of subsurface contamination with a suitable choice of remediation technology and to estimate potential intrusion of volatile contaminants from subsurface into indoor air. Such intrusion is not recognized at the time of selling houses to future residents, but could happen. Subsurface remediation may have removed contaminants that could impact future residents by direct contact with the surficial soils; however, it did not remove all contamination in the subsurface. In addition, foundations of new dwellings, designed to protect against exposure to contaminants, could fail. In particular, some residual contamination may remain deep in the subsurface, beneath the foundations. This contamination may then volatilize and be drawn upwards through a zone of remediation and into indoor air.

For the first element, the multi-phase multi-compositional numerical model, *CompFlow Bio* was applied. Particularly, in Chapter 2 the model was developed to reproduce laboratory-scale LNAPL behavior affected by an ethanol injection as the model validation step. The developed model replicated the complicated evolution of a LNAPL-ethanol source zone within the capillary fringe, which was observed in laboratory experiments. However, the data gap caused the quantitative difference between the model and the experiments; in particular, the imperfect information on contaminant properties resulted in the uncertainty in the model simulation despite the well-developed numerical model. In Chapter 3, the same model was used to assess potential intrusion of volatile contaminants from the saturated zone into indoor air through the vadose zone. Various factors were considered controlling the impact of a saturated zone source on indoor air, including aquifer

heterogeneity, source zone location, barometric pressure fluctuations, foundation slab cracks, indoor air pressure drop, recharge and capillary fringe thickness. Simulation results showed that the uncertainty in the aquifer heterogeneity seemed the most significant factor to cause the uncertainty in future indoor air impact.

The second element involves quantification of risk capitals in brownfields redevelopment investment. This risk capital is required due to hydrogeological and economic uncertainties in contaminated land redevelopment. A developer can budget risk capital as a contingency fee if the developer remains financially responsible, or pay as a premium to an insurer who is willing to underwrite the risk and indemnify the developer. The risk capital valuation process includes (1) estimation of the probability that either subsurface remediation and/or foundation design fail to prevent indoor air concentrations from exceeding regulatory exposure criteria due to the imperfect knowledge of subsurface conditions, or hydrogeological uncertainty; (2) description of loss magnitude at redevelopment failure events, involving economic uncertainty in the market; (3) risk capital valuation using actuarial premium calculations or financial mathematics. Remediation failure means the existence of a residual NAPL source in the subsurface even after cleanups; while foundation design failure indicates the formation of aperture in the foundation slab large enough to flow contaminated soil gas into indoor air. A combination of a remediation method and a foundation design is arranged to provide an engineered strategy for minimizing the potential for contaminants to impact indoor air, but it could fail. The effectiveness of this strategy is considered in terms of the risk (probability) of its failure, called probability of failure in this study. On the other hand, a project-specific loss magnitude called cost of failure is defined based on additional remedial actions agreed to be immediately undertaken so that potential health risks and associated punitive damages of future residents are minimized, subsequent to an event where indoor air concentration exceeds regulatory exposure criteria. Then, the risk capital, or the present value of expected cost of these potential remedial actions, is calculated with hydrogeological uncertainty (probability of failure) and economic uncertainties (cost of failure) combined.

For the second element, the hydrogeological uncertainty was quantified as the risk (probability) that future indoor air concentrations exceed regulatory limits, using the Monte Carlo method with the aquifer heterogeneity and the source zone location remaining uncertain in Chapter 3. The probability of failure represents loss occurrence intensity of redevelopment failure. For loss distribution, information on economic uncertainties, including stochastic housing price, stochastic inflation rate

153

and stochastic interest rate was obtained from the market in Chapter 4. Hydrogeological uncertainty is site-specific and has not been well understood in history, while the economic uncertainties have been relatively well observed in the market for a long time. Next, actuarial premium calculation and financial mathematics were reviewed and applied to price the risk capital from both uncertainties in Chapter 4. All risk capital valuations were based on probability and cost of failure assessed conditional on site-specific and project-specific features, and each method applied a specific safety loading term to represent the developer's risk aversion against uncertainties. Risk capital valuation results indicated that risk capital was more sensitive to hydrogeological uncertainty than economic uncertainty in the given hypothetical redevelopment project. The overview of risk capital valuation methods in Chapter 4 will contribute to facilitating risk-cost-benefit analyses of environmental projects as well as understanding the risk capital, and activating environmental insurance markets, which are not growing as fast as the market expected.

The third element is to frame an optimal investment strategy, such as if and when to invest and to what degree to invest. This element remains incomplete and requires a future study. The framework will help decide optimal remediation strategy and optimal redevelopment time, and be applicable to various contaminated sites. The third element will consist of linking each of the previous two elements into a least-cost strategy for redeveloping an industrial site in order to maximize a net profit. The previous two elements include strategy of remediation and foundation design, numerical simulation of contamination, assessment and integration of uncertainties, and risk management from uncertainties. The process of choosing an optimal strategy of remediation and foundation design was not shown in this thesis, with the assumption of an appropriate redevelopment design chosen, but the assumption can be relaxed. This framework involves balancing the costs associated with each element while maximizing the revenue from land redevelopment. The optimal time to redevelop land and the optimal level to invest are given when the future price of the land (or houses) minus time and material costs as well as the contingency fee or insurance premium maximizes a net profit. The time and material costs associated with redevelopment will follow the spot inflation rate, while the fair market price of the insurance premium or contingency fee will be more complex as discussed in Chapter 4. This framework is applicable to many similar projects to brownfields redevelopment, such as protections against natural disasters, if the probability of failure is assessed by physics-based numerical models and the cost of failure is defined and hedged by tradable assets in the market.

154

Appendices

Appendix A

Supporting Figures for Chapter 2

Figure A. 1. Results of the static water-saturated zone numerical model-experiment comparison one day after gasoline injection, and immediately prior to ethanol injection, for the (a) experiment, as well as the simulated (b) non-aqueous phase saturations, (c) mole fraction of gasoline in the aqueous phase, and (d) aqueous phase saturations with $\vartheta_{Gq} = 0.12$ and $\zeta_{Gq} = 1.0 \times 10^{-5}$.
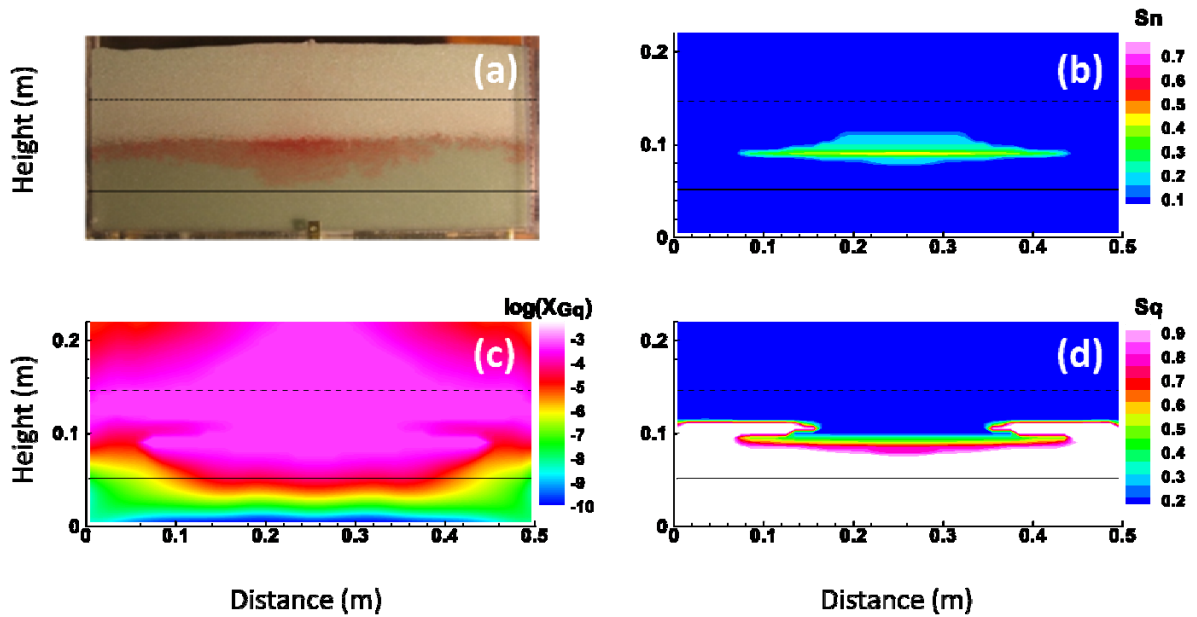
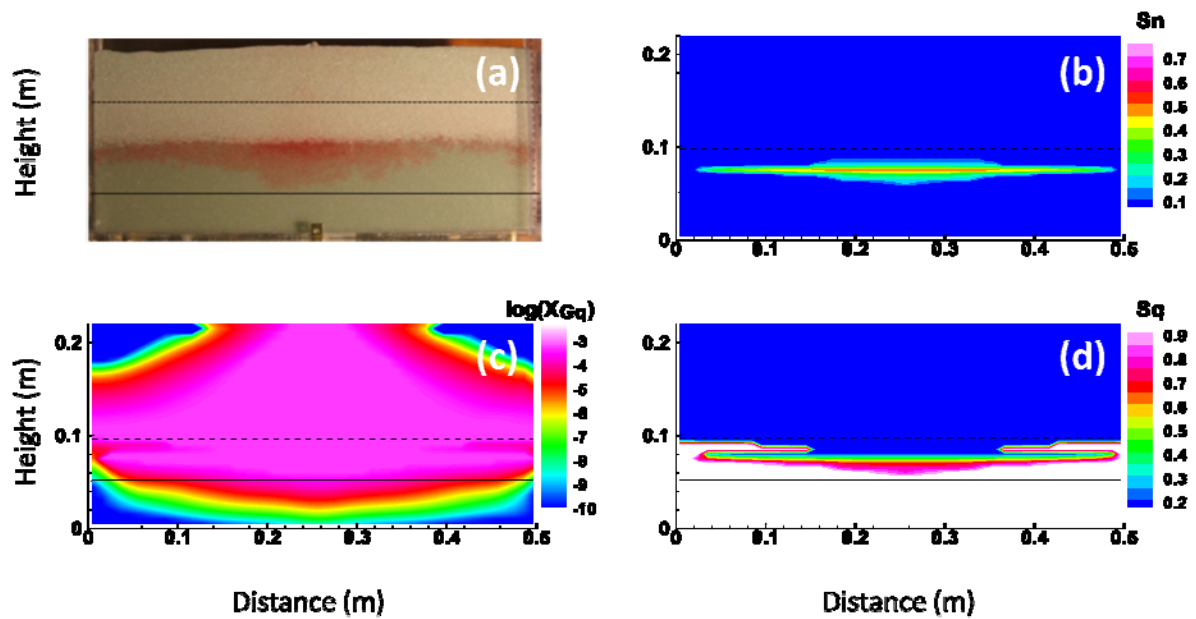Figure A. 2. Results of the static water-saturated zone numerical model-experiment comparison one day after gasoline injection, and immediately prior to ethanol injection, for the (a) experiment, as well as the simulated (b) non-aqueous phase saturations, (c) mole fraction of gasoline in the aqueous phase, and (d) aqueous phase saturations with reducing the height of the capillary fringe by a factor of two.

156

Figure A. 3. (a) Experimental results at times 210, 360, 1080, and 4200 seconds after the start of ethanol injection on rows one to four. Corresponding numerical results of (b) aqueous phase saturations and (c) non-aqueous phase saturations are presented for comparison with $\vartheta_{Gq} = 0.12$ and $\zeta_{Gq} = 1.0 \times 10^{-5}$.
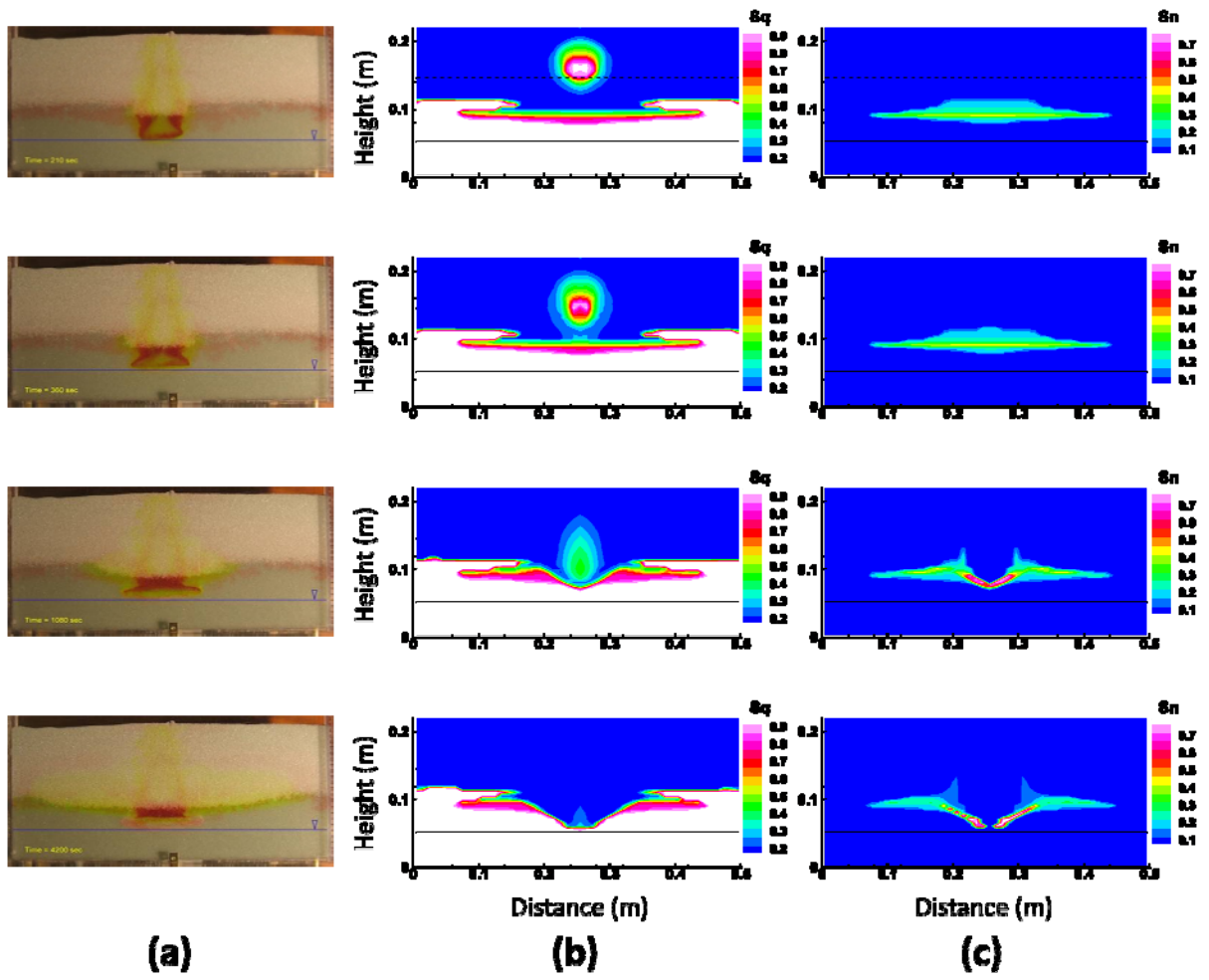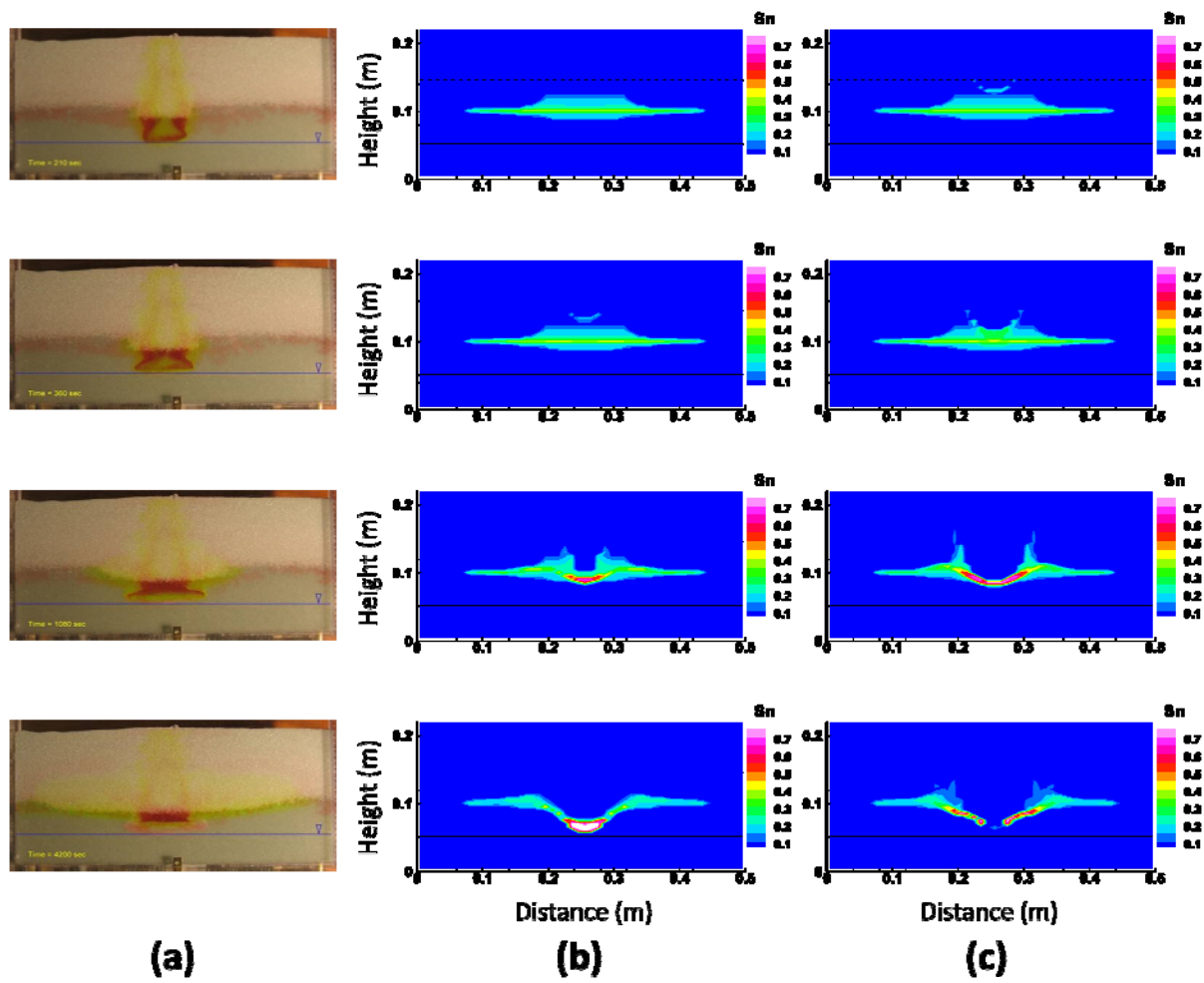
Figure A. 4. (a) Experimental results at times 210, 360, 1080, and 4200 seconds after the start of ethanol injection on rows one to four. Corresponding numerical results of non-aqueous phase saturations with (b) $\alpha_G = 1.3$ and (c) $\alpha_G = 2.0$.

Figure B. 1. Steady state flow fields before construction: (a) contours of aqueous phase potential with pathlines originating from ground surface due to infiltration from precipitation, and (b) contours of gas phase potential.
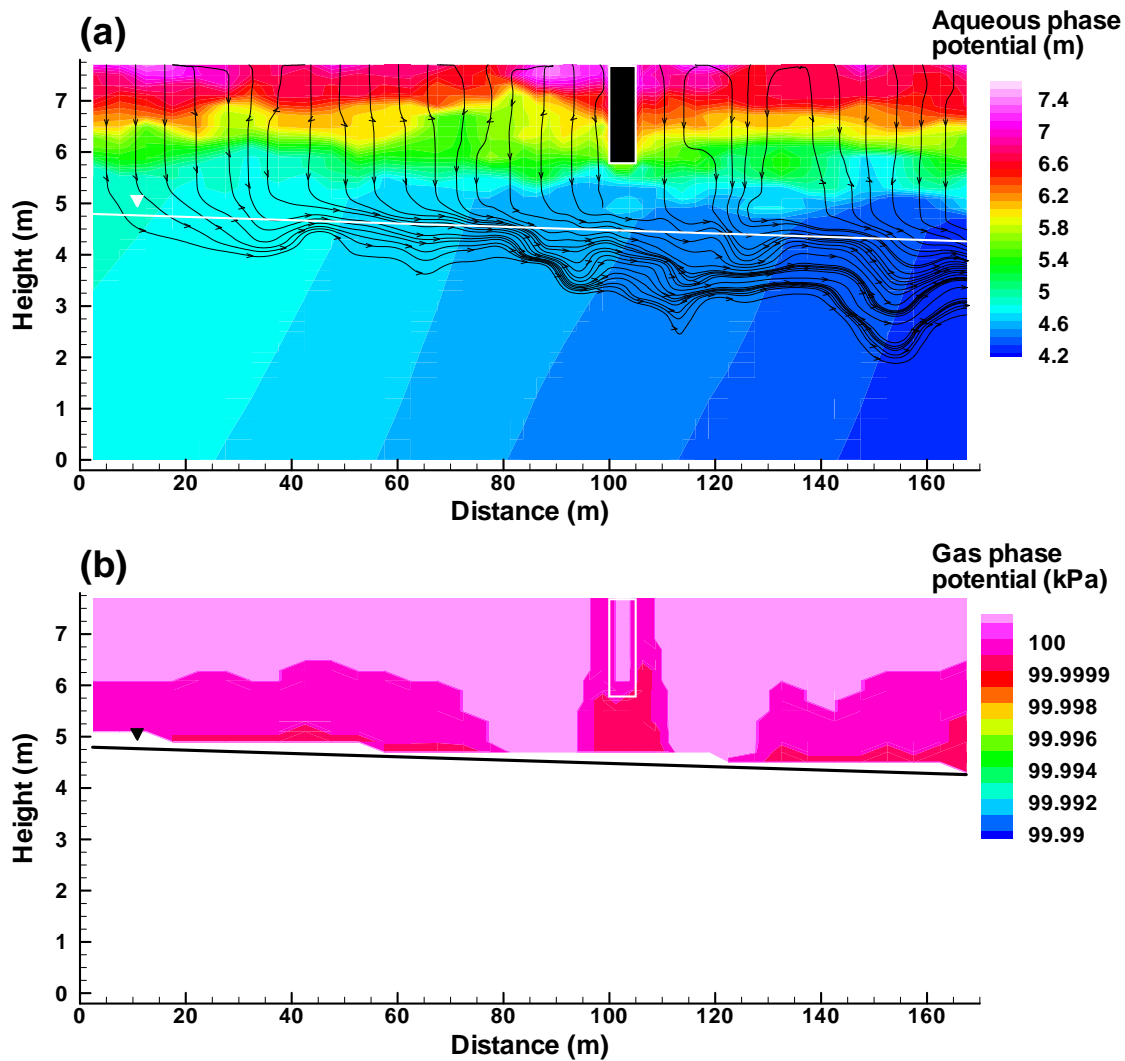
Figure B. 2. Steady state flow fields after construction and before occupation ($\Delta P_g^{basement} = 0$ Pa):
(a) contours of aqueous phase potential with pathlines originating from ground surface due to
infiltration from precipitation, and (b) contours of gas phase potential.
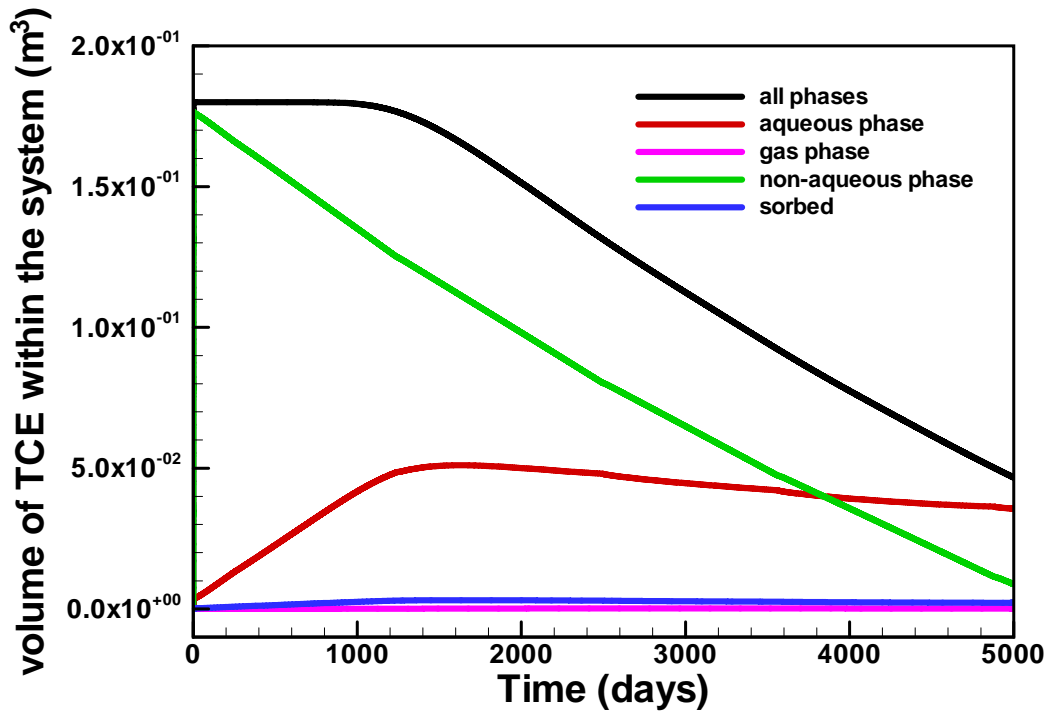
Figure B. 3. Distribution of TCE between the non-aqueous, aqueous, gas and solid (sorbed) phases for the base scenario with the TCE source zone located below the water table (Scenario 1b – see Table 3.8).
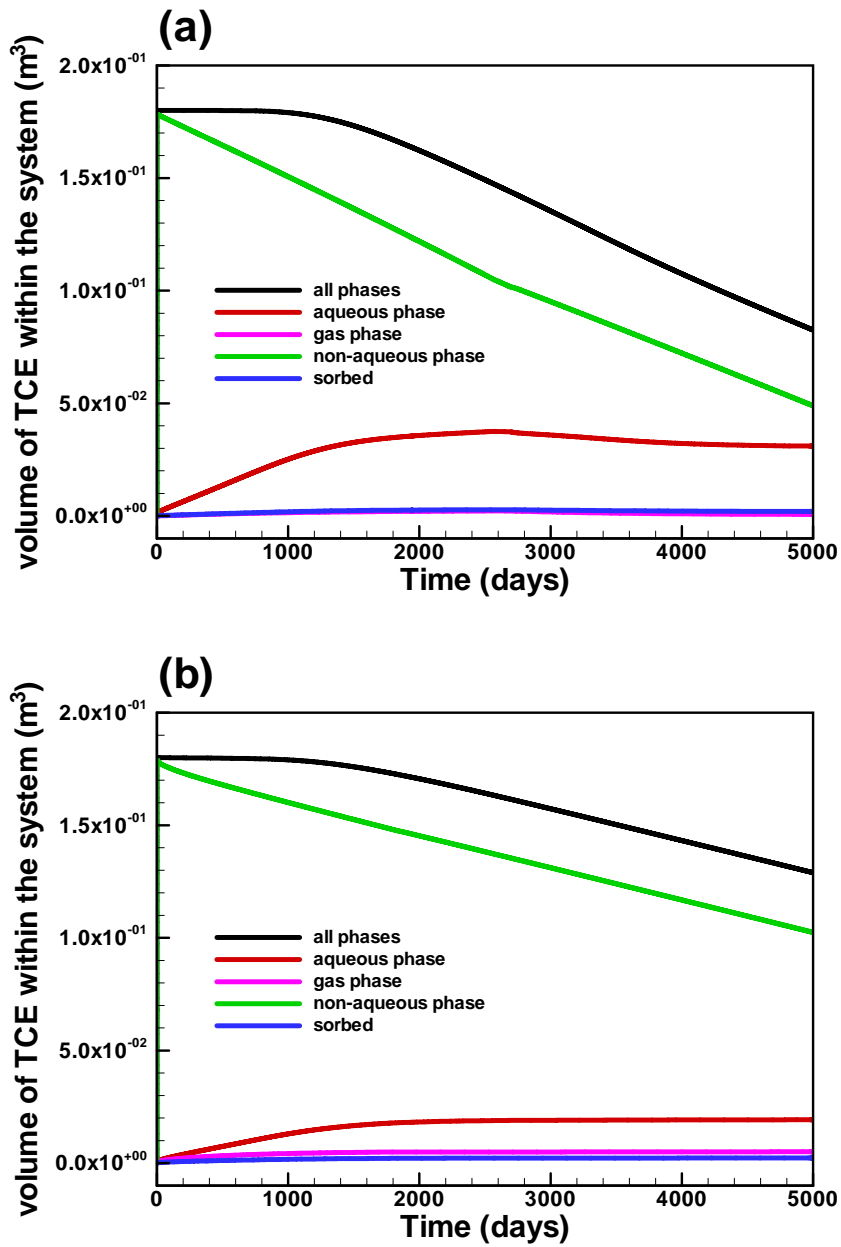
Figure B. 4. Distribution of TCE between the non-aqueous, aqueous, gas and solid (sorbed) phases for the base scenario with (a) the TCE source zone located at the water table (Scenario 2 – see Table 3.8), and (b) the TCE source zone located above the water table (Scenario 3 – see Table 3.8).
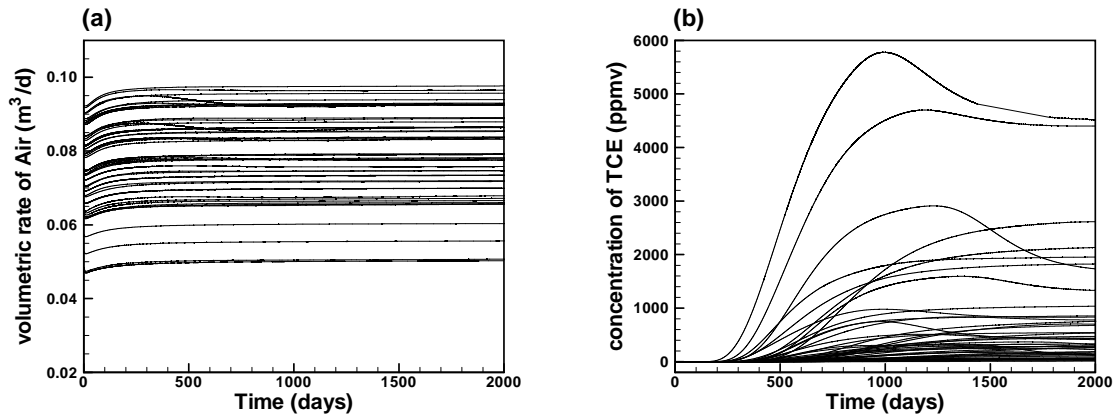
Figure B. 5. (a) the volumetric flow rate of the soil gas $[\mathrm{m}^3/\mathrm{day}]$, represented by component $p = \{a\}$, into the basement across a crack in the foundation slab Q_a, (b) the concentration of TCE within the soil gas entering the basement $\mathbb{C}_{c_{TCE}g}$ for the base scenario with the TCE source zone located below the water table (Scenario 1b – see Table 3.8) for 50 permeability realizations.
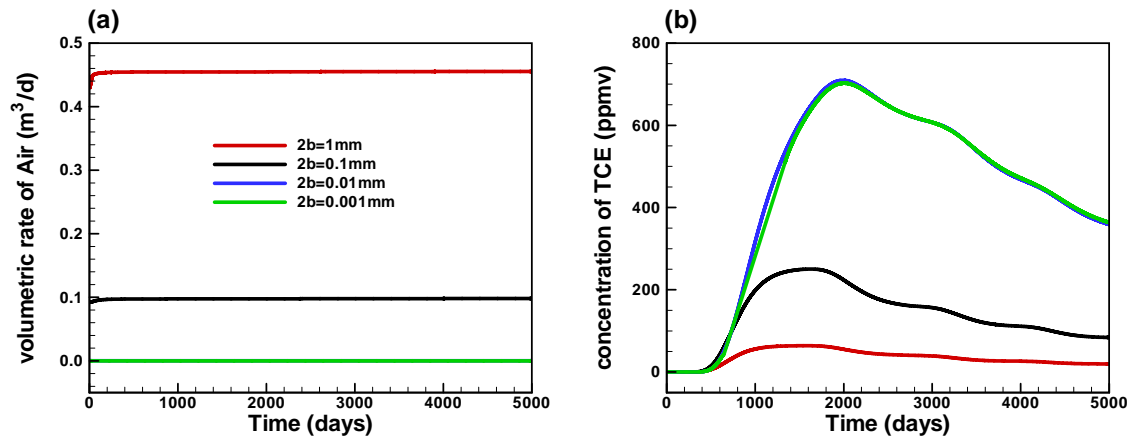
Figure B. 6. (a) the volumetric flow rate of the soil gas $[m^3/day]$, represented by component $p = \{a\}$, into the basement across a crack in the foundation slab Q_a, (b) the concentration of TCE within the soil gas entering the basement $\mathbb{C}_{c_{TCE}g}$: a sensitivity analysis on the aperture of the foundation crack (Scenario 5 – see Table 3.8).
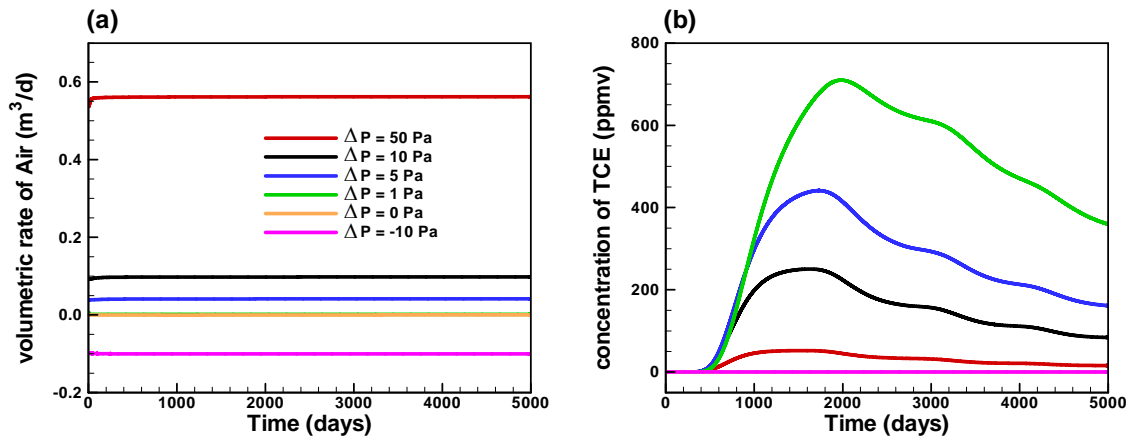
Figure B. 7. (a) the volumetric flow rate of the soil gas $[\text{m}^3/\text{day}]$, represented by component $p = \{a\}$, into the basement across a crack in the foundation slab Q_a, (b) the concentration of TCE within the soil gas entering the basement $\mathbb{C}_{c_{TCE}g}$: a sensitivity analysis on the vacuum induced by the heating/ventilation/HVAC system (Scenario 6 – see Table 3.8).
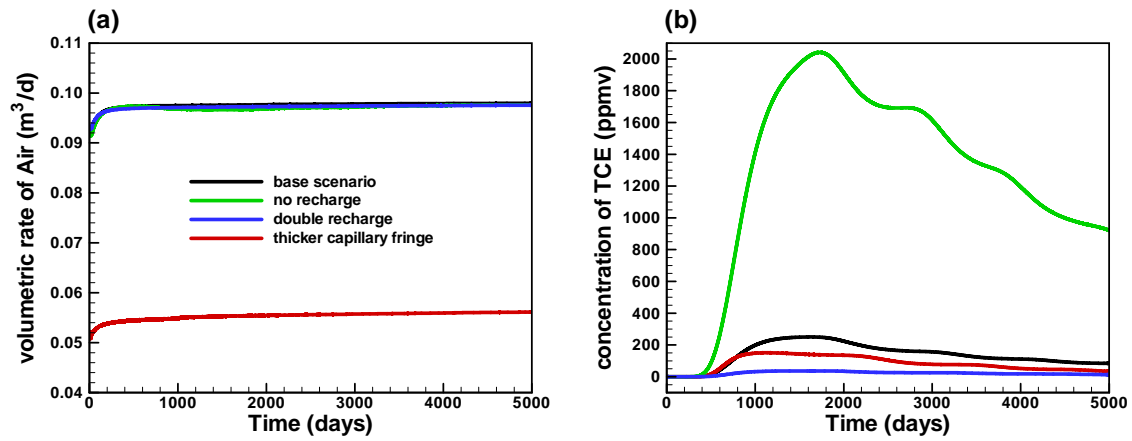
Figure B. 8. (a) the volumetric flow rate of the soil gas $[\text{m}^3/\text{day}]$, represented by component $p = \{a\}$, into the basement across a crack in the foundation slab Q_a, (b) the concentration of TCE within the soil gas entering the basement $\mathbb{C}_{c_{TCE}g}$: a sensitivity analysis on increased thickness of capillary fringe (Scenario 7 – see Table 3.8) and infiltration rate (Scenario 8 – see Table 3.8).

Appendix C
Parameter Estimation

US national housing index: S

Quarterly data for the US national housing index is used to estimate parameters for Equation (4.4). Denote S_i to be the value of the index at time t_i. Next, I calculate:

$$\Delta(\ln S_i) = \ln S_i - \ln S_{i-1} \quad . \tag{C.1}$$

By assuming that S_i follows GBM, then the set of $\Delta(\ln S_i)$ values are normally distributed with a mean and variance of:

$$E[\,\Delta(\ln S_i)\,] = \left(\alpha - \frac{\sigma_S^2}{2}\right)\Delta t$$
$$\text{Var}[\Delta(\ln S_i)\,] = \sigma_S^2\,\Delta t \tag{C.2}$$

where $\Delta t = t_i - t_{i-1} = 0.25$ years.

Consumer price index: $r_{\mathfrak{I}}$

Quarterly data for the US Consumer Price Index CPI_i at time t_i were converted into the annual rate of inflation $r_{\mathfrak{I}}(t_i)$ as follows:

$$r_{\mathfrak{I}}(t_i) = \left(\frac{CPI_i}{CPI_{i-1}}\right)^4 - 1 \quad . \tag{C.3}$$

Next, I estimate parameters, $\kappa_{\mathfrak{I}}$, $\theta_{\mathfrak{I}}$, and $\sigma_{\mathfrak{I}}$ in the Equation (4.8) by describing $\Delta r_{\mathfrak{I}i} = r_{\mathfrak{I}}(t_i) - r_{\mathfrak{I}}(t_{i-1})$ using a discrete time version of the first-order autoregressive process, AR(1) (*Dixit and*

Pindyck, 1994, p.76; *Schwartz*, 1997, footnote 15). In the limiting case as Δt tends to zero, the AR(1) process is:

$$\Delta r_{\jmath i} = \theta_{\jmath}\left(1 - e^{-\kappa_{\jmath}\Delta t}\right) + \left(e^{-\kappa_{\jmath}\Delta t} - 1\right) r_{\jmath}(t_{i-1}) + \varepsilon \tag{C.4}$$

where ε is normally distributed with mean zero and standard deviation σ_{ε} :

$$\sigma_{\varepsilon}^2 = \frac{(1 - \exp\{-2\kappa_{\jmath}\}) \sigma_{\jmath}^2}{2\kappa_{\jmath}} \quad . \tag{C.5}$$

and σ_{ε} is the standard deviation from regression. In order to estimate the parameters, I ran the regression on:

$$\Delta r_{\jmath i} = a + b \, r_{\jmath}(t_{i-1}) + \varepsilon \tag{C.6}$$

where:

$$
\begin{aligned}
\theta_{\jmath} &= -a/b \\
\kappa_{\jmath} &= -\ln(1+b) \\
\sigma_{\jmath} &= \sigma_{\varepsilon}\sqrt{\frac{2\ln(1+b)}{(1+b)^2 - 1}} \quad .
\end{aligned}
\tag{C.7}
$$

CAPM correlation coefficient: β_{SM}

Following the discussion in Section 4.3.6, I need to estimate the CAPM correlation coefficient β_{SM} between the US national housing index S_i and the S&P 500 index M_i, with quarterly data being used for both indices. I begin by first depreciating S_i and M_i by the US Consumer Price Index (CPI) as follows:

$$\hat{S}_i = S_i \frac{CPI_{Dec\,2005}}{CPI_i}$$

$$\widehat{M}_i = M_i \frac{CPI_{Dec\,2005}}{CPI_i} \quad .$$

$$(C.8)$$

Next, I calculated the total return μ_{Si} on S_i and μ_{Mi} on M_i at time t_i as:

$$\mu_{Si} = \frac{\hat{S}_i - \hat{S}_{i-1}}{\hat{S}_{i-1}}$$

$$\mu_{Mi} = \frac{\widehat{M}_i - \widehat{M}_{i-1}}{\widehat{M}_{i-1}} \quad .$$

$$(C.9)$$

Finally, I estimated β_{SM} by OLS regression on the following rearrangement of Equation (4.43):

$$\mu_{Si} - r_{\mathcal{N}} = \beta_{SM}(\mu_{Mi} - r_{\mathcal{N}}) + c$$

$$(C.10)$$

where $r_{\mathcal{N}} = \theta_{\mathcal{N}}$ and is constant. I observe a positive relationship between $\mu_{Si} - r_{\mathcal{N}}$ and $\mu_{Mi} - r_{\mathcal{N}}$, with β_{SM} of 0.0197±0.0666 95% CI and the constant c (*Montgomery and Runger*, 2006, p. 390).

Appendix D

Stochastic inflation and discount rates

Stochastic inflation rate

The stochastic inflation rate is defined by the arithmetic Ornstein-Uhlenbeck process given by Equation (4.8), and has the exact solution $r_{\jmath}(t)$:

$$r_{\jmath}(t) = r_{\jmath}(0)e^{-\kappa_{\jmath}t} + (1 - e^{-\kappa_{\jmath}t})\theta_{\jmath} + \sigma_{\jmath}e^{-\kappa_{\jmath}t}\int_0^t e^{\kappa_{\jmath}t}\, dZ_{\jmath}(t) \tag{D.1}$$

The variable $r_{\jmath}(t)$ has the Normal distribution with the following expressions for the mean and variance:

$$\mathrm{E}[\,r_{\jmath}(t)\,] = r_{\jmath}(0)e^{-\kappa_{\jmath}t} + \theta_{\jmath}(1 - e^{-\kappa_{\jmath}t}) \tag{D.2}$$

$$\mathrm{Var}[\,r_{\jmath}(t)\,] = (1 - e^{-2\kappa_{\jmath}t})\frac{\sigma_{\jmath}^2}{2\kappa_{\jmath}} \tag{D.3}$$

With this information at hand, I can evaluate the exponential of Equation (4.48) using the moment generating function:

$$\mathrm{E}\left[\exp\left\{\int_{t_0}^{t_i} \left(r_{\jmath}(t)\right)_u du\right\}\right] \cong \mathrm{E}[\,\exp\{g(t_i)\}\,] \tag{D.4}$$

where

$$g(t_i) = \int_{t_0}^{t_i} (r_{\jmath})_u\, du = \sum_{k=1}^{\frac{t_i - t_0}{\Delta u}} (r_{\jmath})_k\, \Delta u \; . \tag{D.5}$$

The variable $(r_{\jmath})_k$ has the Normal distribution with a mean and variance given by Equations (D.2) and (D.3), respectively. Thus, $g(t_i)$ also has the Normal distribution:

$$g(t_i) \sim N\left(\mu_g, \sigma_g^2\right) \ . \tag{D.6}$$

Then, E[exp{$g(t_i)$}] can be calculated using the Moment-generating function:

$$\mathrm{E}[\ \exp\{g(t_i)\}\ ] = \ \exp\left(\mu_g + \frac{\sigma_g^2}{2}\right) \tag{D.7}$$

where:

$$\mu_g = \mathrm{E}[\ g(t_i)\ ] = \mathrm{E}\left[\ \Sigma_{k=1}^{\frac{t_i - t_0}{\Delta u}}\ (r_\jmath)_k\ \Delta u\ \right] = \ \Sigma_{k=1}^{\frac{t_i - t_0}{\Delta u}}\ \mathrm{E}[\ (r_\jmath)_k\ ]\ \Delta u \tag{D.8}$$

$$\sigma_g^2 = \mathrm{Var}[\ g(t_i)\ ] = \ \mathrm{Var}\left[\Sigma_{k=1}^{\frac{t_i - t_0}{\Delta u}}\ (r_\jmath)_k\ \Delta u\right] = \ \Sigma_{k=1}^{\frac{t_i - t_0}{\Delta u}}\ \mathrm{Var}[\ (r_\jmath)_k\ \Delta u\ ] \tag{D.9}$$

$$= \Sigma_{k=1}^{\frac{t_i - t_0}{\Delta u}}\ \Delta u^2\ \mathrm{Var}[\ (r_\jmath)_k\ ]$$

Equations (D.8) and (D.9) are then estimated using E[$r_\jmath(t)$] and Var[$r_\jmath(t)$] above, and used to calculate (D.7).

For Method 5 I evaluate Equation (D.4) under the $\mathbb{P}$ measure so that:

$$\mathrm{E}^{\mathbb{P}}\left[\ \exp\left\{\int_{t_0}^{t_i} r_\jmath(t)\ dt\ \right\}\right] \cong \ \mathrm{E}^{\mathbb{P}}[\ \exp\{g(t_i)\}\ ] \ . \tag{D.10}$$

However, Method 4 is defined under the $\mathbb{Q}$ measure. Therefore, I begin by modifying Equation (4.8) as:

$$dr_\jmath = \kappa_\jmath \left(\left[\theta_\jmath - \frac{\hat{q}_\jmath\ \sigma_\jmath}{\kappa_\jmath}\right] - r_\jmath\right) dt + \sigma_\jmath\ dZ_\jmath^{\mathbb{Q}} \tag{D.11}$$

where $\hat{q}_\jmath$ is the market price of risk with respect to the inflation rate, and $Z_\jmath^{\mathbb{Q}}$ is a Wiener process under the risk neutral $\mathbb{Q}$ measure. I then proceed to evaluate:

$$\mathrm{E}^{\mathbb{Q}} \left[\exp \left\{ \int_{t_0}^{t_i} r_{\mathcal{J}}(t) \, dt \right\} \right] \cong \mathrm{E}^{\mathbb{Q}} \left[\exp\{g(t_i)\} \right] \qquad (D.12)$$

after replacing $\theta_{\mathcal{J}}$ with $\theta_{\mathcal{J}} - \frac{\hat{q}_{\mathcal{J}} \, \sigma_{\mathcal{J}}}{\kappa_{\mathcal{J}}}$ in Equation (D.2).

Stochastic discount rate

In this work, I follow the work of *Duan and Simonato* (1999) to simulate the nominal risk free interest rate $r_{\mathcal{N}}$ using the mean-reverting Cox-Ingersoll-Ross (CIR) model (*Cox et al.*, 1985) given by Equation (4.9). Parameters for this model are inferred from US Treasury securities trading in a complete market. As described in Section 4.3.7, this stochastic discount rate is used in Methods 4 and 5 as:

$$D(r_{\mathcal{N}}, t_0, t_i) = \mathrm{E}^{\mathbb{Q}} \left[\exp \left\{ \int_{t_0}^{t_i} -r_{\mathcal{N}}(t) \, dt \right\} \right] . \qquad (D.13)$$

The price of the $T-$Zero Coupon Bond at time t is given by:

$$D(r_{\mathcal{N}}, t, T) = A(t, T) e^{-B(t,T) \, r_{\mathcal{N}}(t)} \qquad (D.14)$$

where

$$A(t, T) = \left[\frac{2\gamma e^{[(\kappa_{\mathcal{N}} + \hat{q}_{\mathcal{N}} + \gamma)(T-t)]/2}}{(\gamma + \kappa_{\mathcal{N}} + \hat{q}_{\mathcal{N}})(e^{\gamma(T-t)} - 1) + 2\gamma} \right]^{2\kappa_{\mathcal{N}} \theta_{\mathcal{N}} / \sigma_{\mathcal{N}}^2}$$

$$B(t, T) = \frac{2(e^{\gamma(T-t)} - 1)}{(\gamma + \kappa_{\mathcal{N}} + \hat{q}_{\mathcal{N}})(e^{\gamma(T-t)} - 1) + 2\gamma} \qquad (D.15)$$

$$\gamma = \sqrt{(\kappa_{\mathcal{N}} + \hat{q}_{\mathcal{N}})^2 + 2\sigma_{\mathcal{N}}^2} .$$

This relationship is then used to evaluate $D(r_{\mathcal{N}}, t_0, t_i)$ in Equation (D.13) with appropriate substitutions for the current time t and the term T.

Bibliography

Abreu, L.D.V., and P.C. Johnson. 2005. Effect of vapor source–building separation and building construction on soil vapor intrusion as studied with a three-dimensional numerical model. *Environmental Science and Technology*, 39, 4550-4561.

Abreu, L.D.V., and P.C. Johnson. 2006. Simulating the effect of aerobic biodegradation on soil vapour intrusion into buildings: influence of degradation rate, source concentration, and depth. *Environmental Science and Technology*, 40, 2304-2315.

Albrecht, P. 1992. Premium calculation without arbitrage? : a note on a contribution by G. Venter. *ASTIN Bulletin*, 22(2), 247-254.

Andersson, C., and G. Destouni. 2001. Risk-Cost analysis in groundwater contaminant transport: The role of random spatial variability and sorption kinetics. *Ground Water*, 39(1) 35-48.

Andrew, J.G., B.B. Cairns, and K. Dowd. 2006. Pricing death: frameworks for the valuation and securitization of mortality risk. *ASTIN Bulletin*, 36(1), 79-120.

Anonymous. 2006. Environmental insurance can reduce liability risk at Brownfield sites (Technical Resources). *HAZARDOUS WASTE CONSULTANT*, 24(4), 1.1-1.5, Aspen Publishers, Inc.

Arey, J.S., and P.M. Gschwend. 2005. Estimating partitioning coefficients foe fuel-water systems: Developing linear salvation energy relationships using linear solvent strength theory to handle mixtures. *Environmental Science and Technology*, 39 (8), 2702-2710.

Aziz, K. and A. Settari. 1979. Petroleum reservoir simulation. Applied Sci. Publ., Essex, England.

Bacinello, A. R., and S.-A. Persson. 2000. Design and pricing of equity-linked life insurance under stochastic interest rates. EFA 2001 Barcelona Meetings, available at http://ssrn.com/abstract=276701.

Bayer, P., M. Finkel, and G. Teutsch. 2005. Cost-optimal contaminant plume management with a combination of pump-and-treat and physical barrier systems. *Ground Water Monitoring & Remediation*, 25(2), 96-106.

Bell, M.J., and J. Pearlson. 2003. Environmental insurance: a financing facilitator. *Briefings in real estate finance*, 3(3), 236-241.

Bennett, D.H., A.L. James, T.E. McKone, and C.M. Oldenburg. 1998. On uncertainty in remediation analysis: variance propagation from subsurface transport to exposure modeling. *Reliability Engineering and System Safety*, 62, 117-129.

Birge, J.R., and R.Q. Zhang. 1999. Risk-neutral option pricing methods for adjusting constrained cash flows. *The Engineering Economist*, 44(1), 36-49.

Booker, J.F., A.M. Michelsen, and F.A. Ward. 2005. Economic impact of alternative policy responses to prolonged and severe drought in the Rio Grande Basin. *Water Resources Research*, 41, W02026, doi:10.1029/2004WR003486.

Bozkurt, O., K.G. Pennel, and E.M. Suuberg. 2003. Simulation of the vapour intrusion process for nonhomogeneous soils using a three-dimensional numerical model. *Ground Water Monitoring & Remediation*, 29(1), 92-104.

Brachinger, H. W. 2002. Measurement of Risk. In: Derigs, U. (Ed.), Optimization and Operations Research, pp 1119-1137, to appear in the Encyclopaedia of Life Support Systems (EOLSS) organized under the auspices of the United Nations Educational, Scientific and Cultural Organization (UNESCO), EOLSS Publishers Co Ltd., available at http://www.unifr.ch/stat/forschung/publikationen/Braching-Risk02.pdf.

Brennan, M.J., and E.S. Schwartz. 1985. Evaluating Natural Resource Investments. *Journal of Business*, 58(2), 135-157.

Brooks, M.C., M.D. Annable, P.S.C. Rao, K. Hatfield, J.W. Jawitz, W.R. Wise, A.L. Wood, and C.G. Enfield. 2004. Controlled release, blind test of DNAPL remediation by ethanol flushing. *Journal of Contaminant Hydrology*, 69, 281-297.

Capiro, N.L., B.P. Stafford, W.G. Rixey, P.B. Bedient, and P.J.J. Alvarez. 2007. Fuel-grade ethanol transport and impacts to groundwater in a pilot-scale aquifer tank. *Water Research*, 41(3), 656-664.

Christensen, C.V. 2001. Implied loss distributions for catastrophe insurance derivatives. Working paper series no. 80., Centre for Analytical Finance, University of Aarhus.

Conant, B.H., R.W. Gillham, and C. A. Mendoza. 1996. Vapor transport of trichloroethylene in the unsaturated zone: field and numerical modelling investigations. *Water Resources Research*, 32 (1), 9-22.

Conrad, J.M., and A. Lopez. 2002. Stochastic water quality: Timing and option value of treatment. *Water Resources Research*, 38(5), 1044, doi:10.1029/2000WR000096.

Corey, A.T. 1954. The interrelation between gas and oil relative permeabilities, *Prod. Mon.*, 19(1), 38-41.

Corey, A.T., C.H. Rathjens, J.H. Henderson, and M.R.J. Wyllie. 1956. Three-phase relative permeability. *Transactions of the American Institute of Mining , Metallurgical and Petroleum Engineers*, 207, 349-351.

Corseuil, H.X., C.S. Hunt, R.C.F. Santos, and P.J.J. Alvarez. 1998. The influence of the gasoline oxygenate ethanol on aerobic and anaerobic BTX biodegradation. *Water Research*, 32 (7), 2065-2072.

Cox, J., J. Ingersoll, and S. Ross. 1985. The term structure of interest rates. *Econometrica*. 53, 385-407.

Cvitanic, J., and F. Zapatero. 2004. Introduction to the economics and mathematics of financial markets. The MIT press.

Da Silva, M., and P.J.J. Alvarez. 2002. Effects of ethanol versus MTBE on benzene, toluene, ethylbenzene, and xylene natural attenuation in aquifer columns, *Journal of Environmental Engineering*, 128 (9), 862-867.

Deeb, R.A., J.O Sharp, A. Stocking, S. McDonald, K.A. West, M. Laugier, P.J.J. Alvarez, M.C. Kavanaugh, and L. Alvarez-Cohen. 2002. Impact of ethanol on benzene plume lengths: Microbial and modeling studies, *Journal of Environmental Engineering*, 128 (9), 868-875.

Delbaen, F., and J. Haezendonck. 1989. A martingale approach to premium calculation principles in an arbitrage free market. *Insurance: Mathematics and Economics*, 8, 269-277.

Dixit, A.K., and R.S. Pindyck. 1994. Investment under Uncertainty. Princeton University Press, New Jersey.

Duan, J-.C., and J.-G. Simonato. 1999. Estimating and testing exponential – affine term structure models by Kalman filter. *Review of Quantitative Finance and Accounting*, 13, 111-135.

Falta, R.W. 1998. Using phase diagrams to predict the performance of cosolvent floods for NAPL remediation. *Ground Water Monitoring Review*, Summer, 94-102.

175

Falta, R.W., C.M. Lee, S.E. Brame, E. Roeder, J.T. Coates, C. Wright, A.L. Wood, and C.G. Enfield. 1999. Field test of high molecular weight alcohol flushing for subsurface nonaqueous phase liquid remediation. *Water Resources Research*, 35 (7), 2095–2108.

Faure, M.G., and K. Fiore. 2008. The civil liability of European nuclear operators: which coverage for the new 2004 Protocols? Evidence from France. *International Environmental Agreements: Politics, Law and Economics*, 8, 227–248.

Fayers, F.J., and J.D. Mathews. 1984. Evaluation of normalized Stone's methods for estimating three-phase relative permeabilities. *Society of Petroleum Engineering Journal*, 24, 230-242.

Fishburn, P. C. (1977), Mean-risk analysis with risk associated with below-target returns. *American Economic Review*, 67(2), 116-126.

Freitas, J.G. 2009. Ethanol spill into a gasoline residual source zone. Ph.D. Thesis – in progress, University of Waterloo, Waterloo, Ontario, Canada.

Forsyth, M. 1997. The economics of site investigation for groundwater protection: Sequential decision making under uncertainty. *Journal of environmental economics and management*, 34, 1-31.

Forsyth, M. 2000. On estimating the Option Value of Preserving a Wilderness Area. *Canadian Journal of Economics*, 33, 413-434.

Forsyth, P.A. 1993. A positivity preserving method for simulation of steam injection for NAPL site remediation. *Advances in Water Resources*, 16, 351-370.

Freeman, P.K., and H. Kunreuther. 1996. The Roles of Insurance and Well-Specified Standards in Dealing with Environmental Risks. *Managerial and decision economics*, 17, 517-530.

Freeze, R.A., and S.M. Gorelick. 1999. Convergence of stochastic optimization and decision analysis in the engineering design of aquifer remediation. *Ground Water*, 37(6), 934-954.

Freeze, R.A., J. Massmann, L. Smith, T. Sperling, and B. James. 1990. Hydrogeological decision analysis: 1. Framework. *Ground Water*, 28(5), 738-766.

Frind, E.O., J.W. Molson, and M. Schirmer. 1999. Dissolution and mass transfer of multiple organics under field conditions: the Borden emplaced source. *Water Resource Research*, 35 (3), 683–694.

Gatzert, N., and A. Kling. 2007. Analysis of participating life insurance contracts: a unification approach. *The Journal of Risk and Insurance*, 74(3), 547-570.

Gerber , H.U., and G. Pafumi. 1998. Utility functions: from risk theory to finance. *North American Actuarial Journal*, 2(3), 74-100.

Gomez Ramos, A., and A. Garrido. 2004. Formal risk-transfer mechanisms for allocating uncertain water resources: The case of option contracts. *Water Resources Research*, 40, W12302, doi: 10.1029/2004WR003340.

Goodman, L.A. 1962. The variance of the product of k random variables. *Journal of the American Statistical Association*, 57(297), 54–60.

Gruber, J. 2007. Chapter 8: Cost-benefit analysis, in *Public Finance and Public Policy*, 201-223. Available at http://bcs.worthpublishers.com/gruber/.

Guilbeault, M.A., B.L. Parker, and J.A. Cherry. 2005. Mass and flux distributions from DNAPL zones in sandy aquifers. *Ground Water*, 43 (1), 70–86.

Hara, D. 2003. Market Failures and The Optimal Use of Brownfield Redevelopment Policy Instruments: National Brownfields Redevelopment Strategy. Canadian Economics Association 37th Annual Meeting, Carleton University, Ottawa, Ontario.

Hardle, W., and B. Lopez Cabrera. 2007. Calibrating CAT bonds for Mexican earthquakes. Available at http://sfb649.wiwi.hu-berlin.de/fedc/discussionPapers_en.php; research supported by the Deutsche Forschungsgemeinschaft through the SFB 649 "Economic Risk".

Harley, R.A., S.C. Coulter-Burke, and T.S. Yeung. 2000. Relating liquid fuel and headspace vapour composition for California reformulated gasoline samples containing ethanol. *Environmental Science & Technology*, 34, 4088-4094.

Hayek, C., and R. Ghanem. 2002. Impact of uncertainty in catastrophe losses on insurance derivatives. 15th ASCE Engineering Mechanics Conference, June 2-5 2002, Columbia University, New York, NY.

Heal, G., and H. Kunreuther. 2009. Environment & Energy: Catastrophic Liabilities. Risk Management and Decision Processes Center, The Wharton School of the University of Pennsylvania, March 2009.

Heermann, S.E., and S.E. Powers. 1998. Modeling the partitioning of BTEX in water-reformulated gasoline systems containing ethanol. *Journal of Contaminant Hydrology*, 34, 315-341.

Henry, E.J., and J.E. Smith. 2002. The effect of surface-active solutes on water flow and contaminant transport in variably saturated porous media with capillary fringe effects. *Journal of Contaminant Hydrology*, 56, 247-270.

Henry, E.J., and E.S. Smith. 2003. Surfactant-induced flow phenomena in the vadose zone: A review of data and numerical modeling. *Vadose Zone Journal*, 2, 154-167.

Hess, K.M., S.H. Wolf, and M.A. Celia. 1992. Large scale natural gradient tracer test in sand and gravel, Cape Cod, Massachusetts: 3. Hydraulic conductivity and calculated macrodispersivities. *Water Resources Research*, 28(8), 2011–2027.

Hollis, S.S., T. Lambert, and P.B. Meyer. 2005. Utilizing environmental insurance for brownfield redevelopment. Practice Guide #4, Southeast Regional Environmental Finance Center, EPA Region 4.

Hull, J.C. 2006. Options, Futures, and other Derivatives, 6th ed., Prentice Hall.

Hyndman, D. W., F. D. Day-Lewis, K. Singha. 2007. Subsurface hydrology: data integration for properties and processes. American Geophysical Union, Washington, DC.

Insley, M. 2002. A Real Options Approach to the Valuation of a Forestry Investment. *Journal of Environmental Economics and Management*, 44, 471-492.

Insley, M. 2003. On the option to invest in pollution control under a regime of tradable emissions allowances. *Canadian Journal of Economics*, 35, 860-883.

Insley, M., and K. Rollins. 2005. On solving the multi-rotational timber harvesting problem with stochastic prices: a linear complementarity approach. *American Journal of Agricultural Economics*, 87(3) 735-755.

Insley, M., and T.S. Wirjanto. 2008. Contrasting two approaches in real options valuation: contingent claims versus dynamic programming. Available at SSRN: http://ssrn.com/abstract=1105588.

Interstate Technology Regulatory Council (ITRC). 2002. DNAPL Source Reduction: Facing the Challenge. Available at http://www.itrcweb.org/Documents/DNAPLs-2.pdf.

Interstate Technology & Regulatory Council (ITRC). 2007a. Vapor Intrusion Pathway: A Practical Guideline. VI-1. Washington, D.C.: Interstate Technology & Regulatory Council, Vapor Intrusion Team. Available at www.itrcweb.org.

Interstate Technology & Regulatory Council (ITRC), 2007b. Vapor Intrusion Pathway: Investigative Approaches for Typical Scenarios. VI-1A. Washington, D.C.: Interstate Technology & Regulatory Council, Vapor Intrusion Team. Available at www.itrcweb.org.

Jaimungal, S., and T. Wang. 2006. Catastrophe Options with stochastic interest rates and compound Poisson losses. *Insurance: Mathematics and Economics*, 38, 469-483.

Jajuee, B., A. Margaritis, D. Karamanev, and M.A. Bergougnou. 2006. Influence of dissolved hydrocarbons on volumetric oxygen mass transfer coefficient in a novel airlift contactor. *Chemical Engineering Science*, 61, 4111-4119.

James, A.L., and C.M. Oldenburg. 1997. Linear and Monte Carlo uncertainty analysis for subsurface contaminant transport simulation. *Water Resources Research*, 33 (11), 2495-2508.

Jawitz, J.W., R.K. Sillan, M.D. Annable, P.S.C. Rao, and K. Warner. 2000. In-situ alcohol flushing of a DNAPL source zone at a dry cleaner site. *Environmental Science and Technology*, 34 (17), 3722– 3729.

Ji, W., and M.L. Brusseau. 1998. A general mathematical model for chemical-enhanced flushing of soil contaminated by organic compounds. *Water Resources Research*, 34(7), 1635-1648.

Johnson, P.C., and R.A. Ettinger. 1991. Heuristic model for predicting the intrusion rate of contaminant vapors into buildings. *Environmental Science and Technology*, 25, 1445-1452.

Kilpatrick, J.A. 2007. Chapter 29: Valuation of Brownfields Properties, in Brownfields Law and Practice: The Cleanup and Redevelopment of Contaminated Land. Matthew Bender & Co., New York.

Kim, S.-B., K.-H. Jo, D.-J. Kim and W.A. Jury. 2004. Determination of two-dimensional laboratory-scale disperisivities. *Hydrological Processes*, 18, 2475-2483.

Kolos, S.P., and E.I. Ronn. 2008. Estimating the community market price of risk for energy prices. *Energy Economics*, 30, 621-641.

Kozlowski, R.T., and S.B. Mathewson. 1997. A primer on catastrophe modeling. *Journal of Insurance Regulation*, 15(3), 322-341.

Laird, C.L., L.T. Biegler, B.G. van Bloemen Waanders, and R. A. Bartlett. 2005. Contamination source determination for water networks. *Journal of Water Resources Planning and Management*, 131(2) 125-134.

Lee, K.Y. and C.A. Peters. 2004. UNIFAC modeling of cosolvent phase partitioning in nonaqueous phase liquid-water systems. *Journal of Environmental Engineering*, 130(4), 478-483.

Lefkoff, L.J., and S.M. Gorelick. 1986. Design and cost analysis of rapid aquifer restoration system using flow simulation and quadratic programming. *Ground Water*, 24(6), 777-790.

Lentz, G.H., and K.S. Maurice Tse. 1995. An Option Pricing Approach to the Valuation of Real Estate Contaminated with Hazardous Materials. *Journal of Real Estate Finance and Economics*, 10, 121-144.

Lesage, S., and R.E. Jackson. 1992. Groundwater contamination and analysis at hazardous waste sites. CRC Press.

Leverett, M.C. 1941. Capillary behaviour in porous solids., *Transactions of the American Institute of Mining , Metallurgical and Petroleum Engineers*, 142, 152-169.

Leverett, M.C., and W.B. Lewis. 1941. Steady flow of gas-oil-water mixtures through unconsolidated sands. *Transactions of the American Institute of Mining , Metallurgical and Petroleum Engineers*, 142, 107-116.

Lide, D.R. 2008. CRC handbook of chemistry and physics. 88ed., Boca Raton, FL, CRC Press/Taylor and Francis.

Longino, B. 2005. DNAPL source zone characterization and remediation: an ongoing challenge. Groundwater Resources Association of California (GRAC). Available at http://www.grac.org/dnaplsummary.asp.

Lovanh, N., C.S. Hunt, and P.J.J. Alvarez. 2002. Effect of ethanol on BTEX biodegradation kinetics: aerobic continuous culture experiments, *Water Research*, 36 (15), 3739-3746.

Mackay, D.M., N.R. De Sieyes, M.D. Einarson, K.P. Feris, A.A. Pappas, I.A. Wood, L. Jacobson, L.G. Justice, M.N. Noske, K.M. Scow, and J.T Wilson. 2006. Impact of ethanol on the natural

attenuation of benzene, toluene and o-xylene in a normally sulphate-reducing aquifer. *Environmental Science & Technology*, 40(19), 6123-6130.

Massmann, J., and R.A. Freeze. 1987a. Groundwater contamination from waste management sites: The interaction between risk-based engineering design and regulatory policy: 1. Methodology. *Water Resources Research*, 23(2), 351-367.

Massmann, J., and R.A. Freeze. 1987b. Groundwater contamination from waste management sites: The interaction between risk-based engineering design and regulatory policy: 2. Results. *Water Resources Research*, 23(2), 368-380.

Massmann, J., R.A. Freeze, L. Smith, T. Sperling, and B. James. 1991. Hydrogeological decision analysis: 2. Applications to Ground-Water contamination. *Ground Water*, 29(4), 536-548.

McCarthy, K.A. and R.L. Johnson. 1993. Transport of volatile organic compounds across the capillary fringe. *Water Resources Research*, 29(6), 1675-1683.

McDowell, C.J., and S.E. Powers. 2003. Mechanisms affecting the infiltration and distribution of ethanol-blended gasoline in the vadose zone. *Environmental Science and Technology*, 37(9), 1803-1820.

McDowell, C.J., T. Buscheck, and S.E. Powers. 2003. Behavior of gasoline pools following a denatured ethanol spill. *Groundwater*, 41(6), 746-757.

Mehta, D. R., M. D. Curley, and H.-G. Fung. 1984. Inflation, Cost of Capital, and Capital Budgeting Procedures. *Financial Management*, 13 (4), 48-54.

Merrifield, J. 2002. A general equilibrium analysis of the insurance bonding approach to pollution threats. *Ecological Economics*, 40, 103–115.

Meyer, P.B. 2003. Brownfields and red ink: The costs of contaminated (and idle) land. *Environmental Practice*, 5, 40-47.

Meyer, P.B., K.R. Yount, and K. Wernstedt. 2002. Brownfield Redevelopers' Perceptions of Environmental Insurance: An Appraisal and Review of Public Policy Options. Lincoln Institute of Land Policy Working Paper. WP02PM1.

Michel-Kerjan, E., and C. Kousky. 2009. Come Rain or Shine: Evidence on Flood Insurance Purchases in Florida. Risk Management and Decision Processes Center, The Wharton School of the University of Pennsylvania, March 2009.

Millington, R.J. 1959. Gas diffusion in porous media. *Science*, 130, 100-102.

Moller, T. 2002. On valuation and risk management at the interface of insurance and finance. *British Actuarial Journal*, 8(4), 787–827.

Molson, J.W., J.F. Barker, E.O. Frind, and M. Schirmer. 2002. Modeling the impact of ethanol on the persistence of benzene in gasoline-contaminated groundwater. *Water Resources Research*, 38(1), 1003. Doi:10.1029/2001WR000589.

Montgomery, D.C., and G.C. Runger. 2006. Applied statistics and probability for engineers. 3rd ed. John Wiley and Sons, Inc.

Morgan, M.G., and M. Henrion. 1990. Uncertainty: A Guide to Dealing with Uncertainty in Qualitative Risk and Policy Analysis. Cambridge University Press, New York.

Munich Re. 2006. Topics – Growth market: Health, new environmental liability, the risk of mega-events. February issue.

National Round Table on the Environment and the Economy (NRTEE) Canada. 2003. Cleaning up the past, Building the future: A National Brownfield Redevelopment Strategy for Canada.

Nazaroff, W.W., H. Feustel, A.V. Nero, K.L. Revzan, D.T. Grimsrud, M.A. Essling, and R.E. Toohey. 1985. Radon transport into a detached one-story house with a basement. *Atmospheric Environment*, 9, 31-46.

New York State Department Of Health (NYSDOH). 2005. Trichloroethene (TCE) in indoor and outdoor air fact sheet. February 2005. Available at http://www.health.state.ny.us/environmental/investigations/soil_gas/svi_guidance/docs/fs_tce.pdf.

Oamek, G.E. 1990. Economic and Environmental impacts of interstate water transfers in the Colorado River Basin. Monograph 90-M3, Center for Agricultural and Rural Development, Iowa State University.

Office of Environmental Health Hazard Assessment – California Environmental Protection Agency (OEHHA-CEPA). 2007. Occupational health hazard risk assessment project for California:

Identification of chemicals of concern, possible risk assessment methods, and examples of health protective occupational air concentrations. Reproductive and Cancer Hazard Assessment Branch, December. Available at http://www.dhs.ca.gov/ohb/HESIS/risksummary.pdf.

Oikarinen, E. 2008. Empirical Application of the Housing Market No-Arbitrage Condition: Problems, Solutions and a Finnish Case Study. Aboa Centre for Economics Discussion Paper No. 39. Available at SSRN: http://ssrn.com/abstract=1280827.

Oliveira, E. 1997. Ethanol flushing of gasoline residuals: Microscale and field experiments., PhD. Thesis, Department of Earth Sciences, University of Waterloo, Ontario, Canada.

Ontario Ministry of the Environment (OME). 1997. Guideline for use at contaminated sites in Ontario, http://www.ene.gov.on.ca/envision/land/decomm/backgd.htm.

Ontario Ministry of Municipal Affairs and Housing (OMMAH). 2007. A Practical Guide to Brownfields Redevelopment in Ontario, http://www.mah.gov.on.ca/AssetFactory.aspx?did=4995.

Paleologos, E.K., and I. Lerche. 2002. Option coverage techniques for environmental projects. *Journal of management in engineering*, 18(1), 3-6.

Parker, B.L., J.A. Cherry, S.W. Chapman, and M.A. Guilbeault. 2003. Review and analysis of chlorinated solvent dense nonaqueous phase liquid distributions in five sandy aquifers. *Vadose Zone Journal*, 2, 116–137.

Peck, A., S. Gorelick, G. de Marsily, S. Foster, and V. Kovalevsky. 1988. Consequences of spatial variability in aquifer properties and data limitations for groundwater modelling practice. *IAHS Publication*, 175.

Powers, S.E., C.S. Hunt, S.E. Heermann, H.X. Corseuil, D. Rice, and P.J.J. Alvarez. 2001. The transport and fate of ethanol and BTEX in groundwater contaminated by gasohol. *Critical Review in Environmental Science & Technology*, 31 (1), 79-123.

Rao, P.C.S., M.D. Annable, R.K. Sillan, D. Dai, K. Hatfield, and W.D. Graham. 1997. Field-scale evaluation of in-situ cosolvent flushing for enhanced aquifer remediation. *Water Resources Research*, 33(12), 2673-2686.

Reckhorn, S.B.F., L.V. Zuquette, and P. Grathwohl. 2001. Experimental investigations of oxygenated gasoline dissolution. *Journal of Environmental Engineering*, 127(3), 208-216.

183

Reinelt, P. 2005. Seawater intrusion policy analysis with a numerical spatially heterogeneous dynamic optimization model. *Water Resources Research*, 41, W05006, doi: 10.1029/2004WR003 111.

Reitsma, S., and B.H. Kueper. 1998a. Non-equilibrium alcohol flooding model for immiscible phase remediation: 1. Equation development. *Advances in Water Resources*, 21(8), 649-662.

Reitsma, S., and B.H. Kueper. 1998b. Non-equilibrium alcohol flooding model for immiscible phase remediation: 2. Model development and application. *Advances in Water Resources*, 21(8), 663-678.

Rivett, M.O. 1995. Soil-gas signatures from volatile chlorinated solvents: Borden field experiments. *Groundwater*, 33(1), 84-98.

Rivett, M.O., and J.A.Cherry. 1991. The effectiveness of soil gas surveys in delineation of groundwater contamination: controlled experiments at the Borden field site. *Proceedings of the Conference on Petroleum Hydrocarbons and Organic Chemicals in Groundwater*. National Water Well Association, Houston, Texas, pp. 107-124. Nov. 20-22, 1991.

Rivett, M. O., D. N. Lerner, and J. W. Lloyd. 1990. Chlorinated Solvents in UK Aquifers. *Water and Environment Journal*, 4(3), 242-250. Available at http://www.dnapl.group.shef.ac.uk/hist.htm.

Rivett, M.O., S. Feenstra, and J.A. Cherry. 1994. Transport of a dissolved-phase plume from a residual solvent source in a sand aquifer. *Journal of Hydrology*, 159, 27-41.

Robin, M.J.L., A.L. Gutjahr, E.A. Sudicky, and J.L. Wilson. 1993. Cross-correlated random field generation with the direct Fourier transform method. *Water Resources Research*, 29(7), 2385-2397.

Russell, D.L. 1992. Remediation manual for petroleum contaminated sites. CRC Press.

Scharlemann, J.P.W., and W.F. Laurance. 2008. How green are biofuels? *Science*, 319 (5859),43-44.

Schirmer, M., J.M. Molson, E.O. Frind, and J.F. Barker. 2000. Biodegradation modeling of a dissolved gasoline plume applying independent laboratory and field parameters. *Journal of Contaminant Hydrology*, 46, 339-374.

Schoenbaum, M. 2002. Environmental contamination, brownfields policy, and economic redevelopment in an industrial area of Baltmore, Maryland. *Land Economics*. 78(1), 60-71.

Schwartz, E. 1994. Review of investment under uncertainty. *The Journal of Finance*, 49(5), 1924-1928.

Schwartz, E. 1997. The Stochastic Behavior of Commodity Prices: Implications for Valuation and Hedging. *Journal of Finance*, 52(3), 923-973.

Schwartz, E. and L. Trigeorgis. 2001. Real options and investment under uncertainty. The MIT Press.

Sillan, R.K., M.D. Annable, P.S.C. Rao, D. Dai, K. Hatfield, W.D. Graham, A.L.Wood, and C.G. Enfield. 1998. Evaluation of in situ cosolvent flushing dynamics using a network of spatially distributed multilevel samplers. *Water Resources Research*, 34 (9), 2191-2202.

Smith, J.E., and R.W. Gillham. 1994. The effect of concentration-dependant surface tension on the flow of water and transport of dissolved organic compounds: A pressure head-based formulation and numerical model. *Water Resources Research*, 30(2), 343-354.

Smith, J.E., and R.W. Gillham. 1999. Effects of solute concentration-dependant surface tension on unsaturated flow: Laboratory and column experiments. *Water Resources Research*, 35(4), 973-982.

Solomon, D. K., R. J. Poreda, S. L. Schiff, J. A. Cherry. 1992. Tritium and Helium 3 as Groundwater Age Tracers in the Borden Aquifer. *Water Resource Research*, 28 (3), 741–755.

Sondermann, D. 1991. Reinsurance in arbitrage-free markets. *Insurance: Mathematics and Economics*, 10, 191-202.

Sorek, S., M. Kuznetsov, A. Yakirevich, and D Ronen. 2005. Multiphase and multi-component interactions through the unsaturated saturated zone field and model study. pages 171-185 in Reactive transport in soil and groundwater, edited by G. Nutzmann, Paolo Viotti and Per Aagaard, published by Springer Berlin Heidelberg, doi: 10.1007/b138022.

Stone, H.L. 1973. Estimation of three-phase relative permeability and residual oil data. *Journal of Canadian Petroleum Technology*, 12, 53-61.

Tesfamichael, A.A., A.J. Caplan, and J.J. Kaluarachchi. 2005. Risk-cost-benefit analysis of atrazine in drinking water from agricultural activities and policy implications. *Water Resources Research*, 41, W05015, doi:10.1029/2004WR003497.

Tiedeman, C., and S.M. Gorelick. 1993. Analysis of uncertainty in optimal groundwater contaminant capture design. *Water Resources Research*, 29(7), 2139-2153.

Torresetti, R., D. Brigo, and A. Pallavicini. 2007. Risk neutral versus objective loss distribution and CDO tranches valuation. Available at SSRN: http://ssrn.com/abstract=900784.

Trigeorgis, L. 1996. Real options: Managerial flexibility and strategy in resource allocation. Cambridge: The MIT Press.

Turckea, M. A., and B. H. Kueper. 1996. Geostatistical analysis of the Borden aquifer hydraulic conductivity field. *Journal of Hydrology*, 178 (1-4), 223-240.

UK Environment Agency. 2003. Brownfield Land Redevelopment: Position Statement. Available at http://www.environment-agency.gov.uk/static/documents/Research/brownfield_land_908146.pdf.

Unger, A.J.A., P.A. Forsyth, and E.A. Sudicky. 1996. Variable spatial and temporal weighting schemes for use in multi–phase compositional problems. *Advances in Water Resources*, 19(1), 1–27.

United States Air Force (USAF). 2006. Guide for the Assessment of the Vapor Intrusion Pathway. prepared by Douglas N. Cox, Mitretek Systems, Inc for Air Force Institute for Operational Health, Risk Analysis Directorate, Risk Assessment Division.

US Environmental Protection Agency (EPA). 1999. A Sustainable Brownfields Model Framework. EPA-500-R-99-001.

US Environmental Protection Agency (EPA). 2002. Draft guidance for evaluating the vapor intrusion to indoor air pathway from groundwater and soils. Washington D.C.: Office of Solid Waste and Emergency Response. Available at www.epa.gov/correctiveaction/eis/vapor/complete.pdf .

US Environmental Protection Agency (EPA). 2008. Brownfields Technology Primer: Vapor Intrusion Considerations for Redevelopment. EPA 542-R-08-001. Available at http://www.brownfieldstsc.org/pdfs/BTSC%20Vapor%20Intrusion%20Considerations%20for%20Redevelopment%20EPA%20542-R-08-001.pdf.

Vrugt, J.A., C.G.H. Diks, H.V. Gupta, W. Bouten, and J.M. Verstraten. 2005. Improved treatment of uncertainty in hydrologic modeling: combining the strengths of global optimization and data assimilation. *Water Resources Research*, 41, W01017, doi:10.1029/2004WR003059.

Ward, C. H., J.A. Cherry, and M. R. Scalf. 1997. Subsurface restoration. CRC Press.

Wladis, D., L. Rosen, and H. Kros. 1999. Risk-based decision analysis of atmospheric emission alternatives to reduce ground water degradation on the European Scale. *Ground Water*, 37(6), 818-826.

Woll, B., J. Mack, F. Ellerbusch, and J.R. Vetter. 2003. Facilitating Brownfield transactions using triad and environmental insurance. *Remediation*, 13(2), 113-130.

Woodbury, A.D., and E.A. Sudicky. 1991. The Geostatistical Characteristics of the Borden Aquifer. *Water Resources Research*, 27 (4), 533-546.

Wyllie, M.R.J. 1962. Relative Permeability, in *Petroleum Production Handbook*, vol. II, *Reservoir Engineering*, edited by T.C. Frick and R.W. Taylor, McGraw-Hill. New York.

Zhang, Y., G.F. Pinder, and G.S. Herrera. 2005. Least cost design of groundwater quality monitoring networks. *Water Resources Research*, 41, W08412, doi:10.1029/2005WR003936.